DESIGN AND ENGINEERING OF NANOSTRUCTURED MULTIFUNCTIONAL ELECTROCATALYST FOR HYDROGEN EVOLUTION, OXYGEN EVOLUTION AND OXYGEN REDUCTION REACTIONS: TOWARDS THE DEVELOPMENT OF SUSTAINABLE ENERGY SYSTEMS

MANISHA

A thesis submitted for the partial fulfillment of
the degree of Doctor of Philosophy

Institute of Nano Science and Technology
Knowledge city, Sector-81, Mohali 140306, Punjab, India

Indian Institute of Science Education and Research Mohali
Knowledge city, Sector 81, Mohali 140306, Punjab, India.

December 2021

Dedicated to

Humanity & Peace

Declaration

The work presented in this thesis has been carried out by me under the guidance of Dr. Ramendra Sundar Dey at the Institute of Nano Science and Technology, Mohali. This work has not been submitted in part or in full for a degree, a diploma, or a fellowship to any other university or institute. Whenever contributions of others are involved, every effort is made to indicate this clearly, with due acknowledgement of collaborative research and discussions. This thesis is a bonafide record of original work done by me and all sources listed within have been detailed in the bibliography.

Manisha

In my capacity as the supervisor of the candidate's thesis work, I certify that the above statements by the candidate are true to the best of my knowledge.

Dr. Ramendra Sundar Dey

Acknowledgements

"It has been said that astronomy is a humbling and character-building experience. There is perhaps no better demonstration of the folly of human conceits than this distant image of our tiny world. To me, it underscores our responsibility to deal more kindly with one another, and to preserve and cherish the pale blue dot, the only home we've ever known."

-Carl Sagan (Pale blue dot)

First and foremost, I bow in reverence to **The Nature,** *and its technologies that always amaze me and inspire me to believe that no matter what "life goes on".*

I must say, the Ph.D. journey was wonderful and unforgettable. The journey shaped my carrier as well as me as a person. The accomplishment of the thesis work is a culmination of many people's efforts, whose support and guidance played an important role throughout my way towards its completion. I, therefore, would like to take this opportunity to extend my sincere gratitude, humility and appreciation to all those who stood by me and helped me during this odyssey of my Ph.D. even in tough times.

First of all, I would like to extend my heartfelt gratitude to my supervisor ***Dr. Ramendra Sundar Dey****, (Scientist, Institute of Nano Science and Technology, Mohali, Punjab, India) for giving me this opportunity pursue my doctoral research under his wonderful guidance. His tireless efforts and dedication towards research work have always inspired me and showed me a real direction to work for the betterment of humankind. His positive and energetic attitude helped me a lot to stand strong and stay focused even during difficult times. His research command, clear vision and exciting ideas helped me overcome the hurdles that I encountered during my research and thesis work. I am greatly privileged to work under his able supervision. I honestly hope to carry forward his enthusiastic pursuit for science and incredible work ethics to shape my future endeavors. Throughout my life, I will be grateful to him for always understanding the critical situations and providing sustained encouragement.*

I am grateful to ***Prof. Amitabha Patra,*** *The Director, INST, Mohali, and our former officiating director* ***Prof. H. N. Ghosh*** *for making a great working atmosphere and all the facilities required to complete our tasks during the PhD tenure. My special thanks go to* ***Prof. A. K. Ganguli,*** *INST, Founding Director, to set-up the pillar of this institution. I also wish to extend my gratitude to the* ***esteemed faculty members of INST,*** *for their guidance and affectionate conversations during this course of time. I am also grateful to all the supporting staffs of the institute for their kind help and cooperation.*

*I wish to extend my acknowledgement to P**rof. Abir De Sarkar,** Scientist, INST Mohali, for collaborating on one of my projects and helping me improve the quality of the thesis by providing the computational investigations.*

*I want to thank my Ph. D. monitoring committee members, **Dr. Kiran Shankar Hazra,** Scientist, INST Mohali, and **Dr. Dipankar Mandal**, Scientist, INST Mohali, for their insightful ideas, valuable time and motivations. I also want to thank **Dr. Bikas Kumar Jena,** for evaluating my SRF presentation and providing useful suggestion to improve my work.*

*I would like to thank and extend my sincere gratitude to the whole **INST family**, for maintaining an appreciable lab culture including team efforts and work ethics. I also want to appreciate the team work and corporation among different groups that we lived in our ex-laboratory, the **Faraday lab,** phase-10, Mohali. Thanks to a smoothly running mechanism established by the **Faraday Lab Committee**, every facility was within reach to carry out experiments and conduct research successfully. I am also grateful to all the **administrative and non-administrative staffs** for their continued and timely support. A special mention to the **security and technical staffs** who have always been there for any technical help.*

*I want to express my deepest gratitude to **INST, Mohali** and **SERB EMR** for providing fellowship, **IISER Mohali** for the Ph. D. registration., **INST, Mohali** for instrumental support, **DST INSPIRE** (DST/INSPIRE/04/2015/000337), **SERB EMR** (EMR/ 2016/000040) and **SERB CRG** (CRG/2020/005683) funding agencies for providing financial support regarding my research.*

*I would like to take this opportunity to thank my M.Tech supervisor, **Dr. Prakash Chand**, for his constant corporation and support. My deepest thank to **Mr. Abhinav** (Engineer, BSNL), my B.Tech teacher, who helped me to clear my GATE examination. His moral thoughts and humility deeply inspired me to think beyond the degree, practice humanity and deal kindlier with one another. I would also want to take this opportunity to thank my school teacher **Late. Mr. A.K Ghatak**, who noticed that student who eventually remain un-noticed. He actually poured the feeling of gratitude and kindness in me.*

*I would like to give my special thanks to my laboratory, DENanoMat group. I never felt alone instead for being far away from home because of my labmates. I must say, officially they are my labmates but they are much beyond that, like my home, my family. I want to sincerely acknowledge them since I share a warm bond with them. First of all, I would like to thank **Navpreet**, she is my personal mentor and a very good friend, no matter what, I ever feel any kind of confusion or problem, she is always there to guide me and support me with love and care. Her research attitude is worth appreciable, which always motivated me. I want to thank **Dr. Taniya Purkait**, the first student of DENanoMat group, she has always been a backbone of our lab with a very helping nature. She was always there whenever I needed her. I want to thank **Dr. Sabuj Kanti Das,** (my food and Ghazal partner) for his constant guidance, emotional support and care throughout. His vision and dedication towards life always motivated me. Thanks to **Ashmita Biswas, Sakshi Bhardwaj** and **Manami Banerjee** for always been there with me like a sister and providing a warm ambience with their presence. I would like to acknowledge **Mr. Greesh**, he is a good friend with a very helping attitude. I would like to thank **Ms. Tribani Boruah** for being always nice and providing a helping attitude. My special thank goes to **Mr.***

__Zubair Bashir__, he helped me a lot in the compilation of this thesis work. Along with that his disciplined and kind behaviour always amaze me. I consider myself fortunate enough to have worked with such wonderful people who have helped tremendously to maintain a healthy lab environment. I cherish our friendly banters as well as stimulating scientific discussions over the never-ending chai breaks. I also wish to extend my thanks to the members who joined our lab at different phases of my Ph. D. and contributed significantly. Special thanks to __Subhajit Sarkar, Nitish__ and __Bikram Ghosh__ from whom I learned a great deal of research crafts during their period at our lab. It had also been a wonderful learning experience to help and learn with __Prashant, Sumukh, Athira__ and __Ghulam__ when they were interning with our group.

__Friends__ are the integral part of our life and they need to be acknowledged and appreciated, because without their support and encouragement. I am indebted to my friends, __Rejaul__, __Ritika, Raihaan__ and __Varun__ for sharing an amazing companionship and beautiful memories. Their emotional support, love and care including my health emergencies and others helped me to stand again whenever I fall. My special regards for __Dr. Nitya, Dr. Krishna, Dr. Rajendra, Dr. Naimat, Deepika, Dr. Arti, Ravi, Pradeep, Amal, Himadri, Hari, Ashish, Shilpa, Sanjhal, Suman__ and __Babita__ for being such a beautiful human with amazing souls. My heartiest regards go to my friends outside the INST family, __Neelam, Aditya, Richa, Neeraj, Ravi, Praveen, Sanghmitra and Abhishek__ for always being just a call away. I owe a deep sense of gratitude to my childhood friend __Late Abhinav__ (Bittu) for being an inspiration always.

Finally, my deep and sincere gratitude to my family for their continuous and unparalleled love and support, which always counts as my strength. Their patience and sacrifices will remain my inspiration all my life. __My father__ and __my mother__ who always taught to help others and practice humanity which have always helped me to embrace myself as a person and aided me to blend in and receive love and care from others. I would like to thank my __Ammajee__ (grandma) for being a good friend and providing a boundaryless communication, regardless of anything and inspiring to develop a reading habit by encouraging to read story books. I hereby, want to acknowledge __my uncles__ for so much love and care since my childhood. I would like to thank my husband, __Mr. Yogendra and In-Laws family__, for their corporation and support. I am also very much grateful to my extended family members, especially __my paternal and maternal uncles and aunts__, who have taken good care of my parents and me, which helped me to focus more on my work. My special thanks to my siblings, __Mukund, Madhumita__ and __Mayank__ for sharing an immense bond of love, trust and togetherness. I thank my cousin brothers and sisters for their support and encouragements. I am thankful to __my grandparents__ for providing me such a beautiful family who has always encouraged me to pursue my dreams in life. This journey would not have been impossible without them, and thus dedicate this milestone to them.

This work is never the work of an individual. It is more a combination of ideas, suggestions, reviews, contributions and efforts of many. I wish to express my appreciation to all those, with whom I have worked, interacted, and whose thoughts and insights have helped me in furthering my knowledge and understanding of the subject.

Date: *Manisha*

Abbreviations

TMO	Transition metal oxides
TMPs	Transition metal phosphides
IPA	Isopropyl alcohol
PVA	Poly(vinyl) alcohol
Cuf	Copper foam
Nif	Nickel foam
EES	Electrochemical energy storage
ORR	Oxygen reduction reaction
GCE	Glassy carbon electrode
RDE	Ring disk electrode
RRDE	Rotating ring disk electrode
SCE	Saturated calomel electrode
RHE	Reversible hydrogen electrode
CV	Cyclic voltammetry
LSV	Linear sweep voltammetry
GCD	Galvanostatic charge discharge
EIS	Electrochemical impedance spectroscopy
XRD	X-ray Diffraction
FTIR	Fourier transform infrared spectrophotometer
BET	Brunauer Emmett Teller
XPS	X-Ray Photoelectron Spectroscopy
SEM	Scanning electron microscopy
TEM	Transmission electron microscopy
HRTEM	High resolution transmission electron microscopy
SAED	Selected area electron diffraction
EDX	Energy dispersive X-ray spectroscopy
DFT	Density functional theory
C_{sp}	Specific capacitance
R_{ct}	Charge transfer resistance
C_{dl}	Double layer capacitance
$E_{1/2}$	Half wave potential
OCP/OCV	Open circuit potential/voltage
J_{sc}	Short circuit current density
E_{cell}	Device energy density
P_{cell}	Device power density
GC	Gas chromatography
ECSA	Electrochemically active surface area
RF	Roughness factor
HAADF-STEM	High-angle annular dark-field scanning transmission electron microscopy

Abstract

The facile synthesis of highly durable, low-cost and robust electrocatalyst for hydrogen generation from water is vital to address the existing environmental issues as well as to provide environmental-friendly clean and green energy supply. The generation of hydrogen via water electrolysis driven from solar power opens up an attractive route to accoplish energy technologies in a fully renewable fashion. Noble metal-based catalysts such as Pt/C and RuO_2 are considered to be the most active electrocatalyst for the generation of hydrogen and oxygen via water splitting, but their limited availibility and high cost prevent them to be used in practical and global-scale applications. Therefore, it is highly desirable to achieve a highly active electrocatalyst which outperforms the activity of noble-metals, which can acts as an electrode material for hydrogen evolution reaction (HER), oxygen evolution reaction (OER) and oxygen reduction reaction (ORR). Present work highlights the design and engineering of electrocatalyst for water oxidation reaction as well as refects the integration of water electrolyzer with solar cell, in order to get hydrogen fuel in a renewable fashion. Along with that the introduction of metal air battery active electrocatalyst in also highlighted to store power in order to receive hygrogen fuel in a fully renewable and non-sporadic fashion. The current research will give us a glimpse towards a way for device engineering towards sustainable energy system in order to supercede the exsiting energy technology which is based on fossil fuels.

TABLE OF CONTENT

Appendix

Appendix B Conference attended

List of figures

List of tables

Chapter 1

Introduction

Abstract: This chapter gives a glimpse of the current energy scenario worldwide and various global challenges to accomplish the current energy demands. The introduction to hydrogen economy and its various production methods have been highlighted. The advantages of using water electrolysis for hydrogen production and the basic mechanism are also discussed. Along with that various parameter for catalyst selection as well as the highlights in the design and engineering of electrocatalyst are placed. An introduction to hydrogen evolution reaction (HER), oxygen evolution reaction (OER) and oxygen reduction reaction (ORR) and the underlying mechanism is covered in this section of the thesis. The development of sustainable energy systems such the hydrogen generation using solar power is considered as a highly acceptable method for energy generation. To generate H_2 from water splitting in a fully renewable and non-sporadic way, the water electrolyzer unit along with solar cell must be integrated with some storage/battery unit, because solar cell mostly depends on climatic conditions. The introduction of metal-air battery (MAB) is highlighted, which requires an electrocatalyst capable of oxygen reduction reaction as well as oxygen evolution reaction. The rational design and engineering of an electrocatalyst towards efficient HER, OER and ORR is been highlighted in this section. Finally, the brief summary of the thesis work, motivation and future perspective of the thesis is discussed.

1.1 Energy

Energy is the backbone of human existence. The energy demands and needs have been compensated by the oxidation of fuels and foods, which made it conceivable for mankind to survive on earth for centuries.[1] Because of environmental concerns and growing energy demands, it has been a challenge for the researchers to develop efficient, clean and renewable energy technologies to replace the conventional energy systems that are mostly generated from the burning of fossil fuels.[2] The rapid innovations in the technologies, the decline in the renewable energy budgets, extensive electrification, refining energy efficiencies, technology breakthrough, concern towards the environmental issues, altogether making it possible to wonder a sustainable future.[3]

1.1.1 Current scenario

In the age of accelerating change, the attempt to clamp down climate change and accomplish sustainable evolution is firming the momentum of the energy transformation worldwide. According to the Statistical Review of World Energy 2020, oil remained on the top having a 33% share of all energy consumption.[4] Rest, the global energy consumption comes from natural gas (24%), coal (27%), hydropower (6%), nuclear power (4%), and renewables (6%). So, in total, 84% of the global energy consumption is accomplished by the use of fossil fuels as shown in Figure 1.1. Presently, our civilization consumes about 17.7 TW of power counting all the sources of energy and will go up to 40 TW by 2040. The burning of fossil fuels compensates a huge amount of energy demand. The burning of fossil fuels is causing toxicity to the environment by generating

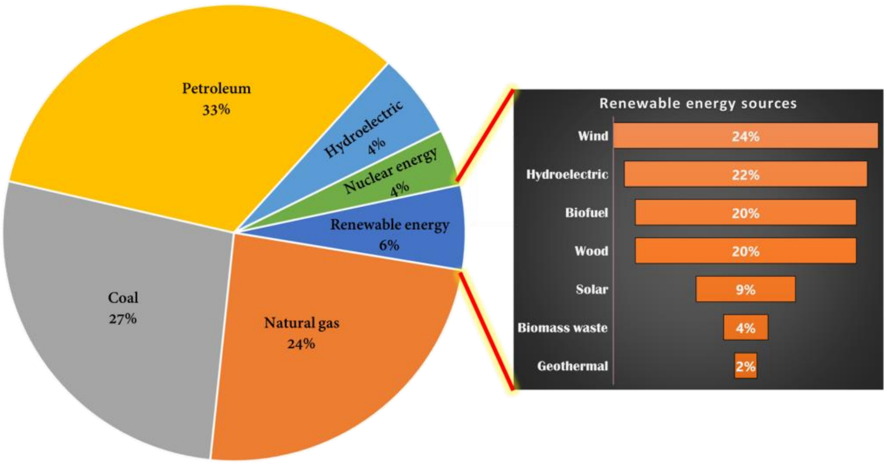

Figure 1.1 *Pie chart showing the percentage of energy from different sources*

greenhouse gases (carbon dioxide, methane, nitrous oxide and fluorinated gases), which leads the planet towards global warming.[5]

1.1.2 Global challenges

It has been estimated that the world energy consumption by 2030 may raise upto two-third as compared to today's statistics. The energy coming from fossil fuels such as coal, petroleum, and natural gases will remain the major sources of energy in the near future according to International Energy Agency (IEA). The oil consumption solely depends upon the rise in the transport sectors. The four major challenges will be encountered by the energy industry in the coming era.[1]

- Oil scarcity
- Energy security
- Environmental degradation
- Meeting the energy demands

These challenges require government initiatives, social awareness, industrial innovations, economic and political impacts, rise in energy efficiency, etc. to fulfil the major challenges that the world is going to encounter in near future. The growing use of fossil fuels will eventually toxify water, air and land and even rising CO_2 levels in the atmosphere.[6] Thus, the revolution for a move from carbon to non-carbon-based economy is greatly expected to confront the growing pollution. So, an active role of the government is required for making decisions, cooperation between the nations, environmental clean-up as well as supporting in the finance towards the sustainable energy technologies.[7–9]

1.1.3 Panacea of the problem

The climate goals can be met by acceleration in the power sector as well as considering the environmental issues. A smooth move from fossil fuel to an alternative energy source, which is renewable in nature, is urgently in demand. The energy generated from renewable energy sources such as wind, solar, hydro, geothermal and biomass must be integrated in order to confront the environmental problems that are arising from the burning of fossil fuels. One such alternative is hydrogen gas, when used as a fuel (H_2). H_2 as fuel produces clean and green energy because upon burning in a fuel cell, it gives only water as a by-product and thus gives zero carbon footprints and CO_2 emission.[10]

1.1.3.1 Hydrogen economy: Renewable energy system

Due to the rapid development in the field of renewable energy, the worldwide energy transformation is gearing momentum. Hydrogen as a fuel has been explored as an alternate energy source to alleviate the emission because when hydrogen is used in a fuel cell, imparts no pollution and gives only water as a by-product. Also because of its high energy density (three times than combustion of gasoline/mass), H_2 as a fuel is highly appreciable. The main advantage of hydrogen is that it can be produced locally. So, the places, which are dependent on external energy supplies, can be benefited immensely.

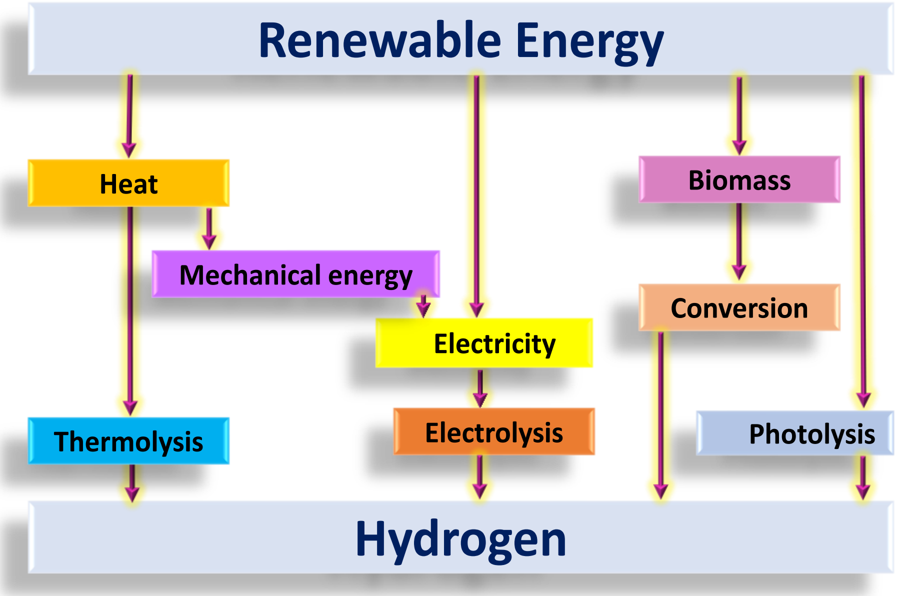

Figure 1.2 *Different ways for the production of hydrogen using renewable energy.*

There are many roots for the production of hydrogen, such as water, gas, biofuels, oil, etc. (Figure 1.2), but its production in a sustainable way is highly appreciable. The production of hydrogen from water splitting has been known to be the best among all the techniques for its generation due to the abundance of water on the planet as well as an easy and eco-friendly production process. Apart from water splitting, there are some important hydrogen production methods that are adopted worldwide.

1.1.3.2 Hydrogen production processes

For the production of hydrogen, it must be separated from the other products in the form of molecules during the generation. There are different ways of hydrogen production that are been adopted widely for its use as a fuel as shown in Figure 1.3.[11–13] There are three categories of the hydrogen generation based on the energy sources for its production. For example, hydrogen generation from renewable energy is known as green hydrogen.

Brown hydrogen is the hydrogen that generates from the burning of coal. The hydrogen produced from natural gases or oil is known as grey hydrogen. Some of the methods, which are mainly used, are listed below.

- Steam reforming
- Coal gasification
- Photochemical water splitting
- Electrochemical water splitting
- Photo-biological water splitting

The two common techniques from which the production of hydrogen is mainly adopted are steam-methane reforming and water electrolysis. The steam reforming method is widely used for commercial hydrogen production. Among steam reforming, steam-methane reforming is practiced by commercial hydrogen producers. In steam-methane reforming process, hydrogen atoms are separated from the carbon atoms present in the methane at a temperature of (1300°F to 1800°F) under a pressure of 3-25 bars. Carbon monoxide and a very small amount of carbon dioxide are produced as a by-product when methane is reacted with steam in the presence of catalyst.[14] The source of methane gas for hydrogen production is mainly natural gas. Biomethane is also a source for steam reforming, which generates from landfill/biogas. This is usually used in fuel cell power plants.

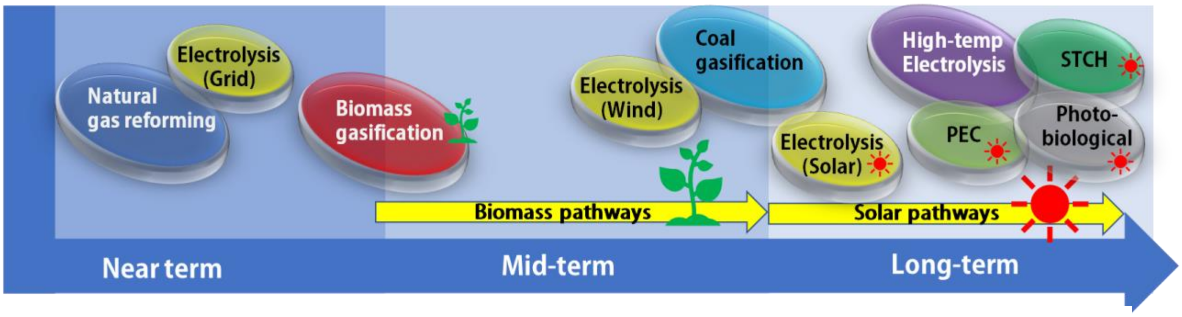

Figure 1.3 *Schematic illustration of near term, midterm and long term* H_2 *fuel generation*

Electrolysis takes electricity to split water into hydrogen and oxygen. The process commonly known as the power-to-gas process, encompasses power as electric current and gas as hydrogen. The production of hydrogen from electrolysis is known to be the purest. To check if any other gases are not present along with hydrogen and oxygen, faradaic efficiency is calculated. In this way, the hydrogen generated from water electrolysis is known to be perfect for their use in fuel cells. The electric current for electrolysis should not come from grid power which generates from fossil fuels (coal, petroleum and natural gases) in order to achieve fully renewable hydrogen fuel generation. In this way, the CO_2 emission and their effect on the environment indirectly relate to electrolysis. Rather, the electric current should come from the sources such as wind, solar, hydro energy.

1.1.3.3 Solar to hydrogen fuel generation

Among all the carbon-free sources, solar energy is considered to have great potential to efficiently replace fossil fuels. To utilize solar energy in order to gain a sustainable future, two major challenges need to be overcome. The first is to integrate any storage system along with photovoltaic for storing the electric current in order to achieve a non-intermittent energy supply. The second challenge is to utilize solar power to generate clean and green fuel for industrial, housing as well as transportation divisions.

There are three processes that are used to generate hydrogen fuel from solar energy: electrolysis of water by solar generated electricity (electrochemical), water splitting using direct solar power (photochemical) and by the combination of both solar and electric energy (photoelectrochemical) as shown in Figure 1.4. The photovoltaic electrolysis was first demonstrated in 1983 by Florida Solar Energy Centre under funding from NASA Kennedy Space Centre. This is a little weird to think that we require electricity to generate hydrogen fuel to again convert that fuel into electricity even when we can generate power using direct sunlight from solar cell, which is well established. The idea and the whole scenario are to avoid any climatic conditions so that we can generate electricity when and where needed. This is the beauty of this whole idea. Although, the phovoltaic power integrated with conventional batteries is commercially well established,

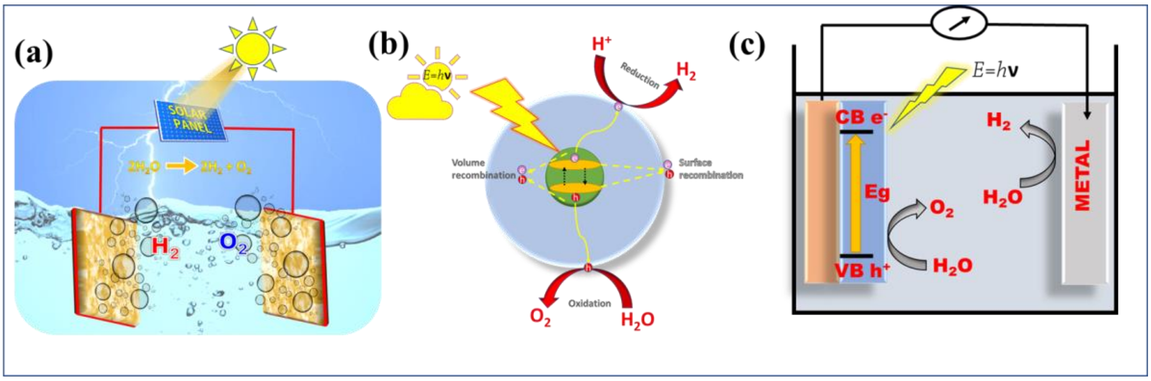

Figure 1.4 *(a) electrochemical water splitting (b) photochemical water splitting (c) photo electrochemical water spitting.*

but due to the bulkiness, short life and expensive nature of batteries it is demanding a substitute. On the other hand, solar-driven water splitting process is gaining much attention because of its easy generation as well as non-complex storage system, where the stored fuel can be applied to the fuel cell for electricity generation. [15–17]

1.1.3.4 Hydrogen economy challenges

For the practicality of hydrogen economy, there are still many challenges that need to be worked upon. Technical issues like stability of the electrode material, electrolytes, and reliability still need to be upgraded. For large-scale hydrogen production, system integration, transportation, infrastructure as well as proper storage planning concerns the cost of the system.

Table 1.1 *The practicality of hydrogen economy; a roadmap.*

Technology	Technical feasibility	Market introduction	Popularization	Complete popularization
Hydrogen power generation		Verification of hydrogen mixed power generation	Verification of hydrogen-only power generation	
Fuel cell for vehicle		Long durability fuel cell vehicle (FCV) for business Use		Precious metal-catalyst
		Technologies for mass production		
Fuel cell for household				
Fuel cell		Long	Cost reduction	Precious metal-

for business		durability realization		catalys
Hydrogen station		Adjustment in regulation/ standard Low-cost station	Security measures for hydrogen economy	
Hydrogen transport, storage, and production	Verification of large-scale hydrogen transportation		Inspection of export/import transportation of hydrogen	Development and verification of CO_2-free hydrogen supply chain

The production of hydrogen and its economic establishment involve technological progress from catalyst design to application. Several steps like production, storage, portability and its operation are involved for its end-to-end utilization. The most popular use of hydrogen technology is its use in fuel cell and fuel cell vehicles (FCV). But there are several issues that are associated, which are listed below.

- Technical compatibility
- Efficiency
- The durability of the system
- Cost
- Selection of the catalyst
- Electrolytes

The improvement in the comprehensive efficiency of the catalyst plays a significant role in a fuel cell. For large-scale hydrogen production, say, at mega watts (MWs), there are lot of parameters that are needed to be verified to supersede the existing coal/petroleum-based energy technology.

1.2 Electrocatalysis

1.2.1 Introduction and historical background

The most widely used method for hydrogen production practised today is the methanol reforming, burning of fossil fuels and water electrolysis [$2H_2O(l) \rightarrow 2H_2(g) + O_2(g)$:

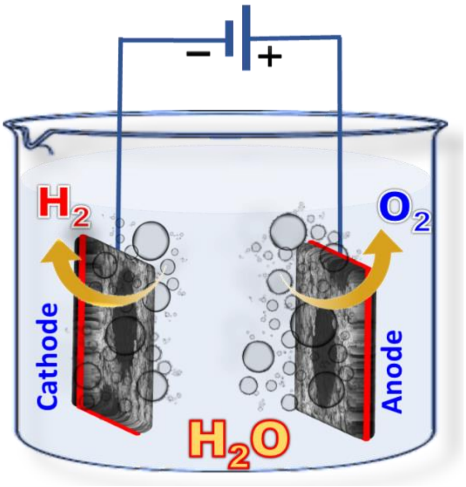

Figure 1.5 *Schematic of electrochemical water splitting.*

$\Delta G° = +237.2$ KJ mol^{-1}, $\Delta E° = 1.23$ V (T = 25°C, P = 1 atm)]. The main problem associated with the production of H_2 by burning of fossil fuels is the production of CO_2, which results in global warming as well as compromises the purity of generated H_2. Methanol reformer methods also produce CO_2 gas as a by-product. Therefore, hydrogen production in a green and clean way is highly desirable for sustainable energy future. Researchers are mainly trying to solve this issue by exploring the production of H_2 by electrocatalysis, photocatalysis and photoelectrocatalysis, where the molecules of water split into hydrogen and oxygen, which is further used in a fuel cell. In this section we will discuss the electrochemical water splitting process and the role of catalyst and design and engineering of the catalyst. The use of fuel cell is an excellent way for the practice of sustainable energy future. According to IEA, the hydrogen production from water electrolysis will reach about 22% till 2050, which is quite a good participation in the fuel energy.[18]

The electrocatalysis of water takes place by splitting the water into H_2 and O_2 in the presence of electric current and to reduce the potential to split water, some kind of catalyst is employed in an electrochemical cell as shown schematically in Figure 1.5. Water splitting comprises two redox half-cell reactions, that is hydrogen evolution reaction (HER) and oxygen evolution reaction (OER). The H_2 will be produced on the cathode and O_2 will be produced on the anode with the help of membrane. PEM (proton exchange membrane) cell membrane is used to produce H_2 and O_2 in two different compartments and allows the passage of protons through it.

1.2.2 Thermodynamics

These reactions are kinetically sluggish because of the involvement of multi-electron/proton transfer during the electrolysis. Therefore, the acceleration in the reaction rate of the catalyst is highly desirable for efficient electrolysis. Noble catalysts like platinum, ruthenium, and iridium are mainly known to be excellent catalyst for water splitting but due to their scarcity and high cost these catalysts are not widely used. The electrolyte used for water splitting is usually acidic and alkaline media. Generally, OER is done under alkaline conditions and HER is performed under acidic media. But in order to accomplish full water splitting, both the OER and HER must takes place in the same electrolytic media. Electrocatalytic water splitting can be conducted in both acidic and alkaline solutions. Mostly, alkaline water electrolyzer are favorable over the acidic one because acidic electrolyte hampers the stability of the electrocatalyst as well as the membrane used in the electrolyzer.[19] But alkaline water electrolyzer are being already commercialized and well established. Therefore, for the practicality of alkaline water electrolysis, alkaline HER must occur efficiently, which is really kinetically sluggish process. The general reaction taking place in water splitting is shown in equation 1.1, 1.2 and 1.3 as:

$$2H_2O + 4h^+ \rightarrow O_2 + 4H^+ \quad \text{(OER at anode)} \qquad (1.1)$$

$$4H^+ + 4e^- \rightarrow 2H_2 \qquad \text{(HER at cathode)} \qquad (1.2)$$

$$2H_2O + \text{Energy} \rightarrow 2H_2 + O_2 \quad \text{(Overall)} \qquad (1.3)$$

1.2.3 Critical parameters for catalyst selection

Based on the activity and efficiency, there are few parameters used to evaluate the catalytic activity of the electrocatalyst like overpotential, Tafel slope and exchange current density, stability, faradic efficiency and turnover frequency.[20] All the parameters are discussed in brief below section.

1.2.3.1 Overpotential

Water electrolysis never occurs at a theoretically determined potential. The difference between the experimental value of voltage and the thermodynamically calculated reduction (H_2, E_0=0.00 V vs RHE)/oxidation (O_2, E_0 = 1.23 V vs RHE) potential is known as overpotential (η). The fundamental requirement of a water splitting system is equilibrium potential E_{eq} = 1.23 V. Thus, a voltage of 1.23 V must be supplied to the water splitting unit to generate H_2 at a particular rate. The overpotential also depends upon the rate of kinetics of water electrolysis reaction taking place between catalyst and electrolyte interfaces as well as design of water splitting unit as shown in equation 1.4:

$$\mathrm{E_{OP}} = \mathrm{E_{eq}} + \eta_\mathrm{A} + \eta_\mathrm{C} + \eta_\Omega \qquad (1.4)$$

Where, E_{OP} is the overall overpotential, η_A is the overpotential required overcoming the kinetic barrier at anode (OER) and η_c is the overpotential for cathodic kinetic barrier, η_Ω is the overpotential due to some additional resistances such as contact and solution resistances. The η_Ω drop in the voltage is known as *iR* drop, which is needed to be subtracted from the overall experimentally calculated potential.

1.2.3.2 Tafel slope

The connection between the current (i) and voltage (V) is very fundamental in electrochemical study of the catalyst. The electrode kinetics change by varying the voltage changes, which as a result changes the current. For basic understanding of electrocatalytic reaction, Tafel plot analysis is very important. Butler and Volmer equation is the root of Tafel slope and Tafel equation[21] as shown in equation 1.5 and 1.6:

$$\mathrm{i} = \mathrm{i_0}\{\exp\left[\frac{\alpha_\mathrm{anodic}\mathrm{nF}\eta}{\mathrm{RT}}\right] - \left[\frac{\alpha_\mathrm{cathodic}\mathrm{nF}\eta}{\mathrm{RT}}\right]\} \qquad \text{(Butler - Volmer equation) (1.5)}$$

$$\mathrm{i} = \mathrm{i_{anodic}} + \mathrm{i_{cathodic}} \qquad (1.6)$$

Where, $\mathbf{i_0}$ is the exchange current density, α_{anodic} is the coefficient (charge transfer) for the anodic reaction, $\alpha_{cathodic}$ is the coefficient (charge transfer) for the cathodic reaction, η is the overpotential, F is Faraday’s constant, R is gas constant and T is the temperature.

1.2.3.3 Stability and durability

The stability of the catalyst is a major parameter for splitting of water at industrial scale. The stability of the catalyst is generally accompanied using cyclic voltammetry, chronopotentiometry and chronoamperometry scan to test its degradation at certain constant parameter for more than 12 hours. After the degradation test, the shift in the overpotential at a certain current density (mainly 10 mA cm^{-2}) is compared with the initial overpotential. For a catalyst to be robust, efficient and stable, the shift in the overpotential at a particular current density should be as minimum as possible. Accelerated durability test (ADT) is the intentional conditions are applied to speed up the catalyst degradation by imposing harsh and rough circumstances. This can be achieved by long term cycling, chrono test at high current densities, multi current step chronopotentiometry etc.

1.2.3.4 Faradaic efficiency

Faradic efficiency is the efficiency by which the electrons delivered by external circuit are accomplished enough to drive the reaction for water electrolysis. The ratio between the experimental and theoretical amount of produced H_2/O_2 are needed for the calculation of faradaic efficiency. The comparison is done because along with the desired gas, some faradaic losses may occur due to the generation of by-products and heat during the reaction.

1.2.3.5 Turn over frequency (TOF)

The measure of number of moles of H_2/O_2 produced per unit time gives the value of turn over frequency (TOF) of the electrocatalyst. This is the very critical parameter for the analysis of the catalyst. The general formula for TOF is depicted in equation 1.7 as:

—— (1.7)

Where, I is current, N_A is the Avogadro constant, A is the geometrical surface area, n is the number of electrons transferred, and Γ is the total concentration of catalyst.

1.2.4 Synthesis methods for electrocatalyst

Few well known routes for nanomaterial-based electrocatalyst synthesis are:

- Carbonisation[22]
- Chemical and hydrothermal methods[23]
- Pyrolysis and high temperature reactions[24]

But there are various problems associated with above mentioned synthesis routes such as; the catalysts are less stable because of the use of binder, the synthesis approach is very expensive and also leads to complexity, the duration for the synthesis of material is long, high temperature requirement for the reaction and also the reaction takes place in multistep. An advanced and very easy route for catalyst synthesis is a method called electrodeposition.

Figure 1.6 *Electrodeposition setup in the electrochemical workstation.*

- **Electrodeposition method**

The electrodeposition method (Figure 1.6) produces improved nanostructures such as less or defect-free, homogeneous layer of material deposition. More importantly, the catalyst synthesis can be done at room temperature and also the synthesis time is very less (even 1s), which leads towards cost effectiveness of the synthesis route. This method is mostly a single step process that makes it less complex compared to other synthesis routes. Also because of binder free material, the catalyst synthesized here is very efficient, stable and robust.[25]

1.2.5 Hydrogen evolution reaction (HER)

To achieve a Faradic efficiency of 100%, the molecules of hydrogen (2e$^-$ pathways) generation should be two times to that of oxygen (4e$^-$ pathways), and must be proportional to the amount of charge present in the electrolytic media.[26] During the water electrolysis, possible chemical reaction is shown in equation 1.8 and 1.9:

$$2H^+(aq) + 2e^- \rightarrow H_2(g) \qquad (HER) \qquad (1.8)$$

$$2H_2O(l) \rightarrow O_2(g) + 4H^+(aq) + 4e^- \quad (OER) \qquad (1.9)$$

Nicholson and Carlisle in 1789 were first observed this phenomenon of electrochemical production of hydrogen and oxygen. More than 500 industrial water electrolyzer units have been installed worldwide till date. Mainly, proton exchange membrane is used to separate both H_2 and O_2 gases. The discussion on the mechanism and thermodynamics that occurs during HER and OER in different electrolytic media is very essential before we move further. The reaction pathways and the polarization curve for HER are shown in Figure 1.7a and b.

Basically, the HER follow two unique reaction mechanisms, which are followed by three reaction steps.

Volmer reaction: This is also known as discharge process. Here, the electron is being transferred to the surface of the catalyst to capture a proton. As shown in equation 1.10, this transfer results in the generation of adsorbed atoms of hydrogen (H_{ads}) at the active sites of the catalyst:

$$H^+(aq) + e^- \rightarrow H_{ads} \qquad (Step\ 1, Volmer\ reaction) \qquad (1.10)$$

This Volmer step undergoes two different possible ways for the production of H_2, which is known as Heyrovsky and Tafel reactions.

In Heyrovsky route, which is also known as desorption step, takes place when the H_{ads} species is found to be low on the surface of the catalyst. And due to low coverage of the

$H_{ads,}$ these adsorbed species of hydrogen prefer to combine with the other proton and an electron for the generation of H_2 atom (equation 1.11):

$$H_{ads} + H^{+}(aq) + e^{-} \rightarrow H_2(g) \qquad \text{(Step 2a, Heyrovsky)} \qquad (1.11)$$

Tafel reaction route, which is also known as chemical desorption step, occurs when there is the sufficient coverage of H_{ads} on the active sites of the catalyst. The recombination of the H_{ads} species on the surface of the catalyst dominates when there is the high coverage of H_{ads} and which results in the production of H_2 as reflects from the equation 1.12:

$$H_{ads} + H_{ads} \rightarrow H_2(g) \qquad \text{(Step 2b, Tafel)} \qquad (1.12)$$

1.2.6 Oxygen evolution reaction (OER)

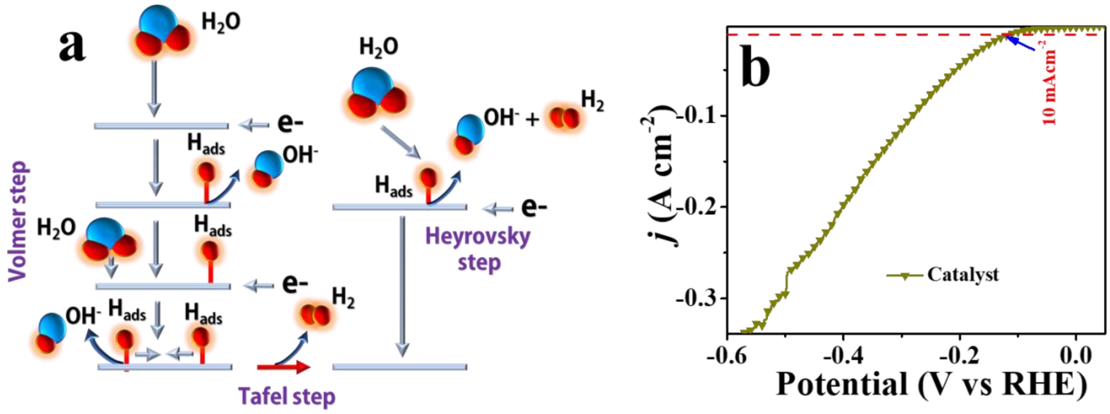

Figure 1.7 *(a) Hydrogen evolution reaction mechanism (b) HER polarization curve*

Thermodynamics of OER is similar in both acidic and alkaline media. For practical purpose the overpotential exceeds the thermodynamically obtained potential (1.23 V). The reaction pathways and the polarization curve for OER is shown in Figure 1.8a and b. Apart from the noble metal catalyst for OER, all the other catalyst generally involves the adsorption of both O and OH group on the surface of the catalyst.[27] The equations 1.13 and 1.14, involved are:

$$OH^{-} + * \rightarrow OH_{ads} + e^{-} \qquad (1.13)$$

$$OH_{ads} + OH^{-} \rightarrow O_{ads} + H_2O + e^{-} \qquad (1.14)$$

Where * is the active site of the catalyst and O_{ads} is the adsorbed oxygen on the catalyst surface. There are basically two pathways for the production of O_2 from the oxygen, which are adsorbing on the catalytic active sites. The first pathways are accomplished when the two O_{ads} couples with each other (equation 1.15):

$$\mathrm{O_{ads} + O_{ads} \rightarrow O_2} \tag{1.15}$$

And in the second step the O_{ads} reacts with OH^- to form intermediate OOH_{ads} species, which finally combines with OH^- to generate O_2 (equation 1.16 and 1.17):

$$\mathrm{O_{ads} + OH^- \rightarrow OOH_{ads} + e^-} \tag{1.16}$$

$$\mathrm{OOH_{ads} + OH^- \rightarrow O_2 + H_2O + e^-} \tag{1.17}$$

Similar trend follows for the generation of oxygen in neutral media but the Volmer reaction begins with water here as shown in equation 1.18, 1.19, 1.20, 1.21:

$$\mathrm{2H_2O + {*} \rightarrow OH_{ads} + H_2O + e^- + H^+} \tag{1.18}$$

$$\mathrm{OH_{ads} + H_2O \rightarrow O_{ads} + H_2O + e^- + H^+} \tag{1.19}$$

$$\mathrm{O_{ads} + H_2O \rightarrow OOH_{ads} + e^- + H^+} \tag{1.20}$$

$$\mathrm{OOH_{ads} \rightarrow O_2 + e^- + H^+} \tag{1.21}$$

Where * is the active site of the catalyst and O_{ads} is the adsorbed oxygen on the catalyst surface.

Following the Nernst equation, HER is favorable in acidic media while OER process is easily going in alkaline media. For demonstrating efficient water splitting, both HER and OER must be taking place in the same electrolyte media. But water splitting in acidic media is not favorable and some issues like the corrosion of the catalyst takes place

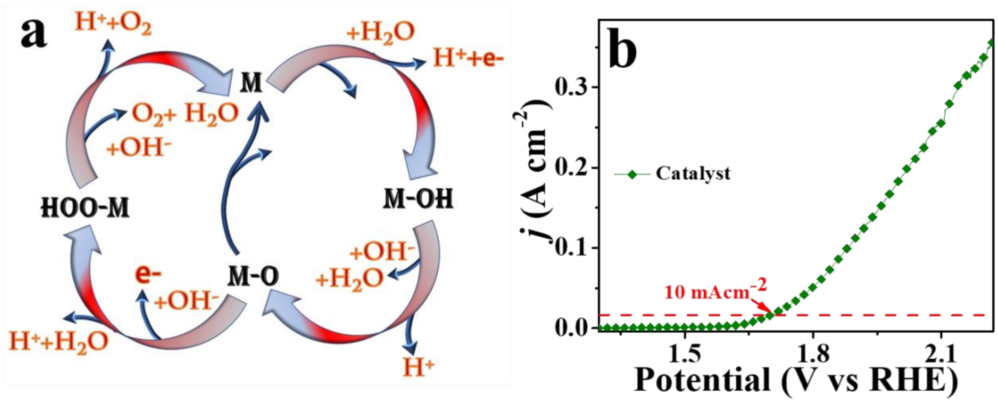

Figure 1.8 *(a) Oxygen evolution reaction mechanism (b) basic OER polarization curve*

and hampers the stability. The water electrolysis in basic media is highly acceptable for large scale hydrogen production but the main challenge associated with this is that the HER in alkaline media is kinetically very sluggish in terms of water dissociation and hydrogen binding energy, which leads to high overpotential and poor power competences in alkaline media. The reaction mechanism proposes that there is an extra barrier for the energy to overcome for the production of hydrogen.

1.2.7 Oxygen reduction reaction (ORR)

Because of the global climatic change and in the search of alternate energy source, oxygen electrocatalysis plays an important role in electrochemical energy conversion, generation as well as storage system. The oxygen reduction reaction (ORR) takes place at the cathode in the electrochemical reaction. The reaction pathways and the polarization curve for ORR is shown in Figure 1.9. Oxygen reduction reaction contains several steps and species like O, OH, HO_2-, H_2O_2, O_2 etc. The final O_2 involves the net transfer of four electrons and four protons. ORR is holding a very significant place in industries, because of the move for energy generation, conversion and storage towards renewable energy technologies etc. like fuel cells, metal-air batteries, etc.[28] Due to the complex reaction pathways, ORR demands a highly efficient electrocatalyst in order to lower down the barrier hill of the reaction steps.

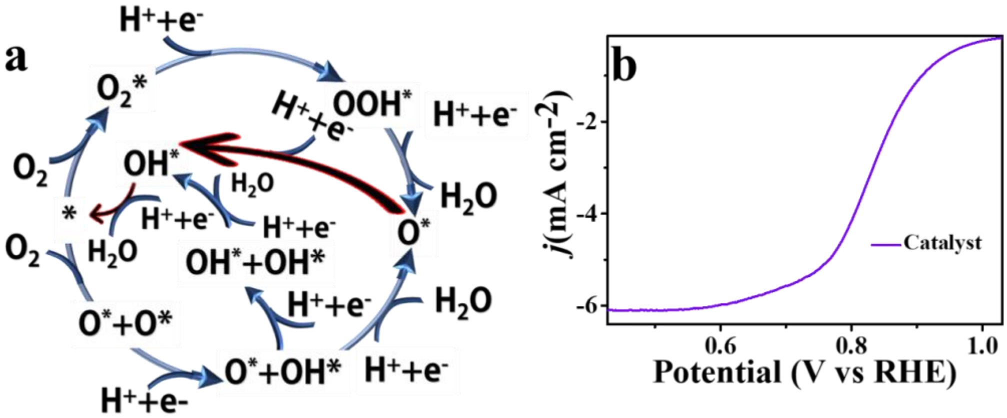

Figure 1.9 *(a) ORR mechanism and their corresponding steps. (b) ORR polarization curve.*

The standard reduction potential from conversion of O_2 to OH^- is 0.401 V vs SHE. For four electron pathways of ORR, the reaction follows the equation given below in equation 1.22:

$$O_2 + 2H_2O + 4e^- \rightleftharpoons 4OH^- \; ; \; E^0 = 0.401 \text{ V } vs \text{ SHE} \qquad (1.22)$$

An alternative four electron pathways, O_2 molecule is first converted into peroxide ion (equation 1.23):

$$O_2 + H_2O + 2e^- \rightleftharpoons HO_2^- + OH^-;\ E^0 = -0.076\ \text{V}\ vs\ \text{SHE} \qquad (1.23)$$

Followed by further reduction (equation 1.24):

$$HO_2^- + H_2O + 2e^- \rightleftharpoons 3OH^-;\ E^0 = -0.878\ \text{V}\ vs\ \text{SHE} \qquad (1.24)$$

Or disproportion reaction as shown in equation 1.25:

$$2HO_2^- \rightleftharpoons 2OH^- + O_2 \qquad (1.25)$$

1.3 Metal air batteries (MABs) and bifunctionalities of the catalyst towards ORR and OER

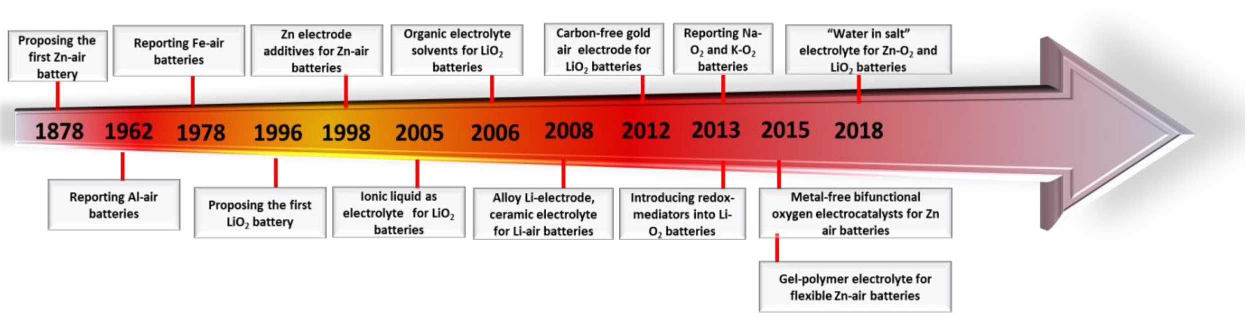

Figure 1.10 *A roadmap for the development of the metal air battery generation*

Because of the emerging energy storage technique and global energy demands, metal air batteries are gaining much attention in research. Because of their high energy density benefits over conventional storage systems, MABs are being researched at its peak in electric vehicle, power plants etc. There are several more advantages of MABs such as low cost, safety, eco-friendliness and stability. In MABs, OER and ORR reactions take place simultaneously at the catalyst, which is working as the cathode material. Therefore, the selection of the catalyst material is very critical in the fabrication of MABs. A roadmap for the progress in MABs is illustrated in Figure 1.10. Several metal oxides/hydroxides or sulphides/selenides, composites, heteroatoms, carbon etc. based catalyst are extensively reviewed and researched in past few decades for MABs catalyst selection.[29,30]

Table 1.2 *A comparison of different metals used in MABs*

Battery systems	**Fe-air**	**Zn-air**	**Al-air**	**Mg-air**	**Na-air**	**K-air**	**Li-air**
Year invented	1968	1878	1962	1966	2012	2013	1996
Cost of metals($kg^{-1})	0.40	1.85	1.75	2.75	1.7	~20	68
Theoretical voltage (V)	1.28	1.65	2.70	3.09	2.27	2.48	2.96
Theoretical energy density (Wh kg^{-1})	763	1086	2796	2840	1106	935	3458
Electrolyte for practical batteries	Alkaline	Alkaline	Alkaline or saline	Saline	Aprotic	Aprotic	Aprotic
Practical voltage (V)	~1.0	1.0-1.2	1.1-1.4	1.2-1.4	~2.2	~2.4	~2.6
Practical energy density (Wh kg^{-1})	60-80	350-500	300-500	400-700	-	-	-
Primary (P) or electrically rechargeable (R)	R	R	P	P	R	R	R

The attention on the electrolyte and its concentration as well as separator also plays a very important role in the stability of the fabricated MABs. Also, the presence of metal is very critical parameter, which also needs much attention. As shown in Table 1.2, the theoretical energy density value of Li-air battery is 3458 Whkg^{-1} due to the fabrication complexity, it is still not holding an admirable place in the design of MABs fabrication. On the other hand, Mg and Al-air batteries also have better theoretical energy density of 2796 Wh kg^{-1}, and 2840 Wh kg^{-1} respectively, but because of several non-issues associated with them like, corrosion, HER at metallic electrode as well as -electrically rechargeable nature, these batteries are not favorable for practical applications. Zn metal and the aqueous electrolytes in Zn-air batteries are much cheaper in cost as compared to Li metal and the electrolytes (non-aqueous) of Li-air batteries. All the sections of Zn-air batteries are quite stable towards moisture, thus making more favorable to fabricate and operate at ambient conditions.[31] Therefore, as compared to Li-ion batteries, it is easier to handle Zn-air batteries. A schematic illustration for ORR and OER taking place in Zn-air battery and corresponding polarization curve is shown in Figure 1.11. So, a trade-off of material fabrication cost as well as energy density is been practiced in the selection of metal in air-batteries. The mechanism and reaction taking place at the cathode as well as anode is given in equation 1.26, 1.27, 1.28, 1.29, 1.30 and 1.31 which is given below:

Anode:

$$\mathrm{Zn} = \mathrm{Zn}^{2+} + 2\mathrm{e}^{-} \qquad (1.26)$$

$$\mathrm{Zn}^{2+} + 4\mathrm{OH}^{-} \rightarrow \mathrm{Zn(OH)}_4^{2-}\ ;\ \mathrm{E}^0 = -1.25\ (\mathrm{V\ vs\ NHE}) \qquad (1.27)$$

$$\mathrm{Zn(OH)}_4^{2-} \rightarrow \mathrm{ZnO} + \mathrm{H_2O} + 2\mathrm{OH}^{-} \qquad (1.28)$$

$$\mathrm{Zn} + \mathrm{H_2O} \rightarrow \mathrm{Zn(OH)}_2 + \mathrm{H}_2 \uparrow \text{(also possible)} \qquad (1.29)$$

Cathode:

$$\mathrm{O}_2 + 2\mathrm{H_2O} + 4\mathrm{e}^{-} \rightarrow 4\mathrm{OH}^{-};\ \mathrm{E}^0 = 0.4\ (\mathrm{V\ vs\ NHE}) \qquad (1.30)$$

Overall reaction:

$$2\mathrm{Zn} + \mathrm{O}_2 \rightarrow 2\mathrm{ZnO}\ (\mathrm{E}^0 = +1.65\ \mathrm{V}) \qquad (1.31)$$

1.4 Fully-renewable and non-sporadic H_2 fuel generation system

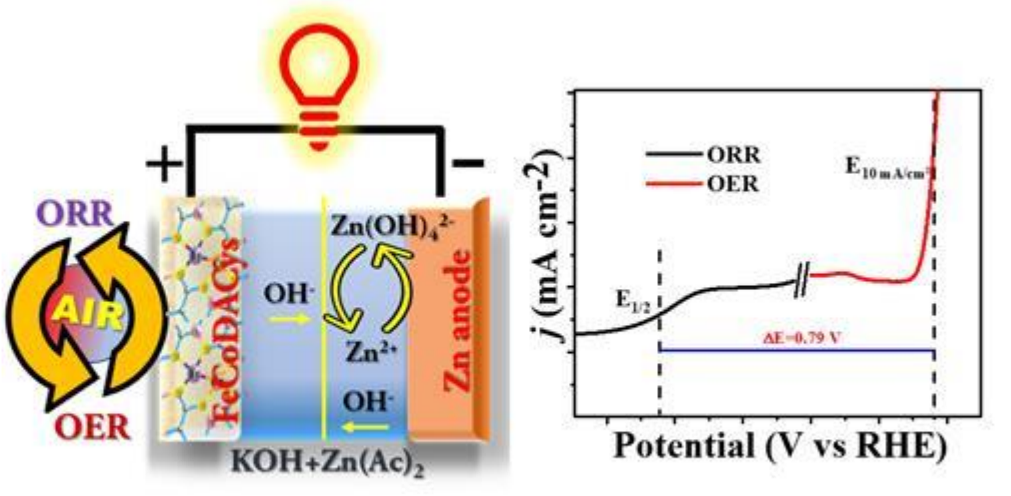

Figure 1.11 *(a) ORR, OER and reaction taking place in Zn-air batterys. (b) polarization curve for bifunctionality towards OER and ORR.*

Water can be directly broken into H_2 and O_2 for the generation of hydrogen gas as a fuel by using electrolysis effect, which was discovered more than 200 years ago. There are so many methods to generate hydrogen but the choice of electrolysis is one of the best ones since it does not pollute environment and also the hydrogen obtained here is of very high purity and can be easily and efficiently used in a fuel cell. However, an external power source is still desired to supply the required electricity for the dissociation of water. The breaking of water in the presence of sunlight is a best way to meet the demands worldwide in the field of energy. A conjectural design for the water electrolysis system, which will have its own power delivery capacity for future clean energy supply is of huge interest and obviously, is a challenge. Development of efficient multi-functional nanomaterial together with device architecture could furnish some lights on this postulation. Understanding the mechanism for storage and conversion of energy may bring hope in this field for the successful implementation of the novel concept. A schematic for the representation of existing self-powered water splitting is shown in Figure. 1.12 and 1.13.

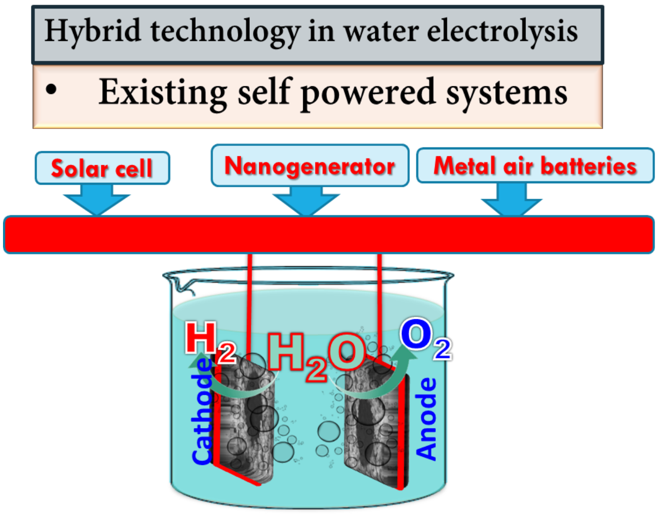

Figure 1.12 *Existing hybrid technology for water splitting.*

The electricity required to split water is still considered from non-renewable energy homes as the main contribution of grid power is fossil fuel. An alternative way to overcome this problem is to use a self-powered system that harvests ambient energy to generate power, which can be integrated with the water electrolyzer. However, the different abundant, easily accessible and renewable forms of energy like solar energy are dependent on weather condition and a continuous and online energy generation is not feasible due to its dependency on climatic condition and sporadic nature. The motivation

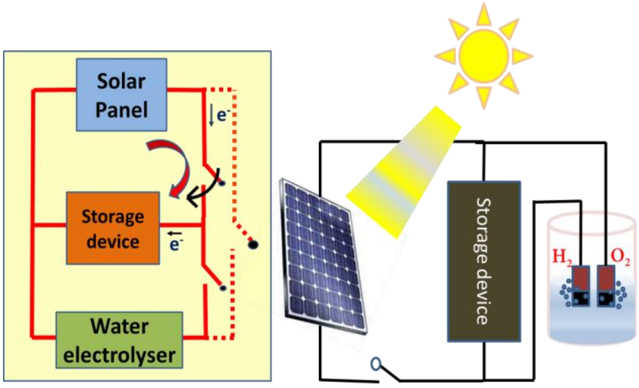

Figure 1.13 *Hybridisation of water electrolyser with solar cell and storage device fashion.*

of complete hybrid energy system of 'generation-storage-supply' is thus essentially required to store the energy generated from different origins in order to obtain a ceaseless and stable progression of water electrolysis whenever it is needed.

1.5 Design and engineering of electrocatalyst

The design and engineering of the catalyst is the main challenge for the researchers because an efficient catalyst plays a crucial role and are considered as the heart of the electrochemical water splitting system. Few parameters like overall cell overpotential (η), mechanical robustness, stability, faradaic efficiency (FE), turn over frequency (TOF) are few critically important parameters based on which a catalyst is been analyzed. Along with the above properties, the surface properties like hydrophilicity and aerophobicity of the catalyst actually plays the main role in the activity of the catalyst. Plenty of bubbles generates on the surface of cathode (H_2) and anode (O_2) during the process of electrolysis. This generation of bubbles on the surface causes the blocking in the diffusion of the electrolyte toward the electrode, which results in the increase in the ohmic resistance between the interface of electrode and electrolyte. This increase in the resistance eventually decreases the actual surface area of the catalyst, which is taking part in the electrochemical reaction, known as electrochemically active surface area (ECSA). Lack in the aerophobicity of the catalyst compromises the stability of catalyst by degrading their micro/nanostructures. Therefore, an efficient behavior of a catalyst, it must be superaerophobic as well as hydrophilic in nature. Researchers monitor this behavior of the catalyst by measuring

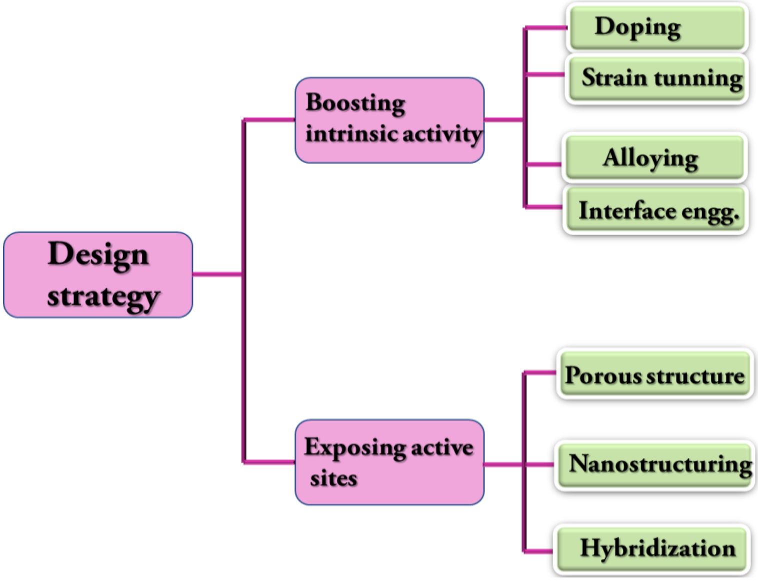

Figure 1.14 *Catalyst design strategies in catalyst synthesis.*

the contact angle and well as observing the bubble behavior that generates on the surface of the electrode during the electrolysis. The catalyst design strategies in illustrated in Figure 1.14.

Full water splitting is a thermodynamically arduous reaction and demands enormously efficient and active electrode materials that considerably accelerate the sluggish kinetics of two half reaction occurring at both cathode (HER) and anode (OER) simultaneously. Metal-air battery involves OER at anode and oxygen reduction reaction (ORR) at cathode. Therefore, electrocatalyst, the heart of hybrid system, is preferred to be trifunctional (HER, OER and ORR) in nature and have attracted immense research interest very recently. The catalyst for water splitting and metal-air battery with respect to commercialization and industrial applications needs to meet some demanding criteria like high current densities, low overpotential, mechanical robustness and durability. Many transitions metal-based phosphides, selenides, sulphides, nitrides, carbide etc. have been reported recently that partially meets the benchmarks.[32–36] However, conventional route for the development of an electrocatalyst involves sol–gel processing, dip-coating, spray pyrolysis, hydrothermal synthesis that involve time-consuming synthetic approaches, high temperature pyrolysis methods, complicated reaction kinetics with multiple steps, even though most of them are not self-supported at the current collector.

Strategic synthetic approaches and stepwise routes will be employed to create rational active sites to achieve superior catalytic activity. Therefore, the designing of active material and understanding the mechanism is very crucial in the field of water electrolysis and metal-air battery research. In past few decades, extensive research has been done in the exploration of better and efficient electrocatalyst, like transition metal oxides (TMOs), transition metal chalcogenides (TMCs), transition metal phosphides (TMPs), etc.[32,37,38] These metal chalcogenides and oxides-based catalyst have several advantages and qualities that favor the electrolysis in the very admirable fashion. Low-cost, porous structure, better electrical conductivity and stability etc. are the benefits of this type of catalyst that are being utilized in the electrochemical process. The engineering of this TMOs, TMCs as well as TMPs based compounds for integrating the active sites and tailoring the electronic behavior various practises like doping, creating defects, forming heterostructures, core-shells and interfaces are done which shows the improved activities to that of pristine catalyst. Theoretical studies of these catalysts for the analysis of electronic band tunings and synergistic effects taking place beneath are also playing an important role and go parallel with the experimental data and studies.

1.5.1 Non-precious materials for electrocatalysis

Hydrogen and oxygen-based energy is highly desirable for clean and green fuel source carrier with a very high energy density. Nobel metals such as Platinum (Pt) are well known for its activity and efficiency in HER. But due to the high price and less durable nature of Pt, the production of hydrogen at a large scale is limited. So, the catalyst selection is a very critical parameter in hydrogen generation. Therefore, a lot of research is being going on the catalyst design and engineering to achieve the efficiency of noble metal with a good stability. Transition metals like, Co, Fe, Mo, Ni, Mn, Al, Cu etc. and their derivatives are extensively explored as a non-precious catalyst towards water oxidation. Single metals/based phosphides, sulphides, selenides etc. (Co, Fe, Cu, CoP, FeP, MoS_2, NiP)[39–42], binary metals/based phosphides, sulphides, selenides etc ($CoMoS_x$, NiCuP, CoNi, NiCoS)[43–46], ternary metals/based phosphides etc. (NiCoW, FeCoNiP)[47,48] have been explored and found to be very efficient as well as cost effective towards water

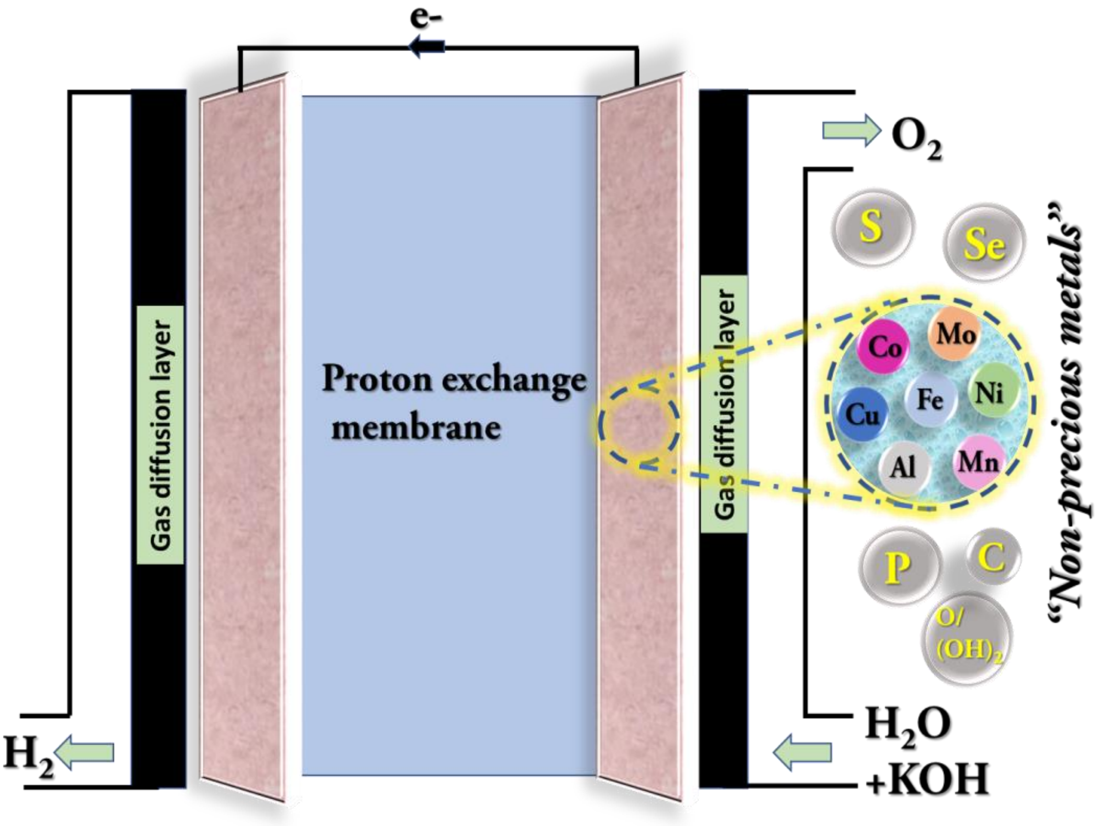

Figure 1.15 *Non-precious catalyst in water electrolysis*

electrolysis. A schematic illustration for non-precious catalyst in water electrolysis is shown in Figure 1.15. A comparison table depicting OER and HER activity utilizing transition-metal based compound is shown in Table 1.3 and 1.4, respectively.

1.5.1.1 Transition metal phosphides (TMPs)

There are many different phases of metal phosphides are reported based on the different P atoms content in the materials such as Ni_2P, Ni_5P_4, $Ni_{12}P_5$, Ni_3P, FeP, Fe_2P, CoP, Co_2P etc.[49–52] In summary, the content of P actually tunes the band structure of the catalyst, as MP and M_2P are generally metallic, where the material rich with P atoms are usually semiconducting in nature. The MP_2 (NiP_2) based catalyst actually are phosphorous rich, and thus contains plenty P-P bonding.[53]This significant amount of P creates the electronegativity, which drags the electrons from metal atoms and thus creates the plenty of hydrogen and oxygen adsorbed sites for further OER and HER. The delocalization of electrons in the metal is restricted by the reduction in the electrical conductivity upon the incorporation of P in the material.[53] The synthesis routes followed in the synthesis of TMPs are most likely, solid-phase reaction, electrodeposition, direct phosphidization, solvo/hydrothermal method.[54,55] Schaak et al. For the first time reported the HER catalyst based on TMPs in alkaline media with a very low OER and HER overpotential.[56] Many non-precious TMPs based catalyst have been reported since then for water splitting applications and the fields is immensely been explored.

1.5.1.2 Transition metal Chalcogenides (TMCs)

Transition metal-based chalcogenides represented by M_xX_y, where M is the metal (Fe, Co, Ni etc) and X is chalcogens, which includes S, Se and Te. These types of materials are attracting the researchers from past decades because of their high conductivity. They are much efficient and deliver better activity as compared to TMOs and TMSs because of the lesser electronegativity character of selenium then oxides and sulphides.[57,58] This results in the improved M-Se bonds and results in faster electron-exchange nature of the compound. Though sufficient research has been done on TMCs type materials, still it requires in context of activity to outperform noble-metal catalysts. $CoSe_2$ catalyst has been explored much for water electrolysis among other metal selenides. $CoSe_2$ have been synthesized by Kong et al. on carbon fiber which showed an admirable activity towards HER.[59] An amorphous CoSe film on titanium was synthesized by Liu et al. have which required a cell potential of 1.65 V for full-cell. It has been reported that hybrid catalyst/multi element materials enhance the activity as compared to the pristine one.

Table 1.3 *A comparison table for OER using transition-metal based catalyst.*

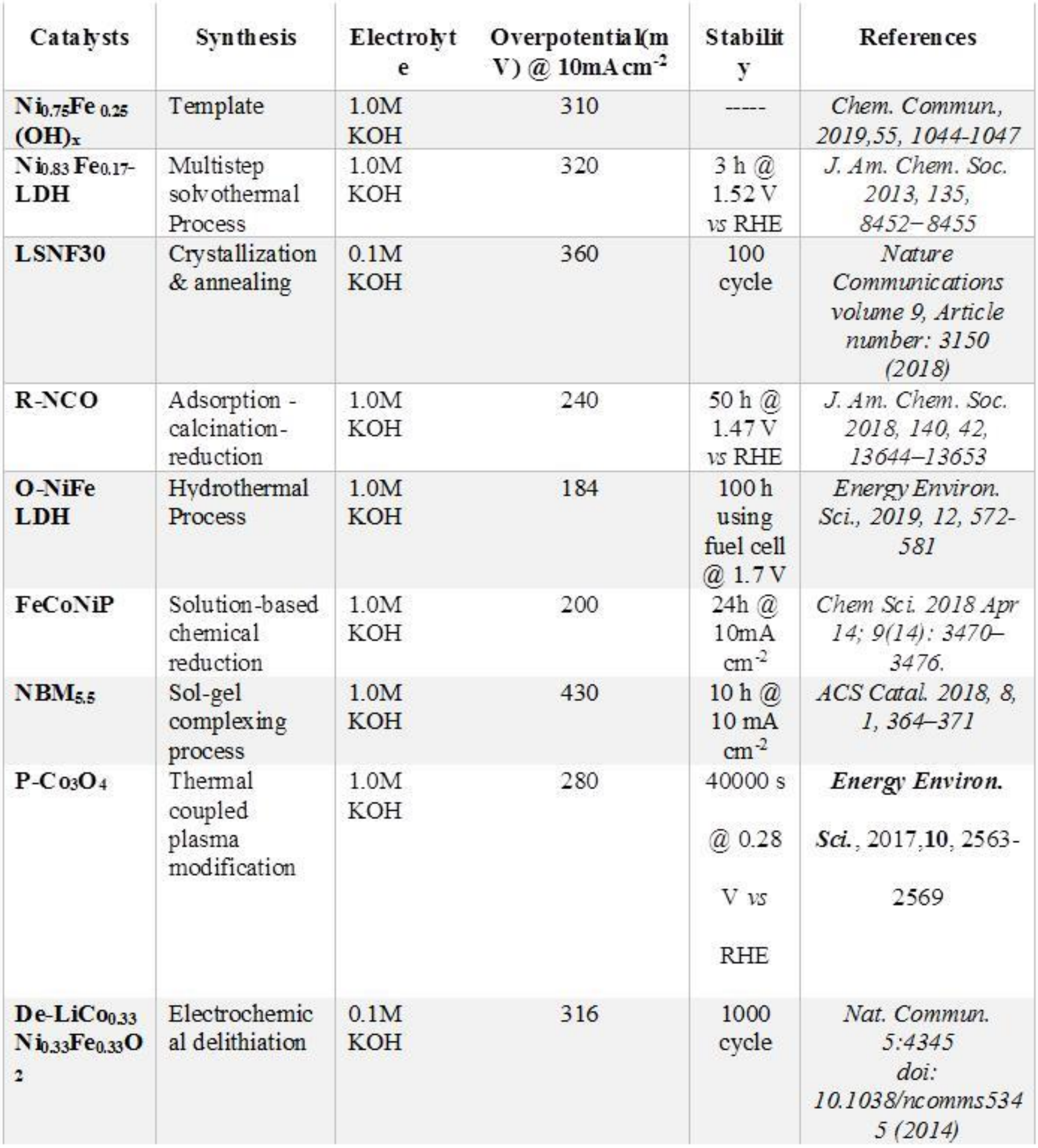

Catalysts	**Synthesis**	**Electrolyte**	**Overpotential(mV) @ 10mA cm^{-2}**	**Stability**	**References**
$Ni_{0.75}Fe_{0.25}(OH)_x$	Template	1.0M KOH	310	-----	*Chem. Commun., 2019,55, 1044-1047*
$Ni_{0.83}Fe_{0.17}$-LDH	Multistep solvothermal Process	1.0M KOH	320	3 h @ 1.52 V *vs* RHE	*J. Am. Chem. Soc. 2013, 135, 8452−8455*
LSNF30	Crystallization & annealing	0.1M KOH	360	100 cycle	*Nature Communications volume 9, Article number: 3150 (2018)*
R-NCO	Adsorption -calcination-reduction	1.0M KOH	240	50 h @ 1.47 V *vs* RHE	*J. Am. Chem. Soc. 2018, 140, 42, 13644–13653*
O-NiFe LDH	Hydrothermal Process	1.0M KOH	184	100 h using fuel cell @ 1.7 V	*Energy Environ. Sci., 2019, 12, 572-581*
FeCoNiP	Solution-based chemical reduction	1.0M KOH	200	24h @ 10mA cm^{-2}	*Chem Sci. 2018 Apr 14; 9(14): 3470–3476.*
$NBM_{5.5}$	Sol-gel complexing process	1.0M KOH	430	10 h @ 10 mA cm^{-2}	*ACS Catal. 2018, 8, 1, 364–371*
P-Co_3O_4	Thermal coupled plasma modification	1.0M KOH	280	40000 s @ 0.28 V *vs* RHE	***Energy Environ. Sci.***, 2017,**10**, 2563-2569
De-$LiCo_{0.33}Ni_{0.33}Fe_{0.33}O_2$	Electrochemical delithiation	0.1M KOH	316	1000 cycle	*Nat. Commun. 5:4345 doi: 10.1038/ncomms5345 (2014)*

The catalytic activity of the TMCs based material tunes upon the addition of different cations/anions into the compound. As an example, Zhang et al. have analyzed the role of addition of Co in WSe_2/MWNTs.[60] The addition of Co enhances the activity of the catalyst by optimizing the adsorption sites of H. Even the addition of P in the metal chalcogenides could tune the activity by introducing the vacancies/defects in MX. Wang et al. have synthesized $CoSe_2$-$MoSe_2$ hybrid catalyst, on reduced graphene (CS-MS/rGO-C) by selenization process which showed an admirable activity for alkaline HER.[61] Talking about the bimetallic selenides, it has better activity than monometallic selenides because of the synergistic effect taking place between both the metals.

Due to earth abundance in nature and high electrochemical activity performance, transition metal sulphides (TMSs) are attracting much attention. The interesting electronic property of S atoms drags the electron from transition metals because of the better high electronegativity.

Table 1.4 *A comparison table for HER using transition-metal based catalyst.*

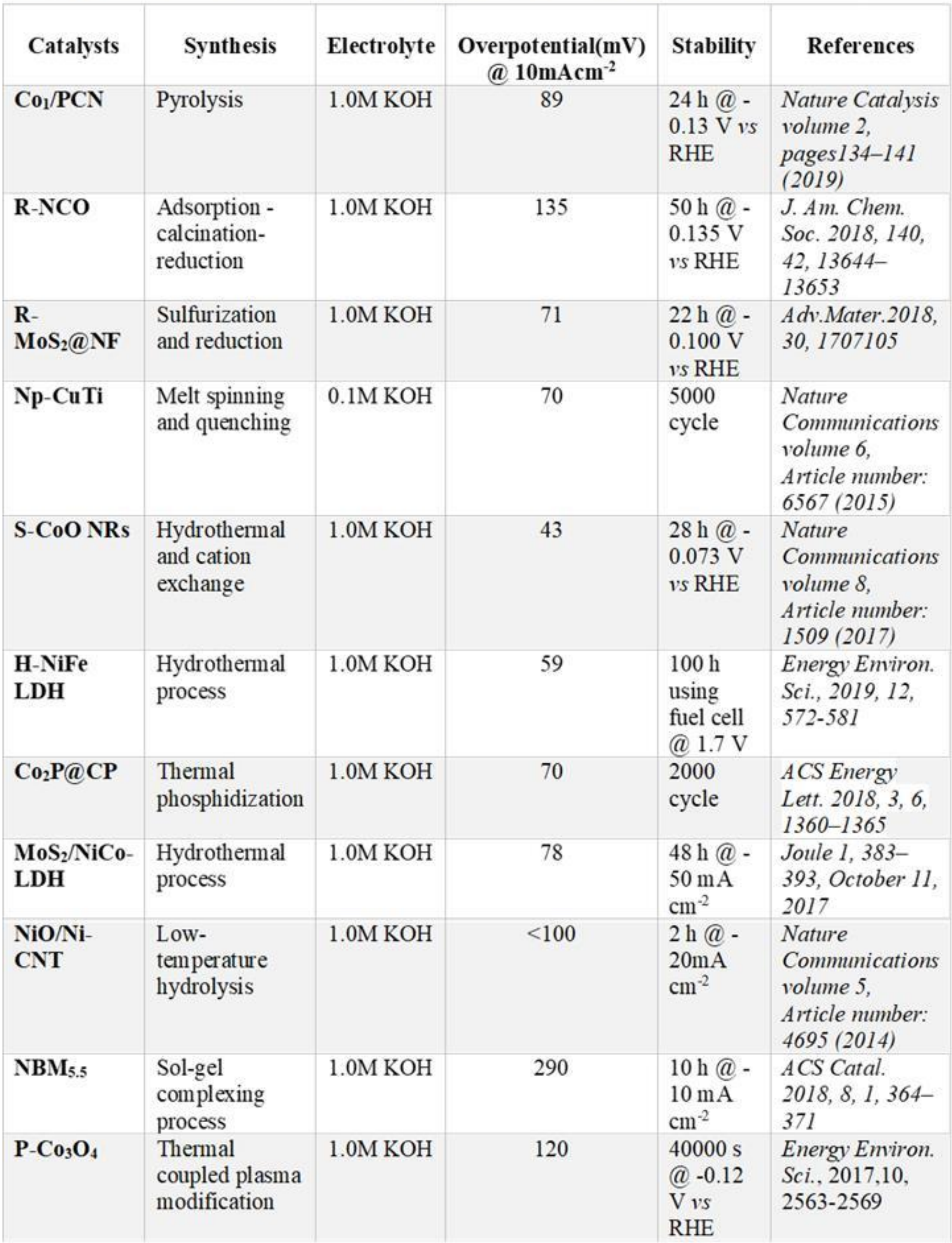

Catalysts	Synthesis	Electrolyte	Overpotential(mV) @ 10mAcm^{-2}	Stability	References
Co$_1$/PCN	Pyrolysis	1.0M KOH	89	24 h @ -0.13 V *vs* RHE	*Nature Catalysis volume 2, pages134–141 (2019)*
R-NCO	Adsorption -calcination-reduction	1.0M KOH	135	50 h @ -0.135 V *vs* RHE	*J. Am. Chem. Soc. 2018, 140, 42, 13644–13653*
R-MoS$_2$@NF	Sulfurization and reduction	1.0M KOH	71	22 h @ -0.100 V *vs* RHE	*Adv.Mater.2018, 30, 1707105*
Np-CuTi	Melt spinning and quenching	0.1M KOH	70	5000 cycle	*Nature Communications volume 6, Article number: 6567 (2015)*
S-CoO NRs	Hydrothermal and cation exchange	1.0M KOH	43	28 h @ -0.073 V *vs* RHE	*Nature Communications volume 8, Article number: 1509 (2017)*
H-NiFe LDH	Hydrothermal process	1.0M KOH	59	100 h using fuel cell @ 1.7 V	*Energy Environ. Sci., 2019, 12, 572-581*
Co$_2$P@CP	Thermal phosphidization	1.0M KOH	70	2000 cycle	*ACS Energy Lett. 2018, 3, 6, 1360–1365*
MoS$_2$/NiCo-LDH	Hydrothermal process	1.0M KOH	78	48 h @ -50 mA cm^{-2}	*Joule 1, 383–393, October 11, 2017*
NiO/Ni-CNT	Low-temperature hydrolysis	1.0M KOH	<100	2 h @ -20mA cm^{-2}	*Nature Communications volume 5, Article number: 4695 (2014)*
NBM$_{5.5}$	Sol-gel complexing process	1.0M KOH	290	10 h @ -10 mA cm^{-2}	*ACS Catal. 2018, 8, 1, 364–371*
P-Co$_3$O$_4$	Thermal coupled plasma modification	1.0M KOH	120	40000 s @ -0.12 V *vs* RHE	*Energy Environ. Sci.*, 2017,10, 2563-2569

1.5.1.3 Modified carbon based electrocatalyst

Because of the associated advantages like, low-cost, surface area, tunable functionalities, conductivity etc. associated with metal-free carbon, conventionally these have been mostly utilized as the current collector/substrate. Now-a-days, following the recent trends, carbons upon modification, are participating in catalyzing water efficiently. The tuning of the electronic, physical, structural properties of carbon atoms are usually practiced by heteroatom doping by creating the defects and functionalizing surface into the carbon matrix. The three key elements, carbon (C), nitrogen (N), Sulphur (S) and metal (M), necessary to produce the M–N–C/N-C/M-N-S-C/C-N-S based catalyst, which can be synthesized using separate precursors.[62–65] The carbonaceous material is used for mainly two purposes: provide an excess of C atoms, and act as an electronically conductive support matrix for the electrocatalytic active sites. The presence of an N-containing molecule is essential to ensure the incorporation of N atoms in the carbonaceous matrix of the support. Among them, N containing ligand molecules, which are able to form complexes in the solution with metallic ions, have been extensively explored. Pyrolysis is a key process, since it enables the formation of the active sites where metallic species are strongly bonded and/or embedded in the carbon support. The redistribution of charges modifies the atoms adsorbing sites on the carbon matrix which boosts up the activity of pristine carbon upon the modifications of heteroatoms. As per the previously reported data, modified/functionalized carbon were found to be much more efficient towards OER, HER and ORR which can be further utilized in the fuel cell technologies and metal air batteries. Because of the less corrosive nature of metal-free-carbon, it has been utilized efficiently in alkaline HER and OER processes. It is also noticed that upon N co-doping with other heteroatoms, the resultant co-doped carbon materials usually are more electrocatalytic active towards ORR than the single-doped counterpart. Binary atomic incorporation of boron, phosphorus, and nitrogen atoms within carbon materials would result in effective improvement of catalytic activity. Moreover, it has been investigated previously that bi-metallic catalysts produce H_2O_2 in significantly lower amounts compared to mono-metallic materials. Apart from single dopant of nitrogen, metal elements, including (M=Fe, Co, Mn, Cu) are often co-doped with nitrogen into carbon materials, forming M_1–M_2–N–C catalysts. Thus, doping carbon with foreign elements, such as N, B, P, or some additional transition metals has emerged as a very competitive candidate for outstanding catalytic performance that mostly attributed to optimized electronic structures.[66,67] The HER activity of carbon based electrocatalyst in different electrolyte is shown in Table 1.5 and 1.6.

Table 1.5 *A comparison table for HER based-on carbon based electrocatalyst in 0.5 M* H_2SO_4.

S.No	Catalyst	Overpotential (mV)@ 10mA/cm^2	References
1	N-doped hexagonal carbon	185	*Sci Rep* **4,** 6843 (2014).
2	Graphitic-C_3N_4 with N-doped graphene	217	Advanced functional material, 27, 15, 2017, 1606352
3	S-doped graphene nanosheets	178	International Journal of Hydrogen Energy 42(7)
4	N/P-co-doped carbon	151	J. Mater. Chem. A, 2016,4, 13726-13730
5	N/S-co-doped carbon	32	Nanoscale Adv., 2021, 3, 5068
6	Graphitic carbon nitride with S/Se-co-doped graphene	92	*J. Mater. Chem. A*, 2015,3, 12810-12819
7	Co/N co-doped carbon nanocomposites	265	ACS Appl. Mater. Interfaces 2015, 7, 15, 8083–8087
8	Co/N co-doped porous carbon	12	J. Mater. Chem. A, 2015,3, 8840-8846

9	CoN_x on carbon	124	International Journal of Hydrogen Energy 43(45)
10	Atomic Co in N-doped graphene	147	Nat. Commun. 6:8668
11	Atomic Ni in graphitic carbon (0.1 M NaOH)	34	Nat. Commun. 7:10667

Table 1.6 *A comparison table for HER based-on carbon based electrocatalyst in 1 M KOH.*

S.No.	Catalyst	Overpotential (mV)@10mA/cm^2	References
1	N-doped porous carbon@graphene	223	Applied Surface Science,493, 1,2019,963-974
2	N-doped mesoporous carbon nanosheet/carbon nanotube hybrids	320	J. Mater. Chem. A, 2016,4, 13133-13141
3	N-doped ordered mesoporous carbon/graphene framework	324	Nano Energy, 30, 2016, 503-510
4	P-doped graphitic carbon nitride grown on carbon-fiber paper	391	Angewandte Chemie International Edition 54(15)
5	N/P co-doped	319	FlatChem Volume

	graphene/carbon nanosheets		27, May 2021, 100250
6	N/S co-doped carbon nanotubes	351	Electrochimica Acta 204
7	S-doped carbon nanotubes	350	Advanced Energy Materials,Volume6, Issue5 March 9, 2016, 1501966
8	Fe-N-co-doped graphene	370	International Journal of Hydrogen Energy,46, 74, 26, 2021,36811-36823
9	Co and N co-doped graphene with inserted carbon nanospheres	443	ACS Sustainable Chem. Eng. 2016, 4, 8, 4131–4136

1.6 About the thesis

The present thesis aims towards the development of sustainable energy systems, which utilizes H_2 as a fuel. Using H_2, we can get the energy in a renewable fashion because when utilized in a fuel cell, H_2 after combustion gives only water as a byproduct. The integration of water splitting unit and solar cell unit has been done in order to split water in a fully renewable fashion. To generate H_2 from water splitting in a fully renewable and non-sporadic way, the water electrolyser unit along with solar cell must be integrated with some storage/battery unit, because solar cell mostly depends on climatic conditions. The introduction of metal-air battery (MAB) is highlighted, which requires an electrocatalyst capable of oxygen reduction reaction as well as oxygen evolution reaction. The design and engineering of an electrocatalyst towards efficient HER, OER and ORR is been highlighted in the thesis.

Chapter 1: Introduction

This **chapter** gives a glimpse of the current energy scenario worldwide and various global challenges to accomplish the current energy demands. The introduction to hydrogen economy and its various production methods have been highlighted. The advantages of using water electrolysis for hydrogen production are and the basic mechanism is also discussed. Along with that various parameter for catalyst selection as well as the highlights in the design and engineering of electrocatalyst are placed. An introduction to hydrogen evolution reaction (HER), oxygen evolution reaction (OER) and oxygen reduction reaction (ORR) and the underlying mechanism is covered in this section of the thesis. The development of sustainable energy systems such the hydrogen generation using solar power is considered as a highly acceptable method for energy generation. To generate H_2 from water splitting in a fully renewable and non-sporadic way, the water electrolyzer unit along with solar cell must be integrated with some storage/battery unit, because solar cell mostly depends on climatic conditions. The introduction of metal-air battery (MAB) is highlighted which requires an electrocatalyst capable of oxygen reduction reaction as well as oxygen evolution reaction. The rational design and engineering of an electrocatalyst towards efficient HER, OER and ORR is been highlighted in this section.

Chapter 2: Material synthesis and analytical techniques

This **chapter** focuses on chemicals, reagents, synthesis techniques and instrumentation utilized in the completion of thesis work. The Electrodeposition techniques, which is a very versatile synthesis method in electrocatalyst synthesis is explained. The analytical instrumental techniques such as Powder X-ray Diffraction (PXRD) (INST, Mohali), Transmission Electron Microscopy (TEM) (INST, Mohali), Field emission scanning electron microscopy (FESEM) (IISER, Mohali), Scanning Electron Microscopy (SEM) (INST, Mohali), High-angle annular dark-field scanning transmission electron microscopy (HAADF-STEM) (IIT-Bombay), Synchrotron for X-ray absorption near-edge structure (XANES) & X-ray absorption fine structure (EXAFS) (RRCAT, Indore), X-ray photon spectroscopy (XPS) analysis (RRCAT-Indore/IISER-Pune), Fourier transform infrared spectroscopy (FTIR) (INST, Mohali), Contact angle measurement (INST, Mohali), Gas Chromatography (INST, Mohali), Nitrogen Adsorption-Desorption Studies (INST, Mohali), Electrochemical workstation (CHI and Metrohm) (INST, Mohali), Density functional theory (DFT) calculations were performed using Vienna ab initio simulation package (VASP) (INST, Mohali) have utilized in material characterization.

Chapter 3: Single-phase Ni_5P_4-copper foam superhydrophilic and aerophobic core-shell nanostructures for efficient hydrogen evolution reaction in acidic medium

This **chapter** provides the facile synthesis of highly durable, low-cost and robust electrocatalyst for hydrogen generation from water in acidic media to address the existing environmental issues as well as to provide environmental-friendly clean and green energy supply. Electrochemical deposition of single-phase nickel phosphide on galvanostatically deposited copper foam (Cuf@Ni_5P_4) core-shell nanostructure offers innovation in structure designing and a new platform for novel electrocatalysts. The Cuf@Ni_5P_4 provides a superior three-dimensional conductive channel for ion transport during the catalysis process. The catalyst exhibits an excellent electrocatalytic activity towards hydrogen evolution reaction (HER) in acidic media. The superhydrophilic and aerophobic property of the porous electrode helps to the in time leaving of H_2 gas bubbles from the surface. Interestingly, it requires very less overpotential of 90 mV for HER at the current density of 10 mA cm^{-2}. A very small Tafel slope of 49 mV dec^{-1} and a very high exchange current density (~0.76 mA cm^{-2}) originate from large electrochemically active surface area and fast mass and electron transfer efficiency of the Cuf@Ni_5P_4 catalyst. A theoretical study was carried out to investigate the mechanism underlying the HER activity in Cu-supported Ni_5P_4 at an atomic-scale. DFT calculations suggest a very high negative Gibbs free energy change (ΔG_{H*}) in Ni_5P_4 (0001)/Cu(111) upon hydrogen adsorption, which is actually responsible for excellent HER activity of the catalyst. Furthermore, it shows remarkable durability of hydrogen generation under low (10 mA cm^{-2}) and high current density (160 mA cm^{-2}) for >84 hours with ~96% retention of overpotential, establishing a low-cost and efficient catalyst for sustainable, future energy generation strategy.

Chapter 4: An ultrastable self-supportive Ni_5P_4-copper foam bifunctional electrocatalyst for solar-driven water splitting

In this **chapter,** an ultrastable electrode material towards the designing of self-supportive electrocatalyst with a budget-friendly and less time-consuming method that is Electrodeposition technique have been highlighted. This electrode worked towards efficient hydrogen and oxygen generation in a fully renewable fashion. It is therefore important to divulge the structural information of a catalyst in order to have the extraordinary stable electrodes for solar-driven water electrolysis system. This chapter discusses a facile electrochemical method for the synthesis of single-phase Cuf@Ni_5P_4

core-shell nanostructures for overall water splitting in alkaline media. The Cuf@Ni_5P_4 based cell shows extraordinary stability in working electrolyte for 150 h at a current density of 10 mA cm^{-2} with 96% retention of its initial potential. The Cuf@Ni_5P_4//Cuf@Ni_5P_4 cell hybridized with a solar cell in order to demonstrate the suitability of the concept towards a hybrid energy device and an impulsive generation of H_2 and O_2. This versatile system opens up a new route for the generation of green fuel towards renewable energy applications.

Chapter 5: Electrochemical growth of bimetallic transition metal selenide as a bifunctional electrocatalyst for water electrolysis

This **chapter** focuses of highly efficient electrocatalyst based on mixed transition metal selenides, Cu_2Se and $CoSe_2$ on the surface of the copper foam. The use of 3D hierarchically dendritic porous Cuf as a substrate leads to the designing of binder-free electrocatalyst, which benefits the overall performance of the catalyst. The mechanism for the deposition process was investigated using the CV technique. The physical characterizations of the catalyst were well correlated and analysed. The overpotential attained by the catalyst was found to be superior to the state-of-the-art RuO_2 for OER and comparable to Pt/C for HER. Further, after the assembly of the catalyst in a two-electrode system, the catalyst attained a potential as low as 1.56 V at a current density of 10 mA cm^{-2}, which is admirable as compared to other recently reported catalysts as well as Pt/C-RuO_2 systems. The multistep current ramping stability demonstrated that the catalyst is mechanically robust, which is favourable for commercialization. Further, the study of the surface property confirmed the superhydrophilic as well as aerophobic behaviour of the catalyst. Therefore, the catalyst is found to be highly efficient concerning electrochemical water splitting activity. This opens up the new door of fabrication of a non-noble metal-based catalyst for H_2 and O_2 generation.

Chapter 6: Triggering the efficiency of electrochemical water splitting by introducing Ni-buffer layer between the copper foam and cobalt selenide

This **chapter** highlights the development of transition metal-based electrocatalyst designed via an electrochemical deposition method. The activity of the electrocatalyst has been improved by introducing a Ni buffer layer deposition in between the Cuf and electrochemically deposited Co-Se. The physical characterizations of the catalyst were well correlated and analysed. The overpotential attained by the catalyst was found to be superior to the state-of-the-art RuO_2 for OER and comparable to Pt/C for HER. Further, after the assembly of the catalyst in a two-electrode system, the catalyst attained a potential as low as 1.52 V at a current density of 10 mA cm^{-2}, which is admirable as compared to other recently reported catalysts as well as Pt/C- RuO_2 systems. The catalyst superior stability of 107 h along with its surface property and the electrochemical measurements have been discussed in this chapter.

Chapter 7: Synergism of binary transition metals and role of M-N-S active sites towards efficient oxygen electrocatalysis

In this **chapter**, a rational design of an electrocatalyst (a binary transition metal with N-S doped carbon matrix) towards efficient oxygen reduction reaction as well as oxygen evolution reaction was introduced and further utilized in metal-air battery application. In this work we successfully identified the strengthened π-electronic interaction between the symmetry-matched orbitals of square-planar Fe and Co atoms respectively in the Fe-Co bimetallic system, which has been so far considered as the "synergistic effect" between the metals. The presence of M-N-S moiety in the bimetal doped carbon matrix increased the reactivity of the metal centers by channelizing the electron flow toward the metals via +R effect, which further triggers the electron drift from Fe^{2+} to Co^{2+} resulting in $Fe^{+(2+\delta)}$ and $Co^{+(2-\delta)}$. Consequently, the so-formed metal centers have optimum binding energy with the intermediates and account for appreciable activity toward ORR and OER. This work thus provides elaborate chemistry of the entire structural finding as well as mechanistic approach occurring at the active site of the Fe-Co bimetallic centers benefitting the two important oxygen electrocatalysis reactions towards the design of metal-air battery.

Chapter 8: Conclusions and prospects

In this **chapter**, the summary of present thesis work has been discussed along with the highlights of future possibilities and applications of the catalysts.

1.7 Motivation

Fashioning a global-scale sustainable energy system for upcoming future while preserving our atmosphere is very crucial. A geared acceleration in energy supply, to diversify our energy sources, reducing our reliance on fossil fuels by turning to renewable energy such as solar, wind, and hydroelectric power is very important. A sustainable, fossil fuel–free path to producing industrial chemicals of global importance, such as hydrogen gas, could play a substantial role in reducing carbon dioxide emissions from earth's atmosphere.

In order to address this current energy and environmental challenge and issue, we tried to develop an economical, eco-friendly, highly stable electrocatalyst for hydrogen evolution, oxygen evolution and oxygen reduction reaction in order to generate, convert and store energy in a fully renewable fashion. The design and engineering of an electrocatalyst to achieve a less overpotential and ultrastable for water oxidation is highly desirable for an electrocatalyst to be commercialized.

1.8 References

1. Dorian, J. P., Franssen, H. T. & Simbeck, D. R. Global challenges in energy. *Energy Policy* **34**, 1984–1991 (2006).
2. Nicoletti, G., Arcuri, N., Nicoletti, G. & Bruno, R. A technical and environmental comparison between hydrogen and some fossil fuels. *Energy Convers. Manag.* **89**, 205–213 (2015).
3. Dincer, I. & Acar, C. Review and evaluation of hydrogen production methods for better sustainability. *Int. J. Hydrogen Energy* **40**, 11094–11111 (2015).
4. Looney, B. Statistical Review of World Energy globally consistent data on world energy markets . and authoritative publications in the field of energy. *Rev. World Energy data* **70**, 8–20 (2021).
5. Veziroğlu, T. & Sahin, S. 21st Century's energy: Hydrogen energy system. *Energy Convers. Manag.* **49**, 1820–1831 (2008).
6. Jarlsby, E. The global energy challenge: Still fuel for progress? *Int. J. Energy Prod. Manag.* **1**, 33–49 (2016).
7. Liu, Z. Chapter 7 - R&D on Global Energy Interconnection and Practice. in (ed. Liu, Z. B. T.-G. E. I.) 273–342 (Academic Press, 2015). doi:https://doi.org/10.1016/B978-0-12-804405-6.00007-5.
8. Painuly, J. P. & Wohlgemuth, N. Chapter 18 - Renewable energy technologies: barriers and policy implications. in (ed. Ren, J. B. T.-R.-E.-D. F.) 539–562 (Academic Press, 2021). doi:https://doi.org/10.1016/B978-0-12-820539-6.00018-2.
9. Dahlke, S., Sterling, J. & Meehan, C. *Policy and market drivers for advancing clean energy*. *Advances in Clean Energy Technologies* (Elsevier Inc., 2021).

doi:10.1016/b978-0-12-821221-9.00012-8.

10. Yue, M. *et al.* Hydrogen energy systems: A critical review of technologies, applications, trends and challenges. *Renew. Sustain. Energy Rev.* **146**, 111180 (2021).
11. Millet, P. & Grigoriev, S. Chapter 2 - Water Electrolysis Technologies. in (eds. Gandía, L. M., Arzamendi, G. & Diéguez, P. M. B. T.-R. H. T.) 19–41 (Elsevier, 2013). doi:https://doi.org/10.1016/B978-0-444-56352-1.00002-7.
12. Shiva Kumar, S. & Himabindu, V. Hydrogen production by PEM water electrolysis – A review. *Mater. Sci. Energy Technol.* **2**, 442–454 (2019).
13. Nikolaidis, P. & Poullikkas, A. A comparative overview of hydrogen production processes. *Renew. Sustain. Energy Rev.* **67**, 597–611 (2017).
14. Ford, A., Gillich, A. & Mirzania, P. 28 - Sustainable Energy and Energy Efficient Technologies. in (ed. Letcher, T. M. B. T.-F. E. (Third E.) 611–630 (Elsevier, 2020). doi:https://doi.org/10.1016/B978-0-08-102886-5.00028-1.
15. Chen, Y., Ji, W., Yan, K., Gao, J. & Zhang, J. Fuel cell-based self-powered electrochemical sensors for biochemical detection. *Nano Energy* **61**, 173–193 (2019).
16. Liu, Y. *et al.* Integrating a Silicon Solar Cell with a Triboelectric Nanogenerator via a Mutual Electrode for Harvesting Energy from Sunlight and Raindrops. *ACS Nano* **12**, 2893–2899 (2018).
17. Zhang, Q. *et al.* Fully Solar-Powered Uninterrupted Overall Water-Splitting Systems. *Adv. Funct. Mater.* **29**, 1808889 (2019).
18. Hoots, W. K. & Nelson, J. A. Treatment of Murine Testicular Leukemia. *Cancer Res.* **44**, 2464–2466 (1984).
19. Schalenbach, M. *et al.* Acidic or Alkaline? Towards a New Perspective on the Efficiency of Water Electrolysis. *J. Electrochem. Soc.* **163**, F3197–F3208 (2016).
20. Anantharaj, S. *et al.* Recent Trends and Perspectives in Electrochemical Water Splitting with an Emphasis on Sulfide, Selenide, and Phosphide Catalysts of Fe, Co, and Ni: A Review. *ACS Catal.* **6**, 8069–8097 (2016).
21. Sci, C. Catalysis Science & Technology Developments and perspectives of oxide-based. 3800–3821 (2014) doi:10.1039/c4cy00669k.
22. Li, X., Hao, X., Abudula, A. & Guan, G. Nanostructured catalysts for electrochemical water splitting: current state and prospects. *J. Mater. Chem. A* **4**, 11973–12000 (2016).

23. Das, A. & Ganguli, A. K. Design of diverse nanostructures by hydrothermal and microemulsion routes for electrochemical water splitting. *RSC Adv.* **8**, 25065–25078 (2018).
24. Pattiya, A. 2 - Catalytic pyrolysis. in (ed. Rosendahl, L. B. T.-D. T. L. for E. A.) 29–64 (Woodhead Publishing, 2018). doi:https://doi.org/10.1016/B978-0-08-101029-7.00002-3.
25. Kale, M. B., Borse, R. A., Gomaa Abdelkader Mohamed, A. & Wang, Y. Electrocatalysts by Electrodeposition: Recent Advances, Synthesis Methods, and Applications in Energy Conversion. *Adv. Funct. Mater.* **31**, 2101313 (2021).
26. Zhu, J., Hu, L., Zhao, P., Lee, L. Y. S. & Wong, K.-Y. Recent Advances in Electrocatalytic Hydrogen Evolution Using Nanoparticles. *Chem. Rev.* **120**, 851–918 (2020).
27. Song, J. *et al.* A review on fundamentals for designing oxygen evolution electrocatalysts. *Chem. Soc. Rev.* **49**, 2196–2214 (2020).
28. Ma, R. *et al.* A review of oxygen reduction mechanisms for metal-free carbon-based electrocatalysts. *npj Comput. Mater.* **5**, 78 (2019).
29. Lu, Y.-T., Neale, A. R., Hu, C.-C. & Hardwick, L. J. Divalent Nonaqueous Metal-Air Batteries. *Front. Energy Res.* **8**, 357 (2021).
30. Wang, H.-F. & Xu, Q. Materials Design for Rechargeable Metal-Air Batteries. *Matter* **1**, 565–595 (2019).
31. Gelman, D., Shvartsev, B. & Ein-Eli, Y. Aluminum-Air Battery Based on an Ionic Liquid Electrolyte. *J. Mater. Chem. A* **2**, (2014).
32. Esposito, D. V, Hunt, S. T., Kimmel, Y. C. & Chen, J. G. A New Class of Electrocatalysts for Hydrogen Production from Water Electrolysis: Metal Monolayers Supported on Low-Cost Transition Metal Carbides. *J. Am. Chem. Soc.* **134**, 3025–3033 (2012).
33. Sinha, A. & Ojha, U. Recent Trends in Development of Metal Nitride Nanocatalysts for Water Electrolysis Application. in (2021). doi:10.5772/intechopen.95748.
34. Xia, X., Wang, L., Sui, N., Colvin, V. L. & Yu, W. W. Recent progress in transition metal selenide electrocatalysts for water splitting. *Nanoscale* **12**, 12249–12262 (2020).
35. Wang, M., Zhang, L., He, Y. & Zhu, H. Recent advances in transition-metal-sulfide-based bifunctional electrocatalysts for overall water splitting. *J. Mater.*

Chem. A **9**, 5320–5363 (2021).

36. Wu, W., Wu, X.-Y., Wang, S.-S. & Lu, C.-Z. Highly efficient hydrogen evolution from water electrolysis using nanocrystalline transition metal phosphide catalysts. *RSC Adv.* **8**, 39291–39295 (2018).
37. Song, F. *et al.* Transition Metal Oxides as Electrocatalysts for the Oxygen Evolution Reaction in Alkaline Solutions: An Application-Inspired Renaissance. *J. Am. Chem. Soc.* **140**, 7748–7759 (2018).
38. Tseng, C.-A. Transition Metal Chalcogenides for the Electrocatalysis of Water. in (2020). doi:10.5772/intechopen.92045.
39. Huang, W.-H. *et al.* Highly efficient electrocatalysts for overall water splitting: mesoporous CoS/MoS2 with hetero-interfaces. *Chem. Commun.* **57**, 4847–4850 (2021).
40. Wang, W., Xu, R., Yu, B., Wang, X. & Feng, S. Electrochemical fabrication of FeSx films with high catalytic activity for oxygen evolution. *RSC Adv.* **9**, 31979–31987 (2019).
41. Ji, L., Wang, J., Teng, X., Meyer, T. J. & Chen, Z. CoP Nanoframes as Bifunctional Electrocatalysts for Efficient Overall Water Splitting. *ACS Catal.* **10**, 412–419 (2020).
42. Das, M. *et al.* Single-phase Ni5P4–copper foam superhydrophilic and aerophobic core–shell nanostructures for efficient hydrogen evolution reaction. *J. Mater. Chem. A* **7**, 23989–23999 (2019).
43. Liu, D., Lu, Q., Luo, Y., Sun, X. & Asiri, A. M. NiCo2S4 nanowires array as an efficient bifunctional electrocatalyst for full water splitting with superior activity. *Nanoscale* **7**, 15122–15126 (2015).
44. Yu, C. *et al.* Bifunctional catalysts for overall water splitting: CoNi oxyhydroxide nanosheets electrodeposited on titanium sheets. *Electrochim. Acta* **301**, (2019).
45. Wei, L. *et al.* A hierarchically porous nickel–copper phosphide nano-foam for efficient electrochemical splitting of water. *Nanoscale* **9**, 4401–4408 (2017).
46. Lu, Y. *et al.* Highly efficient CoMoS heterostructure derived from vertically anchored Co5Mo10 polyoxometalate for electrocatalytic overall water splitting. *Chem. Eng. J.* **394**, 124849 (2020).
47. Zhang, Q. *et al.* Trimetallic Octahedral Ni–Co–W Phosphoxide Sprouted from Plasma-Defect-Engineered Ni–Co Support for Ultrahigh-Performance Electrocatalytic Hydrogen Evolution. *ACS Sustain. Chem. Eng.* **9**, 7454–7465

(2021).

48. Zhou, X. *et al.* Core–Shell-Structured Prussian Blue Analogues Ternary Metal Phosphides as Efficient Bifunctional Electrocatalysts for OER and HER. *Inorg. Chem.* **60**, 11661–11671 (2021).

49. Du, X., Li, J., Tong, K. & Zhang, X. Coupling Co2P/CoSe2 heterostructure nanoarrays for boosting overall water splitting. *Dalt. Trans.* **50**, 6650–6658 (2021).

50. Yao, S. *et al.* From an Fe2P3 complex to FeP nanoparticles as efficient electrocatalysts for water-splitting. *Chem. Sci.* **9**, 8590–8597 (2018).

51. Stern, L.-A., Feng, L., Song, F. & Hu, X. Ni2P as a Janus catalyst for water splitting: the oxygen evolution activity of Ni2P nanoparticles. *Energy Environ. Sci.* **8**, 2347–2351 (2015).

52. Wang, Z. *et al.* Water-Induced Formation of Ni2P–Ni12P5 Interfaces with Superior Electrocatalytic Activity toward Hydrogen Evolution Reaction. *Small* **17**, 2006770 (2021).

53. Shi, Y. & Zhang, B. Recent advances in transition metal phosphide nanomaterials: synthesis and applications in hydrogen evolution reaction. *Chem. Soc. Rev.* **45**, 1529–1541 (2016).

54. Bai, N., Li, Q., Mao, D., Li, D. & Dong, H. One-Step Electrodeposition of Co/CoP Film on Ni Foam for Efficient Hydrogen Evolution in Alkaline Solution. *ACS Appl. Mater. Interfaces* **8**, 29400–29407 (2016).

55. Read, C. G., Callejas, J. F., Holder, C. F. & Schaak, R. E. General Strategy for the Synthesis of Transition Metal Phosphide Films for Electrocatalytic Hydrogen and Oxygen Evolution. *ACS Appl. Mater. Interfaces* **8**, 12798–12803 (2016).

56. Popczun, E. J. *et al.* Nanostructured Nickel Phosphide as an Electrocatalyst for the Hydrogen Evolution Reaction. *J. Am. Chem. Soc.* **135**, 9267–9270 (2013).

57. Ruqia, B. & Choi, S. Il. Pt and Pt–Ni(OH)2 Electrodes for the Hydrogen Evolution Reaction in Alkaline Electrolytes and Their Nanoscaled Electrocatalysts. *ChemSusChem* **11**, 2643–2653 (2018).

58. Wang, T., Wang, X., Liu, Y., Zheng, J. & Li, X. A highly efficient and stable biphasic nanocrystalline Ni-Mo-N catalyst for hydrogen evolution in both acidic and alkaline electrolytes. *Nano Energy* **22**, 111–119 (2016).

59. Kong, D., Wang, H., Lu, Z. & Cui, Y. CoSe2 nanoparticles grown on carbon fiber paper: An efficient and stable electrocatalyst for hydrogen evolution reaction. *J. Am. Chem. Soc.* **136**, 4897–4900 (2014).

60. Zhang, G. *et al.* Carbon nanotube-induced phase and stability engineering: a strained cobalt-doped WSe2/MWNT heterostructure for enhanced hydrogen evolution reaction. *J. Mater. Chem. A* **6**, 4793–4800 (2018).
61. Wang, B. *et al.* Scalable synthesis of porous hollow CoSe2–MoSe2/carbon microspheres for highly efficient hydrogen evolution reaction in acidic and alkaline media. *J. Mater. Chem. A* **6**, 12701–12707 (2018).
62. Jin, H. *et al.* MOF-derived 3D Fe-N-S co-doped carbon matrix/nanotube nanocomposites with advanced oxygen reduction activity and stability in both acidic and alkaline media. *Appl. Catal. B Environ.* **250**, 143–149 (2019).
63. Chen, P. *et al.* Atomically Dispersed Iron–Nitrogen Species as Electrocatalysts for Bifunctional Oxygen Evolution and Reduction Reactions. *Angew. Chemie - Int. Ed.* **56**, 610–614 (2017).
64. Wang, J. *et al.* Synergistic effect of well-defined dual sites boosting the oxygen reduction reaction. *Energy Environ. Sci.* **11**, 3375–3379 (2018).
65. Wang, J. *et al.* Synergistic effect of well-defined dual sites boosting the oxygen reduction reaction. *Energy Environ. Sci.* **11**, 3375–3379 (2018).
66. Liu, D. *et al.* Synergistic effect of an atomically dual-metal doped catalyst for highly efficient oxygen evolution. *J. Mater. Chem. A* **6**, 6840–6846 (2018).
67. Serov, A., Robson, M. H., Smolnik, M. & Atanassov, P. Tri-metallic transition metal–nitrogen–carbon catalysts derived by sacrificial support method synthesis. *Electrochim. Acta* **109**, 433–439 (2013).

Chapter 2

Material synthesis and analytical techniques

Abstract: Exploration of chemical states in nanomaterials and their analysis in details from are critical regarding the formation and applications in the frontiers of research domains today. This thesis work includes different synthesis routes for the design and engineering of electrocatalyst. Also, several instrumentation techniques were adopted for material characterization and applications of the synthesized electrocatalyst. This chapter gives an overview of the methodologies adopted in the thesis work with detailed instrumentation techniques and formula used for the electrocatalysis.

2.1 Introduction

Exploration of chemical states in nanomaterials and their analysis in details from are critical regarding the formation and applications in the frontiers of research areas in the current era.[1,2] This chapter discuss about the chemical/reagents, experimental techniques and several evaluation techniques in the calculation of the parameters used in oxygen evolution reaction, hydrogen evolution reaction and oxygen evolution reaction. For the investigation of physical properties their scope in energy systems, a deep insight is essential which can be accomplished with the help of various analytical characterization techniques.

This chapter deals with a brief overview regarding materials, methods, formula and characterization techniques used in this thesis work.

2.2 Reagents and materials

2.1 Reagents and Materials Chemicals	**Purity (%)**	**Source**
Acetone	≥99.5%	Merck Chemicals India
Hydrochloric acid (HCl)	36%	Merck Chemicals India
Isopropyl alcohol (IPA)	97%	Merck Chemicals India
Sodium dihydrogen phosphate ($NaH_2PO_4 \cdot H_2O$)		Sigma Aldrich
Nickel chloride ($NiCl_2 \cdot 6H_2O$)		Sigma Aldrich
Sulphuric acid (H_2SO_4)		Sigma Aldrich
Copper sulphate pentahydrate (CuSO4.5H2O)	≥99%	Sigma Aldrich
Sodium hypophosphite ($NaH_2PO_2 \cdot H_2O$)		Sigma Aldrich
Nickel foam		Kanopy sales
Graphite plate		Kanopy sales
Platinum on carbon (Pt/C)	20 %	Sigma Aldrich
Copper foil	99%	Gelon LIB group, China
Iron (II) sulphate heptahydrate	98%	Sigma Aldrich
($FeSO_4.7H_2O$)		Sigma Aldrich
Zinc acetate		Sigma Aldrich

Cobalt (II) Chloride hexahydrate ($CoCl_2.6H_2O$)		Sigma Aldrich
Potassium hydroxide (KOH)		Sigma Aldrich
Selenium oxide (SeO_2)		
Nitric acid (HNO_3)		CDH, India
Potassium chloride (KCl),		Sigma Aldrich
Dopamine		Sigma Aldrich
L-cysteine		Sigma Aldrich
Pt/C	20 wt %	Sigma Aldrich
Holey carbon coated Cu grid for TEM analysis		Agar Scientific Ltd. (UK)

2.3 Experimental procedure and parameter evaluation

2.3.1 Electrochemically prepared Copper foam (Cuf) *via* DHBT

Electrochemical preparation of Cuf *via* dynamic hydrogen bubble template (DHBT) technique, using the hydrogen bubbling process, considered to be most appealing process in tailoring the structures and morphology of porous and dendritic branches of 3-dimensional Cuf.[3] The porous architecture of Cuf actually leads to the generation of plentiful active sites which actually helps in the enhancement of the activity during electrocatalysis can thus, considered as a versatile material which is used for various application purposes in energy field (Figure 2.1). [4–8]Copper is known to be a versatile material which actually helps in the design and engineering of multi-metal catalysts, core-shell nanostructures, doping etc. which triggers the activity of the electrocatalyst and thus is demanding in the field of energy applications. [9,10]

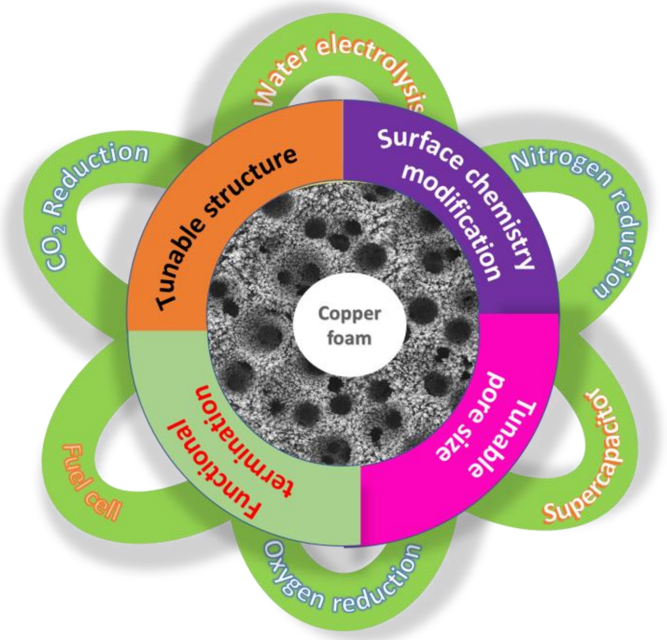

Figure 2.1. *The versatile properties of the electrodeposited Cuf in potential green energy applications.*

The properties and the morphology of Cuf depends on several factors; (a) the state of the metal anode which is being deposited (b) the concentration of the analytical solution (c) the current density and the potential that is being applied for the deposition (d) bath temperature (e) time of the deposition.[11–15]The Cuf can be synthesized using two-electrode (cathode/copper-working electrode and anode/copper-counter electrode) as well as three-electrode system (cathode/copper, anode/copper and a reference electrode) immersed in a solution containing acid and copper salt. At certain current and potential, the hydrogen gas evolution takes place from the acidic electrolyte with the reduction of metal ions. The possible reaction that occurs are shown in equation 2.1, 2.2 and 2.3.

$$M_{n^+}(aq) + ne^- \rightleftarrows M(s) \tag{2.1}$$

$$2H^+(aq) + 2e^- \rightleftarrows H_2(g) \tag{2.2}$$

$$CuSO_4 + 2e^- \rightarrow Cu_{metal} + SO_4^{-2} \tag{2.3}$$

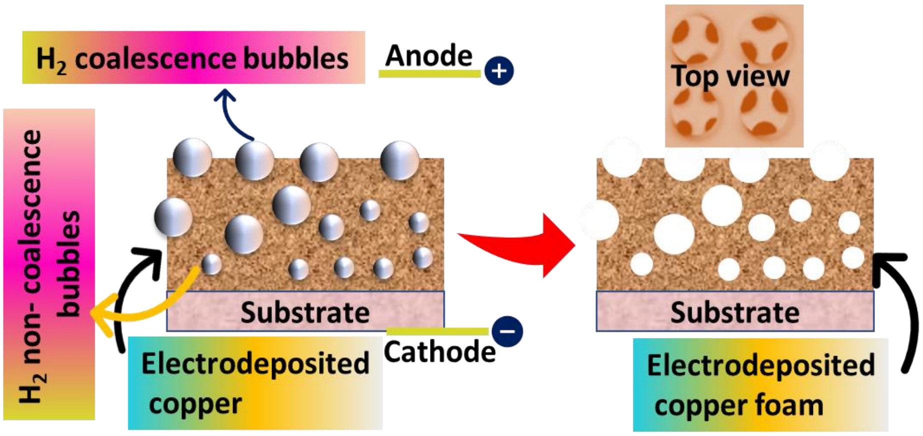

Figure 2.2. *Schematic representation depicting the formation mechanism of electrodeposited copper foam.*

The bubble formation on the Cuf electrode takes place through three basic steps: nucleation, growth and separation. This formation of bubble is due to the reduction of hydrogen species from the electrolytic solution. The coalescence of the small bubble forms the larger sized bubble on the surface and gets detached until the bubble break-off diameter which solely depends on the morphology of the electrode surface.[16] The growth and detachment of the bubble from the electrode surface causes the commotion to the surface and thus effects the formation of porous Cuf. The conceivable paths left for the copper ions to deposit are the areas other than or around the hydrogen bubbles, as the bubbles blocks and insulates the surface sites. At the break off state of the bubble the bubble disrupts or gets apart leaving behind a void space which forms the foam like morphology of the Cuf as shown in Figure 2.2.

2.3.2 Preparation of copper foam electrode as a substrate

Dendritic 3-dimensional copper foam was synthesized on copper foil utilized as the substrate in a two-electrode system using galvanostatic electrodeposition method. A cleaned copper foil (treated with 30% nitric acid followed by deionized (DI) water and finally with acetone) with an area of 1x1 cm^2 was exposed an electrochemical cell containing 0.4 M $CuSO_4$ in 1.5 M H_2SO_4 for deposition. The pre-treated copper foil was used as working as well as counter electrode which was kept at a distance of ~1.5 cm and the deposition was done at a constant current density of 1 Acm^{-2} for 45 s. The synthesized copper foam was washed with DI water several times to remove the acidic residues on the electrode. The method utilized here was dynamic hydrogen bubble template (DHBT) method, where the hydrogen bubbles were utilized as the template. As fabricated Cuf was then washed properly with DI water to remove any present acidic residue.[17]

2.3.3 Electrodeposition method of catalyst synthesis

A few well known routes for nanomaterial-based electrocatalyst synthesis are:

- Carbonisation[18]
- Chemical and hydrothermal/solvothermal methods[19]
- Pyrolysis and high temperature reactions.[20]

But there are various problems associated with above mentioned synthesis routes such as; the catalysts are less stable because of the use of binder, the synthesis approach is very expensive and also leads to complexity, the duration for the synthesis of material is long, high temperature requirement for the reaction and also the reaction takes place in multistep. Electrodeposition method is preferred among all the synthesis procedures because of low cost, ease and fast synthesis duration.[21] Also, this route of synthesis result in the fabrication of self-supporting electrocatalyst that eliminates the use of binders and eventually facilitates the catalyst durability as well as activity.[22–24] An advanced and very easy route for catalyst

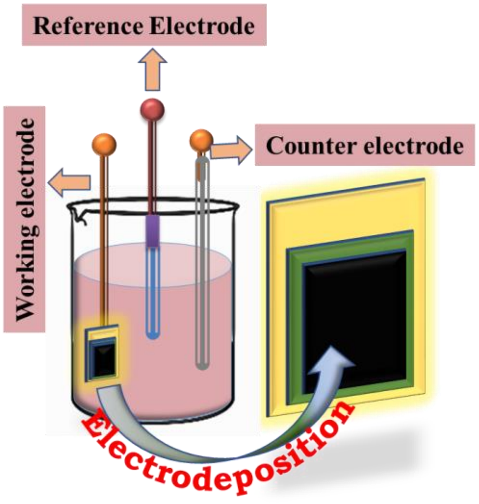

Figure 2.3 *Electrodeposition setup in set up in a three-electrode system.*

synthesis is a method called electrodeposition. A typical set-up of three-electrode system used in the electrodeposition for catalyst synthesis is shown in Figure 2.3.

2.3.4 Pyrolysis

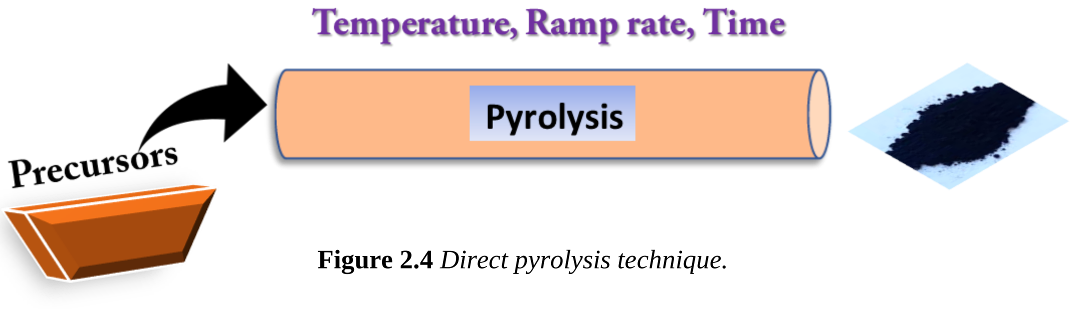

Figure 2.4 *Direct pyrolysis technique.*

Pyrolysis is the high temperature treatment of the material in inert atmosphere (Figure 2.4). Mostly for the synthesis of metal-nitrogen-carbon/sulphur-based (M-N-C/S) catalyst in water electrolysis is prepared via direct pyrolysis technique in order to achieve admirable electrocatalytic activity in terms of water electrolysis. The pyrolysis of the material in a empirical approach or we can say “Edisonian” approach which actually requires control and several optimizations in material engineering. The synthesis of the catalyst entirely depends on the type of precursors, temperature, time and the reaction atmosphere. There are basically three main steps for the pyrolysis process. Below 400˚C, the N-C precursor starts to melt down and decomposes at certain ramp rate and results in the formation of micro-pores and pathway. When the temperature increases from 400 ˚C to around 900˚C, the formation of amorphous carbon domain forms and reduction of metal species takes place. Above 900˚C, the atomically dispersed M-N moieties takes place in the graphitized carbon matrix. Further, advancement in the temperature may lead to the agglomeration of metal-nanoparticles in the carbon matrix. So, proper optimizations are critical in direct pyrolysis for the catalyst synthesis.[20,25]

2.3.5 Cleaning of the electrodes

The glassy carbon electrode (GCE), rotating disc electrode (RDE) and rotating-ring disc electrode (RRDE) were polished with 1 µm, 0.3 µm and 0.05 µm Alumina (Al_2O_3) powder followed by washing ultrasonically with Millipore water for 3.5 min. Further purification of the surface of the electrodes were done electrochemically by performing few cyclic voltammetry (CV) scan in three-electrode systems in the potential range of 0 to 1.4 V in 0.5 M H_2SO_4 at a scan rate of 500 mVs^{-1}.[26]

2.3.6 Electrode modification

The ink of the catalyst was prepared by dispersing the catalyst in a solution containing 1:1 ratio of DI water and isopropyl alcohol (IPA), after which the sonication was done for 1 h. The dropcasting of the ink on electrode was done according to the optimized mass loading.

2.3.7 Pt/C and RuO_2 modification on bare GCE

An amount of 5 mg of the commercially available Pt/C and RuO_2 were taken and dispersed in a 1 mL mixed solution of water and ethanol (volume ratio = 1:1) and sonicated for at least 1-2 h to generate a homogeneous ink. After that both Pt/C and RuO_2 inks ware further dropcasted onto two separate glassy carbon electrodes with a certain optimized mass loading.

2.3.8 Zn-air battery set-up

The homemade Zn-Air Battery were assembled using a two-electrode configuration, where the catalyst served as the cathode, for oxygen evolution reaction (OER) and oxygen reduction reaction (ORR) for charging and discharging, polished Zn foil of 0.25 mm was used as the anode, and 6 M KOH solution with 0.2 M zinc acetate as an electrolyte. The dropcasting of the prepared catalyst ink in order to modify electrode was done on the nickel foam (1 × 1) cm^2 electrodes which was used as current collector with an optimized mass loading.

2.3.9 Electrochemical studies

The electrochemical performances of the catalyst were performed out in a three-electrode system using the prepared catalyst as a working electrode, Hg/Hg_2SO_4 (saturated K_2SO_4)/ Ag/AgCl (3.0 M) as the reference electrode and graphite rod as the counter electrode in 1 M KOH/0.5 M H_2SO_4 solution in ambient atmospheric conditions. The potential scan was scaled to reversible hydrogen electrode (RHE) based on the formula given below in equation 2.4:

$$E_{\mathrm{RHE}} = (E_{\mathrm{Hg/Hg2SO4\ (saturated)}} + 0.65 + 0.0591\ \mathrm{pH})\ \mathrm{V} \qquad (2.4)$$

To rationalize the ohmic drop imparted on the catalyst, the polarisation curves were i*R* corrected (unless mentioned otherwise). There was no i*R* drop compensation done during the electrochemical study carried out with two-electrode system. The electrochemical activity for HER and OER were accomplished with the help of linear sweep voltammetry (LSV) technique at a scan rate of 10 mVs^{-1}, and for Tafel slope analysis, the scan rate was taken to be 1 mVs^{-1}. The surface of the working electrode was electrochemically activated for around 25 cyclic voltammetry (CV) scan. The current obtained by the catalyst during the electrochemical study were normalized by geometrical surface area of the electrode in order to calculate the current density. In order to check the stability and mechanical robustness of the as prepared catalyst, chronopotentiometry (CP)/step CP measurements were performed without compensating i*R*. The electrochemical impedance spectroscopy (EIS) for two electrode system were conducted at a particular potential in a frequency range of 10^5–10^{-2} Hz.

2.3.10 Computational details

In order to reduce the huge computational call of the calculations, the geometry optimization using DFT, a restraint optimization was employed. The surface atomic coordinates were allowed to relax fully, while 2-3 atomic layers underneath the surface layer were held at the primary positions corresponding to their bulk assembly, using the discerning dynamics option implemented within the Vienna *ab initio* imitation package (VASP)[27]. In all cases, a spin-polarized DFT calculation were performed with conjugate gradient algorithm for the geometry optimization. The van der Waals' (vdW) dispersive interactions was performed within the DFT-D2 with a scaling parameter of 0.75 (VDW_SCALING = 0.75) and vdW radius of 30.0 (VDW_RADIUS = 30.0) with VDW_D = 20.0 in the VASP INCAR settings. The DFT harmonic vibrational frequencies for the zero-point energy (ZPE) and entropy, S calculation was calculated using a finite displacement method (IBRION = 5) where the intrinsic VASP symmetry flag (ISYM) was set to zero in order to avoid errors, which could perhaps arise from any incorrect version of thermochemical energies with same settings for the vdW-DFT-D2 and energy threshold as used for the geometry easing.

Surface geometries for H-adsorption: In order to build a Ni_5P_4 (0001) slab geometry, the bulk crystal of Ni_5P_4 in its P*63*mc (186) space group symmetry was optimized first. Upon geometry optimization, the lattice constants converged to a = b = 6.793 Å, c = 10.983 Å, which is in very close agreement with our PXRD analysis (a = b = 6.789 Å, c = 10.986 Å).

2.3.11 Calculation of the evaluation parameters in water electrolysis

2.3.11.1 Electrochemically active surface area calculation (ECSA) and roughness factor (RF)

The surface roughness factor (RF) of electrode was calculated by measuring its electrochemically active surface area (ECSA) from its electrochemical double layer capacitance (C_{dl}). Cyclic voltametery (CV) scans of the electrodes in a non-Faradaic region 1.0 M KOH/0.5M H_2SO_4 electrolyte at different scan rates (25 to 200 mV/s). The potential windows were restricted to a non-faradic region. The double-layer charging current is equal to the product of the scan rate, v, and the electrochemical double-layer capacitance, C_{dl}, as given by equation 2.5:

$$i_c = vC_{dl} \tag{2.5}$$

The difference in the fitted slopes of forward and backward CV scans was used to determine the C_{dl}, which is 33.9 mF cm^{-2}.[28]ECSA is then calculated by dividing the C_{dl} by the specific surface capacitance (Csp) of electrode surface as depicted in equation 2.6:

$$ECSA = C_{dl}/C_{sp} \tag{2.6}$$

The roughness factor was calculated by using formula[29]

RF (catalyst) = catalyst active surface area substrate/geometric surface area

2.3.11.2 Number of electrons and %H_2O_2 calculation in ORR

The calculation for the number of electron (n) and hydrogen peroxide (%H_2O_2) during ORR which the catalyst possesses was analyzed using RRDE measurements using equation 2.7 and 2.8:

$$n = 4 \times \frac{I_\mathrm{D}}{I_\mathrm{D} + \frac{I_\mathrm{R}}{N}} \tag{2.7}$$

$$\%H_2O_2 = 200 \times \frac{\frac{I_\mathrm{R}}{N}}{\frac{I_\mathrm{R}}{N} + I_\mathrm{D}} \tag{2.8}$$

where I_D and I_R represent the disk and ring current, respectively. N accounts to the collection efficiency of Pt ring, which is (N=0.249) in this case.

The J_K value can be analyzed on the basis of Koutecky-Levich (K-L) formula using equation 2.9, 2.10 and 2.11:

$$\frac{1}{J} = \frac{1}{J_\mathrm{L}} + \frac{1}{J_\mathrm{K}} = \frac{1}{B\omega^{\frac{1}{2}}} + \frac{1}{J_\mathrm{K}} \tag{2.9}$$

$$B = 0.62nFC_0 D_0^{2/3} \vartheta^{-1/6} \tag{2.10}$$

$$J_\mathrm{K} = \mathrm{nFk}C_0 \tag{2.11}$$

J is the current density, J_K and J_L are the kinetic and diffusion-limiting current densities, ω is the angular velocity of the disk (ω = 2πN, N is the linear rotation speed), n is the overall number of electrons transferred in O_2 reduction, F is the Faraday constant (F = 96485 C mol^{-1}), C_0 is the bulk concentration of O_2, ϑ is the kinematic viscosity of the electrolyte, D_0 is the diffusion coefficient of O_2 in 0.1 M KOH ($D_0 = 1.9\times10^{-5}$ cm^2 s^{-1}), and k is the electron transfer rate constant. The n value and J_K can be obtained from the slope and intercept of the Koutecky−Levich plots, respectively.

2.4 Instrumentation

2.4.1 Powder X-ray diffraction

For the investigation of the crystalline or amorphous nature, crystal structure and phases present in the sample, X-ray diffraction analysis is done. A monochromatic beam of X-ray, when incident on the sample surface, gets diffracted from the unique crystal planes and the scattered beam of X-ray detected using the detector (digital image of the instrument is shown in Figure 2.5a). X-ray machine utilizes a non-destructive technique. The crystal structure calculated by utilizing Bragg's law, introduced by W. L. Bragg in 1912. The Bragg's equation: $n\lambda=2d\sin\theta$, where θ, λ are the incident angle and wavelength of the radiation (1.5418 Å for Cu Kα), respectively. '*d*' is the perpendicular distance between adjacent planes (Figure 2.5b).[30]

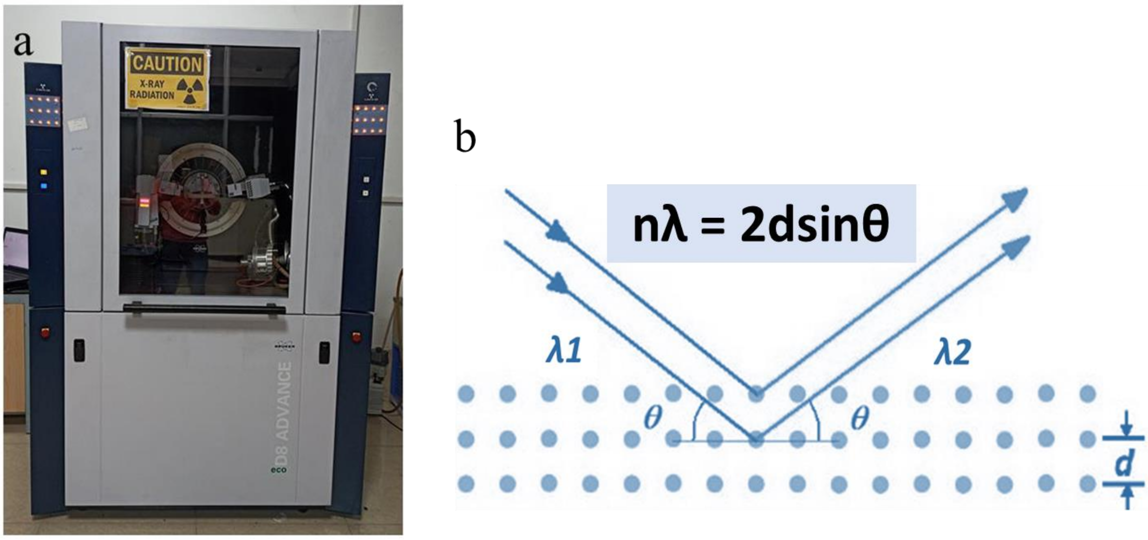

Figure 2.5 *(a) A typical view of PXRD instrument (b) X-ray generation geometry.*

X-ray Diffraction (XRD) analysis was carried out on a Bruker D8 Advances instrument using Cu- Kα (λ = 1.5406 Å) radiation in the 2θ range from 5° to 80° with an acceleration voltage of 40 KV.

2.4.2 Scanning electron microscopy (SEM)

The working of scanning electron microscope (digital image shown in Figure 2.6a) is similar to that of optical electron microscope, however here the electrons are used as a beam rather than light in the case of optical microscope. Using the SEM instrument, one can see a tiny object such as red blood cells (7 μm). Electron microscope encompasses very high resolution and capture the content at the atomic level.[31] In SEM, the beam of electrons, when incident on the surface of specimen and interact with its atoms and generates signals which contains the information regarding surface topology, morphology, composition etc. The SEM instrument works in high vacuum. The signal containing information were detected and processed into the image and other informative contents. After the electron collision with specimen’s atoms, different types of signals such as secondary electrons, backscattered electrons, characteristic x-rays as well as transmitted x-ray are produced as shown in Figure 2.6b. The secondary electrons give the idea about the morphology of the sample.

Surface morphology was investigated using Scanning Electron Microscopy (SEM Jeol JSMIT300) at an acceleration voltage of 10-15 KV.

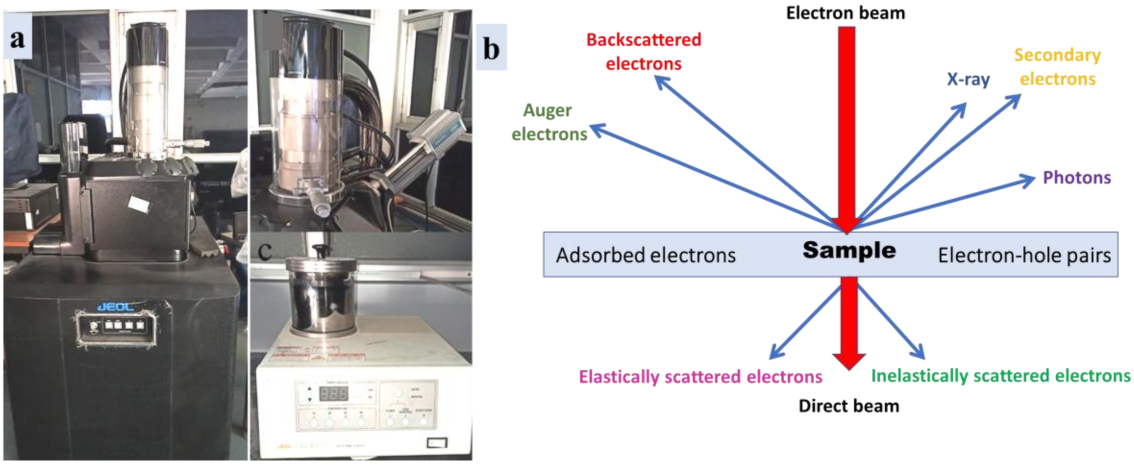

Figure 2.6 *(a) A typical view of SEM column (left), the EDX detector (backside of column, upper right) and gold coater unit (lower right). (b) different signal of generated from specimen upon the interaction with e-beam.*

2.4.3 Field-emission scanning electron microscopy (FE-SEM)

Field Emission Scanning Electron Microscope (FE-SEM) provides the images in ultra-high-resolution range. The main difference between FE-SEM and SEM is the emission source, the SEM utilizes thermionic emitter while FE-SEM uses field-emitter.[32]

The FE-SEM were performed using JEOL JSM-7600F (FESEM).

2.4.4 Transmission electron microscopy (TEM)

Transmission electron microscopy (TEM) is considered as a powerful structural and morphological characterization technique of the sample which is enormously used in material science. TEM working principle is same as that of optical microscope where, high voltage electron beam is used instead of light as a source.[33] In TEM thin of the sample is been exposed to the electron beam have the same current density. The typical acceleration voltage of the instrument is about 100-200 kV. The ejection of the electron from the electron gun are done using three methods such as thermionic, field-emission and Schottky. The field emission pathways are known to provide high brightness and coherent beam during the microscopic study. The selection of aperture and the focus of the electron beam is done using the condenser and electromagnetic lenses. The image was taken after the interaction of the e-beam with the sample on the fluorescent screen after coupling with the CCD camera.

Figure 2.7 *Digital image of transmission electron microscopy.*

Transmission Electron Microscopy (TEM) analysis were carried out on a JEM2100 instrument suitable for High-Resolution TEM (HRTEM) studies (Figure 2.7). The instrument was armed with digital micrograph software for investigating selected area electron diffraction (SAED) pattern of the sample surface. Holey carbon-coated copper grids (Agar Scientific Ltd.) were used as the sample grid in the measurements.

2.4.5 Energy-dispersive X-ray spectroscope (EDX) and elemental mapping

The atomic information of the material is obtained from EDX analysis when coupled with SEM/TEM. The EDX analysis is solely depends upon the atomic number of the elements present in the sample. Basically, the elements having the atomic number higher than that of boron is easily detected. At some special case and certain modification, the Boron can also be detected in EDX. The EDX gives various information of material such as, quantification, evaluation, identification, impurity check etc. Elemental mapping was also done using the same instrument to check the distribution of the elemental entities in the sample.[34,35]

2.4.6 Brunauer Emmett Teller (BET) surface area analysis

For the determination of specific surface area, surface properties and pore size distribution of the material, the investigation of the adsorption of gas molecule on the surface of the material is done and that investigation is accomplished using Brunauer Emmett Teller (BET) technique (digital image of the instrument is shown in Figure 2.8). The porosity behaviour of the material i.e. the confirmation that whether the material is porous or non-porous is done by the calculation of volumetric N_2 adsorption-desorption isotherm at 77K. International Union of Pure and Applied Chemistry (IUPAC) classified a total six types of adsorption isotherms (Type I to VI) of adsorption isotherms according to their characteristics. The type I isotherm is classified for the microporous materials (pore size < 2nm) owing to high adsorption of adsorbent molecules at relatively low partial pressure. Type II isotherm is found in nonporous and macroporous (pore size 2-50 nm) materials.[36,37]

Figure 2.8 *A typical image for surface area analyser instrument.*

Nitrogen adsorption-desorption analysis was done at 77 K on an Autosorb iQ2 instrumental setup to examine the surface area by Brunauer Emmett Teller (BET) method. The samples were degassed at 160 °C for more than 12 h under vacuum conditions. The pore size distribution was computed by the Nonlocal density functional theory (NLDFT).

2.4.7 X-Ray Photoelectron Spectroscopy (XPS)

The X-ray photoelectron spectroscopy (XPS), gives the idea about the chemical states and surface chemistry of the materials. This technique can be done on electrically conducting as well as non-conducting material surface. The sample is irradiated using a monochromatic X-ray having low-energy (Al Kα or Mg Kα) under high vacuum condition. The incident X-ray photon when hits the core level electron present in the material, transfers the energy to the electron (Figure 2.9).[38,39] This results in the ejection of the electron from its initial ground state with certain kinetic energy associated with it. The photo-emitted core electron is been analysed as a function of binding energy and give the information about its chemical environment and states with their composition. The peak position of the spectrum gives the idea about the chemical nature of the material. The depth from which the photoelectrons are originates is <10 nm. X-Ray photoelectron (XPS) spectroscopy was executed on a K-Alpha plus XPS system of ThermoFisher Scientific instruments in an ultrahigh vacuum chamber (7X10^{-9} torr) using Al-K radiation (1486.6 eV).

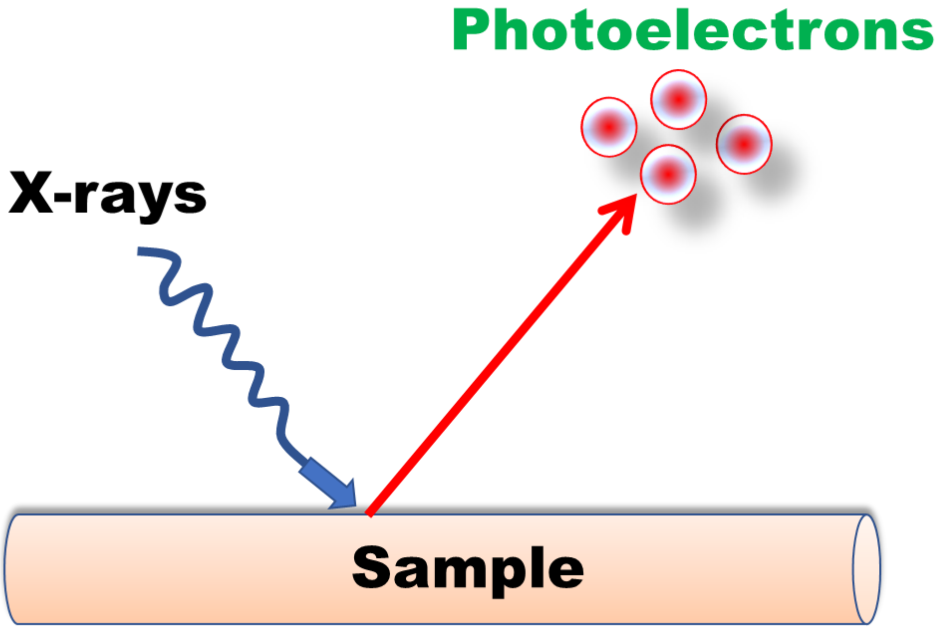

Figure 2.9 Fundamental of *X-Ray Photoelectron Spectroscopy (XPS)*

2.4.8 Fourier transform infrared spectrophotometer (FTIR)

Fourier transform infrared spectrophotometer (FTIR) works on the basis of vibration of the molecules. Each and every functional group has their own and unique vibrational energy, which actually helps in the identification of the bonds present in the sample. This spectroscopy technique gives the idea about the bonds present in the sample which are infrared active.[40]

Fourier transform Infrared (FTIR) spectroscopy was performed out using Agilent technology Cary 600 series FTIR instrument at ambient conditions. For FTIR analysis, all the samples were mixed with KBr and then finely ground to make a pellet.

2.4.9 Extended X-Ray Absorption Fine Structure (EXAFS)

Extended X-Ray Absorption Fine Structure (EXAFS) is the measurement of energy transitions from core electronic states of the metal to the excited electronic states and the continuum. The X-ray absorption near-edge structure (XANES), and extended X-ray absorption fine structure (EXAFS) gives the information regarding the fine structure in the absorption at energies greater than the threshold for electron release. These two methods give complementary structural information, the XANES spectra (Figure 2.10) gives the idea of electronic structure, oxidation states and the symmetry of the metal site, and the EXAFS gives the information for coordination numbers, types, and radial distances and neighbouring atoms from the absorbing element.[41,42]

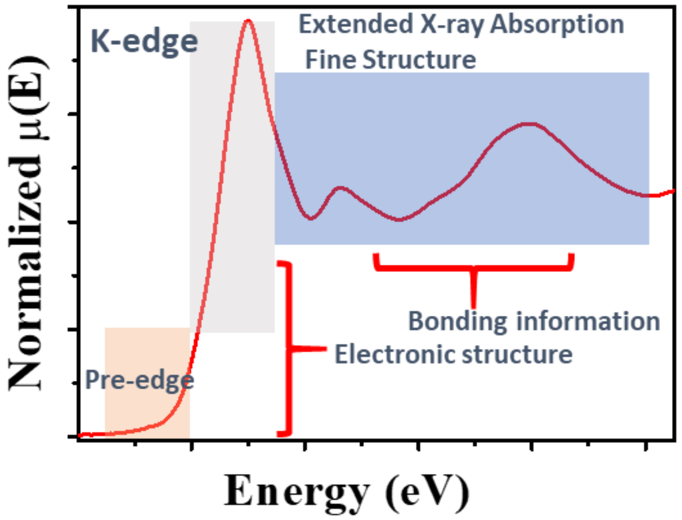

Figure 2.10 *Extended X-ray absorption fine structure*

EXAFS were carried out with the dispersive EXAFS beam line (BL-9) at Indus-2 synchrotron radiation source at the Raja Ramanna Centre for Advanced Technology (RRCAT), Indore, India. The measurements were done in transmission mode. The beamline consisted of Rh/Pt coated meridional cylindrical mirror for collimation and a Si

(111) double crystal monochromator (DCM) to select excitation energy of Fe and Co K-edges. All the spectra were measured under ambient condition. Data analysis was carried out using DEMETER programs. Athena and Artemis codes were utilised to extract the measured data and fit the profiles.

2.4.10 Drop size analyser

The drop size analyser, was used to investigate the surface property/hydrophilic[43] nature of the catalyst and performed using KRUSS (DSA25E, 100 watt) instrument.

2.4.11 Hoffmann voltameter and Gas chromatography (GC)

In order to calculate the faradic efficiency in water splitting, water gas displacement method was utilized using Hoffmann voltameter.[44,45] This method for the calculation of Faradic efficiency is done during water electrolysis. The charge and time were recorded for the corresponding displacement of water assembled separately in a cathode and anode chamber. The displacement in the water level is due to the generation of H_2 and O_2 during water electrolysis. Finally, the faradic efficiency was calculated by evaluating the ratio of experimentally determined H_2/O_2 and theoretically calculated H_2/O_2. A typical digital image of Hoffmann voltameter during water electrolysis is shown in Figure 2.11a.

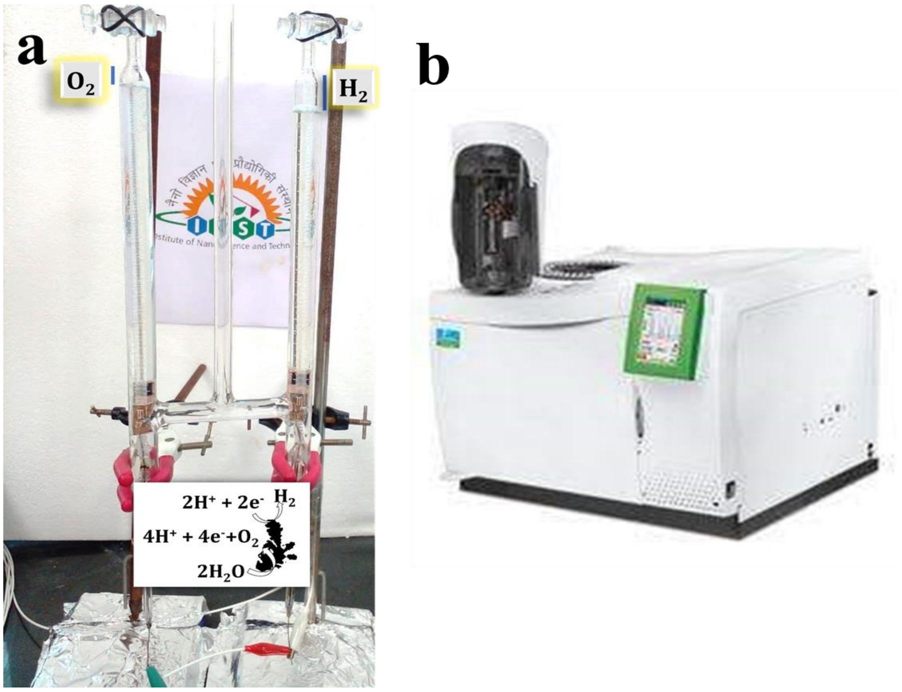

Figure 2.11 *(a) Faradic efficiency calculation of H_2 and O_2 produced during electrolysis analysis (b) A digital image of gas chromatography instrument.*

During the water electrolysis, along with the desired gas (H_2/O_2), there is a probability for the presence of other gases. To check the presence of any other gases in collected H_2, Gas chromatography techniques were utilized (Figure 2.11b).

Gas chromatography experiment were performed with the help of PerkinElmer, Arnel Engineered Solutions, Clarus 680 GC.

2.4.12 Density Functional Theory (DFT) Investigations

Density functional theory (DFT) calculations were performed within the Vienna ab initio simulation package (VASP).[27] The ion-electron exchange correlation functionals were treated with the projector augmented wave (PAW)[46,47] psedopotentials by considering Perdew-Burke-Ernzerhof (PBE)[48] parametrization form of generalized gradient approximation (GGA) with a kinetic energy cutoff of 500 eV to expand the electronic wave functions in a plane wave basis-set. A Γ-centered 5x5x1 k –mesh was used for the Brillouin zone (BZ) sampling with an energy threshold of 1×10^{-5} eV for the total energy convergence and a force tolerance of 0.01 eV/Å for the ionic and electronic relaxation. The periodic replicas of slab geometry were decoupled by considering a large vacuum spacing > 20 Å along the z-axis. Besides, the vans der Waals (vdW) correction to the dispersive forces were explicitly treated by using Grimme's DFT-D2 method for the surface adsorbed geometries.

2.4.13 Electrochemical measurements

To understand the mechanism happening on the surface of the electrode material, electrochemical techniques such as cyclic voltammetry (CV), linear sweep voltammetry (LSV), galvanostatic charge discharge (GCD), Electrochemical Impedance Spectroscopy (EIS), chronoamperometry (CA), chronopotentiometry (CP) etc. are performed. The analysis is basically done using two processes; Faradic as well as non-Faradic process. Faradic process involves the transfer of the electron/charge through the electrode/electrolyte interface following the Faraday law in contrast other is termed as a non-Faradic process. The occurrence of the redox reaction (oxidation and reduction) is due to the transfer of charge through interfaces. This transfer can actually occur through any of the path such as diffusion, convection and migration. The transfer of the charge species greatly affected by the concentration of the reactant, time as well as distance of the electrode as shown in the equation 2.12 and 2.13:

$$I = \frac{dq}{dt} \tag{2.12}$$

$$i_c = -nFAk_{red}[O_{electrode}] \quad (2.13)$$

Where, n, A and F have their usual meaning arising due to the concentration of the redox active entities at the electrode surface.

Ficks law: In a diffusion-controlled process, the movement of the charge/ions species depends upon the time and the distance from the electrode. The equation of the Fick's law[49] is given as:

First law, $$j_0 = -D_0 \frac{d[O]}{dx} \quad (2.14)$$

Second law, $$\frac{d[O]}{dt} = D_0 \frac{d^2[O]}{dx^2} \quad (2.15)$$

2.4.13.1 Electrochemical workstations

Electrochemical measurement techniques such as cyclic voltammetry (CV), linear sweep voltammetry (LSV), galvanostatic charge discharge (GCD), Electrochemical Impedance Spectroscopy (EIS), chronoamperometry (CA), chronopotentiometry (CP) etc. were performed on CHI 660, CHI 760E as shown in Figure 2.12a (CH Instruments, USA) and Metrohm Autolab PGSTAT (302N) (Figure 2.12b) electrochemical workstations. The glassy carbon electrode (area=0.07 cm^2), ring-disk electrode (RDE, 0.03 cm^2) or a rotating ring-disk electrode (RRDE, 0.1964 cm^2), was modified with the prepared ink with the required mass loading as discussed in the above section.

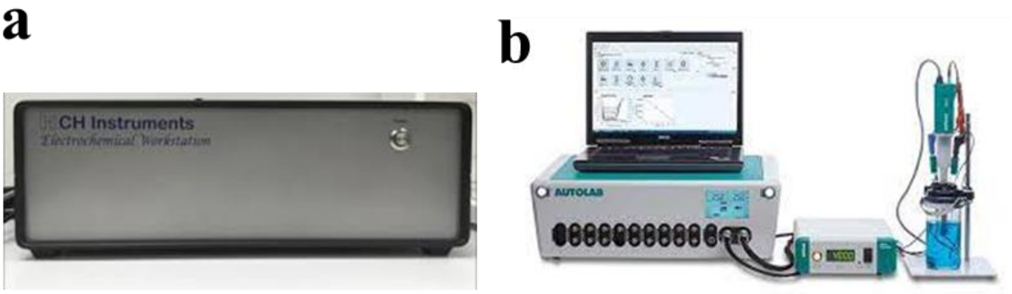

Figure 2.12 *Electrochemical workstations (a) CHI 760E (b) Metrohm Autolab PGSTAT (302N).*

2.4.13.2 Two-electrode and three-electrode system configuration

The electrochemical studies were done in a standard three/two-electrode system electrochemical cell. The as prepared electrode catalyst used as a working electrode, Hg/Hg_2SO_4 (saturated K_2SO_4)/ Ag/AgCl (3.0 M) as the reference electrode and graphite rod as the counter electrode in 1 M KOH/0.5 M H_2SO_4 solution in ambient atmospheric conditions. In contrast, two-electrode system the electrochemical measurement are done between the same working electrode.

2.4.13.3 The linear sweep voltammetry and cyclic voltammetry

Within a fixed potential window, the sweeping of potential is recorded at a certain scan rate is termed as linear sweep voltammetry (LSV). The revert back of the LSV one or many times to complete the redox process is termed as cyclic voltammetry (CV).

2.4.13.4 Impedance measurements

The electrochemical impedance spectroscopy (EIS) for three/two electrode system were conducted at a particular potential in a frequency range of 10^5–10^{-2} Hz.

2.4.13.5 Rotating ring disc electrode (RRDE) and rotating disc electrode (RDE)

The Rotating ring disc electrode (RRDE) is considered as a low-noise disc electrode used to perform the electrochemical analysis (Figure 2.13 a). This is done under the controlled hydrodynamic conditions.[50,51] The ring and the disc in combination gives the information regarding the reaction intermediate occurring in the experiment. The electrode configures to rotate at different RPM depending upon the command given by the autolab software. The rotation speed can also be controlled manually provided by the command button on the motor control unit (Figure 2.13b and Figure 2.13c). The RDE reading is also a hydrodynamic controlled electrochemical measurement process, but there is the absence of ring electrode in it. RDE also measures the experiment by rotating the electrode at different rotating speeds.

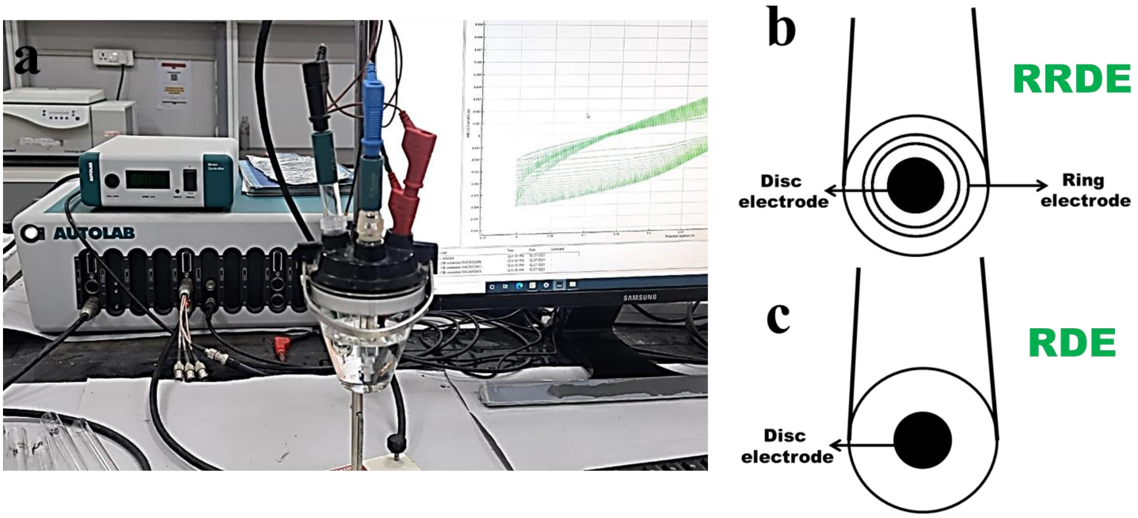

Figure 2.13 *Electrochemical workstation Metrohm Autolab PGSTAT (302N) displaying RRDE set-up (b) a typical RRDE electrode with ring and disc electrode (c) RDE electrode.*

2.5 References

1. Slotwinski, J. *et al.* Physical and Chemical Characterization Techniques for Metallic Powders. *AIP Conf. Proc.* **1581**, (2014).
2. Characterization of Materials — I BT - Biomaterials. in (eds. Park, J. B. & Lakes, R. S.) 41–81 (Springer New York, 2007). doi:10.1007/978-0-387-37880-0_3.
3. Abdel-Karim, R. & El-Raghy, S. Electrochemical Deposition of Nanoporous Metallic Foams for Energy Applications. in *Advanced Materials and their Applications: Micro to nano scale* 69–91 (2017).
4. Kim, Y. K., Cha, S. I. & Hong, S. H. Nanoporous cobalt foam and a Co/Co(OH)2 core-shell structure for electrochemical applications. *J. Mater. Chem. A* **1**, 9802–9808 (2013).
5. Bryce C, T., Stephen A, S. & Luther, E. P. Nanoporous metal foams. *Angew. Chemie - Int. Ed.* **49**, 4544–4565 (2010).
6. Hua, Z., Deng, Y., Li, K. & Yang, S. Low-density nanoporous iron foams synthesized by sol-gel autocombustion. *Nanoscale Res. Lett.* **7**, 1–7 (2012).
7. Liu, P. S. & Chen, G. F. Application of Porous Metals. *Porous Mater.* 113–188 (2014) doi:10.1016/b978-0-12-407788-1.00003-4.
8. Popov, K. I., Djokić, S. S., Nikolić, N. D. & Jović, V. D. *Morphology of Electrochemically and Chemically Deposited Metals*. (Springer International Publishing, 2016). doi:10.1007/978-3-319-26073-0.
9. Zhang, Y., Huang, J. & Ding, Y. Porous Co3O4/CuO hollow polyhedral nanocages derived from metal-organic frameworks with heterojunctions as efficient photocatalytic water oxidation catalysts. *Appl. Catal. B Environ.* **198**, 447–456 (2016).
10. Wang, X. *et al.* Copper Selenide–Derived Copper Oxide Nanoplates as a Durable and Efficient Electrocatalyst for Oxygen Evolution Reaction. *Energy Technol.* **8**, 2000142 (2020).
11. Gamburg, Y. D. & Zangari, G. *Theory and Practice of Metal Electrodeposition*. *Cailiao Rechuli Xuebao/Transactions of Materials and Heat Treatment* vol. 35 (Springer New York, 2011).
12. Niu, J. *et al.* Effect of electrodeposition parameters on the morphology of three-dimensional porous copper foams. *Int. J. Electrochem. Sci.* **10**, 7331–7340 (2015).
13. Nikolić, N. D., Branković, G. & Maksimović, V. M. Morphology and internal

structure of copper deposits electrodeposited by the pulsating current regime in the hydrogen co-deposition range. *J. Solid State Electrochem.* **16**, 321–328 (2012).

14. Dey, R. S., Hjuler, H. A. & Chi, Q. Approaching the theoretical capacitance of graphene through copper foam integrated three-dimensional graphene networks. *J. Mater. Chem. A* **3**, 6324–6329 (2015).
15. Zhang, H., Ye, Y., Shen, R., Ru, C. & Hu, Y. Effect of Bubble Behavior on the Morphology of Foamed Porous Copper Prepared via Electrodeposition. *J. Electrochem. Soc.* **160**, D441–D445 (2013).
16. Shin, H. C., Dong, J. & Liu, M. Nanoporous Structures Prepared by an Electrochemical Deposition Process. *Adv. Mater.* **15**, 1610–1614 (2003).
17. Das, M. *et al.* Single-phase Ni 5 P 4 –copper foam superhydrophilic and aerophobic core–shell nanostructures for efficient hydrogen evolution reaction. *J. Mater. Chem. A* **7**, 23989–23999 (2019).
18. Li, X., Hao, X., Abudula, A. & Guan, G. Nanostructured catalysts for electrochemical water splitting: current state and prospects. *J. Mater. Chem. A* **4**, 11973–12000 (2016).
19. Das, A. & Ganguli, A. K. Design of diverse nanostructures by hydrothermal and microemulsion routes for electrochemical water splitting. *RSC Adv.* **8**, 25065–25078 (2018).
20. Pattiya, A. 2 - Catalytic pyrolysis. in (ed. Rosendahl, L. B. T.-D. T. L. for E. A.) 29–64 (Woodhead Publishing, 2018). doi:https://doi.org/10.1016/B978-0-08-101029-7.00002-3.
21. Xu, X., Du, P., Chen, Z. & Huang, M. An electrodeposited cobalt-selenide-based film as an efficient bifunctional electrocatalyst for full water splitting. *J. Mater. Chem. A* **4**, 10933–10939 (2016).
22. Dogan, F., Sanjeewa, L. D., Hwu, S. J. & Vaughey, J. T. Electrodeposited copper foams as substrates for thin film silicon electrodes. *Solid State Ionics* **288**, 204–206 (2016).
23. Zhou, L. *et al.* Construction of hierarchical CuO/Cu2O@NiCo2S4 Nanowire arrays on copper foam for high performance supercapacitor electrodes. *Nanomaterials* **7**, (2017).
24. Liu, H., Peng, X., Liu, X., Qi, G. & Luo, J. Porous Mn-Doped FeP/Co 3 (PO 4) 2 Nanosheets as Efficient Electrocatalysts for Overall Water Splitting in a Wide pH Range. *ChemSusChem* **12**, 1334–1341 (2019).

25. Huang, Y. *et al.* Catalysts by pyrolysis: Direct observation of chemical and morphological transformations leading to transition metal-nitrogen-carbon materials. *Mater. Today* **47**, 53–68 (2021).
26. McCreery, R. L. Advanced Carbon Electrode Materials for Molecular Electrochemistry. *Chem. Rev.* **108**, 2646–2687 (2008).
27. Kresse, G. & Furthmüller, J. Efficient iterative schemes for ab initio total-energy calculations using a plane-wave basis set. *Phys. Rev. B* **54**, 11169–11186 (1996).
28. Fisica, C. & Milano, U. AND APPLIED CHEMISTRY COMMISSION ON ELECTROCHEMISTRY * REAL SURFACE AREA MEASUREMENTS Prepared for publication b y. *Pure Appl. Chem.* **63**, 711–734 (1991).
29. Benck, J. D., Chen, Z., Kuritzky, L. Y., Forman, A. J. & Jaramillo, T. F. Amorphous Molybdenum Sulfide Catalysts for Electrochemical Hydrogen Production: Insights into the Origin of their Catalytic Activity. 2–9 (2012) doi:10.1021/cs300451q.
30. Ameh, E. S. A review of basic crystallography and x-ray diffraction applications. *Int. J. Adv. Manuf. Technol.* **105**, 3289–3302 (2019).
31. Vernon-Parry, K. D. Scanning electron microscopy: an introduction. *III-Vs Rev.* **13**, 40–44 (2000).
32. El-Eskandarany, M. S. 2 - Characterizations of mechanically alloyed powders. in (ed. El-Eskandarany, M. S. B. T.-M. A. (Third E.) 13–18 (William Andrew Publishing, 2020). doi:https://doi.org/10.1016/B978-0-12-818180-5.00002-9.
33. Franken, L. E., Grünewald, K., Boekema, E. J. & Stuart, M. C. A. A Technical Introduction to Transmission Electron Microscopy for Soft-Matter: Imaging, Possibilities, Choices, and Technical Developments. *Small* **16**, 1906198 (2020).
34. Kohli, R. Chapter 3 - Methods for Monitoring and Measuring Cleanliness of Surfaces. in (eds. Kohli, R. & Mittal, K. L. B. T.-D. in S. C. and C.) 107–178 (William Andrew Publishing, 2012). doi:https://doi.org/10.1016/B978-1-4377-7883-0.00003-1.
35. Ghodke, S. A., Maheshwari, U., Gupta, S., Sonawane, S. H. & Bhanvase, B. A. Chapter 12 - Nanomaterials for adsorption of pollutants and heavy metals: Introduction, mechanism, and challenges. in *Micro and Nano Technologies* (eds. Bhanvase, B., Sonawane, S., Pawade, V. & Pandit, A. B. T.-H. of N. for W. T.) 343–366 (Elsevier, 2021). doi:https://doi.org/10.1016/B978-0-12-821496-1.00032-5.

36. Thommes, M. *et al.* Physisorption of gases, with special reference to the evaluation of surface area and pore size distribution (IUPAC Technical Report). *Pure Appl. Chem.* **87**, 1051–1069 (2015).
37. Kumar, K. V. *et al.* Characterization of the adsorption site energies and heterogeneous surfaces of porous materials. *J. Mater. Chem. A* **7**, 10104–10137 (2019).
38. Baer, D. R. & Thevuthasan, S. Chapter 16 - Characterization of Thin Films and Coatings. in (ed. Martin, P. M. B. T.-H. of D. T. for F. and C. (Third E.) 749–864 (William Andrew Publishing, 2010). doi:https://doi.org/10.1016/B978-0-8155-2031-3.00016-8.
39. Engelhard, M. H., Droubay, T. C. & Du, Y. X-Ray Photoelectron Spectroscopy Applications. in (eds. Lindon, J. C., Tranter, G. E. & Koppenaal, D. W. B. T.-E. of S. and S. (Third E.) 716–724 (Academic Press, 2017). doi:https://doi.org/10.1016/B978-0-12-409547-2.12102-X.
40. JANSSENS, M. 2 - Fundamental measurement techniques. in (ed. Apte Transport and Mining, V. B. B. T.-F. T. of M. U. in C.) 22–62 (Woodhead Publishing, 2006). doi:https://doi.org/10.1533/9781845691042.22.
41. Principi, E. 1 - Extended X-ray absorption fine structure (EXAFS) technique for low temperature fuel cell catalysts characterization. in *Polymer Electrolyte Membrane and Direct Methanol Fuel Cell Technology* (eds. Hartnig, C. & Roth, C.) vol. 2 3–25 (Woodhead Publishing, 2012).
42. Teo, B.-K. Novel method for angle determinations by EXAFS via a new multiple-scattering formalism. *J. Am. Chem. Soc.* **103**, 3990–4001 (1981).
43. Das, M., Kamboj, N., Purkait, T., Sarkar, S. & Dey, R. S. Revealing the Structural Aspect of Ultrastable Self-Supportive Bifunctional Electrocatalyst for Solar-Driven Water Splitting. *J. Phys. Chem. C* **124**, 13525–13534 (2020).
44. Detsi, E. *et al.* Mesoporous Ni60Fe30Mn10-alloy based metal/metal oxide composite thick films as highly active and robust oxygen evolution catalysts. *Energy Environ. Sci.* **9**, 540–549 (2016).
45. Sultan, S. *et al.* Superb water splitting activity of the electrocatalyst Fe3Co(PO4)4 designed with computation aid. *Nat. Commun.* **10**, 5195 (2019).
46. Blöchl, P. E. Projector augmented-wave method. *Phys. Rev. B* **50**, 17953–17979 (1994).
47. Joubert, D. From ultrasoft pseudopotentials to the projector augmented-wave

method. *Phys. Rev. B - Condens. Matter Mater. Phys.* **59**, 1758–1775 (1999).

48. Perdew, J. P., Burke, K. & Ernzerhof, M. Generalized Gradient Approximation Made Simple. *Phys. Rev. Lett.* **77**, 3865–3868 (1996).
49. Neghmouche, N. S. Mass Transport Mechanisms- (17th). *Anal. Electrochem. Basic Concepts* **2**, 2–4 (2007).
50. Kocha, S. S. Chapter 3 - Electrochemical Degradation: Electrocatalyst and Support Durability. in (eds. Mench, M. M., Kumbur, E. C. & Veziroglu, T. N. B. T.-P. E. F. C. D.) 89–214 (Academic Press, 2012). doi:https://doi.org/10.1016/B978-0-12-386936-4.10003-X.
51. Du, C., Tan, Q., Yin, G. & Zhang, J. 5 - Rotating Disk Electrode Method. in (eds. Xing, W., Yin, G. & Zhang, J. B. T.-R. E. M. and O. R. E.) 171–198 (Elsevier, 2014). doi:https://doi.org/10.1016/B978-0-444-63278-4.00005-7.

Chapter 3

Single-phase Ni_5P_4-copper foam superhydrophilic and aerophobic core-shell nanostructures for efficient hydrogen evolution reaction in acidic medium

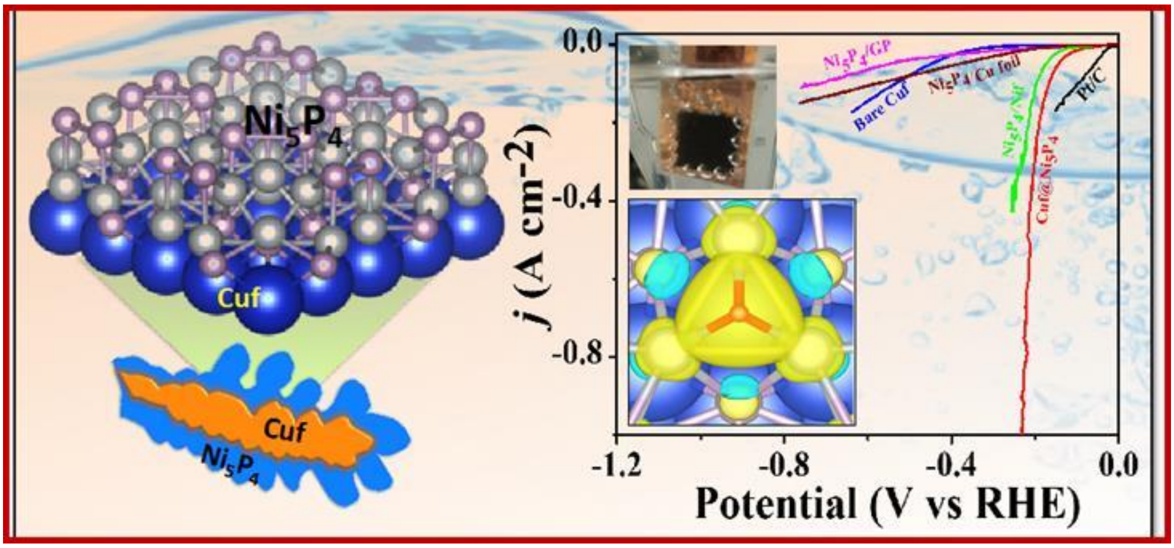

Abstract: The facile synthesis of highly durable, low-cost and robust electrocatalyst for hydrogen generation from water is vital to address the existing environmental issues as well as to provide environmental-friendly clean and green energy supply. Electrochemical deposition of single-phase nickel phosphide on galvanostatically deposited copper foam (Cuf@Ni_5P_4) core-shell nanostructure offers the innovation in structure designing and a new platform for novel electrocatalysts. The Cuf@Ni_5P_4 provides a superior three-dimensional conductive channel for ion transport during catalysis process. The catalyst exhibits an excellent electrocatalytic activity towards hydrogen evolution reaction (HER) in acidic media. The superhydrophilic and aerophobic property of the porous electrode helps to the in-time leaving of H_2 gas bubbles from the surface. Interestingly, it requires very less overpotential of 90 mV for HER at the current density of 10 mA cm^{-2}. A very small Tafel slope of 49 mV dec^{-1} and a very high exchange current density (~0.76 mA cm^{-2}) originate from large electrochemically active surface area and fast mass and electron transfer efficiency of the Cuf@Ni_5P_4 catalyst. Theoretical study was carried out to investigate the mechanism underlying the HER activity in Cu-supported Ni_5P_4 at an atomic-scale. DFT calculations suggest a very high negative Gibbs free energy change (ΔG_{H*}) in Ni_5P_4 (0001)/Cu(111) upon hydrogen adsorption, which is actually responsible for excellent HER activity of the catalyst. Furthermore, it shows remarkable durability of hydrogen generation under low (10 mA cm^{-2}) and high current density (160 mA cm^{-2}) for >84 hours with ~96% retention of overpotential, establishing a low-cost and efficient catalyst for sustainable, future energy generation strategy.

We acknowledge **Prof. Abir De Sarkar** and **Dr. Nitya Sagar Jena** for theoretical support in this chapter.

3.1 Introduction

Electrochemical generation of H_2 from water has become centre of attraction, as is one of the promising approaches for the production of renewable fuels aimed at future energy supply. Hydrogen generation is economically favorable and environmentally friendly as it generally gives pure products, which is free from CO.[1–4] In addition, H_2 not only is required as the starting material for fuel cells, several industries have also demand for them as precursor materials for the production of ammonia and refining of petroleum. Till date, several catalysts for hydrogen evolution reaction (HER) were developed, among them, noble metal catalysts such as platinum for HER are recognized as benchmark catalyst because of their high efficiency and low overpotential towards the electrocatalytic reactions.[5,6] However, due to limited resources and the expensive catalyst cost of noble metal, transition metal (Ni, Co, Fe and Mn)-based catalysts have drawn centre of attraction due to their performance and abundant source.

Transition metal sulfides, phosphides and selenides are mostly studied catalyst and have drafted enormous attention in recent years.[7] Typically phosphorous-based transition metal pnictide with earth abundant element nickel, nickel phosphides have gained immense attentions as a HER catalyst owing to their high activity and stability.[8–11] Nickel phosphide exists several phases in the nanostructures such as Ni_3P, Ni_2P, Ni_5P_2, Ni_5P_4, NiP_2 and $Ni_{12}P_5$.[12] Ni_2P was theoretically predicted to be efficient HER electrocatalyst even better than Pt[13] and experimental validation was carried out by few researcher.[14–19] Recently, Ni_5P_4 crystalline nanoparticles was explored to produce H_2 in acidic media.[8,20,21] Most of the mixed phases nickel phosphides although reported to have good electrocatalytic activity toward HER, but some disadvantages such as uncontrolled agglomeration, less hydrophilicity and poor contact resistance stop them for commercial application.[22] Single-phase Ni_5P_4 has proven to show better electrode kinetics than the multiphase nickel phosphides during catalysis. Pan et al succesfully synthesized single phase NiP_2, $Ni_{12}P_5$ and Ni_5P_4, where they have shown that the single phase Ni_5P_4 is the best electrode material in terms of HER among other nickel phosphide based catalyst.[11] This is due to the amount of positive charge on Ni ($Ni^{\delta+}$) in Ni_5P_4 is more than other nickel phosphides, which helps to achieve better catalytic performances. However, synthesis of single-phase Ni_5P_4 is still a challenge to the researchers in this field.

Strategic synthetic approaches and stepwise routes were employed to create rational active sites to achieve superior catalytic activity of nickel phosphide.[16] Several procedures were recently been explored such as hydrothermal, high temperature reaction and wet chemical route/hydrothermal in combination with high temperature reaction and electrochemical method for the synthesis of nanostructured nickel phosphide catalyst.[7] However, to the best of our knowledge, there is no report on electrochemical synthesis of single-phase nickel phosphide, for instance crystalline Ni_5P_4, towards HER. Electrochemical synthesis has several advantages over other methods as following: (1) electrochemical reaction is usually one-step process; (2) it does not involve high-temperature for phosphorization reaction; (3) diminish the reaction time and (4) self-supported catalyst loading is possible on the electrode surface. It is established that rough electrode surface is known to favor the electrodeposition of desired material.[23] Furthermore, electrodeposited core-shell material offers synergistic effect between core and shell that results in high efficiency of the nanostrutures.[24,25] Electrodeposited porous architecture have the advantages to create hydrophilic as well as aerophobic surface, which helps to decrease the ohmic resistance of electrode with electrolyte and fast removing of gas bubbles from the surface.[26] Taking advantage of these effects, herein, for the first time we have explored single-phase electrochemical synthesis of nickel phosphide (Ni_5P_4) on a galvanostatically deposited copper foam (Cuf) electrode. The dendritic nanostructure of Cuf offers rough surface and act as template for the deposition of Ni_5P_4. The core-shell morphology of Cuf@Ni_5P_4 further shows excellent catalytic activity towards HER in acidic medium.

3.2 Experimental

3.2.1 Electrodeposition of Ni_5P_4 on copper foam

Electrodeposition of Ni_5P_4 on Cuf was carried out under constant potential of -0.8 V in a three-electrode system. Typically, electrodeposition was carried out in an aqueous solution of $NiCl_2 \cdot 6H_2O$ (60 mM), $NaH_2PO_2 \cdot H_2O$ (50 mM), and NaH_2PO_4 (0.5 M) for different time (30, 60, 90 and 120 minutes). Previously deposited Cuf was used as working electrode, platinum wire as the counter electrode, and Ag/AgCl (3 M KCl) as the reference electrode for all the deposition. The as-deposited black layer of nickel phosphide on Cuf thin film was washed thoroughly with Millipore water and stored at vacuum when not in use.

3.2.2 Electrodeposition of Ni_5P_4 on different substrates

For comparison of the catalytic activity, electrodeposition of Ni_5P_4 on different substrate like copper foil (Ni_5P_4/Cu foil), graphite plate (Ni_5P_4/GP) and nickel foam (Ni_5P_4/Nif)

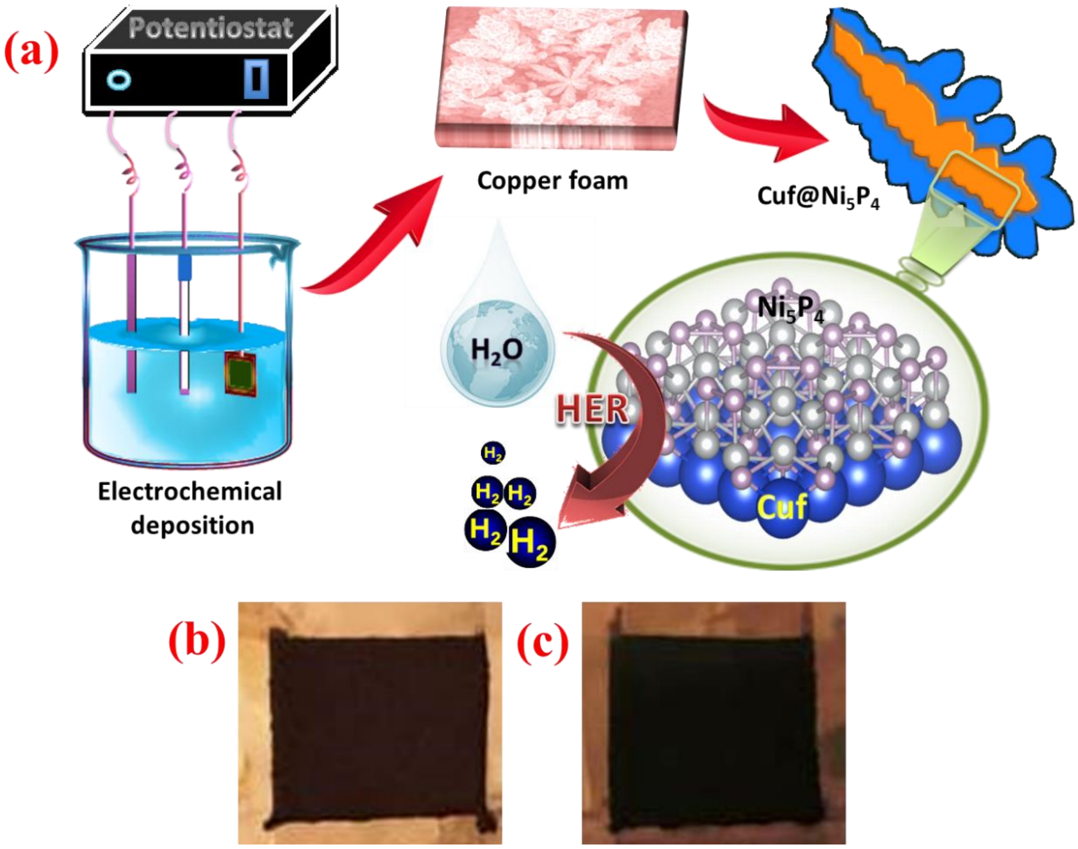

Figure 3.1. *(a) Schematic illustration for the electrochemical synthesis of copper foam-nickel phosphide active material and its HER activity (b) Digital photographs of electrodes (b) bare copper foam (c) Cuf@Ni_5P_4. The deposited electrode area is about 0.5 × 0.5 cm^2.*

were carried out in a three-electrode system at a constant potential of -0.8 V. Before the electrodeposition, the substrates were cleaned in their required way. All other conditions were same as previous section for the electrodeposition of Ni_5P_4 on different substrate.

3.2.3 Electrochemical measurements

All the electrochemical characterization for HER were conducted at room temperature (25°C) with Cuf@Ni_5P_4 (0.5×0.5 cm^2) as working electrode, Ag/AgCl (3M KCl) and graphite rod were used as reference and counter electrode, respectively. All the LSV and CV were carried out to check the HER activity with 0.5 M H_2SO_4 as electrolyte. All the potentials used in this study were calibrated to reversible hydrogen electrode (RHE) based on the formula

$E_{RHE} = (E_{Ag/AgCl\ (3\ M\ KCl)} + 0.210\ V + 0.0591\ pH)\ V$

The chronopotentiometric (CP) measurements were conducted to evaluate the durability of as prepared electrocatalyst under the same experimental conditions without compensating *iR* drop. The commercial Pt/C catalysts were employed for hydrogen evolution, respectively as the baseline catalysts for comparison. Electrochemical impedance spectroscopy (EIS) measurements were carried out at different overpotentials in the frequency range of 10^5-10^{-2} Hz. The polarization curve of all the catalyst was *iR* corrected (unless mentioned otherwise) to minimize the effect of ohmic resistance present at the electrode electrolyte interface and the current densities were normalized with geometrical surface area. The *iR*-correction was performed according to the following equation:

$E_{corr} = E_{mea} - iR_s$

Where E_{corr} is *iR*-corrected potential, E_{mea} experimentally measured potential, and

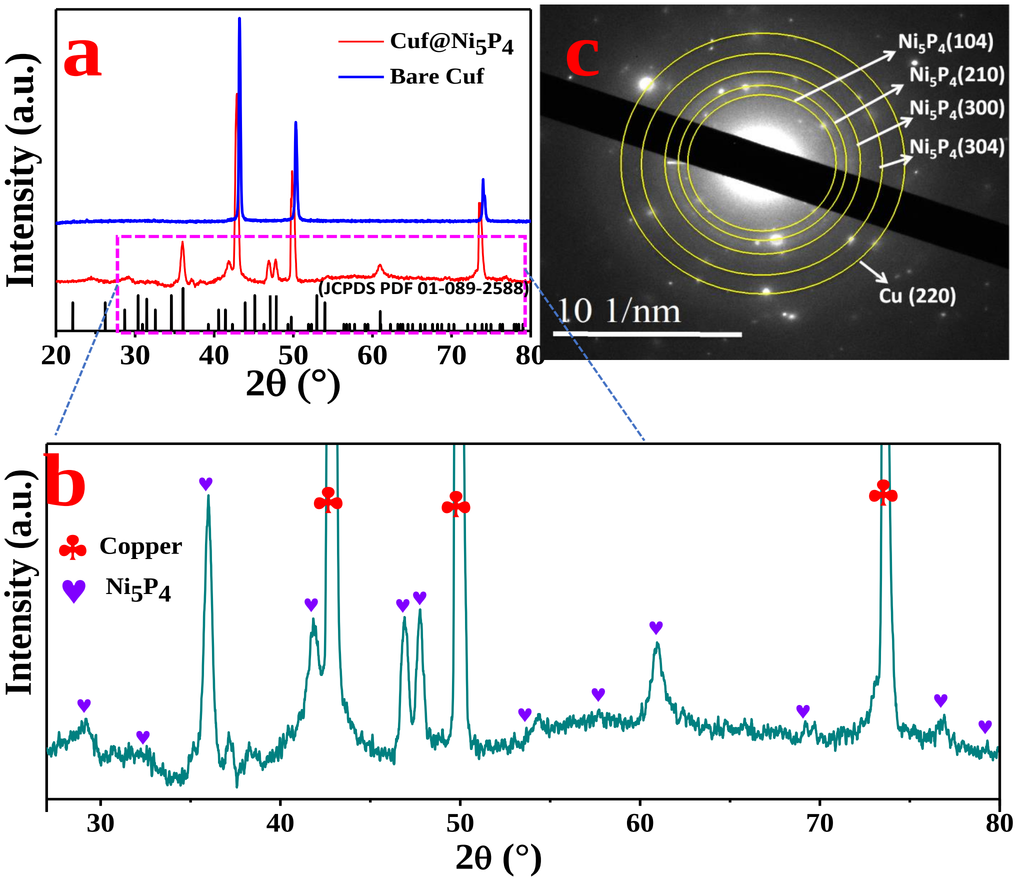

Figure 3.2. *(a) XRD pattern of Cuf (blue) and Cuf@Ni_5P_4 (red), (b) scaled image for XRD of Cuf@Ni_5P_4, (c) selective area electron diffraction pattern of Cuf@Ni_5P_4.*

R_s the equivalent series resistance extracted from the Nyquist plots at open circuit potential.

3.2.4 Computational methodology

Density functional theory (DFT) calculations were performed within the Vienna ab initio simulation package (VASP)[27]. The ion-electron exchange correlation functionals were treated with the projector augmented wave (PAW)[28,29] psedopotentials by considering Perdew-Burke-Ernzerhof (PBE)[30] parametrization form of generalized gradient approximation (GGA) with a kinetic energy cutoff of 500 eV to expand the electronic wave functions in a plane wave basis-set. A Γ-centered 5x5x1 k –mesh was used for the Brillouin zone (BZ) sampling with an energy threshold of 1 x 10^{-5} eV for the total energy convergence and a force tolerance of 0.01 eV/Å for the ionic and electronic relaxation. The periodic replicas of slab geometry were decoupled by considering a large vacuum spacing > 20 Å along the z-axis. Besides, the vans der Waals (vdW) correction to the dispersive forces were explicitly treated by using Grimme's DFT-D2 method for the surface adsorbed geometries.

3.3 Results and discussion

3.3.1 Characterizations of the electrode materials

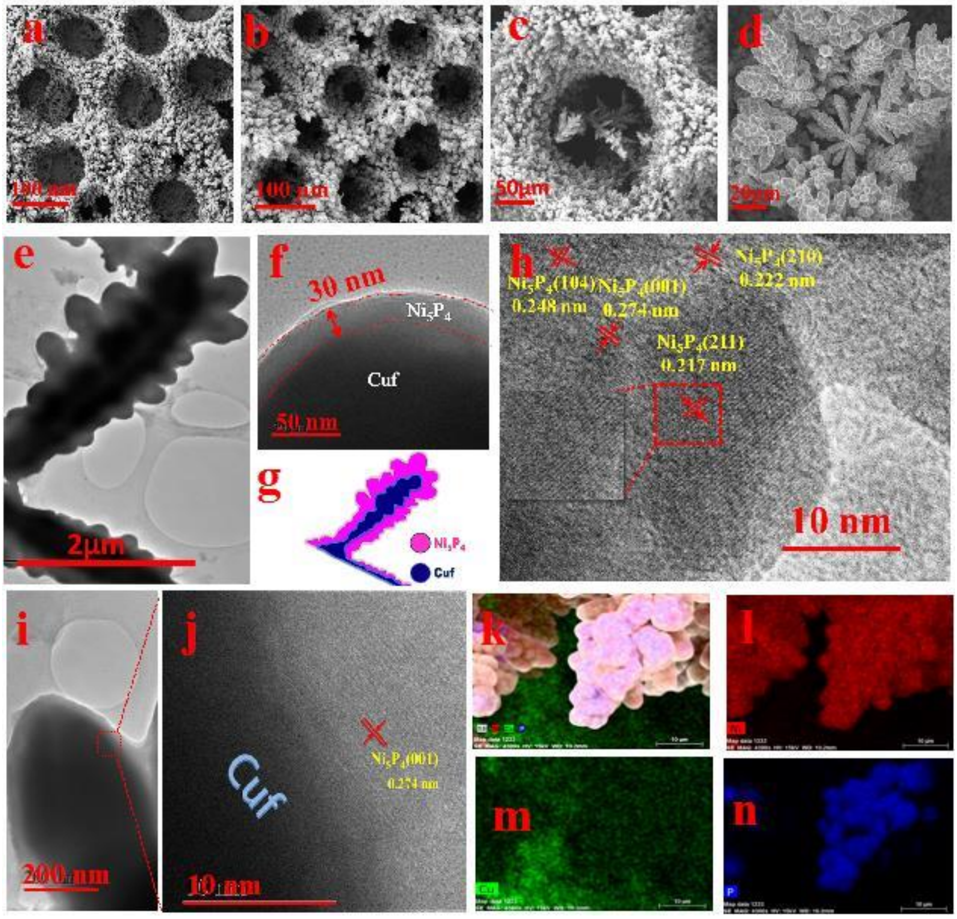

Figure 3.3. *(a) SEM image of bare Cuf, (b-d) SEM images of Cuf@Ni_5P_4 at different magnifications, (e,f) TEM images of Cuf@Ni_5P_4 reflecting core shell nanostructure of the catalyst, (g) schematic illustration showing the core-shell nanostructure of Cuf@Ni_5P_4, (h) high resolution TEM image of Cuf@Ni_5P_4 and inset shows zoom version of the selected area from HRTEM image, (i-j) HRTEM images of the interface of Cuf@Ni_5P_4 showing (001) plane of Ni_5P_4 present at the interface, (k-n) elemental mapping of Cuf@Ni_5P_4.*

The synthesis of core-shell Cuf@Ni_5P_4 electrode is schematically shown in Figure 3.1a, the digital image of as synthesized electrodes is shown in Figure 3.1 b and c). The electrode was synthesized by electrodeposition method in a three-electrode system at a constant potential of -0.8 V, which is schematically shown in (details are given in experimental section). The growth of Ni_5P_4 at different deposition time (30, 60, 90 and 120 min) were performed with the aim to achieve best electrocatalytic activity of Cuf@Ni_5P_4 and optimized time was found to be 90 minutes. All the characterizations were conducted using Cuf@Ni_5P_4 prepared under the optimal condition (i.e deposition time of 90 minutes). The structural analysis was investigated by X-ray powder diffraction (XRD) analysis. Figure 3.2 a,b display the XRD pattern of Cuf@Ni_5P_4, where all the diffraction peaks are in good accordance with hexagonal structure of Ni_5P_4 (JCPDS PDF 01-089-2588). The diffraction peaks at 2θ values of 28.69°, 32.57^0, 36.06°, 41.42°, 47.06°, 47.84°, 52.96°, 53.98°, 57.74°, 61.06°, 69.66°, 76.46° and 79.01° were attributed to the planes of (103), (004), (104), (211), (300), (301), (214), (220), (304), (107), (320), (226) and (413), respectively for Ni_5P_4. However, the diffraction peaks for bare Cuf at 2θ of 43.19°, 50.30° and 73.89° corresponds to (111), (200) and (220) planes, respectively, for cubic lattice (JCPDS PDF 01-070-3038), which were also observed as expected in the diffraction pattern of Cuf@ Ni_5P_4. However, the peaks of cuf@Ni_5P_4 were observed to be sifted by angle of ~0.3° with respect to the peak of bare Cuf towards lower angle of 2θ because of the uniform interfacial strain induced in the geometry of the

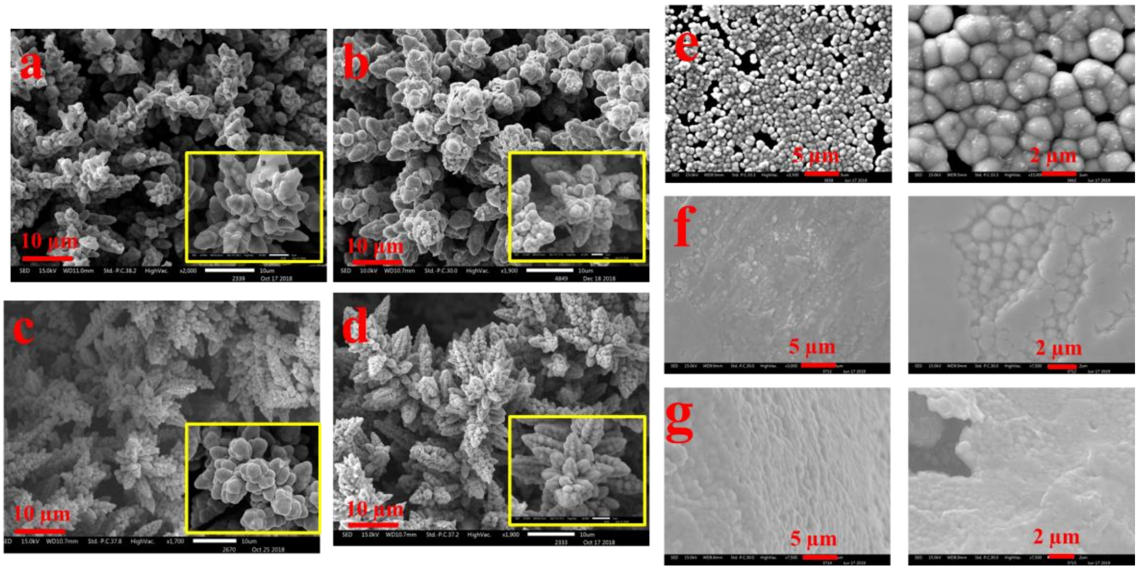

Figure 3.4. *SEM images of electrodeposited samples at different time (a) 30 min (b) 60 min (c) 90 min (d) 120 min. SEM images of* Ni_5P_4 *on different substrates (e)* Ni_5P_4*/GP (f)* Ni_5P_4*/Cu foil (g)* Ni_5P_4*/Nif*

core and shell originated from strong size mismatch between them.[31,32] It confirms the interfacial interaction of hybrid core-shell nanostructure formation during electrochemical synthesis.[33] The two small peaks are observed at 2θ of 37.24° and 38.95°, which corresponds to the (111) plane of NiO (PDF 00-047-1049) and (111) plane CuO (PDF 00-001-1117), respectively. The peak of CuO is arising may be due the exposure of the sample to the air atmosphere and a small oxide peak of nickel (NiO) appeared may be due to its formation in working electrolyte condition during the electrodeposition process.[34,35] The selected area electron diffraction (SAED) pattern obtained during transmission electron microscopic (TEM) measurement (Figure 3.2c), again reveals the single-phase Ni_5P_4 formation on Cuf, which is well correlated with the XRD pattern.

The surface morphological information for as-deposited Cuf and Cuf@Ni_5P_4 was systematically investigated by scanning electron microscopy (SEM) and TEM. SEM images of Cuf (Figure 3.3a) show honeycomb porous structure resulting from the generation and dissipation of H_2 bubbles during electrodeposition process.[36] Cuf@Ni_5P_4 shows similar structure like Cuf with uniformly distributed continuous macropores across

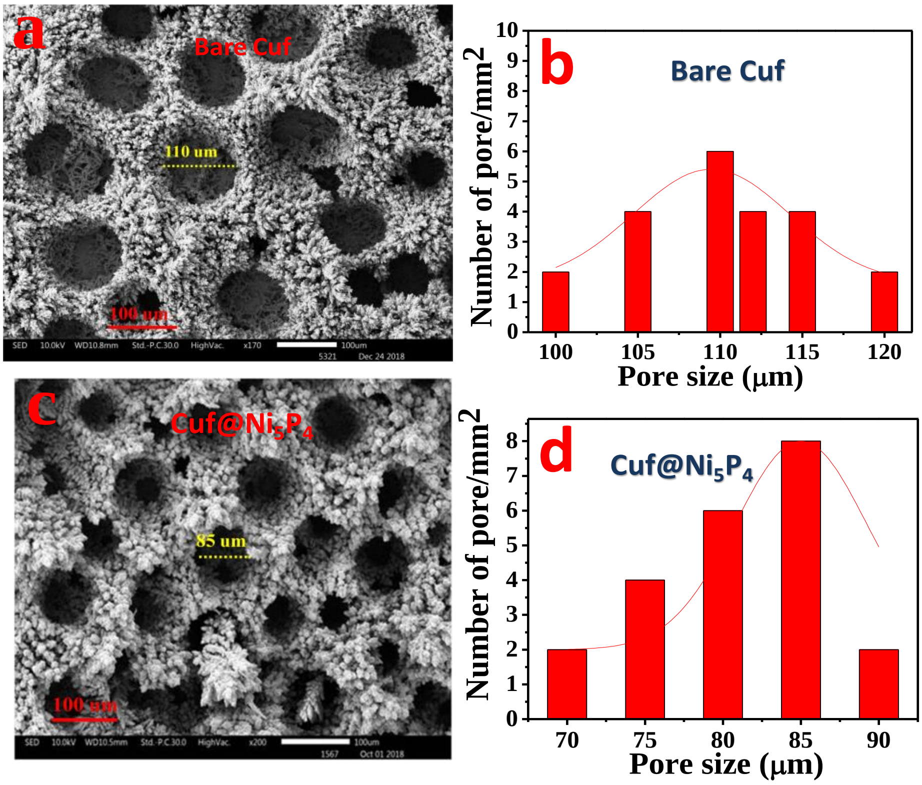

Figure 3.5. *(a) SEM image of bare copper foam at a magnification of 100 µm (b) Average pore size distribution of bare Cuf (c) SEM image of Cuf@*Ni_5P_4 *at a magnification of 100 µm (d) Average pore size distribution of Cuf@*Ni_5P_4

the surface (Figure 3.3b-d). The TEM images of the Cuf@Ni_5P_4 (Figure 3.3e) show the dendritic structure of the material. A close look on the Figure 3.3e and 3.3f display the different intensity of the layer, which arises from the transmission dependency of the different atomic layer as schematically represented in Figure 3.3g. The thickness of the deposited layer calculated from high-resolution TEM (HRTEM) image was 30-40 nm (Figure 3.3f) with a core diameter of 0.4-0.8 μm proves the formation of a core shell nanostructure with copper as the core and Ni_5P_4 as the shell. The hierarchically structured

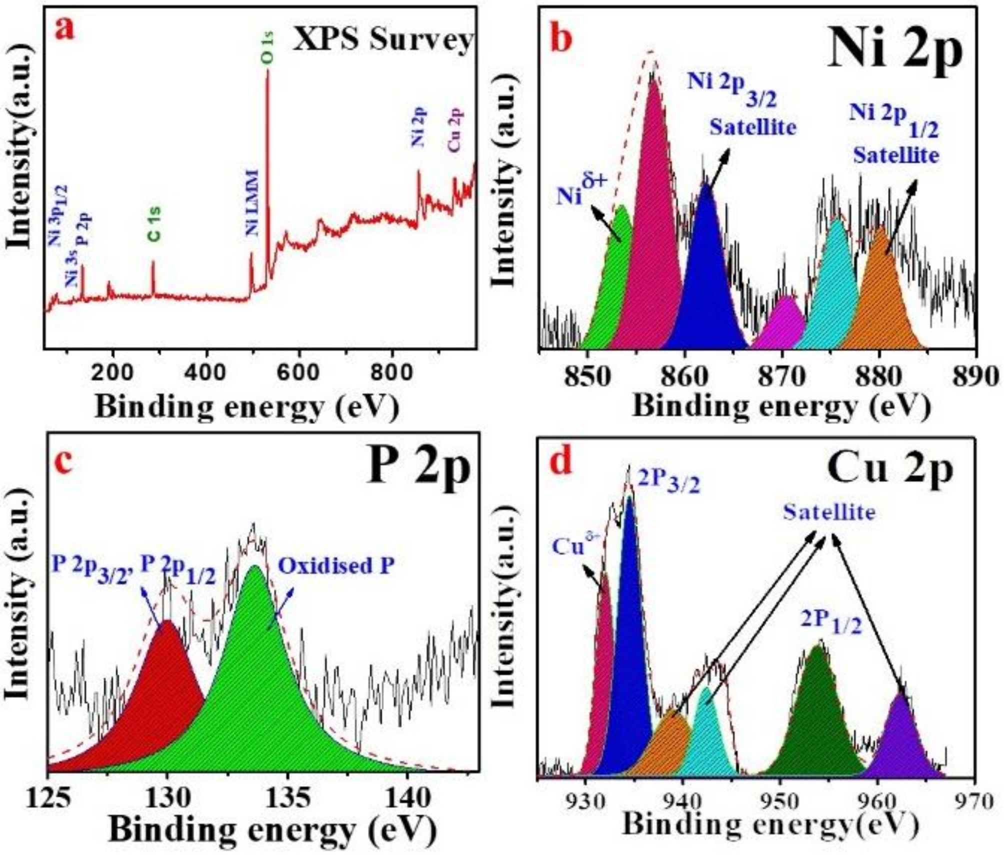

Figure 3.6. *(a) XPS survey spectra of Cuf@Ni_5P_4, high-resolution deconvoluted XPS sspectra for (b) Ni 2p, (c) P 2p and (d) Cu 2p.*

electrode with core-shell configuration is known to show excellent electrocatalytic activity towards hydrogen generation.[25] The HRTEM study was performed with the Ni_5P_4 material at the shell (Figure 3.3h). Well-resolved lattice fringes were observed with a d-spacing values of 0.222, 0.248 and 0.217 nm correspond to the (210), (104) and (211) planes of Ni_5P_4, respectively. The junction of the core-shell heterostructures as revealed from the HRTEM images shown in Figure 3.3i-j, indicates the presence of (001) plane of Ni_5P_4, grown on the copper (111) plane. EDX mapping study was accomplished over a branched structure of Cuf@Ni_5P_4 (Figure 3.3k-n). EDX elemental mapping study proves the homogeneous distribution of nickel, phosphorous and copper element on the branched structure. It is noteworthy from the mapping analysis that the more intense red (for Ni) and blue (for P) colour at the branch structure and green colour (for Cu). The SEM images of Cuf@Ni_5P_4 at different deposition duration demonstrate the growth of Ni_5P_4 with time (Figure 3.4a-d). SEM images of electrodeposited Ni_5P_4/GP, Ni_5P_4/Cu foil and Ni_5P_4/Nif samples are particles in nature (Figure 3.4e-g). Although they have different morphologies, but all the materials exhibit aggregated particles throughout the surface. The pore size distribution (Figure 3.5) reveals that the average pore size of bare Cuf was ~110 μm, which was reduced to an average pore size of ~85 μm in the Cuf@Ni_5P_4, indicates the deposition of Ni_5P_4 *via* electrodeposition technique. X-ray photoelectron spectroscopy (XPS) is an important tool to ascertain the chemical states of the elements present in the sample. As shown in Figure 3.6a, XPS survey scan confirms the presence of Ni, Cu, P, C as well as O elements. The presence of C and O can be attributed to surface adsorbed electrolyte ion or surface oxidation of the material.[14] The high-resolution XPS spectrum of Ni 2P were employed to detect the metallic and oxidized peak corresponding to Ni $2P_{3/2}$ and Ni $2p_{1/2}$ (Figure 3.6b). Interestingly, two metallic peaks of Ni ($Ni^{\delta+}$) corresponding to 853.4 and 870.3 eV were identified.[37,5]The spectrum of Ni 2P also indicates the presence of peaks at 856.8 (oxidized Ni) and 862.3 eV (satellite) for Ni $2p_{3/2}$ and at 875.6 (oxidized Ni) and 880.2 eV (satellite) for the Ni $2p_{1/2}$ energy level.[11] The high-resolution spectrum of P 2p for the Cuf@Ni_5P_4 where the peak at 129.9 eV was assigned to the P $2p_{3/2}$ and P $2p_{1/2}$, whereas the peak at 133.4 eV was attributed to the oxidized P species (Figure 3.6c). The XPS spectra of copper present as a core in Cuf@Ni_5P_4 (Figure 3.6d), indicates three main peaks at 932.1, 934.5, and 953.7eV, which are attributed to metallic Cu ($Cu^{\delta+}$), Cu $2p_{3/2}$ (oxidized Cu) and Cu $2p_{1/2}$(oxidized Cu), respectively. The three peaks with binding energy appeared at 939.1, 942.4, and 962.4eV were attributed to the satellite peaks of the Cu $2p_{3/2}$ and $2p_{1/2}$, respectively.[39,40]

3.3.2 Electrochemical characterizations

Electrocatalytic activity of the as-prepared catalyst was evaluated by means of HER in 0.5 M H_2SO_4. There are only few reports in the literature on single-phase synthesis of Ni_5P_4 used for generation of H_2.[20,22] However, all the reports either failed to achieve high exchange current density or did not perform for long time in acidic medium. In order to assess the electrocatalytic activity of as-prepared Cuf@Ni_5P_4, systematic electrochemical characterization for HER was performed. All the potential used here are converted to reversible hydrogen electrode (RHE) unless mentioned otherwise. The polarization curve of electrodeposited nickel phosphide on Cuf at different deposition duration (Figure 3.7a), which clearly shows that 90 min deposition time gives the best HER activity in terms of overpotential and chemical kinetics. Further deposition (120 min) inhibits the charge transfer between Cuf and Ni_5P_4, which weakens the catalytic performances of the

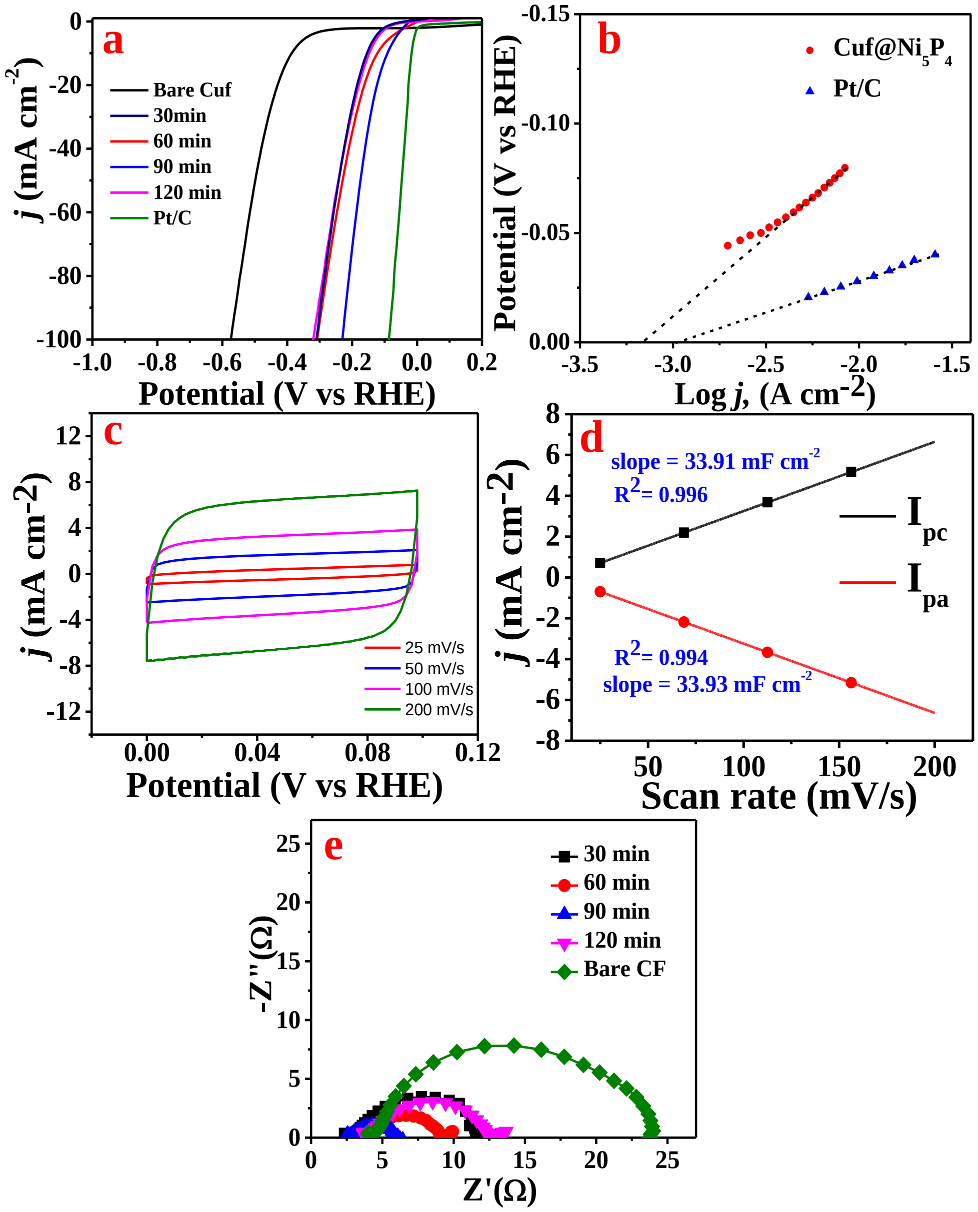

Figure 3.7. *(a) Linear sweep voltammetry of as prepared catalyst for different deposition time at a potential of -0.2 V vs RHE (b) Calculated exchange current densities of Pt/C and Cuf@*Ni_5P_4 *by applying extrapolation method to the Tafel plots. (c) CV scans of Cuf@*Ni_5P_4 *in a non-Faradic region at different scan rates (d) Linear fits of current densities at different scan rates (e) Electrochemical impedance spectroscopy of as prepared catalyst for different deposition time at a potential of -0.2 V vs RHE*

electrode. Electrode with larger exchange current density needs less driving force (smaller current density) to conduct the HER.[11] The exchange current density of Cuf@Ni_5P_4 were calculated to be 0.76 mA cm^{-2} by extrapolating linear part of Tafel plot to X-axis and it was found to be very close to that of the exchange current density of Pt/C (1.00 mA cm^{-2}) in 0.5 M H_2SO_4 (Figure 3.7b). The exchange current density achieved by Cuf@Ni_5P_4 were highest in comparison to the recently reported nickel phosphide based electrocatalysts[41–44] (Table 3.1). The exchange current density is usually expressed in terms of projected or geometric surface area and depends on the surface roughness or roughness factor of the catalyst.[40] The porous nature of the nanostructure offers high electrochemically active surface area (ECSA) and lead to more electrochemically active sites that undoubtedly helps to improve the electrocatalytic activity.[45] A comparative cyclic voltammetry (CV) scan were performed to calculate the ECSA and roughness factor (RF) of Cuf@Ni_5P_4 (Figure 3.7c). The CV response obtained from Cuf@Ni_5P_4 at different scan rate in a non-faradic region (0 to 0.1 V) and corresponding scan rate verses anodic and cathodic peak current for the calculation of double layer capacitance (C_{dl}) value are shown Figure 3.7d. The EIS of nickel phosphide deposited on Cuf for different

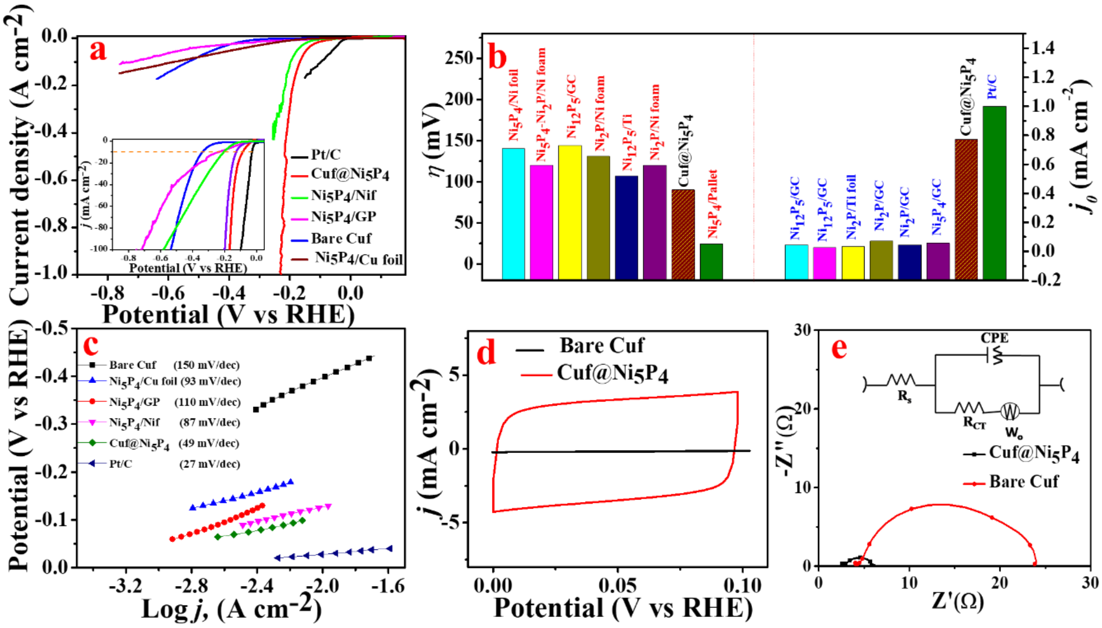

Figure 3.8. *(a) HER Polarization curves of bare Cuf, Ni_5P_4/Cu foil, Ni_5P_4/GP, Ni_5P_4/Nif, Cuf@Ni_5P_4 and Pt/C catalysts recorded at a scan rate of 10 mVs^{-1} (b) Bar diagram depicting the comparison of overpotential and exchange current density of previously reported Nickel phosphide based electrocatalyst. (c) Tafel plots of bare Cuf, Ni_5P_4/Cu foil, Ni_5P_4/GP, Ni_5P_4/Nif, Cuf@Ni_5P_4 and Pt/C (d) Cyclic voltammetery response of bare Cuf and Cuf@Ni_5P_4 at a scan rate of 100 mVs^{-1} (e) Nyquist plot of bare Cuf and Cuf@Ni_5P_4 recorded at -0.2 V (vs RHE), inset shows the equivalent circuit used to fit the EIS data. All the experiments were performed in 0.5 M H_2SO_4 solution.*

time (Figure 3.7e), clearly indicates that the minimum R_{ct} of Cuf@Ni_5P_4 with 90 min deposition time obtained as compared to the other catalyst. The low R_s and R_{ct} value of Cuf@Ni_5P_4 ensues the fast charge transfer kinetics between the catalyst and the electrolyte as well as catalyst to the electrode, which facilitates the faster reaction rate. It is generally accepted that small values of R_s correspond to close contact between current collector and catalysts. Figure 3.8a displays the obtained polarization curve for Pt/C, Cuf@Ni_5P_4, Ni_5P_4/GP, Ni_5P_4/Cu foil, Ni_5P_4/Nif and bare Cuf at a scan rate of 10 mVs^{-1}. The Cuf@Ni_5P_4catalyst attained an overpotential (η) of 90 mV at a current density of 10 $mAcm^{-2}$, which is 239 mV positive than bare Cuf, 148 mV positive than Ni_5P_4/GP, 113 mV positive than Ni_5P_4/Cu foil, 36 mV positive than Ni_5P_4/Nif and 63 mV negative in comparison to Pt/C. Interestingly, the Cuf@Ni_5P_4catalyst displays a η of only 164 mV even at very high current density of 100 $mAcm^{-2}$. It is noteworthy to mention here that the achieved overpotential of Cuf@Ni_5P_4 is very low compared to the previously reported data on Nickel phosphide based electrocatalyst (Table 3.2).[19,22,44] The excellent electrocatalytic activity of Cuf@Ni_5P_4 reveals the important role of core shell nanostructures of the catalyst and confirms that the surface nickel phosphide (shell) exploited copper (core) in terms of porosity and surface area, resulting in superior catalytic performance of such a core/shell nanostructures. The HER electrocatalytic activity crucially depends on the uneven electrode surface.[46] A comparative table for exchange current density and overpotential in context with recently reported catalyst is shown in Figure 3.8b. The corresponding Tafel plots were employed to determine the kinetics of the HER rate for different catalysts (Figure 3.8c). The Tafel slope for Cuf@Ni_5P_4 derived from the Tafel plot was found to be of 49 mV dec^{-1}, which is less than that of Ni_5P_4/Cu foil (slope= 93 mV dec^{-1}), Ni_5P_4/GP (110 mV dec^{-1}), Ni_5P_4/Nif (87 mV dec^{-1}) and bare Cuf (150 mV dec^{-1}) that determines better kinetic rate of Cuf@Ni_5P_4 for hydrogen generation. However, tafel slope of Pt/C was found to be 27 mV dec^{-1}. The ECSA was calculated and found to be 423.5 cm^2 by considering the C_{dl} of 33.9 mF cm^{-2} and specific capacitance (C_{sp} = 0.02 mF cm^{-2}) of Ni surface in 0.5 M H_2SO_4 electrolyte (Figure 3.8d).[47] The roughness factor was calculated to be 1694, which is very high and outperforming state-of-the-art catalyst reported till date.[48–51] To study the electrode kinetics (charge transfer behavior), electrochemical impedance spectroscopy (EIS) of bare Cuf and Cuf@Ni_5P_4 (Figure 3.8e) were recorded at -0.2 V (vs RHE). An equivalent circuit model was employed to fit the Nyquist plot as shown in the inset of Figure 3.8e. Interestingly, Cuf@Ni_5P_4 possesses a very small solution resistance (R_s =

2.59 Ω) indicates a less interfacial resistance and superior catalytic activity of the as-prepared catalyst. A charge transfer resistance (R_{ct}) of

Cuf@Ni_5P_4 were only 3.62 Ω (give rise to rapid charge transfer kinetics), which is much lower than that of bare Cuf (R_{ct} = 20 Ω).

Table 3.1 Comparison of Exchange current density between Cuf@Ni_5P_4 and recently reported catalyst.

Catalyst	**Onset potential (mV)**	**Overpotential mV@mAcm^{-2}**	**Tafel slope**	**Exchange current density (A/cm^2)**	**References**
$Ni_{12}P_5$/ GCE	380	-	270	4.5x10^{-5}	*ACS Energy Lett.* **2016**, *1* (6), 1192–1198
$Ni_{12}P_5$/ GCE	80	208@10	75	2.857x10^{-5}	*J. Mater. Chem. A* **2015**, *3* (4), 1656–1665
Ni_2P/ GCE	62	137@10	49	4.592x10^{-5}	*J. Mater. Chem. A* **2015**, *3* (4), 1656–1665
Ni_5P_4 / GCE	34	118@10	42	5.702x10^{-5}	*J. Mater. Chem. A* **2015**, *3* (4), 1656–1665
Ni_2P/ Ti foil		130@20	46	3.3x10^{-5}	*J. Am. Chem. Soc.* **2013**, *135* (25), 9267–9270
Ni_2P/ GCE	75	172@10	62	7.1x10^{-5}	*RSC Adv.* **2015**, *5* (14), 10290–10295
Cuf@ Ni_5P_4	**54**	**90@10**	**49**	**76x10^{-5}**	**This work**

3.3.3 Wettability

During the catalysis process, plenty of bubbles generates from the surface of the electrode that blocks electrolyte diffusion and increase ohmic resistance between electrode and electrolyte interfaces, which decreases the electrochemical active surface area and eventually leads to degradation of catalytic performance. To overcome this challenge, it is greatly required to design a fine surface catalyst which is hydrophilic as well as aerophobic in nature. [52] To understand the hydrophilicity of as synthesized catalyst, the wettability analysis on the surface of the Cuf@Ni_5P_4 electrode was performed by measuring the contact angle of water drop on the surface of the catalyst. Figure 3.9a shows that the droplet imposing no contact with the surface of Cuf@Ni_5P_4 and when the drop falls on the surface, the Cuf@Ni_5P_4 catalyst absorbed liquid drop instantly (figure 3.9b) with a contact angle of 0^0, indicating that the material is superhydrophilic in nature.

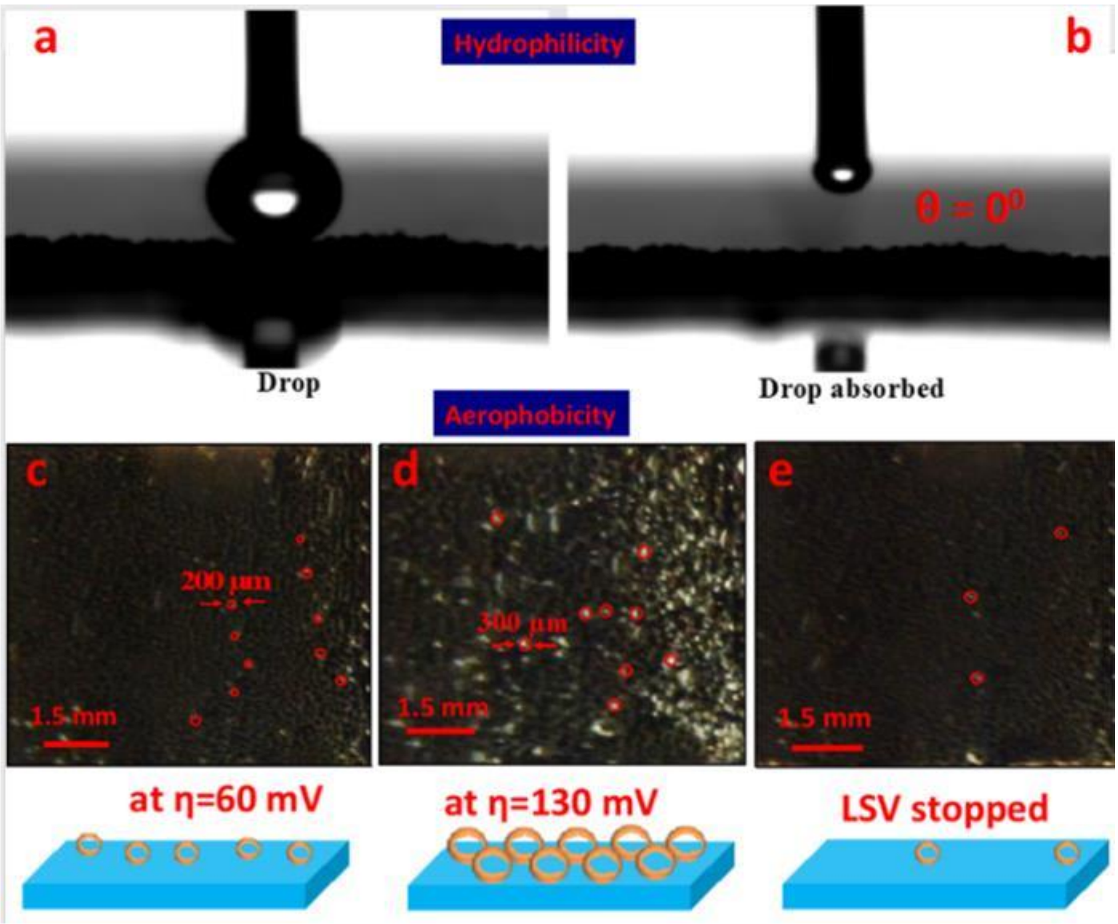

Figure 3.9. *Wettability test of Cuf@Ni_5P_4 surface (a) before and (b) after putting liquid drop with contact angle 0 degree. (c-e) Optical images with scheme at bottom panel showing the bubble formation behavior on Cuf@Ni_5P_4 surface at different overpotential and at the end of LSV.*

The aerophobic study of the catalyst were also done by analysing the bubble formation during and after the LSV run, demonstrated in figure 3.9c-e. The aerophobic nature of the foam-like Cuf@Ni_5P_4 core shell nanostructure provides an abrupt renewal of gas bubbles (as schematically shown in the bottom panel of Figure 3.9),[53] which helps in increasing the efficiency of the catalyst towards hydrogen evolution. When the HER process just started the average size of the bubbles forms on the surface were ~200 µm at an overpotential of ~60 mV and the size started increasing and observed to be ~300 µm at an overpotential of ~130 mV, which is due to the rapid renewal of the minor gas bubbles and interestingly, when the LSV was stopped it has been observed there only few bubbles which were trapped in to the pores were seen resembling the superior areophobic behavior of the catalyst. The superhydrophilic and aerophobic nature of the sample originated from fine nanostructures and proper material selection is crucial for HER electrocatalysis.

3.3.4 Theoritical investigation

To ascertain the origin of high electrocatalytic activity in the as- synthesized materials and deepen the understanding of the HER mechanism, density functional theory (DFT) calculations have been performed. As established, the electrochemical reduction of ionic hydrogen on metal-catalyst surface is a combination of hydrogen adsorption process called as Volmer reaction step followed by either Tafel or Heyrovsky reaction mechanism for H_2 desorption (see supporting information for details).

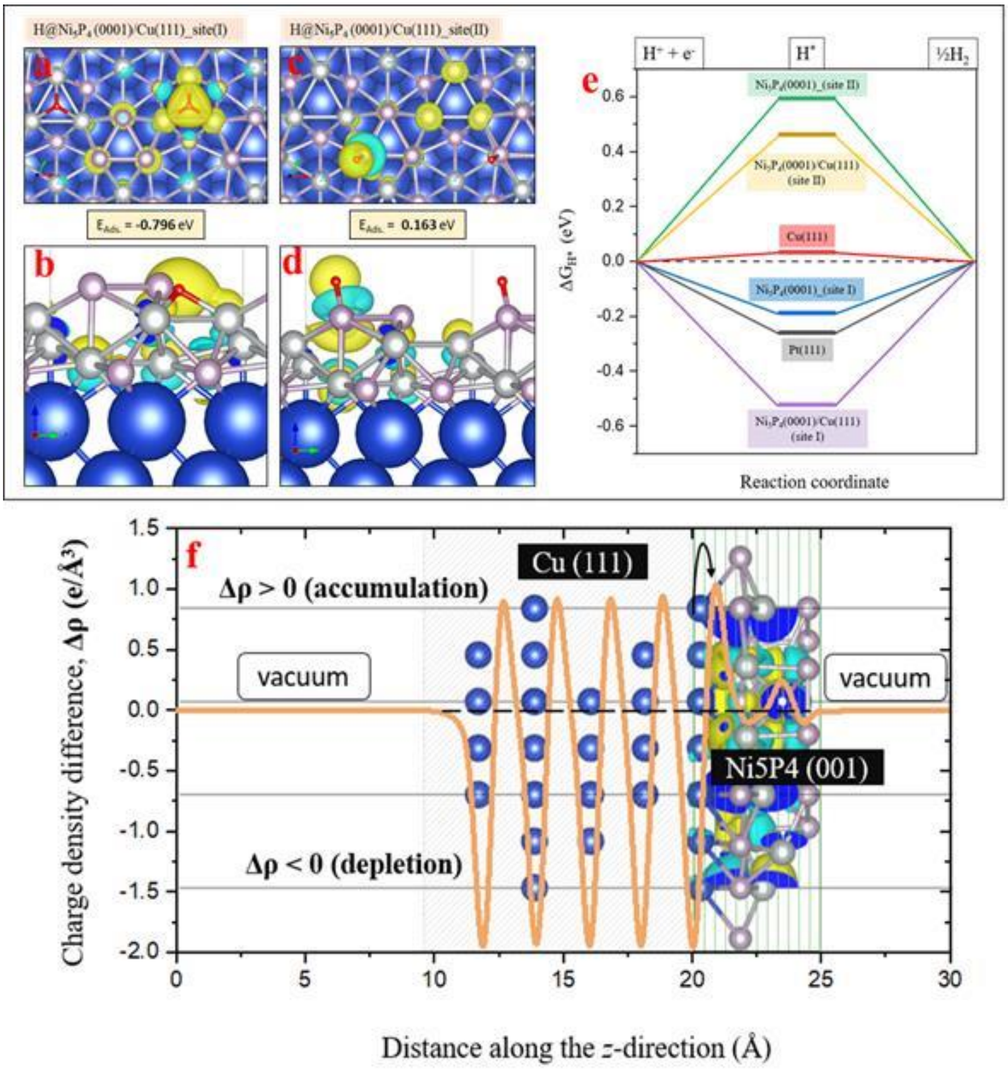

Figure 3.10. *(a-b) A top and side view of H* adsorption over the 3-fold Ni site of Ni_5P_4 (0001)/Cu(111) (site I). (c-d) H* over the on-top P site of Ni_5P_4 (0001)/Cu(111) surface (site II). The differential ground state charge density distribution around the adsorbate (H*) is at an isolevel of 0.59 x 10-2 e/Å3. (e) Gibbs free energy change (ΔGH*) of reaction intermediate (H*) on different metal-catalyst surface.*

Table 3.2 HER performance comparison between Cuf@Ni_5P_4 and recently reported catalyst in 0.5M H_2SO_4

Catalyst	**Electrolyte**	**Overpotential (mV)@10 mA cm^{-2}**	**Overpotential (mV)100 mA cm^{-2}**	**Tafel slope (mV/dec)**	**References**
Ni_5P_4	1 M H_2SO_4	24	-	27	*Energy Environ. Sci.* **2015**, *8* (3), 1027–1034
Ni_5P_4 on Nickel foil	0.5 H_2SO_4	140	-	46	*Angew. Chemie Int. Ed.* **2015**, *54* (42), 12361–12365
Ni_5P_4-Ni_2P NS array/Ni Foam	0.5 M H_2SO_4	120	200	79.1	*Angew. Chemie Int. Ed.* **2015**, *54* (28)
Ni_2P / Ti foil	0.5 M H_2SO_4	-	180	46	*J. Am. Chem. Soc.* **2013**, *135* (25), 9267–9270
Ni_2P-G@NF/Graphene/Ni foam	0.5 M H_2SO_4	55	170	30	*J. Mater. Chem. A* **2015**, *3* (5), 1941–1946
NiP_2NS/ carbon cloth	0.5 M H_2SO_4	75	204	51	*Nanoscale* **2014**, *6* (22), 13440–13445
$Ni_{12}P_5$ hollow spheres/Glass carbon	0.5 M H_2SO_4	144	277	46	*J. Mater. Chem. A Mater. energy Sustain.* **2016**, *4*, 9755–9759
Ni_2P NRs/Ni/NF	0.5 M H_2SO_4	131	300	106.1	*Chem. Commun.* **2015**, *1*, 3–6.
$Ni_{12}P_5$/Ti	0.5 M H_2SO_4	107	-	63	*ACS Appl. Mater. Interfaces* **2015**, *7* (4), 2376–2384
Ni_2P/Ni foam	0.5 M H_2SO_4	-120	-	68	*ACS Appl. Mater. Interfaces* **2015**, *7* (4), 2376–2384
NiP_2 NW/NF	0.5 M H_2SO_4	67	-	109	*Nanoscale* **2017**, *9* (13), 4401–4408
$Ni_{12}P_5$ Ni_2P/NF	0.5 M H_2SO_4	73	-	70.8	*RSC Adv.* **2016**, *6* (109), 107859–107864
CP@Ni-P	0.5 M H_2SO_4	-	164	58.8	*Adv. Funct. Mater.* **2016**, *26* (23), 4067–4077
Ternary $Ni_{2x}Co_xP$	0.5 M H_2SO_4	59	-	50	*Adv. Funct. Mater.* **2016**, *26* (37), 6785–6796

$G_{H*} = E_{Ads.} + \Delta E_{ZPE} - T\Delta S$

The H* (where * refers to the atomic hydrogen over catalyst surface) is the rate determining step for proton adsorption in acidic medium. To estimate the hydrogen adsorption energy ($E_{Ads.}$) and Gibbs free energy change (ΔG_{H*}) of reaction intermediate, H*, different metal-catalyst surfaces have been explored using the computational hydrogen electrode model proposed by Nørskov *et al.*[54] as follows, $E_{Ads.} = E_{surface+H} - E_{surface} - ½ E_{H2}$

where $E_{Ads.}$ is the hydrogen adsorption energy on metal catalyst surface, $E_{surface+H}$ and $E_{surface}$, total ground state energy of H adsorbed surface and pure metal catalyst surface, whereas E_{H2} is the energy of H_2 molecule in the vacuum gas-phase state. ΔE_{ZPE} and ΔS are the zero-point energy and entropy difference between the adsorbed state (H*) and molecular gas-phase state of hydrogen (H_2), and T is the absolute temperature (T = 298.15 K in our calculation). The zero-point energy (E_{ZPE}) of H exposed surfaces has been evaluated from the harmonic vibrational frequencies at 0 K. The entropy of H adsorbed surfaces are found to be very small in our calculation (Table 3.3) and hence, can be safely ignored by assuming the entropy of H_2 molecule, $\Delta S = -1/2\ \Delta S(H_2) = -64.915$ $J.mol^{-1}K^{-1}$ in the standard gas phase state at a pressure of 1 bar, temperature 300 K and pH = 0.

In order to explore the HER activity of pure Ni_5P_4 (0001) and Ni_5P_4 (0001)/Cu (111) hybrid catalyst surface, several hydrogen adsorption sites around the surface Ni and P atoms in the optimized geometry of Ni_5P_4 (0001) have been considered to screen out the most probable ones. As demonstrated in Figure 3i-j, the (001) plane of Ni_5P_4 is present at the Cuf@Ni_5P_4 interface. The 3-fold Ni hollow site (site I) and on-top P site (site II) turns out to be the two favorable hydrogen adsorption sites with binding energies -0.54 eV and 0.21 eV, respectively.

These adsorption sites have been used for further studies on Ni_5P_4 (0001)/Cu (111) hybrid interface structure with Cu (111) surface underneath the Ni_5P_4 (0001) surface. Figure 3.10 a-b shows the adsorption geometry of H* on 3-fold Ni site (site I) of Ni_5P_4 (0001)/Cu (111) with a binding energy of -0.79 eV, which is the highest among all the surfaces explored in this study, indicating the importance of Cuf support in facilitating the HER activity in Ni_5P_4 nanostructures. Similar to the hydrogen adsorption over the on-top P site (site II) of Ni_5P_4 (0001), the interface structure of Ni_5P_4 (0001)/Cu (111) also exhibits a positive H binding energy of 0.16 eV with a strong delocalization of valence charge density around P atom, as shown in Figure 3.10 c-d.

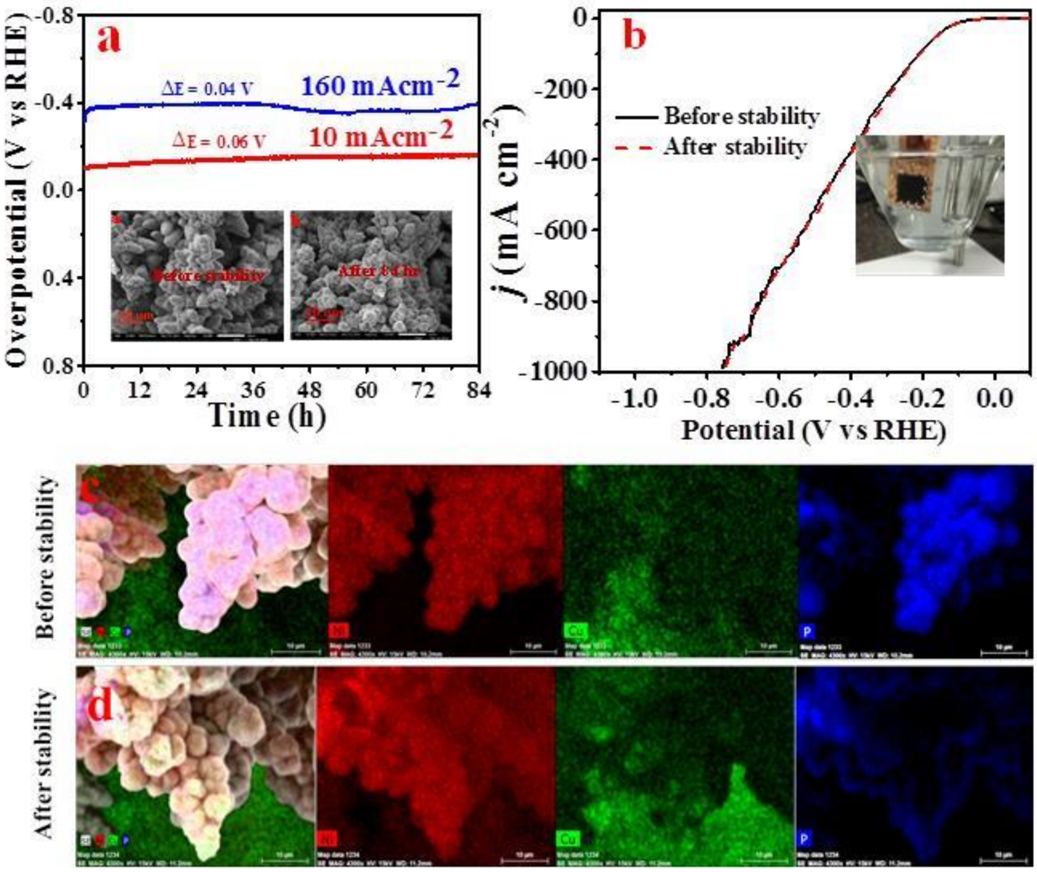

Figure 3.11. *(a) Chronopotentiometric curve of Cuf@Ni_5P_4 at current density of 10 mA cm^{-2} and 160 mA cm^{-2}, inset shows the SEM images obtained before and after test. (b) LSV of Cuf@Ni_5P_4 before and after chronopotentiometric test. Elemental mapping of Cuf@Ni_5P_4 obtained (c) before and (d) after 84 h chronopotentiometry test.*

The Gibbs free energy change (ΔG_{H^*}) of reaction intermediate, say H*, is a well-known descriptor of HER activity of any adsorbate (1/2 E_{H2} in this case) over a metal-catalyst surface. According to Sabatier principle, a good catalyst should have a ΔG_{H^*} value as close as possible to 0 eV. The Gibbs free energy change (ΔG_{H^*}) of reaction intermediate H* on different metal-catalyst surface. The Ni_5P_4 (0001) and Ni_5P_4 (0001)/Cu (111) surface with H* adsorbed over the 3-fold Ni site (site I) exhibit a negative value of ΔG_{H^*}, favoring the HER activity (Figure 3.10 e). Besides, the negative value of ΔG_{H^*} is found to be much higher (-0.52 eV) for Ni_5P_4 (0001)/Cu (111) surface as compared to the value of -0.18 eV for the Ni_5P_4 (0001) surface. It is attributable to very high negative adsorption energy, $E_{Ads.}$ = -0.79 eV of H* over the Ni_5P_4 (0001)/Cu (111) surface and a localized charge density distribution around the 3-fold Ni site of adsorbate, which strongly binds the atomic hydrogen to its surface (Figure 3.10 a-b). While for H* at the on-top P site of Ni_5P_4 (0001) and Ni_5P_4 (0001)/Cu (111) surface, a very high positive value of ΔG_{H^*} indicates a much weaker binding of H* or ease in the desorption of hydrogen, resulting in a much lower HER activity. The adsorption geometry of H* on 3-fold Ni site (site I) of Ni_5P_4 (0001)/Cu (111) with a binding energy of -0.79 eV, which is the highest among all the surfaces explored in this study, indicates the importance of Cuf for the deposition of Ni_5P_4 nanostructures towards HER activity. The high value of H-binding energy is resulting from the charge transfer between Cu (111) and Ni_5P_4 (0001), as the interface is chemical in nature. The interfacial study of the Cuf@Ni_5P_4 was validated by the interfacial charge density distribution. The interface between Cu and Ni_5P_4 is found to be chemical in nature as shown in Figure 3.10f. The charges accumulating at the Cuf@Ni_5P_4 interface is transferred from the portion of Cu (111) surface, which in turn, gets depleted. The charge density difference distribution has been calculated via $\Delta\rho = \rho$ [interface system] - ρ[Cu (111)] - ρ[Ni_5P_4(001)]. This calculation is based on the explicit inclusion of vDW-D3 dispersive interactive forces, which accounts for the long range electronic interactions in surface geometries.

Table 3.3 Thermochemical energies of reaction intermediate (H*) over different metal surfaces and zero-point energy of H_2 molecule in gas-phase state at standard condition.

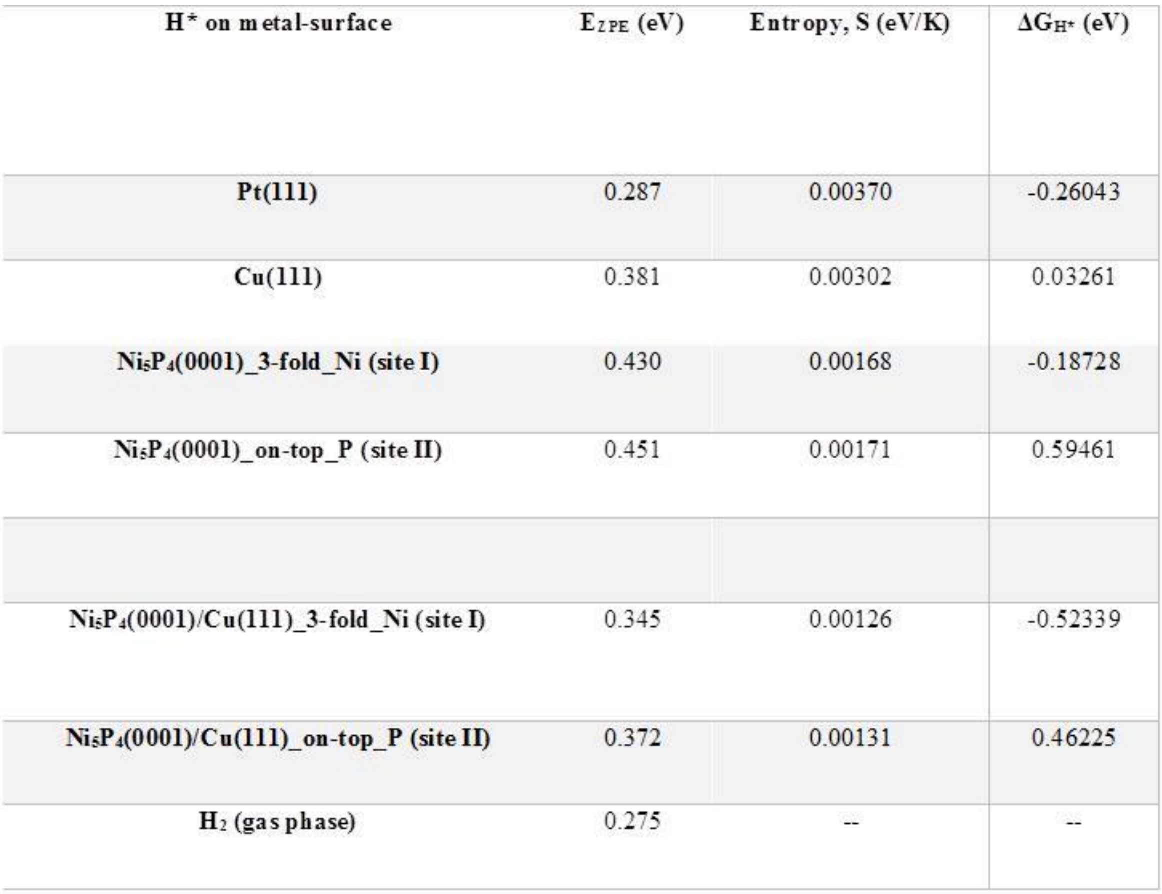

H* on metal-surface	E_{ZPE} (eV)	Entropy, S (eV/K)	ΔG_{H^*} (eV)
Pt(111)	0.287	0.00370	-0.26043
Cu(111)	0.381	0.00302	0.03261
Ni_5P_4(0001)_3-fold_Ni (site I)	0.430	0.00168	-0.18728
Ni_5P_4(0001)_on-top_P (site II)	0.451	0.00171	0.59461
Ni_5P_4(0001)/Cu(111)_3-fold_Ni (site I)	0.345	0.00126	-0.52339
Ni_5P_4(0001)/Cu(111)_on-top_P (site II)	0.372	0.00131	0.46225
H_2 (gas phase)	0.275	--	--

Electrochemical stability or durability of the catalyst in working electrolyte is the important parameter that one should look for in the catalyst. The chronopotentiometry test was performed to check the durability of Cuf@Ni_5P_4 catalyst at a low (10 mA cm^{-2}) as well as high current density (160 mA cm^{-2}) in 0.5 M H_2SO_4 for 84 hours. As demonstrated in Figure 3.11 a, the electrocatalyst showed excellent stability performance with ~96% retention of overpotential even at a high current density of 160 mA cm^{-2}. The LSV pattern of the Cuf@Ni_5P_4 catalyst was recorded before and after chronoamperometry study and found that minute change in the overpotential as shown in Figure 3.11 b, indicates excellent durability of the catalyst. In order to check the structural integrity of the catalyst during stability, SEM (Figure 3.11 a, inset) as well as elemental mapping analysis (Figure 3.11 c-d) were performed before and after the chronoamperometry test. SEM study confirms the morphology of the catalyst does not get altered upon continuous evolution (84 hrs) of hydrogen gas. Elemental mapping further reveals the presence of Ni, Cu and P even after 84 hours of chronoamperometry test, which conclude the structural integrity and superior durability of the Cuf@Ni_5P_4 catalyst. The ultrathin deposited layer (30 nm) of the catalyst on the copper foam could increase the contact areas between them and thus decrease the average stress suffered by the hosts upon H_2 generation ensuring excellent structure integrity during continuous gas evolution by the as prepared catalyst. Excellent durability along with outstanding catalytic activity of the catalyst opens a new way towards the electrochemical generation of hydrogen.

3.4 Conclusions

In summary, we present here a simple electrochemical approach to design a single-phase Ni_5P_4 catalyst deposited on galvanostatically-grown Cuf nanoarchitecture. The core-shell Cuf@Ni_5P_4 catalyst has shown high catalytic activity towards HER in acidic medium with very less overpotential and superior exchange current density. The high ECSA and excessive roughness factor that originates from foam-like surface of Cuf is essentially responsible for high electrocatalytic activity of the catalyst. DFT calculations elucidate the origin of a very high negative Gibbs free energy change (ΔG_{H*}) in Ni_5P_4 (0001)/Cu(111) upon hydrogen adsorption. It arises due to a localized charge density distribution around the 3-fold Ni site of adsorbate, which is favorable for HER activity of the catalyst. The superhydrophilic and aerophobic nanostructured surface is actually helping by reducing the contact resistance and fast releasing the air bubble during the catalysis process. Moreover, the Cuf@Ni_5P_4 catalyst shows long-term durability of 84 hours measured by chronopotentiometry test at a low and high current density with ~96%

retention of initial overpotential and preserving structural consistency, which strongly indicates the superiority of the catalyst. This study opens up a new route for the synthesis of efficient and robust catalyst towards the generation of H_2 in a cost-effective and less time-consuming pathway, which will have encouraging applications in renewable energy future.

3.5 References

1. Crabtree, G. W., Dresselhaus, M. S. & Buchanan, M. V. The hydrogen economy. *Phys. Today* **57**, 39–44 (2004).
2. Esposito, D. V, Hunt, S. T., Kimmel, Y. C. & Chen, J. G. A New Class of Electrocatalysts for Hydrogen Production from Water Electrolysis: Metal Monolayers Supported on Low-Cost Transition Metal Carbides. *J. Am. Chem. Soc.* **134**, 3025–3033 (2012).
3. Dincer, I. & Acar, C. Review and evaluation of hydrogen production methods for better sustainability. *Int. J. Hydrogen Energy* **40**, 11094–11111 (2015).
4. Veziroğlu, T. & Sahin, S. 21st Century’s energy: Hydrogen energy system. *Energy Convers. Manag.* **49**, 1820–1831 (2008).
5. Menezes, P. W. *et al.* Uncovering the Nature of Active Species of Nickel Phosphide Catalysts in High-Performance Electrochemical Overall Water Splitting. *ACS Catal.* **7**, 103–109 (2017).
6. Wang, X., Li, W., Xiong, D., Petrovykh, D. Y. & Liu, L. Bifunctional Nickel Phosphide Nanocatalysts Supported on Carbon Fiber Paper for Highly Efficient and Stable Overall Water Splitting. *Adv. Funct. Mater.* **26**, 4067–4077 (2016).
7. Anantharaj, S. *et al.* Recent Trends and Perspectives in Electrochemical Water Splitting with an Emphasis on Sulfide, Selenide, and Phosphide Catalysts of Fe, Co, and Ni: A Review. *ACS Catal.* **6**, 8069–8097 (2016).
8. Li, J. *et al.* Highly Efficient and Robust Nickel Phosphides as Bifunctional Electrocatalysts for Overall Water-Splitting. *ACS Appl. Mater. Interfaces* **8**, 10826–10834 (2016).
9. Han, A., Chen, H., Sun, Z., Xu, J. & Du, P. High catalytic activity for water oxidation based on nanostructured nickel phosphide precursors. *Chem. Commun.* **51**, 11626–11629 (2015).

10. Li, D., Senevirathne, K., Aquilina, L. & Brock, S. L. Effect of Synthetic Levers on Nickel Phosphide Nanoparticle Formation: Ni 5 P 4 and NiP 2. *Inorg. Chem.* **54**, 7968–7975 (2015).
11. Pan, Y. *et al.* Monodispersed nickel phosphide nanocrystals with different phases: synthesis, characterization and electrocatalytic properties for hydrogen evolution. *J. Mater. Chem. A* **3**, 1656–1665 (2015).
12. Mishra, I. K. *et al.* Hierarchical CoP/Ni 5 P 4 /CoP microsheet arrays as a robust pH-universal electrocatalyst for efficient hydrogen generation. *Energy Environ. Sci.* **11**, 2246–2252 (2018).
13. Liu, P. & Rodriguez, J. A. Catalysts for hydrogen evolution from the [NiFe] hydrogenase to the Ni2P(001) surface: The importance of ensemble effect. *J. Am. Chem. Soc.* **127**, 14871–14878 (2005).
14. Wang, P. *et al.* Iron-Doped Nickel Phosphide Nanosheet Arrays: An Efficient Bifunctional Electrocatalyst for Water Splitting. *ACS Appl. Mater. Interfaces* **9**, 26001–26007 (2017).
15. Du, C., Shang, M., Mao, J. & Song, W. Hierarchical MoP/Ni2P heterostructures on nickel foam for efficient water splitting. *J. Mater. Chem. A* **5**, 15940–15949 (2017).
16. Xiao, X. *et al.* Engineering NiS/Ni2P Heterostructures for Efficient Electrocatalytic Water Splitting. *ACS Appl. Mater. Interfaces* **10**, 4689–4696 (2018).
17. You, B., Jiang, N., Sheng, M., Bhushan, M. W. & Sun, Y. Hierarchically Porous Urchin-Like Ni2P Superstructures Supported on Nickel Foam as Efficient Bifunctional Electrocatalysts for Overall Water Splitting. *ACS Catal.* **6**, 714–721 (2016).
18. Xu, J. *et al.* Al-Induced in Situ Formation of Highly Active Nanostructured Water-Oxidation Electrocatalyst Based on Ni-Phosphide. *ACS Catal.* **8**, 2595–2600 (2018).
19. Wang, X., Kolen’ko, Y. V., Bao, X., Kovnir, K. & Liu, L. One-Step Synthesis of Self-Supported Nickel Phosphide Nanosheet Array Cathodes for Efficient Electrocatalytic Hydrogen Generation. *Angew. Chemie Int. Ed.* **54**, 8188–8192 (2015).
20. Laursen, A. B. *et al.* Nanocrystalline Ni 5 P 4 : a hydrogen evolution electrocatalyst of exceptional efficiency in both alkaline and acidic media. *Energy*

Environ. Sci. **8**, 1027–1034 (2015).

21. Lai, C. *et al.* Rice-shape nanocrystalline Ni5P4: A promising bifunctional electrocatalyst for hydrogen evolution reaction and oxygen evolution reaction. *Inorganic Chemistry Communications* vol. 97 98–102 (2018).
22. Ledendecker, M. *et al.* The Synthesis of Nanostructured Ni 5 P 4 Films and their Use as a Non-Noble Bifunctional Electrocatalyst for Full Water Splitting. *Angew. Chemie Int. Ed.* **54**, 12361–12365 (2015).
23. Neil A C Hirst. Energy Technology. in *The Energy Conundrum* 119–190 (WORLD SCIENTIFIC (EUROPE), 2018). doi:10.1142/9781786344618_0006.
24. Hwang, S. J. *et al.* Supported Core@Shell Electrocatalysts for Fuel Cells: Close Encounter with Reality. *Sci. Rep.* **3**, 1309 (2013).
25. Gawande, M. B. *et al.* Core–shell nanoparticles: synthesis and applications in catalysis and electrocatalysis. *Chem. Soc. Rev.* **44**, 7540–7590 (2015).
26. Lu, Z. *et al.* Ultrahigh hydrogen evolution performance of under-water ‘superaerophobic’ MoS 2 nanostructured electrodes. *Adv. Mater.* **26**, 2683–2687 (2014).
27. Kresse, G. & Furthmüller, J. Efficient iterative schemes for ab initio total-energy calculations using a plane-wave basis set. *Phys. Rev. B* **54**, 11169–11186 (1996).
28. Blöchl, P. E. Projector augmented-wave method. *Phys. Rev. B* **50**, 17953–17979 (1994).
29. Joubert, D. From ultrasoft pseudopotentials to the projector augmented-wave method. *Phys. Rev. B - Condens. Matter Mater. Phys.* **59**, 1758–1775 (1999).
30. Perdew, J. P., Burke, K. & Ernzerhof, M. Generalized Gradient Approximation Made Simple. *Phys. Rev. Lett.* **77**, 3865–3868 (1996).
31. B.D. Cullity and S.R.Stock. *Elements of X-RAY DIFFRACTION Second Edition*. *Plant Management & Physiology* (1978).
32. Meunier, I., Tréglia, G., Gay, J.-M., Aufray, B. & Legrand, B. Ag/Cu(111) structure revisited through an extended mechanism for stress relaxation. *Phys. Rev. B* **59**, 10910–10917 (1999).
33. Shao, S., Shao, J., He, H. & Fan, Z. Stress analysis of ZrO_2/SiO_2 multilayers deposited on different substrates with different thickness periods. *Opt. Lett.* **30**, 2119 (2005).
34. Neuróhr, K. *et al.* Electrodeposition of Ni from Various Non-Aqueous Media: The Case of Alcoholic Solutions. *J. Electrochem. Soc.* **162**, D256–D264 (2015).

35. Ma, X., Chang, Y., Zhang, Z. & Tang, J. Forest-like NiCoP@Cu 3 P supported on copper foam as a bifunctional catalyst for efficient water splitting. *J. Mater. Chem. A* **6**, 2100–2106 (2018).
36. Dey, R. S., Hjuler, H. A. & Chi, Q. Approaching the theoretical capacitance of graphene through copper foam integrated three-dimensional graphene networks. *J. Mater. Chem. A* **3**, 6324–6329 (2015).
37. Jiang, J., Wang, C., Li, W. & Yang, Q. One-pot synthesis of carbon-coated Ni5P4 nanoparticles and CoP nanorods for high-rate and high-stability lithium-ion batteries. *J. Mater. Chem. A* **3**, 23345–23351 (2015).
38. Menezes, P. W., Indra, A., Das, C., Walter, C. & Göbel, C. Supporting Information Uncovering the Nature of Active Species of Nickel Phosphide Catalysts in High Performance Electrochemical Overall. 1–27.
39. Wei, S. *et al.* One-Step Synthesis of a Self-Supported Copper Phosphide Nanobush for Overall Water Splitting. (2016) doi:10.1021/acsomega.6b00366.
40. Tian, J., Liu, Q., Cheng, N., Asiri, A. M. & Sun, X. Self-Supported Cu 3 P Nanowire Arrays as an Integrated High-Performance Three-Dimensional Cathode for Generating Hydrogen from Water. *Angew. Chemie Int. Ed.* **53**, 9577–9581 (2014).
41. Tian, T., Ai, L. & Jiang, J. Metal–organic framework-derived nickel phosphides as efficient electrocatalysts toward sustainable hydrogen generation from water splitting. *RSC Adv.* **5**, 10290–10295 (2015).
42. Pan, Y. *et al.* Monodispersed nickel phosphide nanocrystals with different phases : synthesis , characterization and electrocatalytic. 1–10 (2014).
43. Popczun, E. J. *et al.* Nanostructured Nickel Phosphide as an Electrocatalyst for the Hydrogen Evolution Reaction. *J. Am. Chem. Soc.* **135**, 9267–9270 (2013).
44. Huang, Z. *et al.* Ni 12 P 5 Nanoparticles as an E ffi cient Catalyst for Hydrogen Generation via Electrolysis and Photoelectrolysis. 8121–8129 (2014) doi:10.1021/nn5022204.
45. Chusuei, C. C., Brookshier, M. A. & Goodman, D. W. Correlation of Relative X-ray Photoelectron Spectroscopy Shake-up Intensity with CuO Particle Size. *Langmuir* **15**, 2806–2808 (1999).
46. Suliman, M. H., Adam, A., Siddiqui, M. N., Yamani, Z. H. & Qamar, M. The impact of microstructural features of carbon supports on the electrocatalytic hydrogen evolution reaction. *Catal. Sci. Technol.* (2019) doi:10.1039/c8cy02549e.

47. McCrory, C. C. L., Jung, S., Peters, J. C. & Jaramillo, T. F. Benchmarking Heterogeneous Electrocatalysts for the Oxygen Evolution Reaction. *J. Am. Chem. Soc.* **135**, 16977–16987 (2013).
48. Chang, J. *et al.* Sulfur-Doped Nickel Phosphide Nanoplates Arrays: A Monolithic Electrocatalyst for Efficient Hydrogen Evolution Reactions. *ACS Appl. Mater. Interfaces* **10**, 26303–26311 (2018).
49. Wei, L. *et al.* A hierarchically porous nickel–copper phosphide nano-foam for efficient electrochemical splitting of water. *Nanoscale* **9**, 4401–4408 (2017).
50. Yang, Y., Fei, H., Ruan, G. & Tour, J. M. Porous Cobalt-Based Thin Film as a Bifunctional Catalyst for Hydrogen Generation and Oxygen Generation. *Adv. Mater.* **27**, 3175–3180 (2015).
51. Dutta, A., Samantara, A. K., Dutta, S. K., Jena, B. K. & Pradhan, N. Surface-Oxidized Dicobalt Phosphide Nanoneedles as a Nonprecious, Durable, and Efficient OER Catalyst. *ACS Energy Lett.* **1**, 169–174 (2016).
52. Shi, Y. & Zhang, B. Recent advances in transition metal phosphide nanomaterials: synthesis and applications in hydrogen evolution reaction. *Chem. Soc. Rev.* **45**, 1529–1541 (2016).
53. Li, H. *et al.* Systematic design of superaerophobic nanotube-array electrode comprised of transition-metal sulfides for overall water splitting. *Nat. Commun.* **9**, 1–12 (2018).
54. Greeley, J., Jaramillo, T. F., Bonde, J., Chorkendorff, I. & Nørskov, J. K. Computational high-throughput screening of electrocatalytic materials for hydrogen evolution. *Nat. Mater.* **5**, 909–913 (2006).

Chapter 4

An ultrastable self-supportive Ni_5P_4-copper foam bifunctional electrocatalyst for solar-driven water splitting

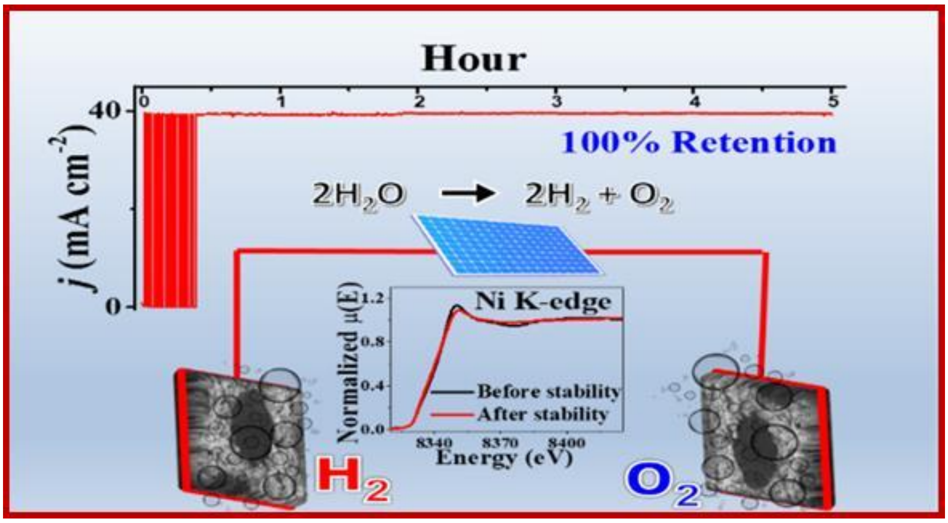

Abstract: Ultrastable electrode material for spontaneous fuel production by electrochemical water splitting has received tremendous attention, because the conventional water electrolysis system is not fully renewable, as it needs power from non-renewable sources. The designing of self-supportive and ultra-durable electrocatalyst with budget-friendly and less time-consuming method is therefore extremely necessary to split the water into hydrogen and oxygen. It is therefore important to divulge the structural information of a catalyst in order to have the extraordinary stable electrodes for solar-driven water electrolysis system. This paper reports a facile electrochemical method for the synthesis of single-phase Cuf@Ni_5P_4 core-shell nanostructures for overall water splitting in alkaline media. The Cuf@Ni_5P_4 based cell shows the extraordinary stability in working electrolyte for 150 h at a current density of 10 mA cm^{-2} with 96% retention of its initial potential. The Cuf@Ni_5P_4//Cuf@Ni_5P_4 cell hybridized with a solar cell in order to demonstrates the suitability of the concept towards a hybrid energy device and an impulsive generation of H_2 and O_2. This versatile system opens up a new route for the generation of green fuel towards renewable energy applications.

4.1 Introduction

Presently, world is facing energy crisis, global warming and climate change due to excessive use of fossil fuels.[1,2] Thus, to avoid such serious issues, a route for the development of completely self-sustainable green energy technology is highly appreciated. Integrated self-powered ultrastable water electrolysis system with sustainable power harvester system is in immense appeal from society to meet the production of green fuel demand.[3,4] The fuel generation from electrolysis of water ($H_2O \rightarrow H_2 + 1/2O_2$, $E_0 = 1.23$ V) is no doubt renewable in nature[5–8], but the electricity required to split water is still considered from non-renewable energy homes. An alternative way to overcome this problem is to use a self-powered system that harvest ambient energy to generate power, which can be integrated with the water electrolyzer.[9–14] There are several forms of energy available in the environment for producing electricity, like mechanical, solar, thermal and wind energy, those are of the recent research interest for long-time need towards clean and sustainable fuel generation.[15,16] The efficient and influential source of energy is solar energy for the production of electricity.[17] The photovoltaics units when coupled with electrolysers for direct conversion of solar energy into hydrogen fuel is a best choice for energy conversion systems.[10,12,13] The proposed electrocatalyst efficiently splits water utilizing the power coming from solar panel when illuminated in a very stable way. Sivanantham et. al. demonstrated full water splitting electrolyzer using the catalyst hierarchical $NiCo_2S_4$ nanowire arrays on Ni foam using commercially available GaAs based thin film solar cell for the first time, but the current density achieved in that case was very less.[18] Another example for electrochemical full water splitting using solar energy was represented by Ali Han et. al. where they have shown Janus like Cu_3P@NF electrode and the catalytic current density of 10 mA/cm^2 were achieved at 1.7 V when the potential was supplied using solar cell.[19] Overall water splitting is a thermodynamically arduous reaction and demands enormously efficient and active electrode materials that considerably accelerate the sluggish kinetics of two half reaction occurring at both cathode (HER) and anode (OER) simultaneously.[20–22] Electrocatalysts, the heart of electrochemical water splitting system, is preferable to be bifunctional in nature, have been attracted immense research interest since a decade. There are two critical points that should be considered for the development of water splitting catalyst with respect to commercialization and industrial applications. First, the electrocatalyst needs to meet the criteria of self-supportive to the electrode that should work at high current densities.[23] Second demanding criteria is the mechanical robustness and ultralong stability without changing its chemical composition.[24,25] Many transition metal-based phosphides, selenides, sulphides, nitrides, [26–28] have been reported recently that partially meets the benchmarks. However, conventional route for the development of an electrocatalyst involves sol–gel processing[29], dip-coating[30], spray pyrolysis[30], hydrothermal synthesis[31] that involved long-time synthetic approaches, high temperature pyrolysis methods, complicated reaction kinetics and multistep process, even though most of them are not self-supported at the current collector. Moreover, most of the conventional electrocatalysts experienced with the corrosion by oxide formation during long time cycling, which hinder their use in commercial sector. Therefore, there is a vital need from industry for the rational development of self-supportive non-precious electrocatalyst for overall water splitting that can work at high current density and ensure ultralong lifetime. Herein, a facile electrochemical route is developed for the synthesis of single-phase Ni_5P_4 nanofilm that was self-supported on galvanostatically grown copper foam/copper electrode. The core-shell architecture of Cuf@Ni_5P_4 was exploited as bifunctional electrocatalyst for evolution of H_2 and O_2 from water in alkaline medium for 150 hours. Electrocatalyst, Cuf@Ni_5P_4 having core shell nanostructures and due to the difference in the geometry between the core and the shell there is a synergistic effect between them produces. Because of the interfacial mixing of two phases and strong size mismatch between the core and the shell, a large interfacial strain induces. This effect decides the kinetic rate of the catalyst and thus improves the catalytic activity.[32–34] The advantage of the Cuf@Ni_5P_4//Cuf@Ni_5P_4 cell over the other state-of-the-art cells as well as Pt-C//RuO_2 is that it not only has comparable overpotential but also unveiled the long-term durability, which is the main challenge for commercialization. The electrochemical cell was then autonomously hybridized with solar cell to make it a renewable system for long-time fuel generation.

4.2 Experimental section

4.2.1 Synthesis and modifications of different electrocatalyst materials

The Cuf@Ni_5P_4 electrocatalyst was prepared by electrochemical approach following our recent report.[35] Briefly, first copper foam was prepared from H_2 bubble templated electrodeposition method[36,37], which is the finest way to synthesize any porous material. The electrodeposition of Ni_5P_4 on copper foam (Cuf) was galvanostatically deposited at a constant potential of -0.8 V (*vs* Ag/AgCl) for the duration of 90 min with three-electrode electrochemical cell in an aqueous solution containing $NiCl_2.6H_2O$ (60 mM), $NaH_2PO_2.H_2O$ (50 mM) and NaH_2PO_4 (0.5 M). The electrochemical cell consists of Cu/Cuf as the working electrode, platinum wire as the counter electrode and Ag/AgCl (3 M KCl) as reference electrode. Similar deposition conditions were followed for the deposition of nickel phosphide on different substrates such as copper foil (Ni_5P_4/Cu), graphite plate (Ni_5P_4/GP) by keeping the area constant (1×1 cm^2) in order to compare the activity of the catalyst.

4.2.2 Assembling of solar cell-water electrolysis hybrid system

Solar cell-water electrolysis hybrid unit was assembled using 6 V solar cell illuminated by a solar simulator Xenon lamp. The solar cell was wired in series with the water electrolysis unit. The electrochemical cell (EC) was composed of electrode Cuf@Ni_5P_4 serving as both cathode and anode in 1 M KOH electrolyte. The H_2 and O_2 gas formation were observed when the light illuminated the solar panel. The electrochemical responses of water splitting upon hybridization were recorded using CHI 760E workstation.

4.2.3 Electrochemical activity towards catalysis

The electrochemical activity of the catalyst was tested in a three-electrode system with Cuf@Ni_5P_4 (1×1 cm^2) as the working electrode, graphite rod as the counter electrode and Hg/Hg_2SO_4 (saturated) as the reference electrode in 1M KOH at ambient conditions. For comparison of the catalytic activity, electrodeposition of Ni_5P_4 on different substrate like copper foil (Ni_5P_4/Cu), graphite plate (Ni_5P_4/GP) was carried out in a three-electrode system at a constant potential of -0.8 V. The response of bare Cuf and noble metal like Pt/C (HER) and RuO_2 (OER) were also recorded for the comparison. All the potentials used here were calibrated to reversible hydrogen electrode (RHE) based on the formula:

$$E_{RHE} = \left(E_{Hg/Hg_2SO_4(saturated)} + 0.65 + 0.0591\, pH\right) V$$

Polarization curves were *iR* corrected (unless mentioned otherwise) within the electrolyte. The catalysts were activated by the minimum of 20 CV cycles scan till the stabilization of the active surface area at a scan rate of 100 mV $s^{-1.}$ The HER and OER measurements were carried out by linear sweep voltammetry at a scan rate of 10 mVs^{-1}. All the current obtained were normalized by the geometrical surface area. The ohmic drop of the catalytic activity was corrected by compensating *iR* drop manually by obtaining the R_s (solution resistance) value through EIS at an open circuit potential. For the analysis of durability of the catalyst chronopotentiometric (CP) measurements were conducted under the same experimental conditions without compensating *iR* drop. Electrochemical impedance spectroscopy (EIS) measurements were carried out at a potential of 1.56 V vs RHE in the frequency range of 10^5-10^{-2} Hz.

4.3 Results and discussion

4.3.1 Physical characterizations

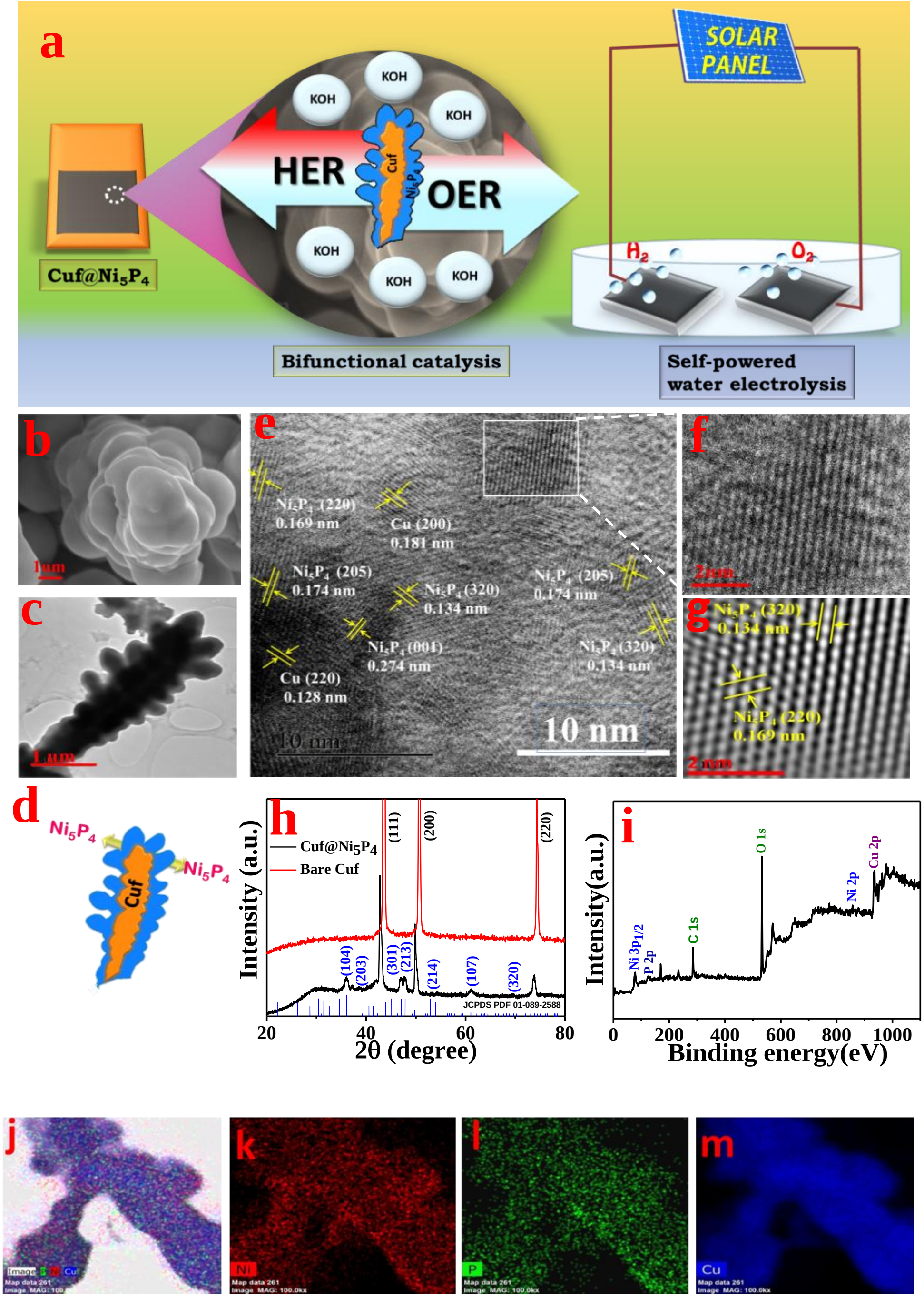

Figure 4.1. *(a) Schematic illustration of Cuf@Ni_5P_4 as bifunctional electrocatalysis its hybridization and (b) Scanning electron micrograph (SEM) of Cuf@Ni_5P_4. (c) Transmission electron micrograph (TEM) of Cuf@Ni_5P_4. (d) Schematic illustration of electrodeposited Cuf@Ni_5P_4 showing dendritic branch (e-g) HRTEM (h) XRD and (i) XPS survey of Cuf@Ni_5P_4. (j-m) Elemental mapping of Cuf@Ni_5P_4 taken from TEM*

The synthetic approach and the hybrid unit are schematically represented in Figure 4.1a. The morphology of the electrodes was first analyzed by scanning electron microscopy (SEM). The SEM image for the electrochemically grown Ni_5P_4 on Cuf can be seen in Figure 4.1b. A uniform layer of nickel phosphide was deposited on Cuf for the formation of core-shell nanostructure acting Ni_5P_4 as a shell and Cuf as a core. The synergistic effect between core and the shell is an advantage for efficient evolution of H_2 and O_2.[38] A well-defined porous network structure of Cuf@Ni_5P_4 proficiently offers an ion-diffusion path that effectively enables charge transfer and electron mobility. The transmission electron microscopy (TEM) of Cuf@Ni_5P_4 was carried out for detailed morphological analysis as represented in Figure 4.1c which resembles a clear contrast different for the core-shell formation of the catalyst with the shell thickness of about 30-50 nm, as depicted schematically in Figure 4.1d. The high-resolution TEM (HRTEM) was employed to affirm the formation of different phases in Cuf@Ni_5P_4 (Figure 4.1e-g). The HRTEM studies, however, confirmed the presence of the planes for the Ni_5P_4 and Cuf in Cuf @Ni_5P_4. The crystallinity and structure of the as-synthesized catalyst was analyzed in detail through X-ray diffractometer (XRD). As shown in Figure 4.1h, the diffraction pattern of Ni_5P_4 nanofilm indicates hexagonal crystal structure formation (JCPDS PDF 01-089-2588) having peaks at 2θ values of 36.6°(104), 39.28°(203), 47.06°(301), 47.84°(213), 52.96°(214), 61.06°(107) and 69.66°(320). The XRD of bare Cuf confirms a cubic lattice (JCPDS PDF 01-070-3038) and the peaks were found at 43.19°, 50.3° and 73.89° attributed to (111), (200) and (220) planes. However, the peak of copper in Cuf@Ni_5P_4 was observed to be shifted by 0.3° towards lower angles. This shifting of diffraction angle is because of the uniform interfacial strain on the lattice ‘d’ spacing upon the layer formation at the junction of core-shell nanostructures[32,39–41]. Two negligibly small peaks of copper oxide (CuO) and nickel oxide (NiO) were also observed at an angle of 37.24° (111) and 38.95° (111), which appeared either due to areal oxidation or formed during electrochemical synthesis. It should be noted that the d spacing obtained from HRTEM were well correlated with the planes obtained from XRD. The X-ray photon spectroscopy (XPS) was employed on Cuf@Ni_5P_4 surface to analyze the chemical composition of surface and their valance states. The XPS survey in Figure 4.1i clearly presents the coexistence of Ni, P, Cu, C and O elements. Elemental mapping obtained from TEM (Figure 4.1 j-m) of the catalyst have proven that nickel and phosphorous uniformly resides over copper foam forming a uniform core-shell nanostructure. The local bonding state, chemical and structural information of Ni and Cu in Cuf@Ni_5P_4 were revealed through X-ray absorption near-edge structure (XANES) and extended X-Ray absorption fine structure (EXAFS) spectroscopy analysis for both Ni and Cu K-edges. Figure 4.2a shows Ni K-edge XANES spectra of Cuf@Ni_5P_4 sample along with Ni metal and NiO (Ni^{2+}) standard references. The XANES spectrum of Ni K-edge of Cuf@Ni_5P_4 displays a strong black line signal at 8350 eV for electronic transition for 1s orbital to 4p orbital, which resembles with the Ni K-edge of NiO, indicating the oxidation state of Ni in Ni_5P_4 is +2.[42,43] The Fourier transforms (FTs) of the EXAFS spectrum found at the Ni K-edges analysis of the sample is shown is Figure 4.2b, where the peak at 1.78 Å corresponds to Ni-P interactions of Ni_5P_4.[44,45] The presence of metallic Ni-Cu bond at 2.99 Å interatomic radial distance, indicates the presence of bimetallic interface, which is responsible for an admirable performance of the catalyst.[46,47] The presence of two peaks of Ni-Ni interactions were found between 3 and 5 Å.[48] The EXAFS and XANES analysis of Cuf@Ni_5P_4 at Cu K-edge is performed for the examination of the state of Cuf in the sample.[49,50]

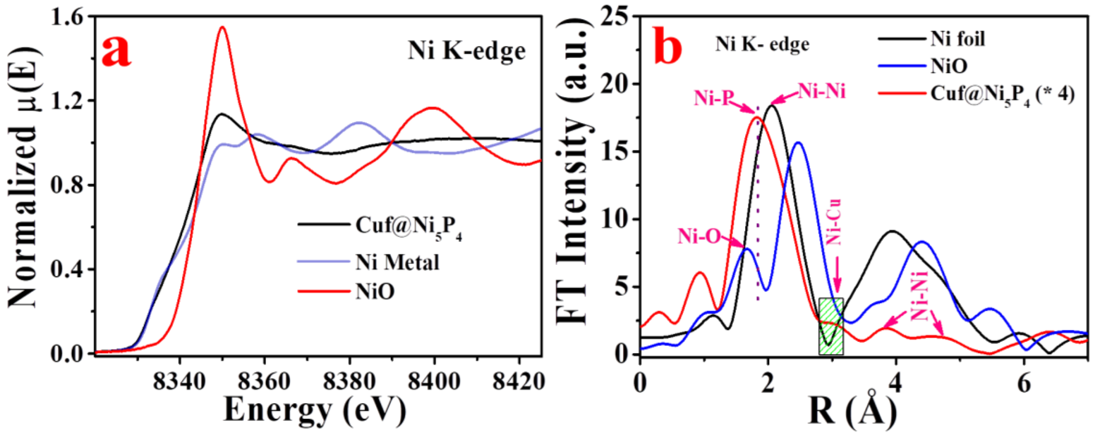

Figure 4.2. *(a) A comparison for the XANES spectra of the catalyst Cuf@Ni_5P_4 with references NiO and Ni foil for Ni K-edge. (b) FT-EXAFS spectra of Cuf@ Ni_5P_4 showing the oxide as well as metallic peak in the spectrum for Ni K-edge.*

4.3.2 Electrochemical performance of the catalyst

In order to check the bifunctional electrocatalytic activity of the material, individual catalysis for OER and HER were examined in a three-electrode system using 1 M KOH as an electrolyte and all the potentials used here were calibrated to reversible hydrogen electrode (RHE). All the polarization curves were corrected by compensating i*R* drop based on electrochemical impedance spectroscopy (EIS) measurements.

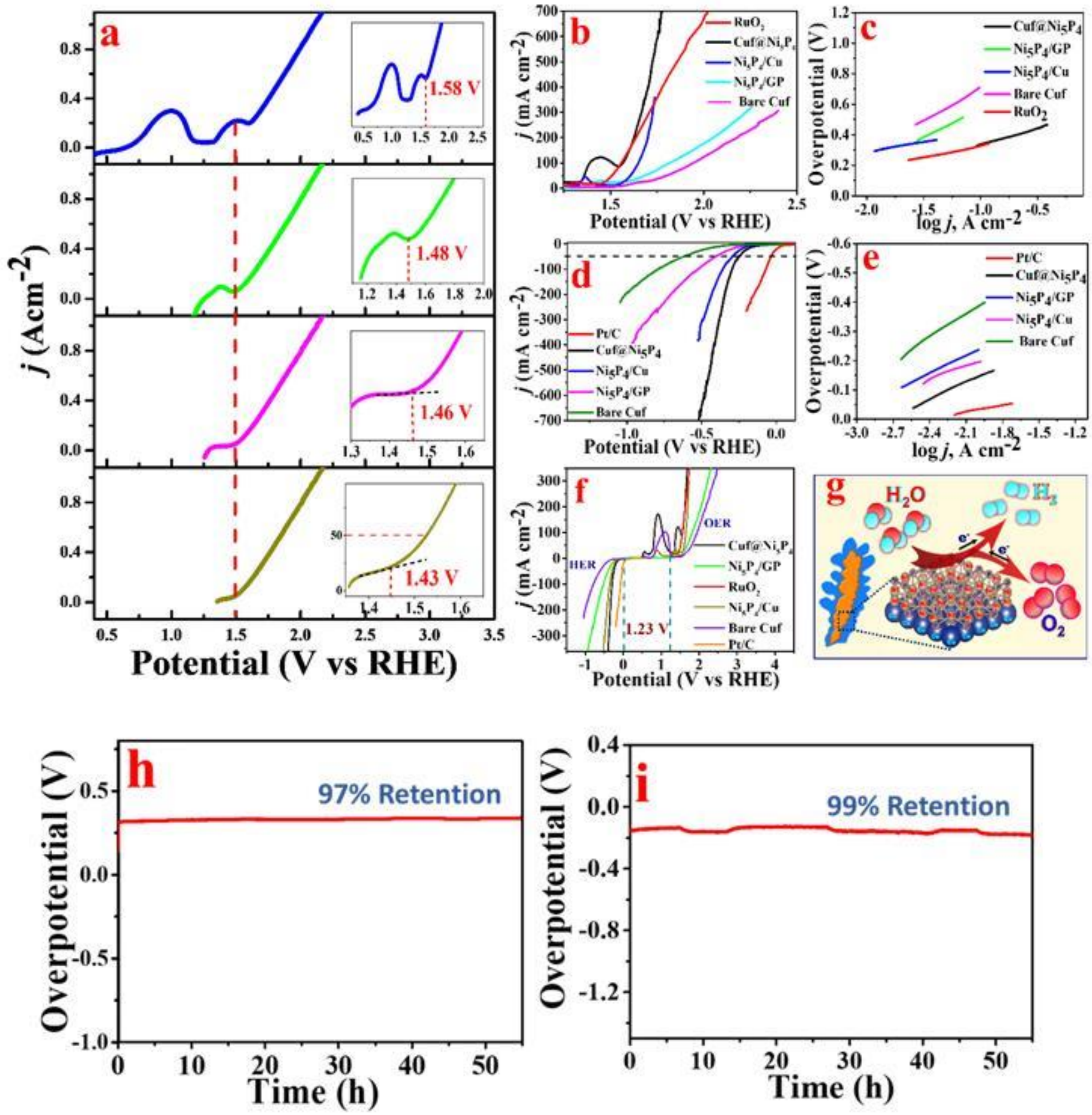

Figure 4.3. *(a) Control potential LSV scan to determine actual onset potential. (b) OER Polarization curves of Cuf@Ni_5P_4 including all the control catalysts. (c) Tafel plots of all the catalyst corresponding to the OER polarization curves. (d) HER Polarization curves of the catalysts. (e) Tafel plots of all the catalyst corresponding to the HER polarization curves. (f) Polarization curve of all the catalyst in HER and OER region. (g) Schematic for water splitting mechanism of Cuf@Ni_5P_4. (h) Chronopotentiometric curve of Cuf@Ni5P4 for OER at J = 100 mA cm^{-2} (i) Chronopotentiometric curve of Cuf@Ni_5P_4 for HER at J = 10 mA cm^{-2}. All experiments were carried out in 1M KOH for 55 h*

Figure 4.3a displays the polarization curves of Cuf@Ni_5P_4 catalyst for OER with different potential window. The determination of OER onset potential and/or overpotential at 10 mA cm^{-2} for Ni-based catalyst is a long standing problem as the faradic current corresponding to the oxidation of Ni^{2+}/Ni^{3+} and OER overlaps in the potential range between 1.32 V to 1.54 V (*vs* RHE) in alkaline medium.[51,52] Here, we have proposed a possible solution *via* restricting the potential window of the OER polarization curve in order to avoid the oxidation potential of Ni^{2+}. The onset potential of the Cuf@Ni_5P_4 catalyst is found to be 1.43 V (Figure 4.3a, inset), which is much superior to the noble metal-based catalyst, RuO_2 and most of state-of-the-art catalyst reported recently (Table 4.1). The overpotential of the catalyst, Cuf@Ni_5P_4 at current density of 20, 50 and 100 mA cm^{-2} was found to be 210 mV (1.44 V), 290 mV (1.52 V) and 330 mV (1.56 V), respectively (Table 4.2), which is much better than the other catalyst, such as Ni_5P_4/Cu (410 mV), Ni_5P_4/GP (580 mV), bare Cuf (710 mV) and similar like RuO_2 at 100 mA cm^{-2} (Figure 4.3b).

Table 4.1 Comparison for OER onset potentials of Cuf@Ni_5P_4 with recently developed catalysts

Catalyst	η_{onset} (V vs RHE)	References
Ni_2P- NW	1.54	Chem. Commun., *2015, 51, 11626--11629*
Ni_2P- NP	1.61	Energy Environ. Sci., *2015,8, 2347-2351*
N-CG–CoO	1.55	Energy Environ. Sci., *2014, 7, 609–616*
IPNT	1.48	Chem. Eur. J. *2015, 21, 18062 – 18067*
Ni-Co Oxide	1.49	ACS Nano, *2014, 8, 9, 9518–9523*
$LiCoO_2$	1.55	Nature Communications volume 5, Article number: *3949 (2014)*
Au@Co_3O_4	1.53	Adv. Mater. *2014, 26, 23, 3950-3955*
CoMn LDH	1.5	J. Am. Chem. Soc. *2014, 136, 16481−16484*
$Ni_xCo_{3-x}O_4$	1.53	Adv. Mater. *2010, 22, 1926–1929*
$Mn_{0.1}Ni$	1.59	Adv. Funct. Mater. *2014, 25, 3*, 393-399
NiFe-LDH	1.45	J. Am. Chem. Soc. *2013, 135, 8452−8455*
FeCoNi-ATNs/NF	1.46	Adv. Energy Mater. *2019, 1901312*
NCN/CC	1.48	J. Mater. Chem. *A, 2018, 6, 4466–4476*
Cuf@Ni_5P_4	**1.43**	**This Work**

NW (Nanowires), NP (Nanoparticles), N-CG–CoO (3D crumpled graphene–cobalt oxide), IPNT (iron phosphide nanotube), LDH (Layered double hydroxide), ATNs (Atomically thin nanosheets), NF (Nickel Foam), NCN/CC (nickel–cobalt nitride on carbon cloth),

The interconnected conductive paths formed between copper foam and nickel phosphide due to core-shell morphology is responsible for fast electron transfer kinetics, which results in the superior rate performance.[34] The corresponding Tafel slope as depicted in Figure 4.3c, clearly demonstrates that the Cuf@Ni_5P_4 has a lower Tafel slope than other comparative samples. The Tafel slope of Cuf@Ni_5P_4 was calculated to be 127 mV dec^{-1}, which is lower than RuO_2 (138 mVdec^{-1}) and all other catalyst, such as Ni_5P_4/Cu (154 mV dec^{-1}), Ni_5P_4/GP (165 mV dec^{-1}), bare Cuf (416 mV dec^{-1}), illustrates a better kinetics behaviour of the Cuf@Ni_5P_4 catalyst in 1M KOH. The HER performance of all the catalyst was also evaluated using LSV in alkaline media as shown in Figure 4.3d. The overpotential of the Cuf@Ni_5P_4 were only 146 mV and noticeably lesser than all other prepared catalysts at 10 mA cm^{-2}. The polarization curve of Ni_5P_4/Cu, Ni_5P_4/GP, bare Cuf and Pt/C has showed overpotential of 197 mV, 236 mV, 394 mV and 26 mV, respectively at 10 mA cm^{-2} (Table 4.4). The Tafel slope that governs the chemical kinetics of the electrocatalyst,[53] was found to be 180 mVdec^{-1}, which is apparently lower than that of Ni_5P_4/Cu (194 mV dec^{-1}), Ni_5P_4/GP (198 mV dec^{-1}) and bare Cuf (274 mV dec^{-1}), indicating the favorable kinetics of the as-prepared catalyst (Figure 4.3e).

Table 4.2 OER Potential of the electrodes at different current densities

	Catalyst	**η@Onset**	**η@20 mA cm^{-2}**	**η@50 mA cm^{-2}**	**η@100 mA cm^{-2}**	**η@500 mA cm^{-2}**	**η@700 mA cm^{-2}**
OER	Cuf@Ni_5P_4	1.42 V	1.44 V	1.52 V	1.56 V	1.72 V	1.77 V
	Ni_5P_4/Cu	1.52 V	1.56 V	1.60 V	1.64 V	-	-
	Ni_5P_4/GP	1.57 V	-	1.68 V	1.82 V	-	-
	Cuf	1.68 V	-	1.80 V	1.94 V	-	-
	RuO_2	1.43 V	1.45 V	1.50 V	1.55 V	1.85 V	2.02 V

However, the Tafel slope for Pt/C was calculated to be 80 mV dec^{-1}. The overpotential retention the catalyst was 99% of its initial potential, indicates remarkable durability of the catalyst. In order to assess the bifunctional activity a full polarization curve in a three-electrode configuration covering HER and OER (Figure 4.3f) were taken for all the catalysts. Figure 4.3g provides a schematic illustration for the role of core-shell electrocatalyst towards simultaneous H_2 and O_2 formation. The anodic and cathodic stability of Cuf@Ni_5P_4 was evaluated by chronopotentiometry (CP) measurement at a high current density of 100 mA cm^{-2} and 10 mA cm^{-2} and found that the retention of initial overpotential is almost 97% and 99 %, respectively, even after 55 h, evidences of exceptional durability of the catalyst (Figure 4.3h-i). The electrochemically active surface area (ECSA) of Cuf@Ni_5P_4 were calculated to be 331 cm^2 and 1325, respectively, which is very high comparing the recently developed nickel phosphide-based catalyst for water splitting.[54,55] Interestingly, the 3D interconnected porous nanofilm shell of Ni_5P_4

over Cuf core substrate is accountable for very high surface area and electrical conductivity.

Table 4.3 HER Potential of the electrodes at different current densities

	Catalyst	η@Onset	η@20 mA cm^{-2}	η@50 mA cm^{-2}	η@100 mA cm^{-2}	η@500 mA cm^{-2}	η@700 mA cm^{-2}
HER	Cuf@Ni_5P_4	53 mV	192 mV	247 mV	298 mV	446 mV	514 mV
	Ni_5P_4/Cu	115 mV	232 mV	298 mV	360 mV	-	-
	Ni_5P_4/GP	147 mV	298 mV	403 mV	528 mV	-	-
	Cuf	224 mV	474 mV	622 mV	798 mV	-	-
	Pt/C	13 mV	46 mV	83 mV	122 mV	-	-

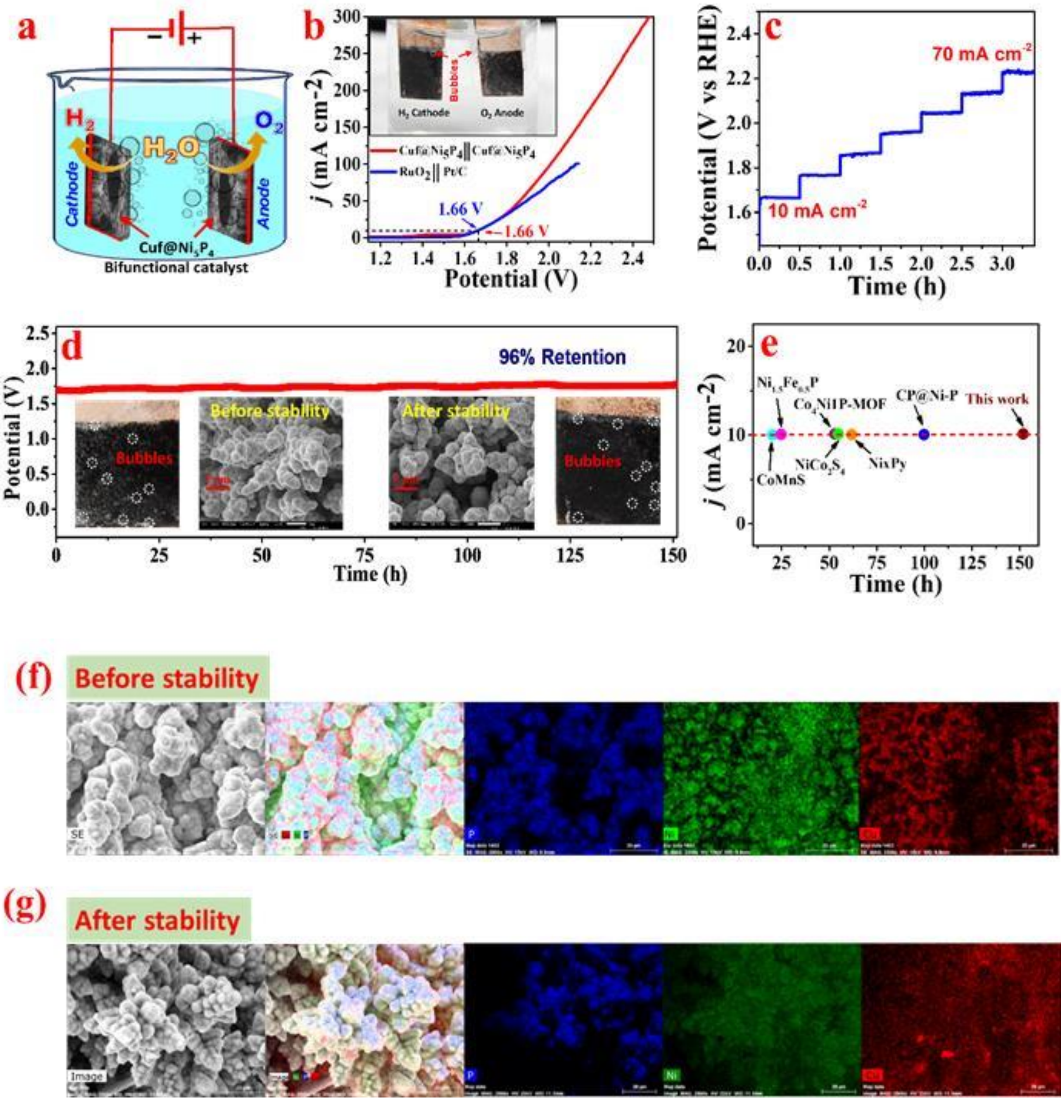

Figure 4.4. *(a) Schematic illustration of catalyst in a two-electrode system. (b) LSV curves of Cuf@Ni_5P_4 || Cuf@Ni_5P_4 and Pt/C || RuO_2 overall water splitting in a two-electrode configuration and the inset shows the digital image of two electrode configuration of Cuf@Ni_5P_4. (c) Chronopotentiometery current ramping of Cuf@Ni_5P_4 at different current density. (d) Chronopotentiometry (CP) plot of Cuf@Ni_5P_4 in a two electrode system at a current density of 10mA cm^{-2}, inset shows the bubble formation at the cathode and anode during stability and SEM images of Cuf@Ni_5P_4 before and after 150 h CP run.(e) A comparison plot for stability of recently reported and Cuf@Ni_5P_4 catalyst.*

Considering the worthy overall performances of Cuf@Ni_5P_4 catalyst towards HER and OER, a home-made alkaline electrolyzer was constructed with two similar electrodes of alike dimension and were assembled as cathode and anode, as schematically depicted in Figure 4.4a.

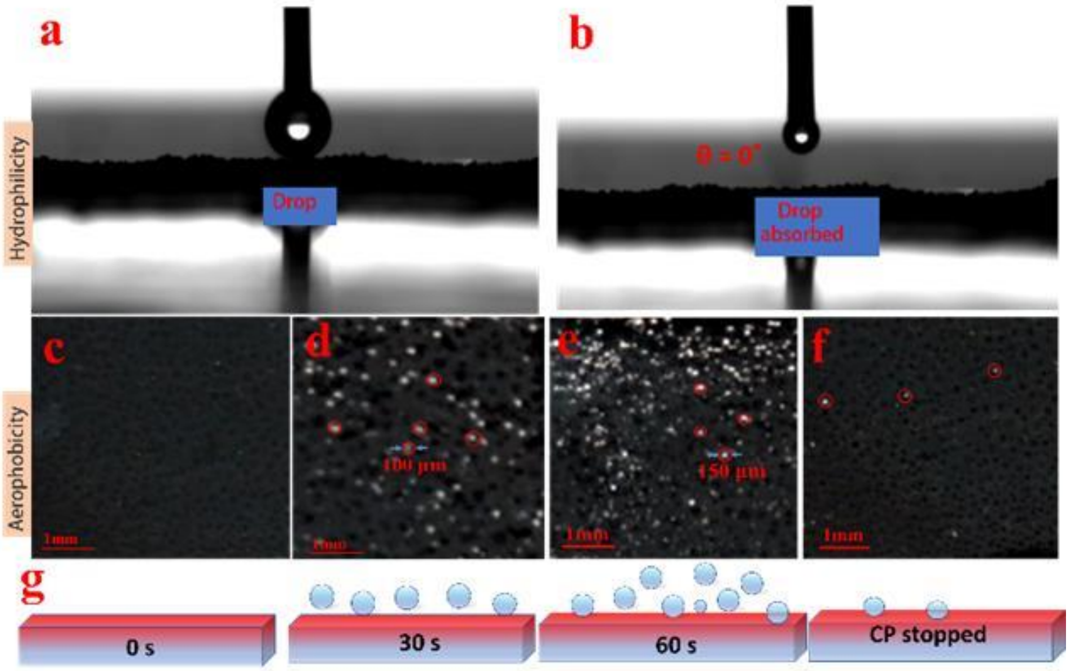

Figure 4.5. *Hydrophilicity analysis of Cuf@Ni_5P_4. (a) before and (b) after dropping the liquid on to the surface of the catalyst (c-f). Optical images with scheme at bottom panel showing the bubble formation behavior on Cuf@Ni_5P_4 surface at different time showing exceptional aerophobic behavior of the catalyst.*

Another electrolyzer with commercial Pt/C as cathode and RuO_2 as anode was counterfeited for comparison purpose. The Cuf@Ni_5P_4//Cuf@ Ni_5P_4 cell has shown an outstanding overall performance with a cell voltage of 1.66 V to obtain a current density of 10 mA cm^{-2}, which is comparable to RuO_2//Pt/C cell (Figure 4.4b) and lower than that of most of the bifunctional catalysts reported recently (Table 4.4). A digital image of the assembled two electrodes comprising the catalyst with bubbles in an alkaline media is shown in the inset of Figure 4.4b. The core shell nanostructures of Cuf@Ni_5P_4 is playing a crucial role in the increased catalytic activity of the catalyst. The mechanical robustness of the catalyst is a critical parameter to use it for commercial application and can be evaluated by performing current ramping stability through multi-step chronopotentiometry measurement. Figure 4.4c shows the CP curve of Cuf@Ni_5P_4 for 5 h at different current densities gradually amplified from 10 to 70 mA cm^{-2} with holding each current density step for 1800 s. The quick response time at each step assured that the catalyst is very stable at different current density with no degradation of the potential recommends the tremendous mechanical robustness of the catalyst. Furthermore, long-term durability of the catalyst was tested by CP technique at a constant current density of 10 mA cm^{-2} for 150 h. The catalyst retained 96% of its initial potential even after ultralong duration of CP for 150 h as shown in Figure 4.4d. A graph to compare extralong stability of the as prepared catalyst with the existing recently reported material is illustrated in Figure 4.4e. The bubble formation at cathode surface during stability run is shown in the inset of Figure 4.4d. Further, microscopic structure and elemental composition of the catalyst before and after 150 h of the long-lasting stability experiment were investigated from SEM images and elemental mapping study of the cathode surface (inset of Figure 4.4d). It is interesting to note that the catalyst surface maintained its structural integrity with almost negligible degradation in its morphology as well as no dissolution or detachment of the electrochemically grown ultrathin thin layer of Ni_5P_4 from the Cuf was detected. Furthermore, the elemental mapping study was conducted to confirm the homogeneous distribution of elements (Cu, Ni, and P) even after 150 h CP stability run (Figure 4.4f-g). The excellent response from multistep as well as long-term CP measurements further guides that the chemical nature of the catalyst does not changed at different current density as well as pores of the catalyst were not blocked upon the formation of the bubbles, which notified about the surface property of the catalyst.

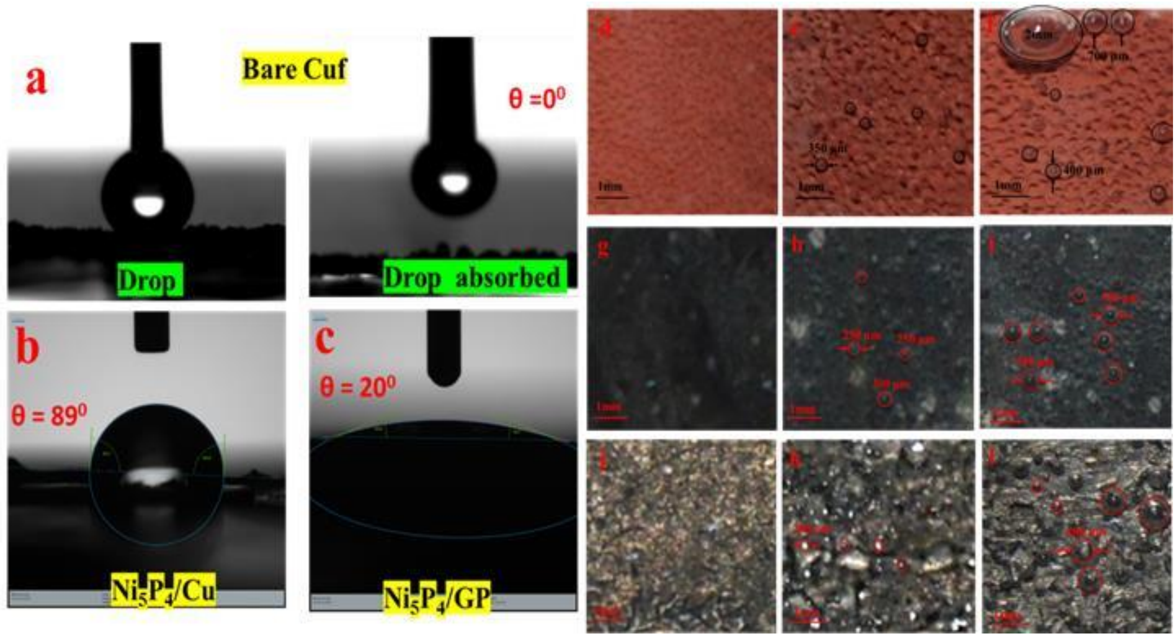

Figure 4.6. *Hydrophilicity analysis of the control samples (a) Bare Cuf (b) Ni_5P_4/Cu (c) Ni_5P_4/GP. Aerophobic behaviour of the control samples (a-c) bare Cuf, (d-f) Ni_5P_4/Cu, (g-i) Ni_5P_4/GP*

4.3.3 Catalyst Surface property

Motivated from this study have encouraged us to examine the nature and the behavior of the surface. The surface properties of Cuf@Ni_5P_4 along with other catalysts were analyzed by performing hydrophilicity and aerophobicity test. Figure 4.5a and b shows that the Cuf@Ni_5P_4 surface is superhydrophilic in nature as the drop absorbed instantly through the catalytic surface unlike other catalysts. Aerophobicity study was performed through observing the bubble formation during CP measurement.

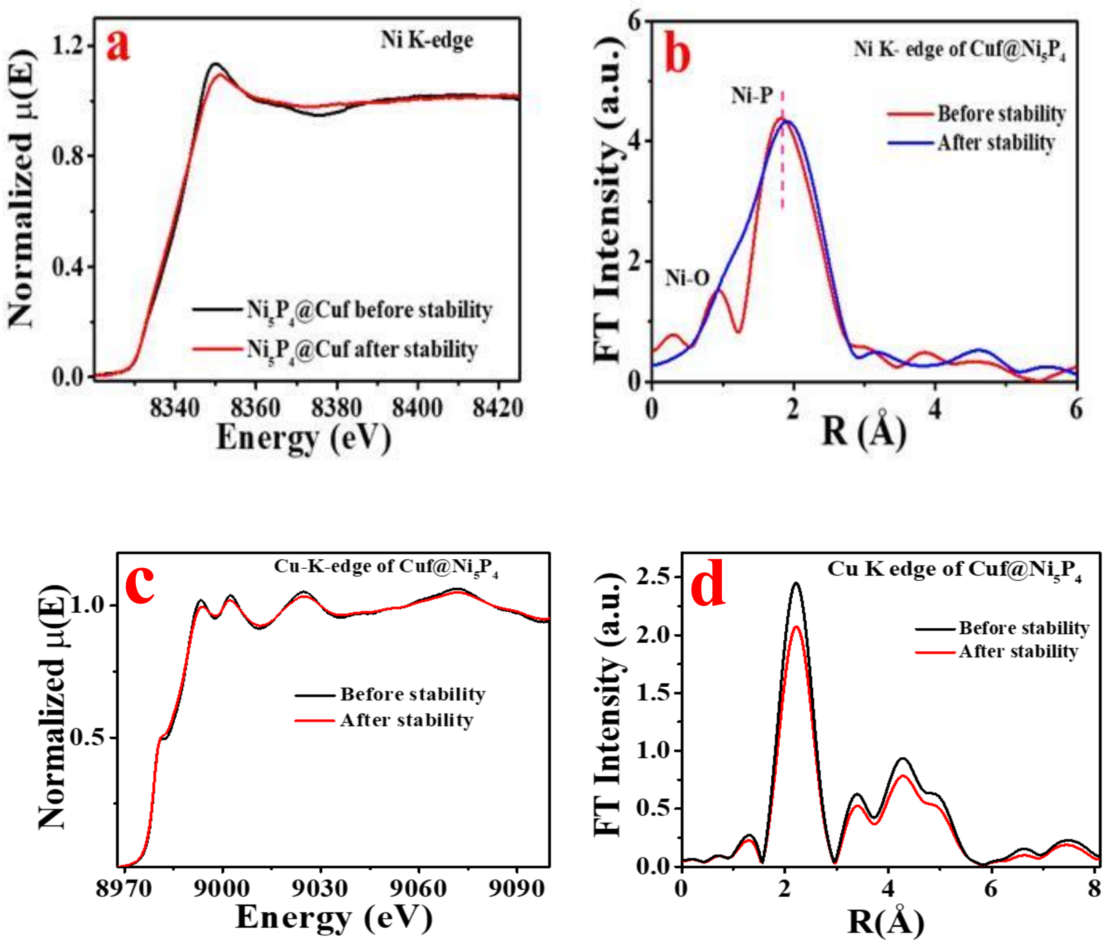

Figure 4.7. *(a) XANES spectra and (b) FT-EXFAS spectra of the catalyst Cuf@Ni_5P_4 for before and after stability aimed at Ni K-edge (c) XANES spectra and (d) FT-EXFAS signal of Cuf@Ni_5P_4 for before and after stability at Cu K-edge.*

As shown in Figure 4.5c-f and the schematic representation in Figure 4.5g, during the course of the experiment, bubble starts to grow from 100 µm (Figure 4.5d) to a maximum of 150 µm (Figure 4.5e) and then leaves surface as soon as it grows further at varying time and a very few bubbles were observed on the surface of the catalyst when the CP experiment was stopped (Figure 4.5f), demonstrates the excellent aerophobic behaviour of the catalyst. The hydrophilicity (Figure 4.6a-d) as well asaerophobicity behaviour of the control samples were also investigated. The aerophobic behaviour of other control samples were also analysed (Figure 4.6d-l) and found that the Cuf@Ni_5P_4 surface is more aerophobic in nature than other as prepared control catalysts. The superhydrophilic nature of the sample facilitates the fast formation of bubbles due to less contact resistance with the electrolyte, whereas, the aerophobic nature of the catalyst advantages for self-renewable of bubbles from the surface, which answers for achieving excellent stability and fast response during multistep CP as well as ultralong durability of the catalyst.

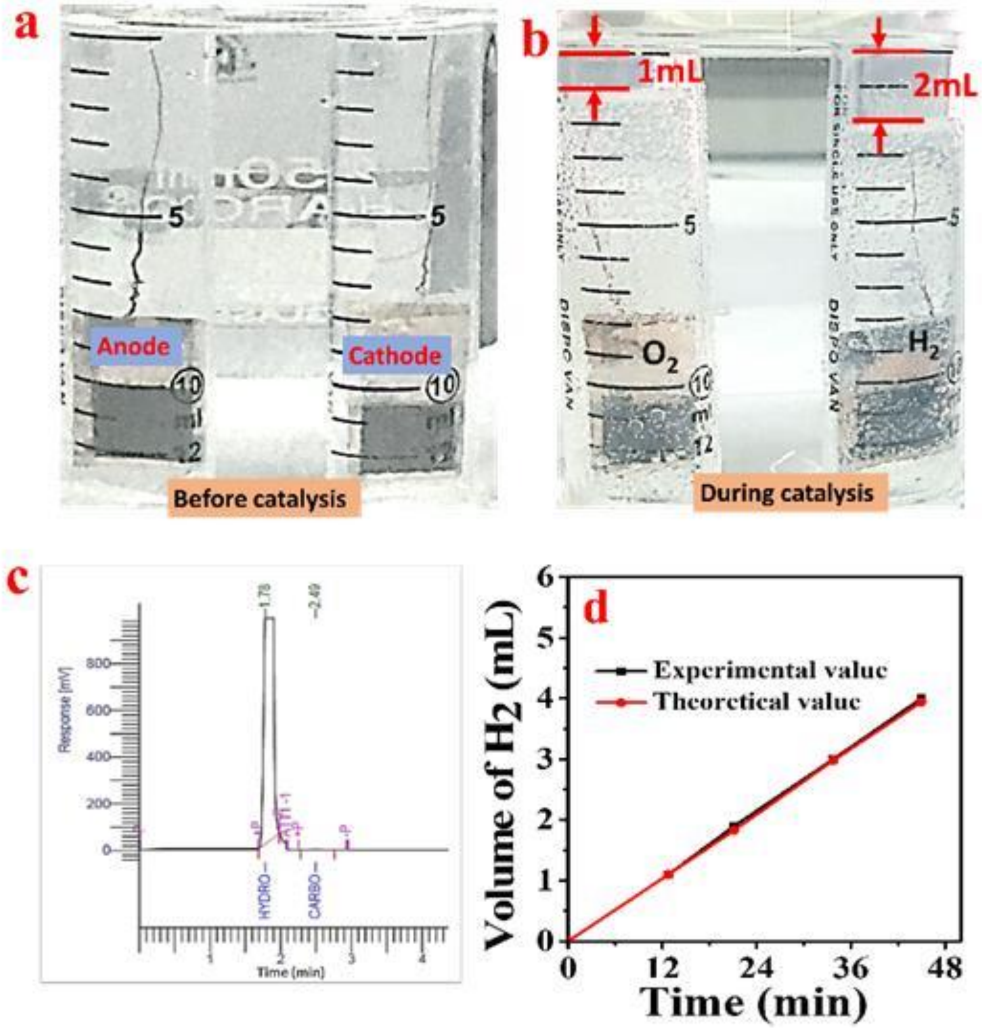

Figure 4.8. *(a) Optical image for the level of* H_2/O_2 *before catalysis of Cuf@*Ni_5P_4 *electrode (b) optical image for the level of* H_2/O_2 *during catalysis (c) GC response upon the injection of 40µl of* H_2 *gas (d) Volume of* H_2 *gas evolved as a function of time.*

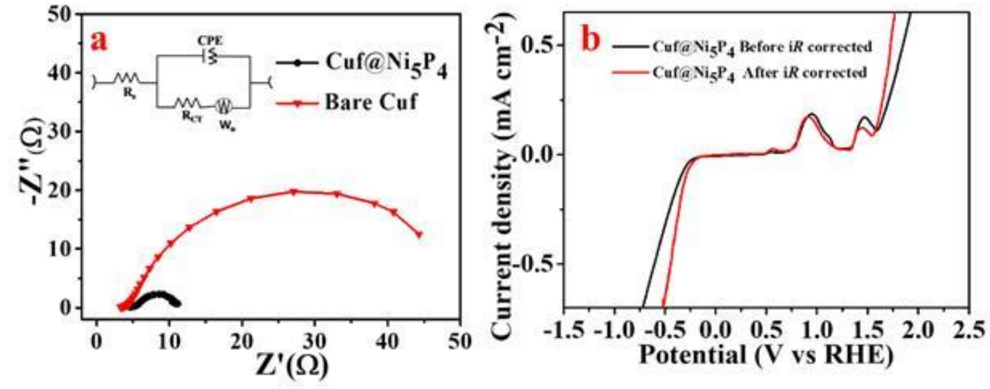

Figure 4.9. *(a) Nyquist plot of bare Cuf and Cuf@*Ni_5P_4 *at 1.58 V (vs RHE) (b) LSV curve full scan before and after iR compensation*

The Ni and Cu K-edge X-ray absorption near-edge structure (XANES) spectra and extended X-ray absorption fine structure (EXAFS) spectroscopy were collected for Cuf@Ni_5P_4 catalyst before and after stability for the cathode surface. In Figure 4.7a, XANES spectra for the catalyst before and after stability are almost similar, proves the oxidation states of Ni does not change even after long cycling hour. However, a slight shift in the Ni K-edge peak can be observed for the catalyst after stability towards higher energy suggesting a slight formation of oxidized species on the surface of the catalyst. The EXAFS analysis at Ni K-edge (Figure 4.7b) shows the interplanar distance of Ni-P remained same indicating the local structure and chemical composition of the Ni_5P_4 sample retained even after long period cycling performance.[56–58] The XANES and EXAFS spectra of Cu K-edge (Figure 4.7c-d) before and after the course of stability is almost same, which resembles the core of the catalyst was unaffected during stability experiment. Therefore, as the edge energy for both Ni and Cu K-edge of after stability sample is as similar as fresh sample, suggesting the catalyst is ultrastable in alkaline media even after long time (150 h) CP experiment.

4.3.4 Faradic efficiency

In order to check the Faradic efficiency (FE) and rate of gas evolution, H_2 and O_2 gas were separately collected, analyzed and calculated by the technique called water gas displacement method, where both the volume and time were recorded for experimental value of the generated gas.[59] The electrolysis of Cuf@Ni_5P_4 was performed at a constant potential of 1.66 V in a homemade two-electrode configuration, where both the electrodes were hanged from top of the tube filled with electrolyte and sealed with epoxy as represented by a digital image in Figure 4.8a-b.

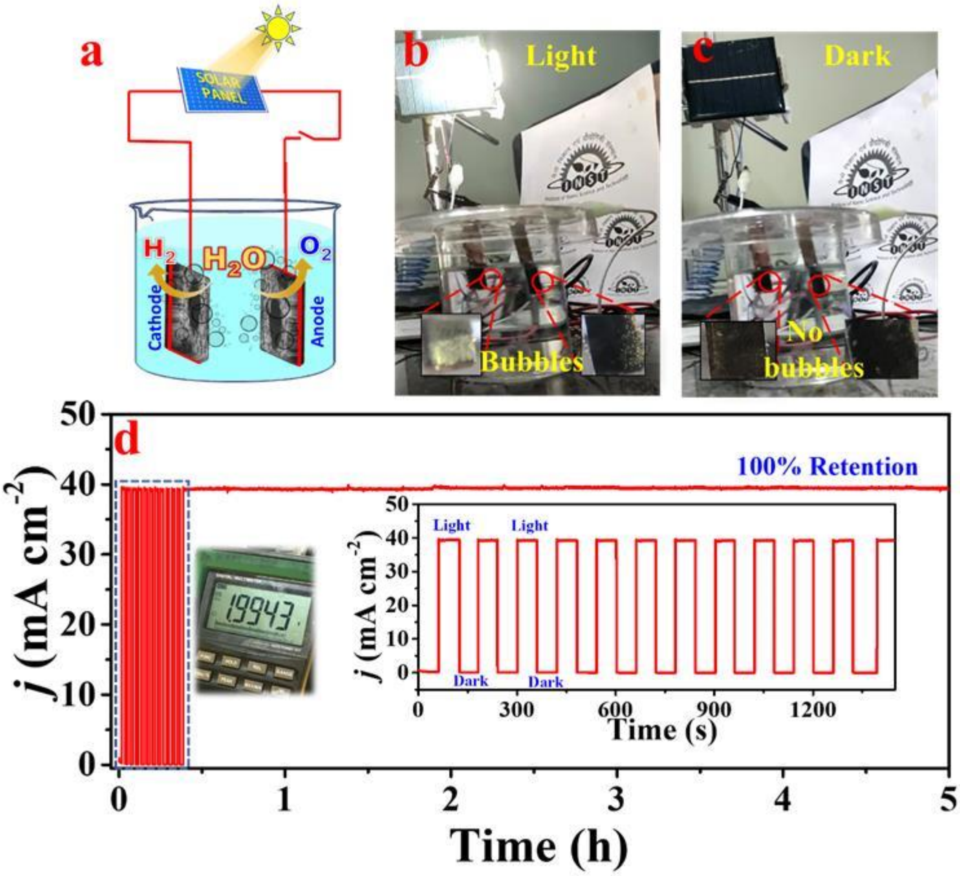

Figure 4.10. *(a) Schematic illustration for the hybridization of solar cell with water electrolysis. (b-c) Digital image of solar cell - water splitting hybrid unit assembled using Cuf@Ni_5P_4 electrodes in light and dark. (d) Current vs time response of water electrolysis, its retention under continuous illumination for 5 h and inset shows the current response of the catalyst under illumination (light) and de-illumination (dark).*

The collection of H_2 and O_2 were done separately at atmospheric pressure and the level of electrolyte at initial state (Figure 4.8a) and during electrolysis (Figure 4.8b) were noted in order to calculate the FE. To analyse the purity of hydrogen produced, 40 µL of gas was collected from cathodic side of the cell through a syringe and injected into gas chromatography (GC) instrument. As demonstrated in Figure 4.8c, the peak of H_2 is saturated at time 1.78 min and no other peaks were observed, indicates that the evolved H_2 gas as fuel is of very high purity and can be utilized efficiently in a fuel cell. The ratio of generation of H_2:O_2 remained in the ratio of 2:1 over the duration of electrolysis. As depicted in Figure 4.8d, the FE of the catalyst with respect to H_2 generation was found to be almost 99.8%. Also, a quite high hydrogen production rate was estimated to be 12.488 Kg of H_2/day means 4380 Kg of H_2/year (at room temperature and 1 atm, STP). According to survey, the fuel needs of 1-5 cars can be served with a hydrogen production rate of 200-1000 kg H_2/year.[60,61] Electrochemical impedance spectroscopy (EIS) investigations were conducted to investigate the kinetics of the Cuf@Ni_5P_4 catalyst. The EIS experiments for Cuf@Ni_5P_4 catalyst and bare Cuf were carried out at an applied potential of 1.56 V (vs RHE) (Figure 4.9a) in a frequency range of 0.001 Hz to 100000 Hz (inset of Figure 9a). The fitted Nyquist plot clearly shows a very low solution resistance (R_s) of 5.9 Ω, which is attributed to the less ohmic resistance of the electrode-electrolyte interface. The charge transfer resistance (R_{ct}) of the Cuf@Ni_5P_4 is only 7.5 Ω, which is far less than bare Cuf (~45 Ω), clearly indicates the Cuf@Ni_5P_4 catalyst promotes rapid charge transfer kinetics.[62,63] Additionally, the difference between the i*R* corrected and non-i*R* corrected full LSV scan have been shown in Figure 4.9b.

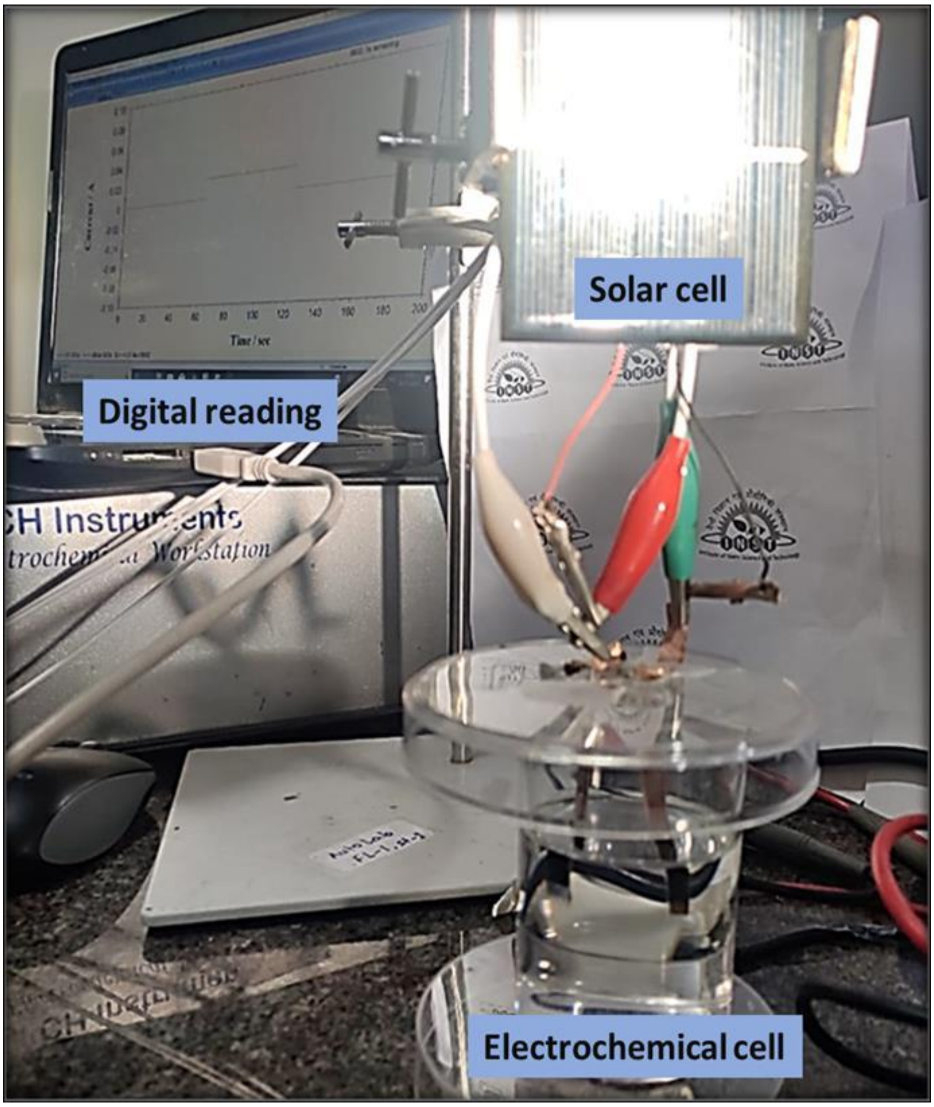

Figure 4.11. *Digital image of Solar cell-water electrolysis hybrid with electrochemical reading.*

Since, the as prepared catalyst showed up an extraordinary durability and comparable efficiency of the electrolyzer with benchmark catalyst, the possibility of hybrid technology was explored. Solar power radiation is undoubtedly an abundant and renewable energy source and thus very much useful for self-powered devices. The energy storage devices mainly acquire energy for charging from conventional non-renewable power grid that impede its application for renewable hybrid system, so solar power as a source to split water is a better way to go for renewable energy system.

Table 4.4. Electrochemical activities of the catalytic electrodes for overall water splitting.

Catalyst	η@10 mA cm^{-2}	Electrolyte	Stability (h)	References
EG/$Co_{0.85}$Se/NiFe-LDH	1.67 V	1 M KOH	10	*Energy Environ. Sci.*, 2016, 9, 478-483
$NiCo_2O_4$	1.65 V	1M NaOH	36	*Angew. Chem. Int. Ed.* 2016, 55, 6290-6294
CP/CTs/Co-S	1.743 V	1 M KOH	1.94	*ACS Nano* 2016, 10, 2342−2348
NiS/NF	1.64 V	1 M KOH	35	*Chem. Commun.*, 2016, 521,1486-1489
Ni/Ni_8P_3	1.61 V	1 M KOH	4.1	*Adv. Funct. Mater.* 2016, 26, 3314–3323
PNC/Co	1.64 V	1 M KOH	9.7	*J. Mater. Chem. A*, 2016, 4, 3204-3209
NiFe LDH/ NF	1.7 V	1 M NaOH		*Science*, 2014, 345, 1593
Ni@NC	1.81 V	1 M KOH	10	*Adv. Energy Mater.* 2015, 5, 1401660
$Ni_{2/3}Fe_{1/3}$-rGO	2.02 V	1 M KOH	10	*ACS Nano*,2015,92,1977-1984
$NiMoP_2$/CC	1.67 V	1 M KOH	24	*J. Mater. Chem. A*, 2017, 5, 7191–7199
NiCoP	1.77 V	1 M KOH	20	*Nano Res. 2016*, 9(8): 2251−2259
Ni_8P_3/NF	1.79 V	1 M KOH	22.2	*ACS Appl. Mater. Interfaces* 2016, 8, 27850−27858
C@Ni_8P_3	1.65 V	1 M KOH	22.2	*ACS Appl. Mater. Interfaces* 2016, 8, 27850−27858
Ni_5P_4/Ni foil	1.69 V	1 M KOH	-	*Angew. Chem.*, 2015, 127, 12538
Ni_2P/NF	1.63 V	1 M KOH	10	*Energy Environ. Sci.*, 2015, **8**, 2347
CoP-Cu foil	1.65 V	1 M KOH	24	*Angew. Chem., Int. Ed.*, 2015, 54, 6251
Co_xPO_4/CoP -Au	1.91 V	1 M KOH	-	*Adv. Mater.*, 2015, 27, 3175.
CoP/GO-400 -GCE	1.70 V	1 M KOH	24	*Chem. Sci.*, 2016, 7, 1690
$Co_{0.13}Ni_{0.87}Se_2$/Ti plate	1.62 V	1 M KOH	10	*Nanoscale*, 2016, 8, 3911.
NiFeP/NF	1.67 V	1 M KOH	40	*ACS Appl. Mater. Interfaces*, 2017, 9, 31, 26134–26142
NCN/CC	1.56 V	1 M KOH	250	J. Mater. Chem. *A, 2018, 6, 4466–4476*
Cuf@Ni_5P_4	**1.66 V**	**1 M KOH**	**150**	**This work**

4.3.5 Solar cell powered water splitting

First, a solar cell-powered water splitting system has been proposed with the aim to its practical use and commercialization. The water splitting system externally hybridized with commercially available solar panel has been demonstrated as depicted schematically in Figure 4.10a. The solar panel was illuminated by xenon lamp with various intensity (by varying distance), in order to generate the required potential to the electrodes for electrolysis of water. Figure 4.10b-c is the digital images of the assembled solar cell-water splitting hybrid system in illuminated and non-illuminated mode of solar cell. As depicted in Figure 4.10d, the obtained current density was found to be constant at ~39.5 mA cm^{-2} corresponding to the cell voltage of 1.99 V, which is also confirmed by a multimeter (Figure 4.10 d, inset), at a solar intensity of 144 mW cm^{-2}. Interestingly, the current density was dropped suddenly when the light source was removed (inset of Figure 4.10 d). The response time for on-off cycle was calculated to be 0.3 s, indicating very fast response of the material in hybrid system. The repeated ‘on-off’ test was continued for few cycles, in order to check its performance and mechanical robustness in the hybrid system. An appreciable amount of H_2 and O_2 bubbles on cathode and anode catalyst surface were observed under solar and in contrast almost no bubbles were visible in dark condition. After few on-off cycles, the analysis was continued for 5 hours to check the stability of the material during daytime. Interestingly, it was found that the electrodes were extremely stable and almost no degradation in the current density (retention was ~100%) under the continuous illuminated state of solar cell for 5 hours. The corresponding chronoamperometric response from the hybrid device was recorded with the electrochemical workstation (Figure 4.11). The extraordinary durability of the catalyst in hybridized state approved the urgency of such catalyst for the generation of green fuel in renewable pathway.

4.4 Conclusions

Electrochemically synthesized Cuf@Ni_5P_4 core-shell nanostructure based self-supportive electrode has been successfully synthesized that have proven to be an efficient bifunctional catalyst for overall water splitting. An ultralong durability of 150 h with a potential retention of 96% was achieved with the catalyst in two-electrode configuration. This outstanding bifunctional activity and ultralong stability of cost-effective and robust catalyst opens up the possibility to generate fuel for commercialization.

The water electrolysis system integrated with Cuf@Ni_5P_4 as both cathode and anode catalyst in 1M KOH has also shown its compatibility upon hybridization with externally powered devices. Herein, we have demonstrated a fully self-powered water electrolysis system with the help of solar cell. For commercialization and large scale solar to hydrogen production in a renewable way, the water electrolysis unit was wired with photovoltaics. This particular system responded extreme satisfactorily and an appreciable amount of bubble were generated on electrodes upon the illumination of light on solar cell for long duration. In conclusion, by utilizing ambient renewable energy (solar) for catalysing water splitting is a best possible way to produce H_2 and O_2 and the practice for designing and assembling a fully renewable and self-powered water splitting system that can achieve renewable energy conversion is optimal route for leading the world towards sustainable growth.

4.5 References

1. Dresselhaus, M. S. & Thomas, I. L. Alternative energy technologies. *Nature* **414**, 332–337 (2001).
2. York, R. Do alternative energy sources displace fossil fuels? *Nat. Clim. Chang.* **2**, 441–443 (2012).
3. Yang, Y. *et al.* A hybrid energy cell for self-powered water splitting. *Energy Environ. Sci.* **6**, 2429 (2013).
4. Balogun, M.-S. *et al.* Cost-Effective Alkaline Water Electrolysis Based on Nitrogen- and Phosphorus-Doped Self-Supportive Electrocatalysts. *Adv. Mater.* **29**, 1702095 (2017).
5. Li, X., Hao, X., Abudula, A. & Guan, G. Nanostructured catalysts for electrochemical water splitting: current state and prospects. *J. Mater. Chem. A* **4**, 11973–12000 (2016).
6. Zhang, B. *et al.* Homogeneously dispersed multimetal oxygen-evolving catalysts. *Science (80-.).* **352**, 333–337 (2016).
7. Turner, J. A. Sustainable Hydrogen Production. *Science (80-.).* **305**, 972–974 (2004).
8. Luo, J. *et al.* Water photolysis at 12.3% efficiency via perovskite photovoltaics and

Earth-abundant catalysts. *Science (80-.).* **345**, 1593–1596 (2014).

9. Wei, A. *et al.* Triboelectric nanogenerator driven self-powered photoelectrochemical water splitting based on hematite photoanodes. *ACS Nano* **12**, 8625–8632 (2018).
10. Balabel, A., Zaky, M. S. & Sakr, I. Optimum Operating Conditions for Alkaline Water Electrolysis Coupled with Solar PV Energy System. *Arab. J. Sci. Eng.* **39**, 4211–4220 (2014).
11. Yang, J. *et al.* Novel Iron/Cobalt-Containing Polypyrrole Hydrogel-Derived Trifunctional Electrocatalyst for Self-Powered Overall Water Splitting. *Adv. Funct. Mater.* **27**, (2017).
12. Qian, Z. *et al.* Hollow Nanocages of NixCo1−xSe for Efficient Zinc–Air Batteries and Overall Water Splitting. *Nano-Micro Lett.* **11**, (2019).
13. Zhang, Q. *et al.* Fully Solar-Powered Uninterrupted Overall Water-Splitting Systems. *Adv. Funct. Mater.* **29**, 1808889 (2019).
14. Zhao, W. *et al.* Amorphous Iron(III)-Borate Nanolattices as Multifunctional Electrodes for Self-Driven Overall Water Splitting and Rechargeable Zinc–Air Battery. *Small* **14**, 1–8 (2018).
15. Züttel, A., Remhof, A., Borgschulte, A. & Friedrichs, O. Hydrogen: The future energy carrier. *Philos. Trans. R. Soc. A Math. Phys. Eng. Sci.* **368**, 3329–3342 (2010).
16. Yang, Y. & Wang, Z. L. Hybrid energy cells for simultaneously harvesting multi-types of energies. *Nano Energy* **14**, 245–256 (2015).
17. Li, J. *et al.* Nanoparticle Superlattices as Efficient Bifunctional Electrocatalysts for Water Splitting. *J. Am. Chem. Soc.* **137**, 14305–14312 (2015).
18. Sivanantham, A., Ganesan, P. & Shanmugam, S. Hierarchical NiCo2S4 Nanowire Arrays Supported on Ni Foam: An Efficient and Durable Bifunctional Electrocatalyst for Oxygen and Hydrogen Evolution Reactions. *Adv. Funct. Mater.* **26**, 4661–4672 (2016).
19. Han, A., Zhang, H., Yuan, R., Ji, H. & Du, P. Crystalline Copper Phosphide Nanosheets as an Efficient Janus Catalyst for Overall Water Splitting. *ACS Appl. Mater. Interfaces* **9**, 2240–2248 (2017).
20. Hong, W. T., Risch, M., Stoerzinger, K. A. & Grimaud, A. Environmental Science Toward the rational design of non-precious transition metal oxides for oxygen electrocatalysis. *Energy Environ. Sci.* **8**, 1404–1427 (2015).

21. Sun, W. *et al.* Synthesis of Highly Conductive PPy/Graphene/MnO2 Composite Using Ultrasonic Irradiation. *Synth. React. Inorganic, Met. Nano-Metal Chem.* **46**, 437–444 (2016).
22. Yan, Y., Xia, B. Y., Zhao, B. & Wang, X. A review on noble-metal-free bifunctional heterogeneous catalysts for overall electrochemical water splitting. *J. Mater. Chem. A* **4**, 17587–17603 (2016).
23. Cao, X., Jie, Y., Wang, N. & Wang, Z. L. Triboelectric Nanogenerators Driven Self-Powered Electrochemical Processes for Energy and Environmental Science. *Adv. Energy Mater.* **6**, (2016).
24. Ghosh, S. & Basu, R. N. Multifunctional nanostructured electrocatalysts for energy conversion and storage: current status and perspectives. *Nanoscale* **10**, 11241–11280 (2018).
25. Wang, X., Li, W., Xiong, D., Petrovykh, D. Y. & Liu, L. Bifunctional Nickel Phosphide Nanocatalysts Supported on Carbon Fiber Paper for Highly Efficient and Stable Overall Water Splitting. *Adv. Funct. Mater.* **26**, 4067–4077 (2016).
26. Anantharaj, S. *et al.* Recent Trends and Perspectives in Electrochemical Water Splitting with an Emphasis on Sulfide, Selenide, and Phosphide Catalysts of Fe, Co, and Ni: A Review. *ACS Catal.* **6**, 8069–8097 (2016).
27. Li, A., Sun, Y., Yao, T. & Han, H. Earth-Abundant Transition-Metal-Based Electrocatalysts for Water Electrolysis to Produce Renewable Hydrogen. *Chem. - A Eur. J.* **24**, 18334–18355 (2018).
28. Li, S. *et al.* Co–Ni-Based Nanotubes/Nanosheets as Efficient Water Splitting Electrocatalysts. *Adv. Energy Mater.* **6**, 1501661 (2016).
29. Niu, J., Maharana, D., Xu, J., Chai, Z. & Bao, Y. A high activity of Ti/SnO2-Sb electrode in the electrochemical degradation of 2,4-dichlorophenol in aqueous solution. *J. Environ. Sci.* **25**, 1424–1430 (2013).
30. Yao, P. Effects of Sb doping level on the properties of Ti/SnO2-Sb electrodes prepared using ultrasonic spray pyrolysis. *Desalination* **267**, 170–174 (2011).
31. Xu, H., Zhang, Q., Yan, W. & Chu, W. A composite Sb-doped SnO 2 electrode based on the TiO 2 nanotubes prepared by hydrothermal synthesis. *Int. J. Electrochem. Sci.* **6**, 6639–6652 (2011).
32. Meunier, I., Tréglia, G., Gay, J.-M., Aufray, B. & Legrand, B. Ag/Cu(111) structure revisited through an extended mechanism for stress relaxation. *Phys. Rev. B* **59**, 10910–10917 (1999).

33. Shao, S., Shao, J., He, H. & Fan, Z. Stress analysis of ZrO2?SiO2 multilayers deposited on different substrates with different thickness periods. *Opt. Lett.* **30**, 2119–2121 (2005).
34. Li, X. *et al.* Strong Metal-Phosphide Interactions in Core-Shell Geometry for Enhanced Electrocatalysis. *Nano Lett.* **17**, 2057–2063 (2017).
35. Das, M. *et al.* Single-phase Ni5P4-Copper foam superhydrophilic and aerophobic core-shell nanostructures for efficient hydrogen evolution reaction. *J. Mater. Chem. A* (2019) doi:10.1039/c9ta06729a.
36. Shin, H. C., Dong, J. & Liu, M. Nanoporous Structures Prepared by an Electrochemical Deposition Process. *Adv. Mater.* **15**, 1610–1614 (2003).
37. Dey, R. S., Hjuler, H. A. & Chi, Q. Approaching the theoretical capacitance of graphene through copper foam integrated three-dimensional graphene networks. *J. Mater. Chem. A* **3**, 6324–6329 (2015).
38. Gawande, M. B. *et al.* Core-shell nanoparticles: synthesis and applications in catalysis and electrocatalysis. *Chem. Soc. Rev.* **44**, 7540–7590 (2015).
39. B.D. Cullity and S.R.Stock. *Elements of X-RAY DIFFRACTION Second Edition. Plant Management & Physiology* (1978).
40. Shao, S., Shao, J., He, H. & Fan, Z. Stress analysis of ZrO_2/SiO_2 multilayers deposited on different substrates with different thickness periods. *Opt. Lett.* **30**, 2119 (2005).
41. Jiang, J. *et al.* Ni-Pd core-shell nanoparticles with Pt-like oxygen reduction electrocatalytic performance in both acidic and alkaline electrolytes. *J. Mater. Chem. A* **5**, 9233–9240 (2017).
42. Tsai, C.-W., Chen, H. M., Liu, R.-S., Asakura, K. & Chan, T.-S. Ni@NiO Core–Shell Structure-Modified Nitrogen-Doped InTaO4 for Solar-Driven Highly Efficient CO2 Reduction to Methanol. *J. Phys. Chem. C* **115**, 10180–10186 (2011).
43. Zhou, T. *et al.* Increased activity of nitrogen-doped graphene-like carbon sheets modified by iron doping for oxygen reduction. *J. Colloid Interface Sci.* **536**, 42–52 (2019).
44. Cho, K.-S., Seo, H.-R., Kim, S.-H. & Lee, Y.-K. Nickel Phosphide Catalysts Supported on SBA-15 for Hydrodesulfurization of 4,6-Dimethyldibenzothiophene. *J. Japan Pet. Inst.* **53**, 173–177 (2010).
45. Seo, H., Cho, K. & Lee, Y. Formation mechanisms of Ni 2 P nanocrystals using

XANES and EXAFS spectroscopy. *Mater. Sci. Eng. B* **176**, 132–140 (2011).

46. Huang, C.-P. *et al.* Engineering heterometallic bonding in bimetallic electrocatalysts: towards optimized hydrogen oxidation and evolution reactions. *Catal. Sci. Technol.* **10**, 893–903 (2020).
47. Wang, X. *et al.* Strain Effect in Bimetallic Electrocatalysts in the Hydrogen Evolution Reaction. *ACS Energy Lett.* **3**, 1198–1204 (2018).
48. Wang, D., Li, Q., Han, C., Xing, Z. & Yang, X. When NiO@Ni Meets WS2 Nanosheet Array: A Highly Efficient and Ultrastable Electrocatalyst for Overall Water Splitting. *ACS Cent. Sci.* **4**, 112–119 (2018).
49. Ma, R. *et al.* Sulfidation of copper oxide nanoparticles and properties of resulting copper sulfide. *Environ. Sci. Nano* **1**, 347–357 (2014).
50. Bae, J. *et al.* Single-Fiber-Based Hybridization of Energy Converters and Storage Units Using Graphene as Electrodes. *Adv. Mater.* **23**, 3446–3449 (2011).
51. Wang, X., Li, W., Xiong, D. & Liu, L. Fast fabrication of self-supported porous nickel phosphide foam for efficient, durable oxygen evolution and overall water splitting. *J. Mater. Chem. A* **4**, 5639–5646 (2016).
52. Li, W. *et al.* From water reduction to oxidation: Janus Co-Ni-P nanowires as high-efficiency and ultrastable electrocatalysts for over 3000 h water splitting. *J. Power Sources* **330**, 156–166 (2016).
53. Shi, Y. & Zhang, B. Recent advances in transition metal phosphide nanomaterials: synthesis and applications in hydrogen evolution reaction. *Chem. Soc. Rev.* **45**, 1529–1541 (2016).
54. Chang, J. *et al.* Sulfur-Doped Nickel Phosphide Nanoplates Arrays: A Monolithic Electrocatalyst for Efficient Hydrogen Evolution Reactions. *ACS Appl. Mater. Interfaces* **10**, 26303–26311 (2018).
55. Wei, L. *et al.* A hierarchically porous nickel–copper phosphide nano-foam for efficient electrochemical splitting of water. *Nanoscale* **9**, 4401–4408 (2017).
56. Liu, K. *et al.* High-Performance Transition Metal Phosphide Alloy Catalyst for Oxygen Evolution Reaction. *ACS Nano* **12**, 158–167 (2018).
57. Huang, H. C. *et al.* Effect of a sulfur and nitrogen dual-doped Fe-N-S electrocatalyst for the oxygen reduction reaction. *J. Mater. Chem. A* **5**, 19790–19799 (2017).
58. Huang, J., Liu, Q., Yao, T., Pan, Z. & Wei, S. XAFS study on structure-activity correlations of α-Co(OH)2nanosheets water oxidation catalysts. *J. Phys. Conf. Ser.*

712, 12128 (2016).

59. Costa, J. D. *et al.* Electrocatalytic performance and stability of nanostructured Fe-Ni pyrite-type diphosphide catalyst supported on carbon paper. *J. Phys. Chem. C* **120**, 16537–16544 (2016).

60. Shiva Kumar, S. & Himabindu, V. Hydrogen production by PEM water electrolysis – A review. *Mater. Sci. Energy Technol.* **2**, 442–454 (2019).

61. Acar, C. & Dincer, I. Comparative assessment of hydrogen production methods from renewable and non-renewable sources. *Int. J. Hydrogen Energy* **39**, 1–12 (2014).

62. Kauffman, G. B. Electrochemical Impedance Spectroscopy. By Mark E. Orazem and Bernard Tribollet. *Angew. Chemie Int. Ed.* **48**, 1532–1533 (2009).

63. Zhou, H. *et al.* Highly active catalyst derived from a 3D foam of Fe(PO3)2/Ni2P for extremely efficient water oxidation. *Proc. Natl. Acad. Sci. U. S. A.* **114**, 5607–5611 (2017).

Chapter 5

Electrochemical growth of bimetallic transition metal selenide as a bifunctional electrocatalyst for water electrolysis

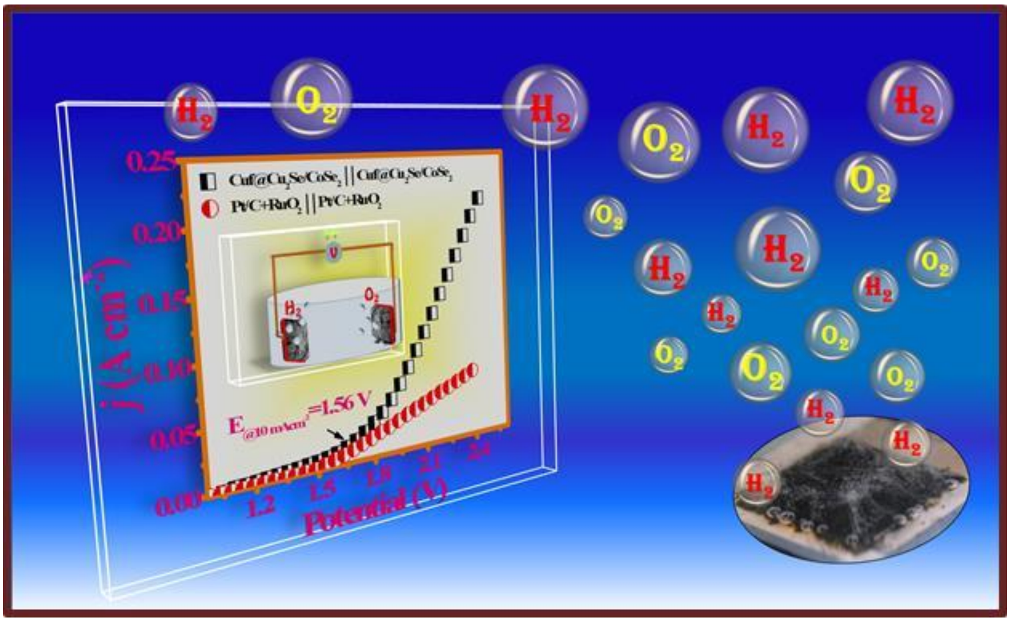

Abstract: The advancement in the non-noble metal-based catalyst design for water oxidation with an admirable performance is crucial for a sustainable and green energy future. Electrochemical growth for the synthesis of the catalyst has been known to be an appealing method due to its shorter reaction time, low cost and renewable nature. In this article, a simple electrochemical deposition method for the synthesis of hybrid nanostructures of earth-abundant transition metal selenides ($Cu_2Se/CoSe_2$) on copper foam (Cuf) has been explored the bifunctional electrochemical activity of hydrogen evolution reaction (HER) and oxygen evolution reaction (OER) in alkaline medium. The HER exhibited an overpotential of only 110 mV at a current density of 10 mA cm^{-2} and OER required the potential of only 1.4 V (outperforming noble metal catalyst RuO_2) at a current density of 20 mA cm^{-2}. The electrochemical cell composed of $Cuf@Cu_2Se/CoSe_2$ catalyst in a two-electrode system as an anode as well as a cathode showed high-performance overall water oxidation reaction with a very low applied potential of only 1.56 V at a current density of 10 mA cm^{-2}. The as-prepared electrode was proven to be superhydrophilic as well as aerophobic in nature, which enhances the stability and thus suited the best candidate for industrialization and practical applications.

5.1 Introduction

Hydrogen energy is so far known to be the best among all the existing energy resources because of its clean and renewable nature. The generation of hydrogen via the electrolysis of water opens up an attractive route to store energy driven from solar power in a fully renewable fashion.[1,2] The quality of H_2 gas (absence of other gases) obtained from water electrolysis is of high purity.[3] Noble metal-based catalysts such as Pt/C and RuO_2 are considered to be the most active electrocatalyst for the generation of hydrogen and oxygen, respectively, from water, but their limited abundance and scary cost prevent them to be used in practical and global-scale applications.[4,5] Since the electrochemical water splitting involves multi-electron transfer, it becomes a kinetically sluggish process that requires high overpotentials to attain the desired current density. Presently, the available commercial water electrolyzers mainly operate at a cell voltage of 1.8-2.0 V, which is substantially higher than the thermodynamic potential of water splitting i.e., 1.23 V.[6–8] Therefore, it is highly desired to reduce the overall cell voltage by introducing an efficient bifunctional catalyst, which can acts as cathode material for hydrogen evolution reaction (HER) and anode material for oxygen evolution reaction (OER).

To date, an appreciable effort has been given to modulate the chemical and physical properties of the electrocatalyst such as porosity, surface area, binding strength to the substrate and electrical conductivity in order to have fast electron transfer kinetics during water oxidation. First row transition metals are earth abundant materials and their derivatives such as sulphides, oxides[9,10], phosphides[11,12], selenides[13,14] have emerged as highly efficient electrocatalysts for electrochemical water oxidation.[15] Although, transition metal oxides and sulphides are earth abundant materials and due to their electronic configurations, they have been studied more in electrocatalysis. However, lower electrical conductivity and poor stability in alkaline medium restrict the use of transition metal oxides and sulphides in the water oxidations. Recently transition metal selenides have drawn growing attention in the field of water electrolysis due to their improved band structure.[16,17] The electronegativity of selenium (2.55) is lesser than that of the sulphur (2.58) and oxygen (3.44), which helps to improve better covalency of the metal-chalcogen bond in selenide than sulphides and oxides.[16] Higher covalency represents higher bond strength and as a result metal selenides exhibit lower band gap and better electrical conductivity. Among other metal selenides, $CoSe_2$ catalyst has been explored for water electrolysis. [18–20] Kong et al. have synthesized $CoSe_2$ grown on carbon fibre by selenization process to check the HER activity and found an overpotential of 137 mV at a current density of 10 $mAcm^{-2}$ in acidic media. Liu et al. have synthesized an amorphous CoSe film on titanium, which required a cell potential of 1.65 V in 2-electrode configuration.[21] Many researchers have reported that hybrid catalyst/multi element materials enhance the activity as compared to the pristine one.[22–25] Cao et al. have recently synthesized $CuCo_2Se_4$ for overall water splitting. They have shown that the presence of Cu atoms actually boosts up the activity of Co sites by redistribution of electrons.[16] The presence of bimetal in the catalyst imparts the synergistic effect that supplements the structural deficit and triggers the inert sites, which enhances the catalytic activity. It has been proven that the presence of Cu in the catalyst adds more metallic character, which facilitates the rate of charge transfer.[26] However, the hybrid structure of cobalt and copper-based selenide is still not explored much for overall water splitting in alkaline media. Moreover, the synthesis of hybrid binary metal selenide and its fabrication onto the metal substrate is considered a challenging issue to the electrochemists.

Researchers have synthesized Co and Cu based selenides via different techniques such as hydrothermal, selenization process, electrodeposition methods etc.[16,25,27] Electrodeposition method is preferred among all the synthesis procedures because of low cost, ease and fast synthesis duration.[26] Also, this route of synthesis result in the fabrication of self-supporting electrocatalyst that eliminates the use of binders and eventually facilitates the catalyst durability as well as activity. The synthesis of 3-dimensional dendritic copper foam on a copper foil was performed utilizing a well-known dynamic hydrogen bubble template (DHBT) method, where the hydrogen bubbles were employed as the template for creating a porous structure. Copper foam (Cuf) with a porous rough surface as a substrate plays a crucial role in the activity of the catalyst.[28,29] The perks of using Cuf are following (1) Cu promotes the excellent reactivity being both one and two electron pathways. (2) Offers plentiful active sites because of the 3D porous structure. (3) Increases the surface area and thus reducing the electron diffusion path length. (4) Dendritic structure of Cuf leads to the superhydrophilic as well as aerophobic nature of the catalyst.

In this study, we have synthesized a highly efficient electrocatalyst, Cuf@Cu_2Se/$CoSe_2$ hybrid catalyst, which was electrochemically grown on copper foam (Cuf) substrate. The hybrid catalyst is composed of Cu_2Se and $CoSe_2$, and found to be responsive efficiently towards electrochemical water splitting. The catalytic activity of the as prepared catalyst outperformed the noble RuO_2 catalyst in OER with a potential of 1.4 V at 20 mA cm^{-2} and has overpotential of only 110 mV at 10 mA cm^{-2} for HER. The performance of the catalyst in a two-electrode cell was very good as proved from the cell voltage of only 1.56 V to drive a current density of 10 mA cm^{-2}. Such enhanced activity can be explained by listing some influential facts such as (1) the essentially admirable activity of Cuf@Cu_2Se/$CoSe_2$ is due to the synergistic effect taking place between Cu_2Se and $CoSe_2$. (2) The high electrochemically active surface area (ECSA) of the catalyst offered abundant active sites and displayed excellent electrical conductivity and electron exchange for hydrogen adsorption. (3) The hierarchically designed porous three-dimensional (3D) Cuf as a substrate exhibits a high surface area that indorses the easy diffusion of the electrolytic solution as reported in our previous work.[30] (4) Electrodeposition technique (direct growth on the substrate) for the synthesis of Cuf@Cu_2Se/$CoSe_2$ catalyst eliminates the use of binder that ensures better contact as well as non-blocking of active sites, which leads to the mechanical robustness of the catalyst. (5) The 3D dendric structure of the catalyst was found to be superhydrophilic and aerophobic in nature. The hydrophilic behaviour ensures better contact between the electrolyte and electrode thus minimizing the intrinsic resistance of the catalyst and the aerophobicity nature promotes the fast dissociation of the bubbles from the surface of the electrodes which favours the stability of Cuf@Cu_2Se/$CoSe_2$ catalyst.

5.2 Experimental

5.2.1 Preparation of Cuf@Cu_2Se/$CoSe_2$ catalyst through electrodeposition

The electrodeposition of Cu_2Se/$CoSe_2$ on Cuf was performed on freshly prepared Cuf electrode in a three-electrode cell (schematically illustrated in Figure 5.1a) at a constant potential of -0.7 V (vs Ag/AgCl, 3 M KCl) using the chronoamperometry technique (Figure 5.1b). The deposition was carried out at different time (30, 45, 60 and 90 minutes) in order to achieve the best catalytic performance, where the sample prepared at 60 min was found to deliver better electrocatalytic activity. The deposition was carried out in a solution containing 15 mM $CoCl_2.6H_2O$, 10 mM SeO_2 and 60 mM KCl. After the electrodeposition, the as-synthesized Cuf@Cu_2Se/$CoSe_2$ electrode turned into black from brown, as shown in the digital image depicted in Figure 5.1c. The as prepared Cuf@Cu_2Se/$CoSe_2$ catalyst was washed with Millipore water and kept under vacuum when not in use to avoid the aerial oxidation. The reduction process of Co, Cu and Se were investigated using cyclic voltammetry technique to reveal the electrodeposition behaviour of Cu_2Se and $CoSe_2$ on Cuf, which is elaborately discussed in the later section.

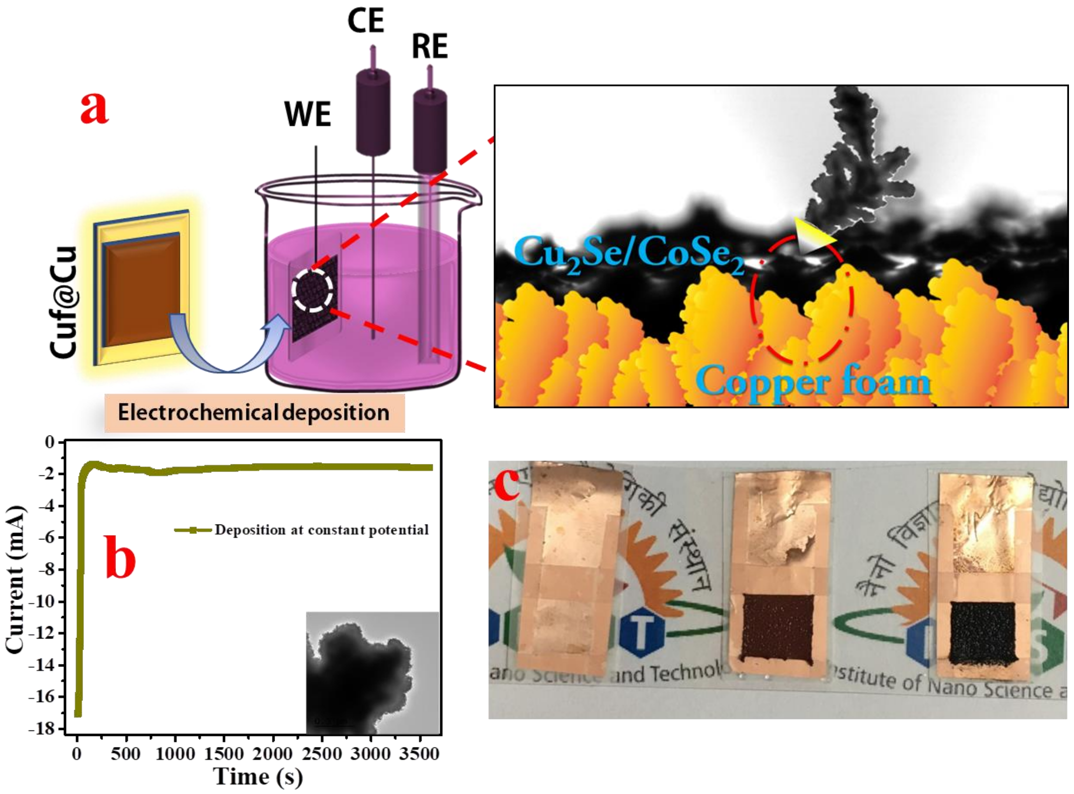

Figure 5.1. *(a) Schematic illustration for the synthesis of Cuf@$Cu_2Se/CoSe_2$ (b) Electrochemical deposition done via chronoamperometery technique. (c) Digital images for Cu foil, bare Cuf synthesized from Cu foil and electrodeposited Cuf@$Cu_2Se/CoSe_2$.*

5.2.3 Electrochemical measurements

The electrochemical performances of the catalyst were carried out in a three-electrode system using Cuf@$Cu_2Se/CoSe_2$ as a working electrode, Hg/Hg_2SO_4 (saturated K_2SO_4) as the reference electrode and graphite rod as the counter electrode in 1 M KOH solution under ambient atmosphere. To compare the activity of as synthesized Cuf@$Cu_2Se/CoSe_2$ electrode, the electrodeposition was done using the same reaction conditions at different substrates like copper foil (Cu foil) and Ni foam (Nif). The potential scan was scaled and calibrated to reversible hydrogen electrode (RHE) based on the formula given below:

$E_{\mathrm{RHE}} = (E_{\mathrm{Hg/Hg2SO4\ (saturated)}} + 0.65 + 0.0591\ \mathrm{pH})$ V.

To rationalize the ohmic drop imparted on the catalyst, the polarisation curves were iR corrected with 50% compensation (unless mentioned otherwise). There were no iR drop compensation done during the electrochemical study carried out with two-electrode system. The electrochemical activity for HER and OER were accomplished with the help of linear sweep voltammetry (LSV) technique at a scan rate of 10 mVs^{-1}, (while for Tafel slope analysis, the scan rate was 1 mVs^{-1}). The surface of the electrode was electrochemically activated for at least 25 cyclic voltammetry (CV) scan. The geometrical surface area of the electrode was used to calculate the current density for normalization. To check the stability, durability and mechanical robustness of the catalyst, chronopotentiometry (CP)/step CP measurements were performed without i*R* compensation. The electrochemical impedance spectroscopy (EIS) for two electrode system were conducted at a potential of 1.5 V with a frequency range of 10^5–10^{-2} Hz.

5.3 Results and discussion

5.3.1 Electrochemical deposition mechanism of hybrid electrocatalyst Cuf@$Cu_2Se/CoSe_2$

In this study, the electrodeposition of hybrid catalyst Cuf@$Cu_2Se/CoSe_2$ was performed at a potential of -0.7 V (vs Ag/AgCl) for 60 min by using chronoamperometry technique. The possible formation mechanism of Cuf@$Cu_2Se/CoSe_2$ catalyst using electrodeposition technique was further investigated using Cyclic voltammetry (CV) studies. Figure 5.2a depicts the CV profile of the electrodeposited $Cu_2Se/CoSe_2$ material at a scan rate of 10 mV/s where a sharp oxidation peak (I_a) appeared at a potential of 0.73 V *vs* Ag/AgCl, which is ascribed for the formation of $CoSe_2$.[31,32] A pair of peaks (II_a &II_c) were also observed at 0.42 V (anodic) and -0.68 V (cathodic), respectively. To the identification of these peaks, the CV profile was examined after the electrodeposition was carried out in the electrolytic solution containing only SeO_2 (in absence of Co^{2+}) as shown in Figure 5.2b. As observed

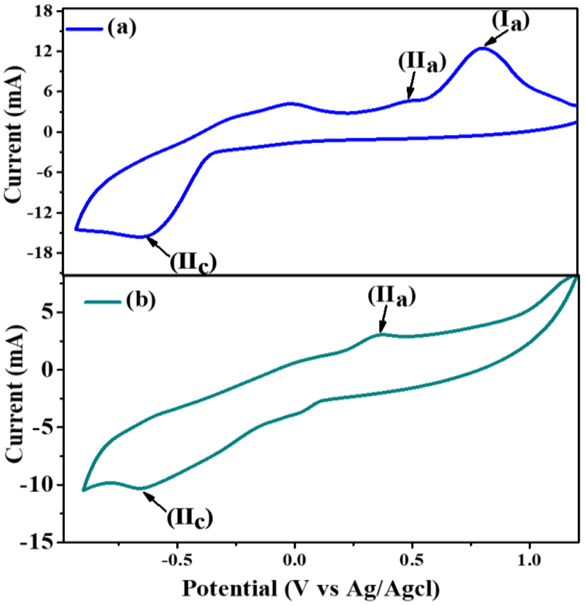

Figure 5.2 *Cyclic voltammetry after electrochemical deposition (a) CV curve taken after chrono deposition in presence of SeO_2 and $CoCl_2$ in electrolytic solution (b) CV curve taken after chrono deposition in presence of SeO_2 in electrolytic solution.*

from the CV curve, a pair of peaks (cathodic and anodic) at similar positions appeared, which was identified for the formation of Cu_2Se.[32]

The electrodeposition process is comprised of the following multistep reactions (equation 5.1-5.6).

$$SeO_2 + H_2O \rightarrow H_2SeO_3 \tag{5.1}$$

$$H_2SeO_3 + 4H^+ \; 4e^- \rightarrow Se(s) + 3H_2O \tag{5.2}$$

$$2Se(s) + 2e^- \rightarrow Se_2^{2-} \tag{5.3}$$

$$Se_2^{2-} + 2e^- \rightarrow 2Se^{2-} \tag{5.4}$$

$$Co^{2+} + Se_2^{2-} \rightarrow CoSe_2(s) \tag{5.5}$$

$$2Cu + Se^{2-} - 2e^- \rightarrow Cu_2Se(s) \tag{5.6}$$

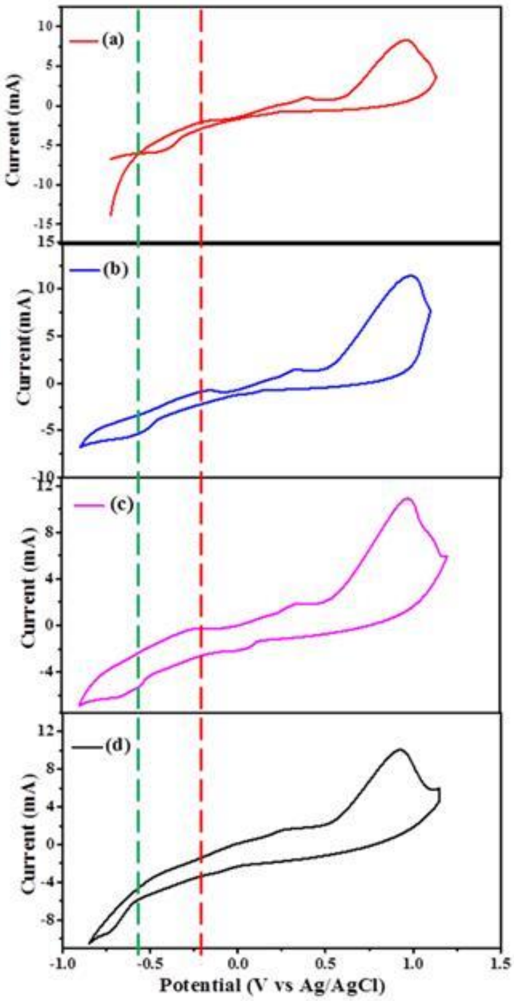

Figure 5.3. *Cyclic voltammetry curve of Cuf@Cu_2Se/$CoSe_2$ through CV cycling at 10mV/s scan rate: (a) 1st cycle, (b) 3rd cycle, (c) 25th cycle (d) CV curve after completion of deposition in fresh electrolyte*

In the first step, SeO_2 got hydrolysed to form H_2SeO_3, which is further reduced to Se, followed by the reduction of Se to Se_2^{2-} and subsequently Se^{2-}. The Co^{2+} from the electrolyte solution reacted with the *in situ* generated Se_2^{2-} and deposited on the Cuf surface as $CoSe_2$. Besides this, copper from the surface of the Cuf simultaneously reacted with Se^{2-} during the electrodeposition process to form Cu_2Se. The CV techniques were further used for the investigation of the reaction pathway and identified the intermediates. CV cycling was performed at a scan rate of 10 mV/s and step-wise segments have been plotted in Figure 5.3 (a-d). From eq. 1-4, it can be seen that the SeO_2 converted to Se^{2-} followed by multistep reactions, which was confirmed from the appearance of the reduction peak at -0.57 V and another small anodic peak appeared at -0.27 V, which is identified for the presence of SeO_3^{2-} as shown in Figure 5.3 (a-c).[33,34] Eventually, the peaks corresponding to the Se^{2-} and SeO_3^{2-} disappeared eventually after completion of CV cycling (Figure 5.3d). Therefore, the above discussion infers that the hybrid electrocatalyst Cuf@$Cu_2Se/CoSe_2$ was synthesized electrochemically via the process as discussed above, which was further used for other characterizations.

5.3.2 Morphological and structural analysis

The physical characterization techniques were adopted to investigate the structural and morphological details of the deposited layer of Cu_2Se and $CoSe_2$ on Cuf surface. Figure 5.4a is the schematic illustration of the catalyst reflecting its main highlights. The XRD profile revealed the existence of Cu, Cu_2Se and $CoSe_2$. As can be seen from Figure 5.4b, it displays three peaks for Cuf with cubic lattice in the 2θ range at 43.19°, 50.3° and 73.89° ascribed to (111), (200) and (220) planes, respectively (JCPDS PDF 01-070-3038). The peak position of Cu_2Se was found to be at 2θ of 25.35° (400) and 42.74° (541) (JCPDS PDF-00-058-0228). The lattice structure is found to be monoclinic for Cu_2Se. The peaks for $CoSe_2$ were found to be at a 2θ value of 29.28° (011), 36.46° (120), 50.7° (022), 61.90° (230) and 73.89° (132) having an orthorhombic crystal lattice (JCPDS card number PDF-00-004-0836) structure. The morphological and structural features of the catalyst were performed through field emission scanning electron microscopy (FESEM) and transmission electron microscopy (TEM) characterizations. The copper dendrites, which after the electrodeposition transformed into a wrinkled surface due to the deposition of a thin layer of $Cu_2Se/CoSe_2$ on Cuf as shown from FESEM images reflected in Figure 5.4c-d. The TEM images (Figure 5.4e-f) disclose a deposited layer on the surface of the Cuf. As clearly visible from the intensity contrast of the TEM images, the catalyst has different intensities layered structure.

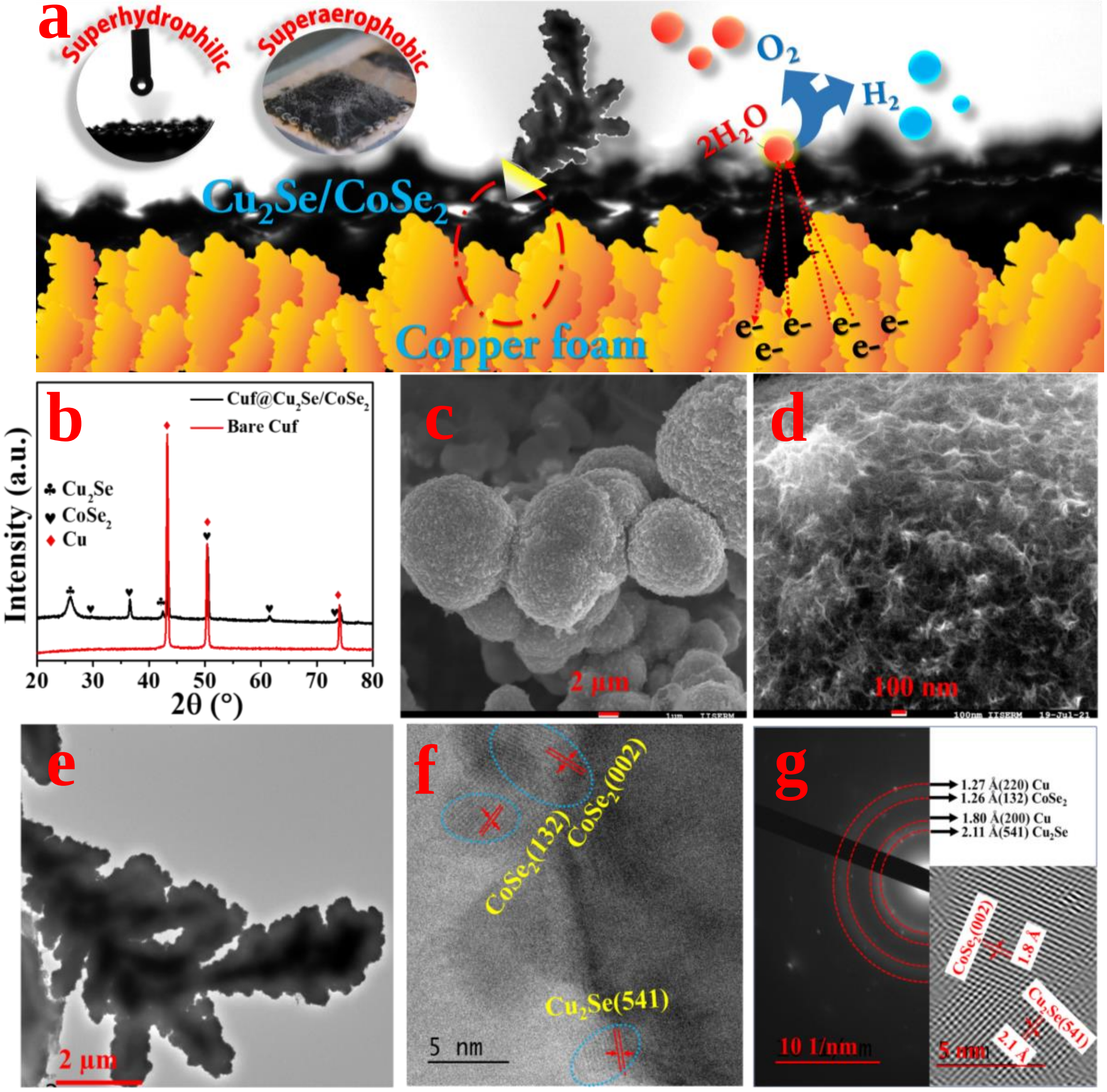

Figure 5.4. *(a) Schematic illustration of Cuf@$Cu_2Se/CoSe_2$ as bifunctional electrocatalysis (b) XRD pattern of Cuf@$Cu_2Se/CoSe_2$ compared with Cuf. Field emission scanning electron micrograph (FESEM) of Cuf@$Cu_2Se/CoSe_2$ at (c) 2 µm and (d) 100 nm (e) Transmission electron microscopy (TEM) of Cuf@$Cu_2Se/CoSe_2$ showing electrodeposited dendrites of Cuf. (f) TEM image showing thin layer of electrodeposited material with fringes. (g) SAED pattern related with the planes and HRTEM fringe width shown from Invert FFT (lower right).*

The intensity difference of the image arises due to the presence of different transmission dependencies that occurred from different atomic layers present in it, which indicate that a thin layer has been electrodeposited onto the surface of Cuf. A well-defined dendritic pathway and a porous network of Cuf@$Cu_2Se/CoSe_2$ were formed, which boosts up the ionic-diffusion and results in the enhancement of the charge transfer and mobility of the electron. The selected area electron diffraction (SAED) pattern, as well as the high-resolution TEM (HRTEM) images, (Figure 5.4g) were taken for the confirmation of the

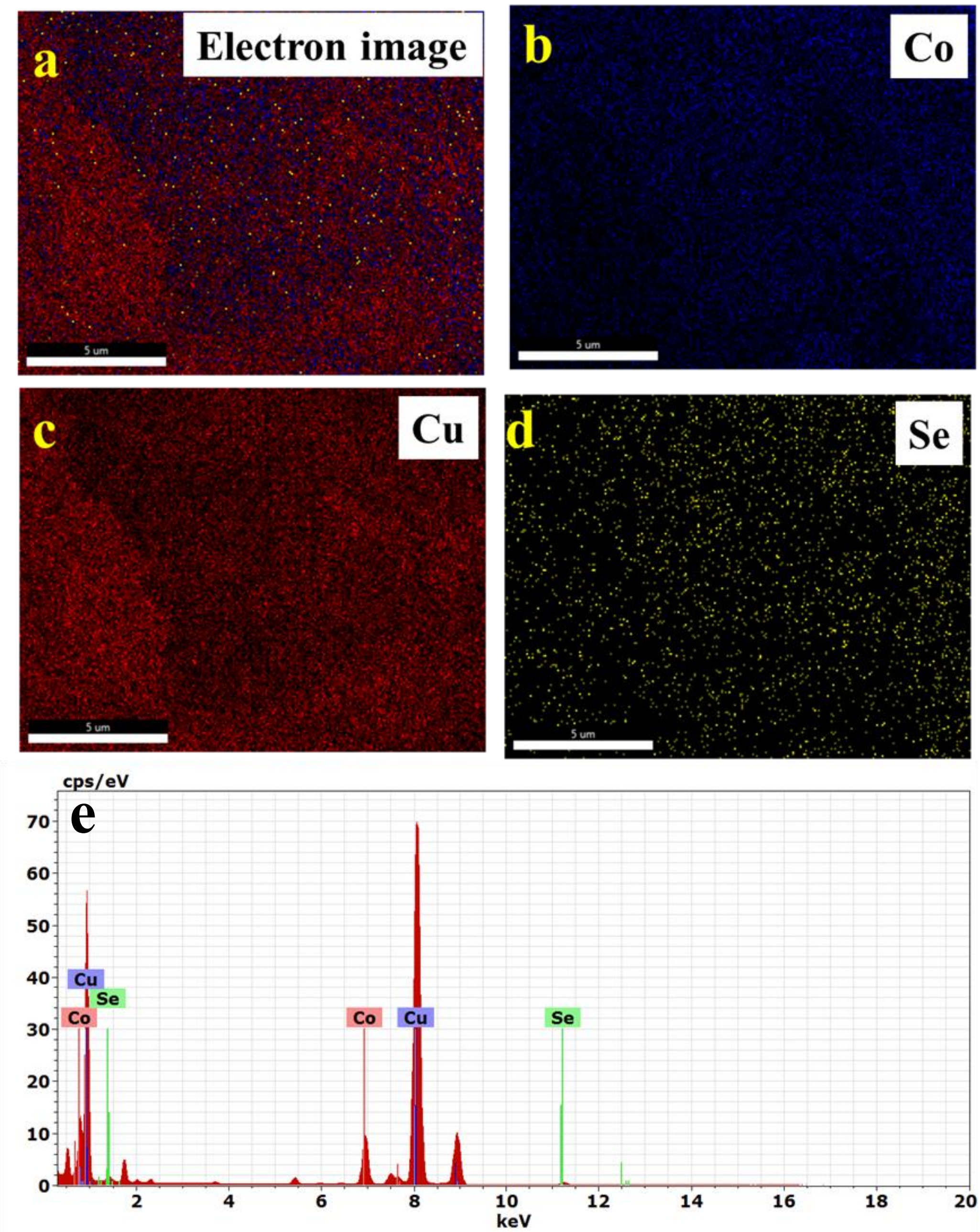

Figure 5.5. *Elemental mapping of Cuf@$Cu_2Se/CoSe_2$ with (a) cumulative electron image (b) Cobalt (c) Copper (d) Selenium (e) Corresponding EDAX data of Cuf@$Cu_2Se/CoSe_2$ showing the presence of Co, Cu and Se in the sample.*

phase formation of the catalyst. This result confirmed that the planes found through the HRTEM micrographs were well accorded with the XRD data, where the d-spacing was found to be 1.27Å (220), 1.8 Å (200) for Cu, 1.26 Å (132) for $CoSe_2$ and 2.11 Å (541) for

Cu_2Se. This resemblance of the XRD and SAED pattern further confirms the formation of Cu_2Se and $CoSe_2$ hybrid catalyst on Cuf substrate. The energy-dispersive X-ray spectroscopy (EDX) profile and corresponding elemental mapping of the sample (Figure 5.5 a-e) shows the well distribution of Cu, Co and Se in the sample. For the analysis of chemical composition and the valance states of Cuf@Cu_2Se/$CoSe_2$ catalyst, X-ray photon spectroscopy (XPS) was employed on the surface of the sample. It is well understood that the water splitting (HER and OER) is very much dependent to the chemical states and coordination environment.[35,36] In Figure 5.6a, the XPS data disclose the binding energies of Co2$p_{3/2}$ and Co2$p_{1/2}$, present at 781.0 eV and 797.5 eV, which is attributed to oxidized Co species of $CoSe_2$ present in Cuf@Cu_2Se/$CoSe_2$ electrocatalyst.[37,38] The peak located at 778.9 eV, 783.2 eV and 794.3 eV indicates the presence of Co^{+2} species of $CoSe_2$.[16,33] Satellite peaks 785.0 eV and 801.1 eV corresponds to the antibonding orbital of $CoSe_2$ present in the catalyst. Figure 5.6b denotes the binding energy spectra of Cu2$p_{3/2}$ and Cu2$p_{1/2}$ at 934.7 eV and 953.2 eV, respectively, which corresponds to oxidized Cu of Cu_2Se.[30,39] As can be seen from energy spectra of Se in Figure 5.6c, the binding energy with Se 3d spin of Se 3$d_{5/2}$ and 3$d_{3/2}$ are centred at around 55 eV. These peaks were divided into two separate oxidation states of Se species, preciously, Se(-2) for the peak present at 54.4 eV and 55.5 eV and Se(-1) for the peak at 56.4 eV and 57.5 eV. The peak of Se(-2) originated from Cu_2Se phase while Se(-1) from $CoSe_2$ phase. The peak around 63.2 eV gives the evidence of SeO_x species, which might arises due to the surface oxidation of selenide species present in the sample[40,41]

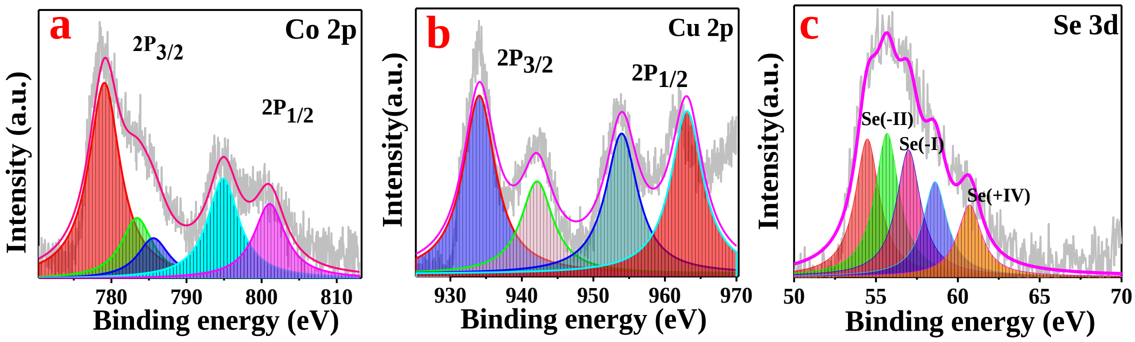

Figure 5.6. *High resolution XPS spectra of (a) Co 2P (b) Cu 2P (c) Se 3d*

5.3.4 Electrochemical characterization

Electrochemical studies have been conducted to evaluate the bifunctional activity of the catalysts in a three-electrode system using Cuf@$Cu_2Se/CoSe_2$ and other control samples as a working electrode in 1 M KOH electrolyte solution. For comparison, cobalt selenide was electrochemically deposited on Ni foam (CoSe/Nif) and copper foil (CoSe/Cu foil) under the same conditions to check the role of substrate in catalysis. The activity of bare Cuf was also studied for comparison purposes. To check the performances of the as-prepared catalyst to benchmark catalyst, Pt/C and RuO_2 were also modified to the electrode surface and studied the electrochemical responses. Polarisation curves as depicted in Figure 5.7a shows the activity of the catalyst Cuf@$Cu_2Se/CoSe_2$ in the hydrogen evolution region in terms of onset (E_{onset}), overpotential (E_{η}) as well as current density as compared with the other control samples. The overpotential of the catalysts was determined from the LSV curve at a scan rate of 10 mVs^{-1}. To normalize the intrinsic behaviour of the catalysts occurring due to ohmic resistance, an i*R* compensation was applied in all the primary data.[42]

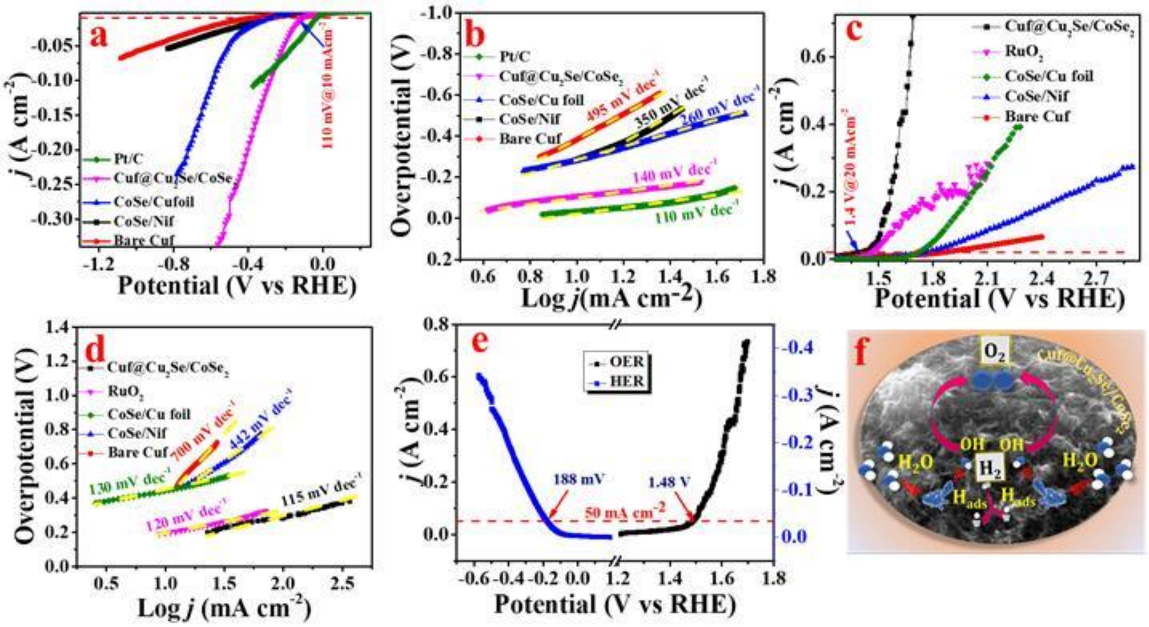

Figure 5.7. *(a) HER activity of Cuf@$Cu_2Se/CoSe_2$ compared with different control samples (b) Corresponding Tafel slope of HER activity of Cuf@$Cu_2Se/CoSe_2$ catalyst (c) OER activity of Cuf@$Cu_2Se/CoSe_2$ compared with different control samples (d) Corresponding Tafel slope of OER activity of Cuf@$Cu_2Se/CoSe_2$ catalyst (e) Bifunctional activity of Cuf@$Cu_2Se/CoSe_2$ catalyst taken in a three-electrode system in 1 M KOH at a scan rate of 10 mVs^{-1} (f) Schematic illustration for the pathways for the bifunctional activity.*

The Cuf@$Cu_2Se/CoSe_2$ catalyst showed significantly improved activity with an onset value of only 36 mV and needed only 110 mV (± 3 mV based on the individual scan of 4 independent samples) of the overpotential to drive a current density of 10 mA cm^{-2}.

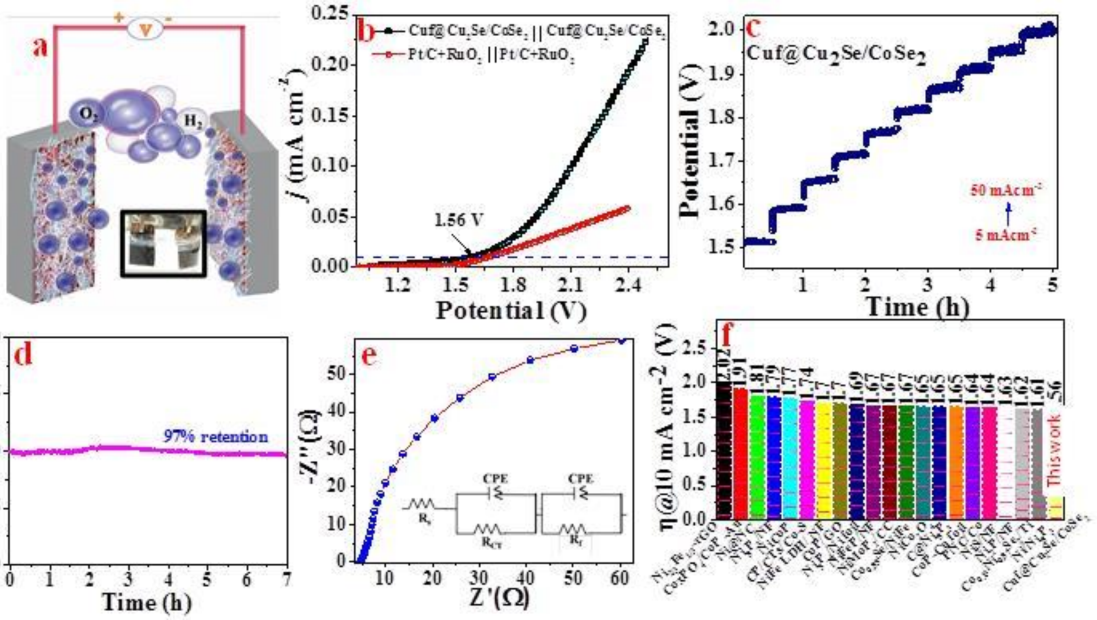

Figure 5.8. *(a) Schematic illustration for the Cuf@$Cu_2Se/CoSe_2$ catalyst in a two-electrode system (b) Polarisation curve of Cuf@$Cu_2Se/CoSe_2$ compared with Pt/C and RuO_2 in a two electrode system (c) Chronopotentiometry (CP) current ramping of Cuf@$Cu_2Se/CoSe_2$ at different current density ranging from 2 mA cm^{-2} (d) CP plot of Cuf@$Cu_2Se/CoSe_2$ in a two electrode system at a current density of 10mA cm^{-2} (e) EIS analysis and Nyquist plot with fitted circuit in inset (f) Comparison bar diagram of recently reported catalyst with Cuf@$Cu_2Se/CoSe_2$ in terms of overpotential in a two electrode system.*

It has been observed that at higher current density of 100 mA cm^{-2} the catalyst Cuf@$Cu_2Se/CoSe_2$ ($E_{\eta@100\ mAcm^{-2}}$=278 mV) outperforms the activity of Pt/C ($E_{\eta@100\ mAcm^{-2}}$=347 mV). The activity was found to be better than all the control samples namely, CoSe/Cu foil (E_{onset}=166 mV, $E_{\eta@10\ mAcm-2}$=280 mV), CoSe/Nif (E_{onset}=151 mV, $E_{\eta@10\ mAcm-2}$=305 mV) and bare Cuf (E_{onset}=226 mV, $E_{\eta@10\ mAcm-2}$=379 mV). The comparison of the HER overpotentials of Cuf@$Cu_2Se/CoSe_2$ with the control catalyst at different current density is summarized in Table 5.1. Figure 5.7b depicts the Tafel slope plot (overpotential(η) vs log(j)) to access the HER kinetics, extracted from the voltammetry curve taken at a scan rate of 1 mVs^{-1}.

The Tafel slope of the as synthesized catalyst was found to be 140 mV dec^{-1}, which is comparable to Pt/C (110 mV dec^{-1}) and lower than that of CoSe/Cu foil (260 mV dec^{-1}), CoSe/Nif (350 mV dec^{-1}) and bare Cuf (495 mV dec^{-1}), indicating faster kinetics of hydrogen evolution reaction of the catalyst.[43]

Table 5.1. Overpotentials for HER of Cuf@$Cu_2Se/CoSe_2$ catalyst with comparison samples

HER	**Catalyst**	**η@Onset**	**η@10mAcm^{-2}**	**η@20mAcm^{-2}**	**η@50mAcm^{-2}**	**η@100mAcm^{-2}**
	Pt/C	27 m V	33 mV	66 mV	149 mV	347 mV
	Cuf@$Cu_2Se/CoSe_2$	**36 mV**	**110 mV**	**146 mV**	**188 mV**	**278 mV**
	CoSe/Cu foil	166 mV	280 mV	375 mV	508 mV	586 mV
	CuSe/Nif	151 mV	305 mV	429 mV	787 mV	-
	Bare Cuf	226 mV	397 mV	576 mV	890 mV	-

The electrocatalytic activity of Cuf@$Cu_2Se/CoSe_2$ catalyst towards OER was also examined at a scan rate of 10 mVs^{-1} in 1 M KOH solution as shown in Figure 5.7c. The LSV of Cuf@$Cu_2Se/CoSe_2$ along with other control samples i.e., CoSe/Cu foil, CoSe/Nif as well as bare Cuf and RuO_2 catalyst was evaluated. The OER overpotential of all the as prepared catalysts at different current densities are listed in Table 5.2. Interestingly, the OER activity of the catalyst Cuf@$Cu_2Se/CoSe_2$ with potential of only 1.4 V (E_{onset}=1.36 V) was superior to the state-of-the-art catalyst RuO_2, which needed a potential of 1.46 V (E_{onset}=1.35 V) to attain a current density of 20 mA cm^{-2}, respectively. The activity of Cuf@$Cu_2Se/CoSe_2$ was found to be far better than CoSe/Cu foil (E_{onset}=1.63 V, $E_{@20\ mAcm-2}$=1.71 V), CoSe/Nif (E_{onset}=1.67 V, $E_{@20\ mAcm-2}$=1.75 V) and bare Cuf (E_{onset}=1.79 V, $E_{@20\ mAcm-2}$=1.86 V). The Tafel slope of Cuf@$Cu_2Se/CoSe_2$ (Figure 5.7d) is found to be 115 mVdec^{-1}, which is lesser than all other samples i.e., RuO_2 (120 mVdec^{-1}), CoSe/Cu foil (130 mVdec^{-1}), CoSe/Nif (442 mVdec^{-1}) and bare Cuf (700 mVdec^{-1}), indicates the catalyst has faster kinetics and rapid evolution rate of oxygen. Figure 5.7e shows the bifunctional activity of Cuf@$Cu_2Se/CoSe_2$ sample that dictates the efficient activity of HER (188 mV@50 mAcm^{-2}) and OER (250 mV@50 mAcm^{-2}) in a three-electrode system. The hydrogen adsorption and possible pathways for H_2 and O_2 generation on the catalyst surface is schematically illustrated in Figure 5.7f. The excellent electrochemical activity of the catalyst may arise due to the strong electronic coupling that might have taking place between Cu_2Se and $CoSe_2$ with Cuf which is accelerating the catalyst to perform even better than the benchmark RuO_2 and found comparable to Pt/C in terms of water splitting activity.[44,45]

Table 5.2. Overpotentials for OER of Cuf@$Cu_2Se/CoSe_2$ catalyst with comparison samples

OER	**Catalyst**	**η@Onset**	**η@20mAcm^{-2}**	**η@50mAcm^{-2}**	**η@100mAcm^{-2}**
	RuO_2	120 mV	230 mV	290 mV	360 mV
	Cuf@$Cu_2Se/CoSe_2$	**130 mV**	**170 mV**	**260 mV**	**280 mV**
	CoSe/Cu foil	400 mV	480 mV	560 mV	650 mV
	CuSe/Nif	440 mV	520 mV	630 mV	880 mV
	Bare Cuf	560 mV	630 mV	970 mV	-

To explore further the bifunctional activity of Cuf@$Cu_2Se/CoSe_2$, as schematically represented in Figure 5.8a, the catalyst was subjected to electrolysis in 1 M KOH using a two-electrode system. As shown in Figure 5.8b, the overall water splitting electrolyzer attended a potential of 1.56 V at 10 mA cm^{-2}, which is 100 mV less than Pt/C (+) and RuO_2 (-) assembled electrolysis cell and even have a higher current density. The Cuf@$Cu_2Se/CoSe_2$ catalyst was compared with the recently reported Co and Cu based catalyst as listed in Table 5.3 and found that the catalyst displays up-performed water splitting catalyst than the majority of reported literature. The current ramping stability study was performed through multistep chronopotentiometry (CP) technique to check the mechanical robustness of the catalyst, which is regarded as a critical requirement of the catalyst for commercialisation. It can be seen from Figure 5.8c, the catalyst was subjected to gradually increasing current densities ranging from 5 mA cm^{-2} to 50 mA cm^{-2} with a difference of 5 mA cm^{-2} having a hold time of 1800 s for each step and a total duration of 5 h. It was confirmed from the plot that a stepwise increase in the current density even up to 50 mA cm^{-2} does not lead to the degradation of the potential, exhibiting the catalyst is mechanically very stable. The long-term durability is a critical benchmark parameter for a catalyst that was studied from CP measurements (Figure 5.8d). The CP test was performed at a current density of 10 mAcm^{-2} and found that 97% retention of the initial potential even after 7 h test demonstrates the adequate durability of the catalyst.

Table 5.3. HER, OER and Full water splitting (2-electrode system) overpotential comparison table based on Co and Cu based catalyst.

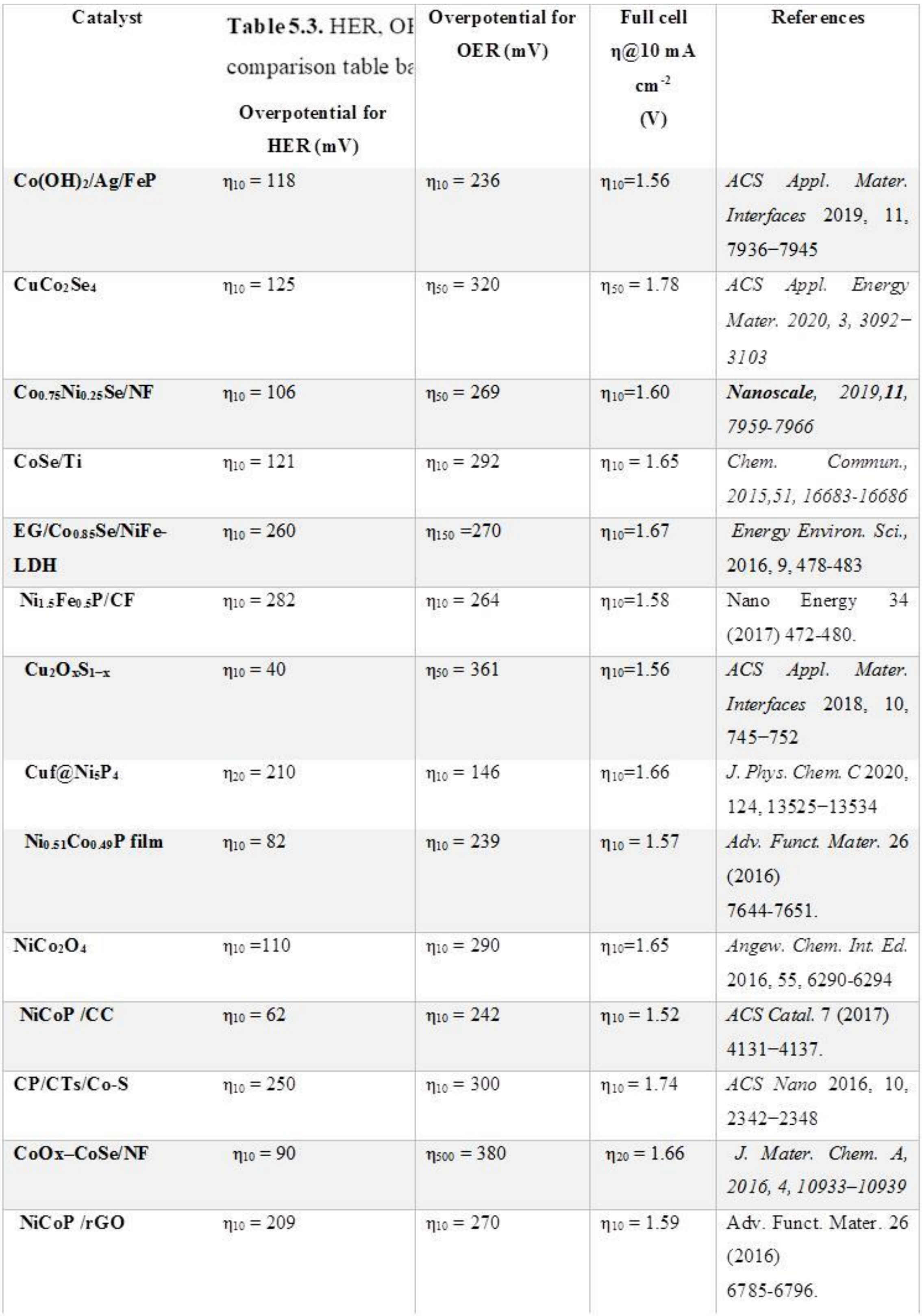

Catalyst	Table 5.3. HER, OI comparison table ba Overpotential for HER (mV)	Overpotential for OER (mV)	Full cell η@10 mA cm^{-2} (V)	References
$Co(OH)_2/Ag/FeP$	$\eta_{10} = 118$	$\eta_{10} = 236$	$\eta_{10}=1.56$	*ACS Appl. Mater. Interfaces* 2019, 11, 7936−7945
$CuCo_2Se_4$	$\eta_{10} = 125$	$\eta_{50} = 320$	$\eta_{50} = 1.78$	*ACS Appl. Energy Mater. 2020, 3, 3092−3103*
$Co_{0.75}Ni_{0.25}Se/NF$	$\eta_{10} = 106$	$\eta_{50} = 269$	$\eta_{10}=1.60$	***Nanoscale,** 2019,**11**, 7959-7966*
CoSe/Ti	$\eta_{10} = 121$	$\eta_{10} = 292$	$\eta_{10} = 1.65$	*Chem. Commun., 2015,51, 16683-16686*
$EG/Co_{0.85}Se/NiFe$-LDH	$\eta_{10} = 260$	$\eta_{150} = 270$	$\eta_{10}=1.67$	*Energy Environ. Sci.,* 2016, 9, 478-483
$Ni_{1.5}Fe_{0.5}P/CF$	$\eta_{10} = 282$	$\eta_{10} = 264$	$\eta_{10}=1.58$	Nano Energy 34 (2017) 472-480.
$Cu_2O_xS_{1-x}$	$\eta_{10} = 40$	$\eta_{50} = 361$	$\eta_{10}=1.56$	*ACS Appl. Mater. Interfaces* 2018, 10, 745−752
$Cuf@Ni_5P_4$	$\eta_{20} = 210$	$\eta_{10} = 146$	$\eta_{10}=1.66$	*J. Phys. Chem. C* 2020, 124, 13525−13534
$Ni_{0.51}Co_{0.49}P$ film	$\eta_{10} = 82$	$\eta_{10} = 239$	$\eta_{10} = 1.57$	*Adv. Funct. Mater.* 26 (2016) 7644-7651.
$NiCo_2O_4$	$\eta_{10} =110$	$\eta_{10} = 290$	$\eta_{10}=1.65$	*Angew. Chem. Int. Ed.* 2016, 55, 6290-6294
NiCoP /CC	$\eta_{10} = 62$	$\eta_{10} = 242$	$\eta_{10} = 1.52$	*ACS Catal.* 7 (2017) 4131−4137.
CP/CTs/Co-S	$\eta_{10} = 250$	$\eta_{10} = 300$	$\eta_{10}= 1.74$	*ACS Nano* 2016, 10, 2342−2348
CoOx–CoSe/NF	$\eta_{10} = 90$	$\eta_{500} = 380$	$\eta_{20} = 1.66$	*J. Mater. Chem. A, 2016, 4, 10933–10939*
NiCoP /rGO	$\eta_{10} = 209$	$\eta_{10} = 270$	$\eta_{10} = 1.59$	Adv. Funct. Mater. 26 (2016) 6785-6796.

To further understand the worthy electrochemical performances of Cuf@$Cu_2Se/CoSe_2$ catalyst, electrochemical impedance spectroscopy (EIS) was recorded and analysed to estimate the internal as well as charge transfer resistance at electrode-electrolyte interface. The Nyquist plot of the catalyst as shown in Figure 5.8e was obtained at a potential of 1.5 V. The fitted Nyquist plot revealed that the catalyst Cuf@$Cu_2Se/CoSe_2$ have very low resistance (R_s) of 4.5 Ω from the electrolyte. The charge transfer resistance (R_{ct}) of the catalyst was calculated to be 45.4 Ω. The smaller value of R_s and R_{ct} confirmed that the very less resistance of catalyst-electrolyte interface leading to the faster kinetics of electrocatalysis reactions. Figure 5.8f shows the bar diagram for Cuf@$Cu_2Se/CoSe_2$ catalyst compared with the recently reported catalyst towards water splitting and it is found that the performance of the Cuf@$Cu_2Se/CoSe_2$ catalyst is superior to the others. The electrochemically active surface area (ECSA) directly affects the roughness factor (RF) of the catalyst. The Cuf is known as a highly porous material that could offer high surface area. Therefore, to check the ECSA and RF of the catalyst, the CV scan was taken in non-faradic region (0 to 0.1 V) at different scan rates as shown in Figure 5.9a. Figure 5.9b depicted the slope taken from the plot of scan rate versus the average of anodic and cathodic peak current. Using the double layer capacitance (C_{dl}=143 mF), the ECSA was calculated to be 529 cm^2 which is very high as compared to recently reported values.[16,46,47]

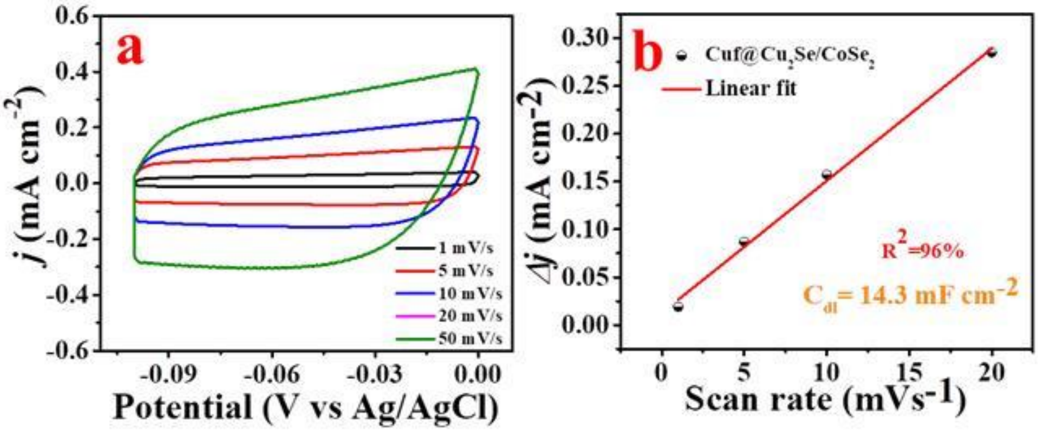

Figure 5.9. *(a) Cyclic voltammetry of Cuf@$Cu_2Se/CoSe_2$ at different scan rates in non-faradic region for the calculation of electrochemically active surface area (ECSA). (b) Linear slope of Cuf@$Cu_2Se/CoSe_2$ with respect to current density and scan rate extracted from CV taken at different scan rate in a non-faradaic region.*

Electrochemical evolution rate of H_2 and O_2 and their respective Faradaic efficiency (FE) were measured using water-gas displacement method.[48,49] Cuf@$Cu_2Se/CoSe_2$ electrocatalyst were utilized as both cathode and anode in a two-electrode system emersed in 1 M KOH electrolytic solution assembled in a Hofmann voltammeter as shown in Figure 5.10a. A chronoamperometry scan were taken at a potential of 1.6 V for certain duration and the corresponding water-gas displacement were recorded. The collection of H_2 and O_2 were done separately along with recording the displaced volume at a particular time with acquired charge. During the whole time of chronoamperometry the level of the displaced H_2 and O_2 were maintained at 2:1 ratio. As shown in Figure 5.10b, the faradic efficiency of the electrode was found to be 99.9%. The generated H_2 were injected into the column of gas chromatography (GC) in order to check the purity of the produced fuel. As shown in the Figure 5.10c, upon the injection of 20 μL of H_2, the GC response showed the presence of H_2 peak at 1.76 min. No other gaseous peak as an impurity were witnessed other the peaks of instrumental argon (Ar) and nitrogen (N_2). The injection of 20 μL of H_2 yields 7113.266 ppm of H_2, which is an admirable amount. This yield amount and the high purity of the produced H_2 can be efficiently used commercially at industrial purposes in the application like fuel cell, H_2 generation etc.

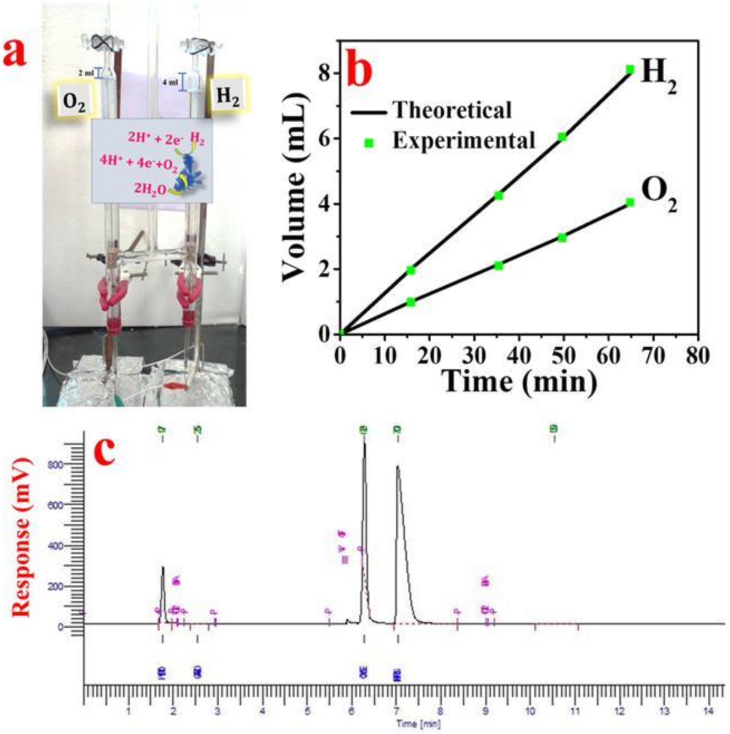

Figure 5.10. *(a) Water-gas displacement setup using electrodes Cuf@$Cu_2Se/CoSe_2$ (cathode and anode) emerged in 1 M KOH in a Hofmann voltameter using chronopotentiometery technique. (b) Faradic efficiency calculation of H_2 and O_2 produced during electrolysis. (c) Gas chromatography response upon the injection of 20 µl of H_2showing no gas impurity other that instrumental nitrogen and argon.*

5.3.5 Catalyst surface property

The catalytic performance of the catalyst is usually hampered by the generation of bubbles on the suface of the catalyst during electrolysis. The stacked bubbles on the surface block the diffusion of the electrolyte, which as a result decreases the ECSA of the electrocatalyst. Also, the catalyst should make proper contact with the electrolyte to decrease the resistance between the electrolyte and electrode interface. Therefore, a good electrocatalyst for water electrolysis must have aerophobic as well as hydrophilic properties for better activity.[50,51] Interestingly, the Cuf@$Cu_2Se/CoSe_2$ catalyst was found to have both the effects of superaerophobicity as well as superhydrophilicity. In detail, the wettability study of the catalyst was performed (Figure 5.11 a and b) by using a drop size analyser. After the suspension of the water drop on the surface of the electrocatalyst, the drop instantly got absorbed without making any contact angle (0 degree), which confirms the superhydrophilic behaviour of the catalyst. For aerophobicity analysis, the bubble behaviour was monitored during the CP run (Figure 5.11 c-f), which is schematically represented in Figure 5.11 g. It has been observed that almost no bubbles were left on the surface of the catalyst (few were trapped in the larger pores) after the CP

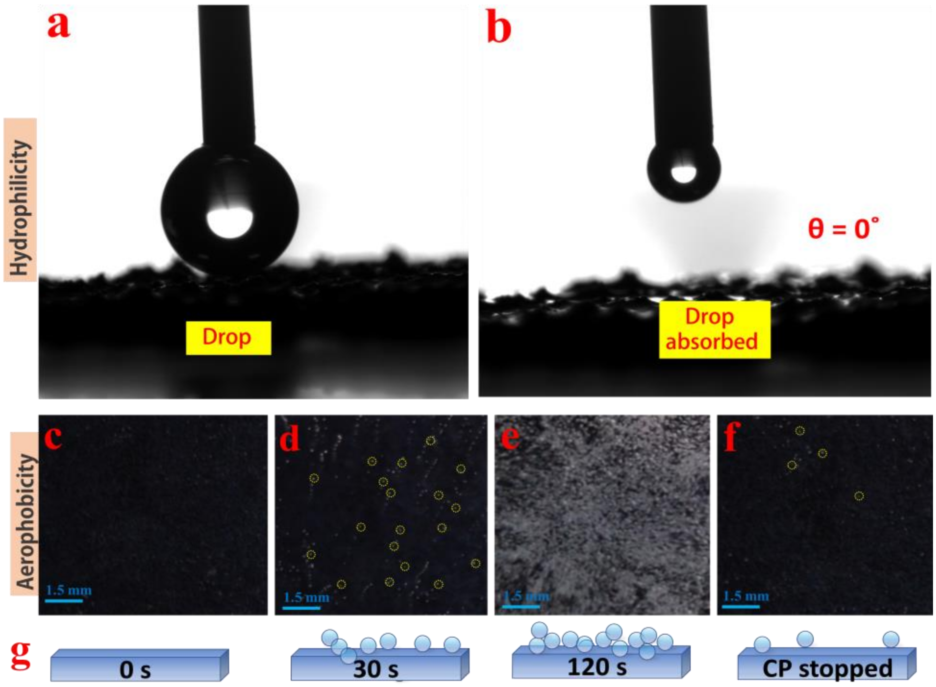

Figure 5.11. *Hydrophilicity analysis of Cuf@$Cu_2Se/CoSe_2$ (a) before and (b) after the drop absorbed on the surface (c-f) digital images illustrated schematically at bottom panel sdepicting the bubble behaviour on the surface of Cuf@$Cu_2Se/CoSe_2$ catalyst at different time during the run of CP, showing the excellent aerophobic surface of the catalyst.*

experiment stopped. This study demonstrated that the catalyst is superaerophobic in nature, which profoundly contributes to the excellent activity of the catalyst.

5.4 Conclusion

In summary, we have reported an electrochemical method for the synthesis of highly efficient electrocatalyst based on mixed transition metal selenides, Cu_2Se and $CoSe_2$ on the surface of the copper foam. The use of 3D hierarchically dendritic porous Cuf as a substrate leads to the designing of binder-free electrocatalyst, which benefits the overall performance of the catalyst. The mechanism for the deposition process was investigated using the CV technique. The physical characterizations of the catalyst were well correlated and analysed. The overpotential attained by the catalyst was found to be superior to the state-of-the-art RuO_2 for OER and comparable to Pt/C for HER. Further, after the assembly of the catalyst in a two-electrode system, the catalyst attained a potential as low as 1.56 V at a current density of 10 mA cm^{-2}, which is admirable as compared to other recently reported catalysts as well as Pt/C- RuO_2 systems. The multistep current ramping stability demonstrated that the catalyst is mechanically robust, which is favourable for commercialization. Further, the study of the surface property confirmed the superhydrophilic as well as aerophobic behaviour of the catalyst. Therefore, the catalyst is found to be highly efficient concerning electrochemical water splitting activity. This opens up the new door of fabrication of a non-noble metal-based catalyst for H_2 and O_2 generation.

5.5 References

(1) Gray, H. B. Powering the Planet with Solar Fuel. *Nat. Chem.* **2009**, *1* (1), 7. https://doi.org/10.1038/nchem.141.

(2) Lewis, N. S.; Nocera, D. G. Powering the Planet: Chemical Challenges in Solar Energy Utilization (Proceedings of the National Academy of Science of the United States of America (2006) 103, 43, (15729-15735) DOI:10.1073/Pnas.0603395103). *Proc. Natl. Acad. Sci. U. S. A.* **2007**, *104* (50), 20142. https://doi.org/10.1073/pnas.0710559104.

(3) Gong, M.; Zhou, W.; Tsai, M. C.; Zhou, J.; Guan, M.; Lin, M. C.; Zhang, B.; Hu, Y.; Wang, D. Y.; Yang, J.; Pennycook, S. J.; Hwang, B. J.; Dai, H. Nanoscale Nickel Oxide/Nickel Heterostructures for Active Hydrogen Evolution

Electrocatalysis. *Nat. Commun.* **2014**, *5*, 1–6. https://doi.org/10.1038/ncomms5695.

(4) Carim, A. I.; Saadi, F. H.; Soriaga, M. P.; Lewis, N. S. Electrocatalysis of the Hydrogen-Evolution Reaction by Electrodeposited Amorphous Cobalt Selenide Films. *J. Mater. Chem. A* **2014**, *2* (34), 13835–13839. https://doi.org/10.1039/c4ta02611j.

(5) Schuldiner, S.; Castellan, G. W.; Hoare, J. P. Electrochemical Behavior of the Palladium-Hydrogen System. I. Potential-Determining Mechanisms. *J. Chem. Phys.* **1958**, *28* (1), 16–19. https://doi.org/10.1063/1.1744059.

(6) Yang, J.; Wang, D.; Han, H.; Li, C. Roles of Cocatalysts in Photocatalysis and Photoelectrocatalysis. *Acc. Chem. Res.* **2013**, *46* (8), 1900–1909. https://doi.org/10.1021/ar300227e.

(7) Zeng, K.; Zhang, D. Recent Progress in Alkaline Water Electrolysis for Hydrogen Production and Applications. *Prog. Energy Combust. Sci.* **2010**, *36* (3), 307–326. https://doi.org/10.1016/j.pecs.2009.11.002.

(8) Bajdich, M.; García-Mota, M.; Vojvodic, A.; Nørskov, J. K.; Bell, A. T. Theoretical Investigation of the Activity of Cobalt Oxides for the Electrochemical Oxidation of Water. *J. Am. Chem. Soc.* **2013**, *135* (36), 13521–13530. https://doi.org/10.1021/ja405997s.

(9) Liang, Y.; Li, Y.; Wang, H.; Zhou, J.; Wang, J.; Regier, T.; Dai, H. Co3O4 Nanocrystals on Graphene as a Synergistic Catalyst for Oxygen Reduction Reaction. *Nat. Mater.* **2011**, *10* (10), 780–786. https://doi.org/10.1038/nmat3087.

(10) Ma, T. Y.; Dai, S.; Jaroniec, M.; Qiao, S. Z. Metal-Organic Framework Derived Hybrid Co3O4-Carbon Porous Nanowire Arrays as Reversible Oxygen Evolution Electrodes. *J. Am. Chem. Soc.* **2014**, *136* (39), 13925–13931. https://doi.org/10.1021/ja5082553.

(11) Kanan, M. W.; Nocera, D. G. In Situ Formation of an Oxygen-Evolving Catalyst in Neutral Water Containing Phosphate and Co2+. *Science (80-.).* **2008**, *321* (5892), 1072–1075. https://doi.org/10.1126/science.1162018.

(12) Tian, J.; Li, H.; Asiri, A. M.; Al-Youbi, A. O.; Sun, X. Photoassisted Preparation of Cobalt Phosphate/Graphene Oxide Composites: A Novel Oxygen-Evolving Catalyst with High Efficiency. *Small* **2013**, *9* (16), 2709–2714. https://doi.org/10.1002/smll.201203202.

(13) Liu, Y.; Cheng, H.; Lyu, M.; Fan, S.; Liu, Q.; Zhang, W.; Zhi, Y.; Wang, C.; Xiao,

C.; Wei, S.; Ye, B.; Xie, Y. Low Overpotential in Vacancy-Rich Ultrathin CoSe2 Nanosheets for Water Oxidation. *J. Am. Chem. Soc.* **2014**, *136* (44), 15670–15675. https://doi.org/10.1021/ja5085157.

(14) Zheng, Y. R.; Gao, M. R.; Gao, Q.; Li, H. H.; Xu, J.; Wu, Z. Y.; Yu, S. H. An Efficient CeO2/CoSe2 Nanobelt Composite for Electrochemical Water Oxidation. *Small* **2015**, *11* (2), 182–188. https://doi.org/10.1002/smll.201401423.

(15) Hou, Y.; Qiu, M.; Nam, G.; Kim, M. G.; Zhang, T.; Liu, K.; Zhuang, X.; Cho, J.; Yuan, C.; Feng, X. Integrated Hierarchical Cobalt Sulfide/Nickel Selenide Hybrid Nanosheets as an Efficient Three-Dimensional Electrode for Electrochemical and Photoelectrochemical Water Splitting. *Nano Lett.* **2017**, *17* (7), 4202–4209. https://doi.org/10.1021/acs.nanolett.7b01030.

(16) Cao, X.; Medvedeva, J. E.; Nath, M. Copper Cobalt Selenide as a High-Efficiency Bifunctional Electrocatalyst for Overall Water Splitting: Combined Experimental and Theoretical Study. *ACS Appl. Energy Mater.* **2020**, *3* (3), 3092–3103. https://doi.org/10.1021/acsaem.0c00262.

(17) Sun, Y. Y.; Jiang, M. Y.; Wu, L. K.; Hou, G. Y.; Tang, Y. P.; Liu, M. Ultra-Thin NiFeSe Nanosheets as a Highly Efficient Bifunctional Electrocatalyst for Overall Water Splitting. *Sustain. Energy Fuels* **2020**, *4* (2), 582–588. https://doi.org/10.1039/c9se00905a.

(18) Sun, Y.; Liu, C.; Grauer, D. C.; Yano, J.; Long, J. R.; Yang, P.; Chang, C. J. Electrodeposited Cobalt-Sulfide Catalyst for Electrochemical and Photoelectrochemical Hydrogen Generation from Water. *J. Am. Chem. Soc.* **2013**, *135* (47), 17699–17702. https://doi.org/10.1021/ja4094764.

(19) Paquin, F.; Rivnay, J.; Salleo, A.; Stingelin, N.; Silva, C. Multi-Phase Semicrystalline Microstructures Drive Exciton Dissociation in Neat Plastic Semiconductors. *J. Mater. Chem. C* **2015**, *3* (207890), 10715–10722. https://doi.org/10.1039/b000000x.

(20) Xu, Y. F.; Gao, M. R.; Zheng, Y. R.; Jiang, J.; Yu, S. H. Nickel/Nickel(II) Oxide Nanoparticles Anchored onto Cobalt(IV) Diselenide Nanobelts for the Electrochemical Production of Hydrogen. *Angew. Chemie - Int. Ed.* **2013**, *52* (33), 8546–8550. https://doi.org/10.1002/anie.201303495.

(21) Liu, T.; Liu, Q.; Asiri, A. M.; Luo, Y.; Sun, X. An Amorphous CoSe Film Behaves as an Active and Stable Full Water-Splitting Electrocatalyst under Strongly Alkaline Conditions. *Chem. Commun.* **2015**, *51* (93), 16683–16686.

https://doi.org/10.1039/c5cc06892d.

(22) Liu, H.; Peng, X.; Liu, X.; Qi, G.; Luo, J. Porous Mn-Doped FeP/Co 3 (PO 4) 2 Nanosheets as Efficient Electrocatalysts for Overall Water Splitting in a Wide PH Range. *ChemSusChem* **2019**, *12* (7), 1334–1341. https://doi.org/10.1002/cssc.201802437.

(23) Wang, X.; Ma, W.; Ding, C.; Xu, Z.; Wang, H.; Zong, X.; Li, C. Amorphous Multi-Elements Electrocatalysts with Tunable Bifunctionality toward Overall Water Splitting. *ACS Catal.* **2018**, *8* (11), 9926–9935. https://doi.org/10.1021/acscatal.8b01839.

(24) Hu, C.; Zhang, L.; Zhao, Z. J.; Li, A.; Chang, X.; Gong, J. Synergism of Geometric Construction and Electronic Regulation: 3D Se-(NiCo)Sx/(OH)x Nanosheets for Highly Efficient Overall Water Splitting. *Adv. Mater.* **2018**, *30* (12), 1–8. https://doi.org/10.1002/adma.201705538.

(25) Kong, D.; Wang, H.; Lu, Z.; Cui, Y. CoSe2 Nanoparticles Grown on Carbon Fiber Paper: An Efficient and Stable Electrocatalyst for Hydrogen Evolution Reaction. *J. Am. Chem. Soc.* **2014**, *136* (13), 4897–4900. https://doi.org/10.1021/ja501497n.

(26) Xu, X.; Du, P.; Chen, Z.; Huang, M. An Electrodeposited Cobalt-Selenide-Based Film as an Efficient Bifunctional Electrocatalyst for Full Water Splitting. *J. Mater. Chem. A* **2016**, *4* (28), 10933–10939. https://doi.org/10.1039/c6ta03788g.

(27) Du, S.; Ren, Z.; Zhang, J.; Wu, J.; Xi, W.; Zhu, J.; Fu, H. Co3O4 Nanocrystal Ink Printed on Carbon Fiber Paper as a Large-Area Electrode for Electrochemical Water Splitting. *Chem. Commun.* **2015**, *51* (38), 8066–8069. https://doi.org/10.1039/c5cc01080b.

(28) Purkait, T.; Singh, G.; Kumar, D.; Singh, M.; Dey, R. S. High-Performance Flexible Supercapacitors Based on Electrochemically Tailored Three-Dimensional Reduced Graphene Oxide Networks. *Sci. Rep.* **2018**, *8* (1), 640. https://doi.org/10.1038/s41598-017-18593-3.

(29) Gomez, R.; Pereyra, A.; Ravi, V. Developing Novel Copper Foam Electrodes for Water Splitting. **2020**.

(30) Das, M.; Jena, N.; Purkait, T.; Kamboj, N.; De Sarkar, A.; Dey, R. S. Single-Phase Ni5P4-Copper Foam Superhydrophilic and Aerophobic Core-Shell Nanostructures for Efficient Hydrogen Evolution Reaction. *J. Mater. Chem. A* **2019**, *7* (41), 23989–23999. https://doi.org/10.1039/c9ta06729a.

(31) Zhang, H.; Yang, B.; Wu, X.; Li, Z.; Lei, L.; Zhang, X. Polymorphic CoSe2 with

Mixed Orthorhombic and Cubic Phases for Highly Efficient Hydrogen Evolution Reaction. *ACS Appl. Mater. Interfaces* **2015**, *7* (3), 1772–1779. https://doi.org/10.1021/am507373g.

(32) Thouin, L.; Rouquette-Sanchez, S.; Vedel, J. Electrodeposition of Copper-Selenium Binaries in a Citric Acid Medium. *Electrochim. Acta* **1993**, *38* (16), 2387–2394. https://doi.org/https://doi.org/10.1016/0013-4686(93)85107-A.

(33) Guo, X.; Xu, R.; Li, D.; Yang, Y.; Tian, Q. One-Step Electrodeposited CoSe2 Nano-Reticular with High Electroconductivity and Electrocatalytic as a Counter Electrode for Dye Sensitized Solar Cell. *J. Alloys Compd.* **2020**, *831*, 154712. https://doi.org/https://doi.org/10.1016/j.jallcom.2020.154712.

(34) Jee, H.-W.; Paeng, K.-J.; Myung, N.; Rajeshwar, K. Electrodeposition of Cobalt Selenide Thin Films: An Electrochemical Quartz Crystal Microgravimetry Study. *J. Electrochem. Soc.* **2017**, *164* (13), D861–D866. https://doi.org/10.1149/2.1321713jes.

(35) Merki, D.; Fierro, S.; Vrubel, H.; Hu, X. Amorphous Molybdenum Sulfide Films as Catalysts for Electrochemical Hydrogen Production in Water. *Chem. Sci.* **2011**, *2* (7), 1262–1267. https://doi.org/10.1039/c1sc00117e.

(36) Cao, B.; Veith, G. M.; Neuefeind, J. C.; Adzic, R. R.; Khalifah, P. G. Mixed Close-Packed Cobalt Molybdenum Nitrides as Non-Noble Metal Electrocatalysts for the Hydrogen Evolution Reaction. *J. Am. Chem. Soc.* **2013**, *135* (51), 19186–19192. https://doi.org/10.1021/ja4081056.

(37) Huang, J.; Qian, W.; Ma, H.; Zhang, H.; Ying, W. Highly Selective Production of Heavy Hydrocarbons over Cobalt-Graphene-Silica Nanocomposite Catalysts. *RSC Adv.* **2017**, *7* (53), 33441–33449. https://doi.org/10.1039/c7ra05887j.

(38) Li, S.; Peng, S.; Huang, L.; Cui, X.; Al-Enizi, A. M.; Zheng, G. Carbon-Coated Co3+-Rich Cobalt Selenide Derived from ZIF-67 for Efficient Electrochemical Water Oxidation. *ACS Appl. Mater. Interfaces* **2016**, *8* (32), 20534–20539. https://doi.org/10.1021/acsami.6b07986.

(39) Chen, X. Q.; Li, Z.; Dou, S. X. Ambient Facile Synthesis of Gram-Scale Copper Selenide Nanostructures from Commercial Copper and Selenium Powder. *ACS Appl. Mater. Interfaces* **2015**, *7* (24), 13295–13302. https://doi.org/10.1021/acsami.5b01085.

(40) Cao, X.; Johnson, E.; Nath, M. Expanding Multinary Selenide Based High-Efficiency Oxygen Evolution Electrocatalysts through Combinatorial

Electrodeposition: Case Study with Fe-Cu-Co Selenides. *ACS Sustain. Chem. Eng.* **2019**, *7* (10), 9588–9600. https://doi.org/10.1021/acssuschemeng.9b01095.

(41) Yuan, X.; Xue, S.; Liao, J.; Peng, F.; Shao, L.; Zhang, J. A Robust Approach to Fabricate CZTSSe Absorber Layer for Solar Cells via a Self-Selenizations Process Conducted by Concentrated Selenium Solution. *Mater. Res. Express* **2018**, *5* (1), 16413. https://doi.org/10.1088/2053-1591/aaa6df.

(42) Guo, C. X.; Zhang, L. Y.; Miao, J.; Zhang, J.; Li, C. M. DNA-Functionalized Graphene to Guide Growth of Highly Active Pd Nanocrystals as Efficient Electrocatalyst for Direct Formic Acid Fuel Cells. *Adv. Energy Mater.* **2013**, *3* (2), 167–171. https://doi.org/10.1002/aenm.201200527.

(43) Mahmood, N.; Yao, Y.; Zhang, J. W.; Pan, L.; Zhang, X.; Zou, J. J. Electrocatalysts for Hydrogen Evolution in Alkaline Electrolytes: Mechanisms, Challenges, and Prospective Solutions. *Adv. Sci.* **2018**, *5* (2). https://doi.org/10.1002/advs.201700464.

(44) Suryanto, B. H. R.; Wang, Y.; Hocking, R. K.; Adamson, W.; Zhao, C. Overall Electrochemical Splitting of Water at the Heterogeneous Interface of Nickel and Iron Oxide. *Nat. Commun.* **2019**, *10* (1), 1–10. https://doi.org/10.1038/s41467-019-13415-8.

(45) O'Mullane, A. P. Creating Active Interfaces as a Strategy to Improve Electrochemical Water Splitting Reactions. *JPhys Energy* **2020**, *2* (4). https://doi.org/10.1088/2515-7655/ab8c5f.

(46) Wei, L.; Goh, K.; Birer, Ö.; Karahan, H. E.; Chang, J.; Zhai, S.; Chen, X.; Chen, Y. A Hierarchically Porous Nickel–Copper Phosphide Nano-Foam for Efficient Electrochemical Splitting of Water. *Nanoscale* **2017**, *9* (13), 4401–4408. https://doi.org/10.1039/C6NR09864A.

(47) Chang, J.; Li, K.; Wu, Z.; Ge, J.; Liu, C.; Xing, W. Sulfur-Doped Nickel Phosphide Nanoplates Arrays: A Monolithic Electrocatalyst for Efficient Hydrogen Evolution Reactions. *ACS Appl. Mater. Interfaces* **2018**, *10* (31), 26303–26311. https://doi.org/10.1021/acsami.8b08068.

(48) Anantharaj, S.; Ede, S. R.; Sakthikumar, K.; Karthick, K.; Mishra, S.; Kundu, S. Recent Trends and Perspectives in Electrochemical Water Splitting with an Emphasis on Sulfide, Selenide, and Phosphide Catalysts of Fe, Co, and Ni: A Review. *ACS Catal.* **2016**, *6* (12), 8069–8097. https://doi.org/10.1021/acscatal.6b02479.

(49) Chhetri, M.; Maitra, S.; Chakraborty, H.; Waghmare, U. V; Rao, C. N. R. Superior Performance of Borocarbonitrides{,} BxCyNz{,} as Stable{,} Low-Cost Metal-Free Electrocatalysts for the Hydrogen Evolution Reaction. *Energy Environ. Sci.* **2016**, *9* (1), 95–101. https://doi.org/10.1039/C5EE02521D.

(50) Das, M.; Kamboj, N.; Purkait, T.; Sarkar, S.; Dey, R. S. Revealing the Structural Aspect of Ultrastable Self-Supportive Bifunctional Electrocatalyst for Solar-Driven Water Splitting. *J. Phys. Chem. C* **2020**, *124* (25), 13525–13534. https://doi.org/10.1021/acs.jpcc.0c01409.

(51) Kim, B. K.; Kim, M. J.; Kim, J. J. Impact of Surface Hydrophilicity on Electrochemical Water Splitting. *ACS Appl. Mater. Interfaces* **2021**, *13* (10), 11940–11947. https://doi.org/10.1021/acsami.0c22409.

Chapter 6

Triggering the efficiency of electrochemical water splitting by introducing Ni-buffer layer between the copper foam and cobalt selenide

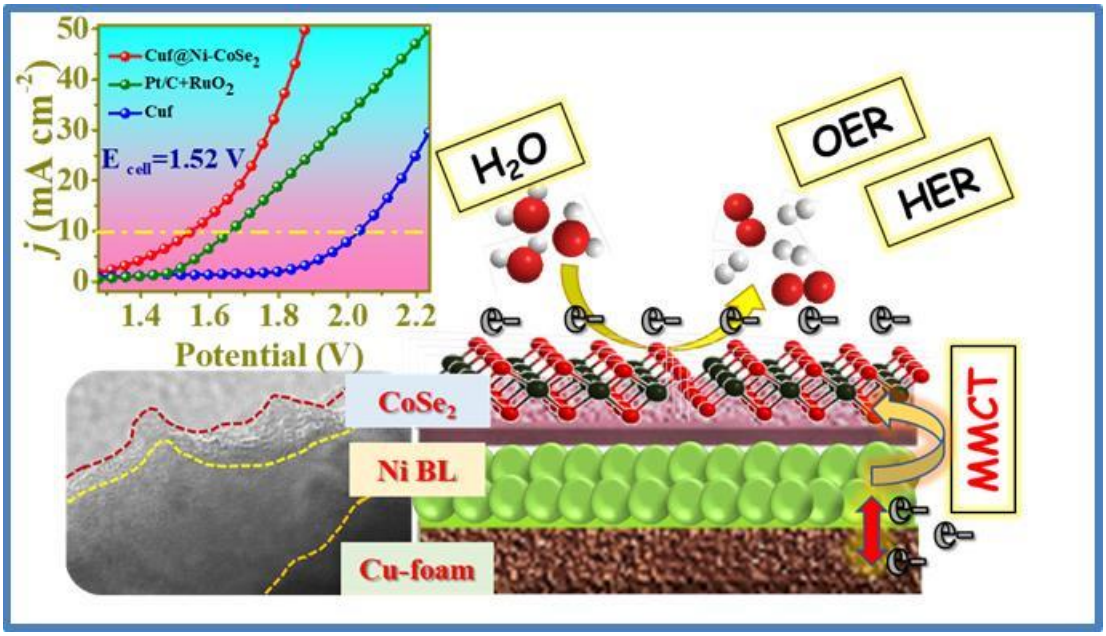

Abstract: For future renewable and sustainable energy technologies, the development of a cost-effective, highly efficient and stable bifunctional electrocatalyst is foremost requirement of water splitting to generate H_2 fuel. A 3-dimensional (3D) porous Copper foam (Cuf), when electrochemically decorated with transition metal selenides, resulted in a highly active electrocatalyst towards efficient water splitting. The role of cobalt selenide and Cuf have already proven to be remarkable in terms of water splitting. The introduction of Ni-buffer layer between Cuf and cobalt selenide (Cuf@Ni-$CoSe_2$) not only increases the efficiency and activity rather improves the stability of the catalytic surface. The self-supported as synthesized catalyst material was found to show an admirable activity toward oxygen evolution reaction (OER) and hydrogen evolution reaction (HER) in alkaline media. The performance of the catalyst was found to significantly better than the noble catalyst RuO_2. The catalyst was very stable up to 107 h and attained a full cell voltage of only 1.52 V at a current density of 10 mA cm^{-2}. Therefore, for a large-scale production of hydrogen, this as synthesized catalyst holds potential towards the replacement of conventional fossil fuel-based energy systems.

6.1 Introduction

The world is moving toward zero-carbon-based renewable energy technology due to the rapid consumption of fossil fuels in the last few decades. Sustainable energy systems are engrossed in the rational adoption of traditional resources and higher use of renewable energy in the next 20–30 years.[1–4] Winds and solar energy technology are the primary environmentally favorable renewable energy sources, however, the accessibility of these sources is depending on seasonal and regional changes. Electrochemical water electrolysis for the production of hydrogen and oxygen is considered as another source of the green energy system that converts electrical energy to chemical energy. This process is dynamic and flexible, and almost 100 percent pure fuels can be obtained. However, electrochemical water spitting still demands further research and fundamental improvements on the development of highly efficient and long-lasting electrocatalysts.[5,6] The two half-cell reactions involved in electrochemical water electrolysis are hydrogen evolution reaction (HER) and oxygen evolution reaction (OER) occurring at cathode and anode, respectively. However, most of HER catalysts favors an acidic environment, whereas OER prefers an alkaline environment.[7,8] The OER encounter sluggish reaction kinetics due to four electron transfer process, which results in higher overpotential than that of HER.[9,10] Therefore, it is desired to develop a bifunctional electrocatalyst that can overcome these barriers and is able to reduce the overpotential for efficient water electrolysis.[11] Noble metal such as Pt, Ru, and Ir-based electrocatalysts are considered to be the benchmark materials for the HER and OER,[12,13] however, exorbitant cost and scarcity limit their practical application.[14]

Recently, non-precious transition metal dichalcogenides are being widely used due to their emerging physical and chemical properties. Transition metal selenides have shown great importance as electroctalyst compared to transition metal oxides because of less electronegativity of selenium (2.55) than oxygen (3.44).[15–19] Less electronegative selenium will show greater covalency with transition metal and thus better charge transfer will be resulted during water oxidation. Bimetallic catalysts enhance HER and OER activity due to its synergistic effect. They have shown that addition of copper is expected to boost the metallic character of the catalyst that allows for faster charge transfer.[15]–In recent years, a number of studies are being performed on growth of thin buffer layers on different substrates which have led to enhancement in water oxidation by improving its properties.[20–22] Song et.al have synthesized Ni interfacing between Ni_3N and Nickel foam

($Ni_3N/Ni/NF$) electrocatalyst towards hydrogen evolution reaction (HER) and hydrogen oxidation reaction (HOR).[23] The catalyst imparted closely zero onset potential in alkaline and neutral electrolytes, demanding only 12 to 19 mV overpotential to attend a current density of −10 mA cm^{-2} for HER. The results suggested the presence of electrodeposited Ni layer facilitates rich interfacial active sites evidenced from theoretical study that confirmed the interfacial sites between Ni_3N and Ni provides best hydrogen adsorption sites with a ΔGH^* of only 0.01 eV which is very close to ideal value of 0 eV. Ni is known to have a better metal-metal charge transfer (MMCT) activity with Co, as Ni is able to anodically shift the $Co^{2+/3+}$ redox wave.[22–24] Synthesis of transition metal-based diselenides have been reported using various techniques like selenization, hydrothermal, electrodeposition, etc.[27,28] Electrodeposition is the most suitable method among others as it involves aqueous electrolytes at ambient condition, fast synthesis and can be easily scaled up.[29]

Taking advantages of electrodeposition method and Ni buffer layer between $CoSe_2$ and Cuf, herein we have developed a dynamic electrocatalyst, Cuf@Ni-$CoSe_2$ to boost the performance of overall water splitting. The three-dimensional Cu foam (Cuf) is the great choice for a substrate material because of its superior electrical conductivity and high porosity.[30,31] A thin Ni layer was deposited on Cuf using the electrophoretic deposition method, due to the sheer fine-tuning of their surface adsorption properties by a synergistic neighboring element. Moreover, Ni-based hetero-structures are found to have the most potential electrocatalytic activity and durability.[32] The catalytic activity of as developed catalyst has an overpotential of 90 mV at 10 mA cm^{-2} for HER and 1.39 V at 20 mA cm^{-2} for OER, which was found to be better than our previous report where the electrocatalyst based on Cu_2Se and $CoSe_2$ which was grown on Cuf without the insertion of Ni buffer layer (Ni BL) (Cuf@Cu-Co-Se).[33] In two-electrode cell, the performance was excellent as only 1.52 V was required to oxidize the water at 10 mA cm^{-2} current density. The advantage for the inclusion of Ni BL between Cuf and $CoSe_2$ can be noticed as the improvement in overpotential take place.

6.2 Experimental section

6.2.1 Layering of Nickel buffer on copper foam (Cuf@Ni)

The thin layer of Ni was deposited on as-prepared copper foam (Cuf) electrochemically based on previously reported method.[34] Firstly, copper foam of 1x1 cm^{-2} area was prepared on Cu foil following previous reports. The deposition of Ni BL on Cuf

(Cuf@Ni) was carried out by using two-electrode deposition method, where copper foam was used as a cathode and nickel sheet as an anode. The deposition was carried out for a time span of 60 sec and a constant current density of 0.7 A cm^{-2} was applied between the electrodes that were kept at a distance of 1.5 cm in an electrochemical cell consisting of 0.1 M $NiCl_2.6H_2O+H_2SO_4$. Post deposition sample was washed with DI water for several times to remove any acidic leftovers and finally it was kept in argon atmosphere for future use.

6.2.2 Electrodeposition of $CoSe_2$ on Cuf@Ni

Electrochemical deposition of $CoSe_2$ on Cuf@Ni was carried out under the constant potential of -0.7 V following three-electrode deposition technique. Electrodeposition of $CoSe_2$ was conducted by taking an aqueous solution of $CoCl_2.6H_2O$ (10 mM), KCl (50 mM) and SeO_2 (10 mM) in an electrochemical cell for different time spans (15, 30, 45, 60, 75, 90 and 105 minutes) as schematically illustrated in Figure 6.1.

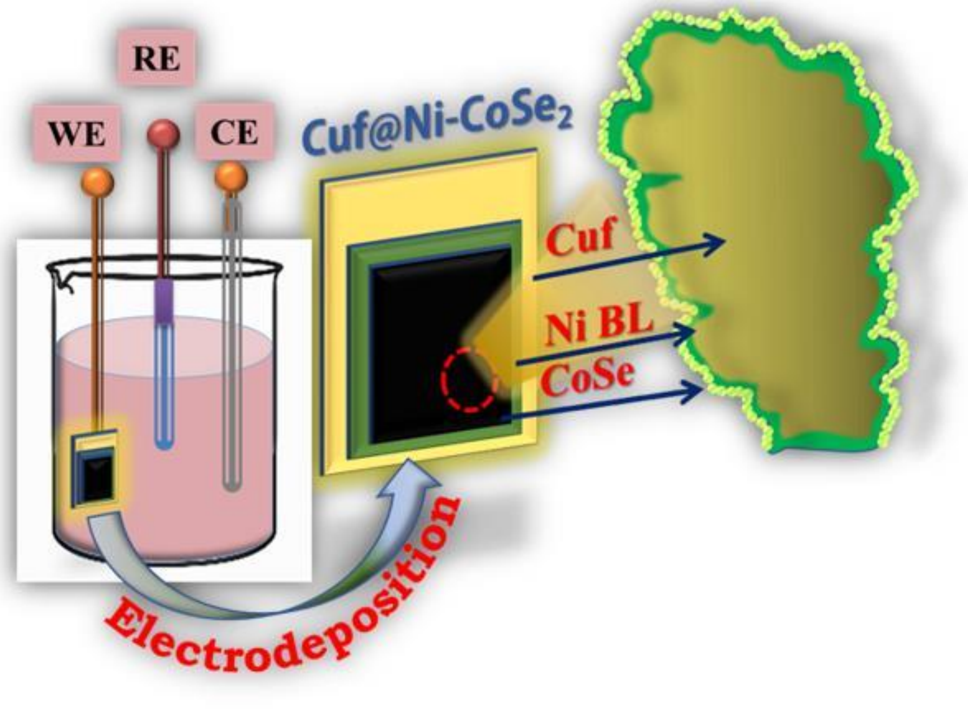

***Figure 6.1**. Schematic illustration for the synthesis of Cuf@Ni-$CoSe_2$ electrocatalyst.*

The optimized time of the as prepared catalyst was finalized to be 90 min after studying their electrochemical activities. The as-prepared electrode was used as working electrode, graphite rod and Ag/AgCl (3M KCl) were used as counter and reference electrodes, respectively as shown in Figure S1, Supporting information. After deposition (as shown in Figure S2, supporting information), the sample was washed thoroughly with DI water and stored under vacuum conditions when not in use.

6.2.3 Electrochemical measurements

The electrocatalytic performances of the as synthesized catalyst were carried out primarily in a three-electrode system using Cuf@Ni-$CoSe_2$ as a working electrode, Hg/Hg_2SO_4 (saturated K_2SO_4) as the reference electrode and graphite rod as the counter electrode in 1 M KOH solution under ambient temperature and pressure. The activity of Cuf@Ni-$CoSe_2$ catalyst were compared with other control samples such as Pt/C, RuO_2, Cuf@$Cu_2Se/CoSe_2$ (Cuf@Cu-Co-Se), Cuf@Ni and bare Cuf. The obtained potential was calibrated to reversible hydrogen electrode (RHE) using the formula (unless mentioned otherwise).

$E_{\mathrm{RHE}} = (E_{\mathrm{Hg/Hg2SO4\ (saturated)}} + 0.65 + 0.0591\ \mathrm{pH})$ V.

i*R* compensation was done using the impedance taken at open circuit potential (OCP). The i*R* compensation was not done when the scan was taken in a two-electrode system. The electrochemical activity for HER and OER were accomplished with the help of linear sweep voltammetry (LSV) technique at a scan rate of 10 mV s^{-1} and for calculation of Tafel slope, the scan rate was taken as 1 mV s^{-1}. To activate the active sites of the catalyst, the electrode was electrochemically activated for few cyclic voltammetry (CV) scan. The current was normalized with the geometrical surface area of the electrode. For the analysis of stability and durability of the catalyst, chronopotentiometry (CP)/step CP measurements were investigated. The electrochemical impedance spectroscopy (EIS) was conducted at a potential of 1.5 V in the frequency range of 10^5–10^{-2} Hz.

6.3 Results and discussion

6.3.1 Physical characterizations

The structural and morphological investigations were performed to analyze the physical properties of the as-synthesized catalyst. The structure of the catalyst has been schematically represented in Figure 6.2a. First, the X-ray diffraction (XRD) analysis was performed to understand the crystallinity of the material as shown in Figure 6.2b. The plane (111), (200) and (220), corresponds to Ni, appeared at an angle of 44.5˚, 51.8 ˚ and 76.3˚, respectively (JCPDS card no. 00-004- 0850). The planes (111) and (200) at an angle of 43.9°and 51.02 attributed for the cubic lattice planes Cu (JCPDS card no. 01-070-3038). The planes corresponding to 2θ of 29.2°(011), 37.1°(200), 64.4° (202), 75.1° (132), 77.4° (330) and 82.7°(103) are observed in the final catalyst sample for $CoSe_2$ species.

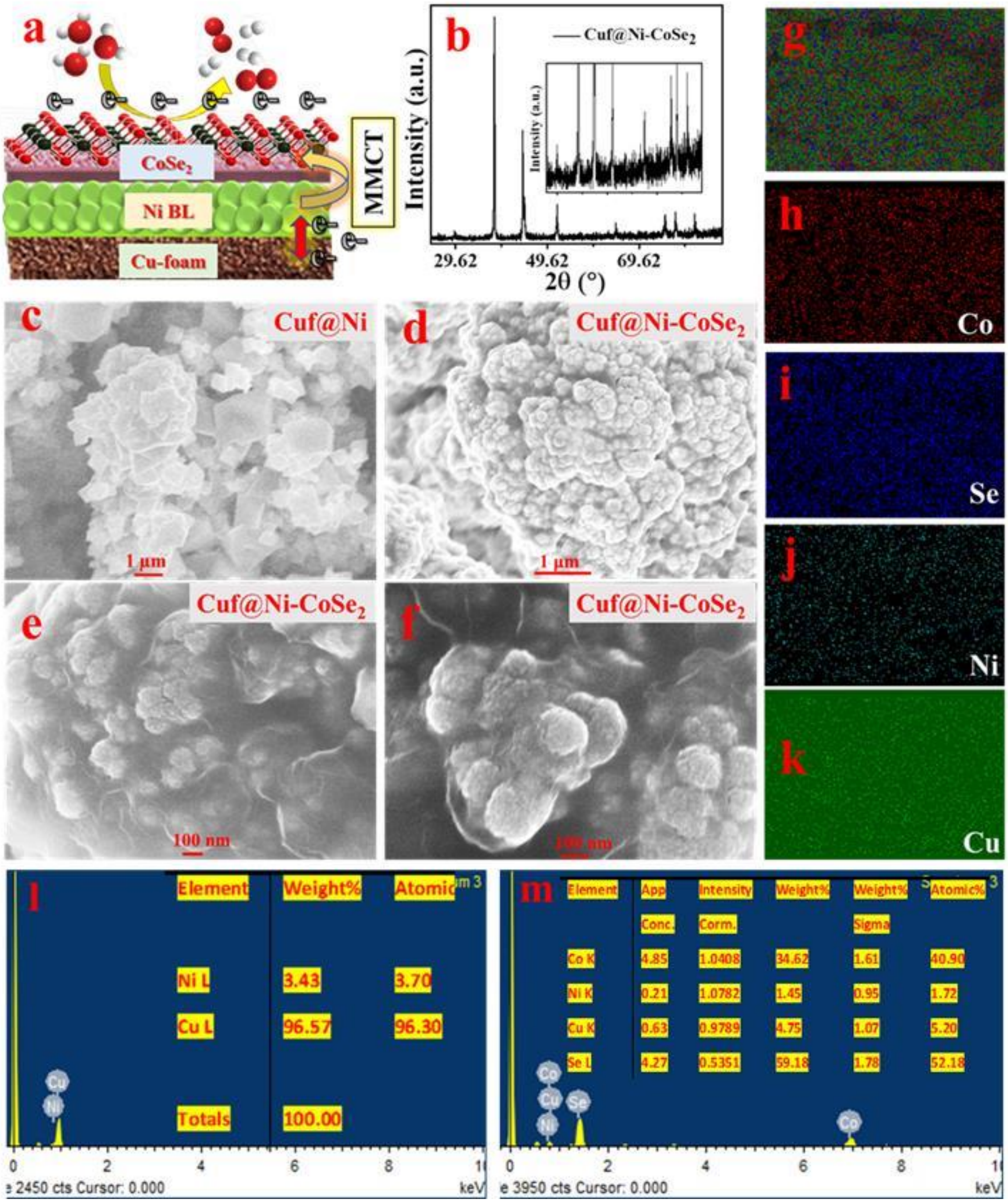

Element	Weight%	Atomic%
Ni L	3.43	3.70
Cu L	96.57	96.30
Totals	100.00	

e 2450 cts Cursor: 0.000

Element	App Conc.	Intensity Corrn.	Weight%	Weight% Sigma	Atomic%
Co K	4.85	1.0408	34.62	1.61	40.90
Ni K	0.21	1.0782	1.45	0.95	1.72
Cu K	0.63	0.9789	4.75	1.07	5.20
Se L	4.27	0.5351	59.18	1.78	52.18

e 3950 cts Cursor: 0.000

Figure 6.2. *(a) Synthetic pathways of the Cuf@Ni-$CoSe_2$ catalyst (b) corresponding XRD of the sample (c) FESEM image of Cuf@Ni (d-f) FESEM images of Cuf@Ni-$CoSe_2$ catalyst. (g-k) elemental mapping of the element (l) EDAX and atomic percentage of Cuf@Ni (m) EDAX and atomic percentage of Cuf@Ni-$CoSe_2$*

All these planes resemble with the orthorhombic lattice of $CoSe_2$ species (JCPDS card no. 01-089-2003), indicates the formation of $CoSe_2$ on the Cuf@Ni substrate. The XRD analysis suggests that the Ni buffer layer was formed on the copper foam onto which a layer of $CoSe_2$ were electrochemically deposited. The morphological studies of the catalysts have been investigated using field emission scanning electron microscopy (FESEM) as shown in Figure 6.2c-f. The FESEM image of as-deposited Ni on Cuf (Figure 6.2c) clearly shows a layer of Ni film covering the dendritic surface of Cuf. After the deposition of $CoSe_2$ (Figure 6.2d-f), a 3D coral like network structure with several loaded coarse were deposited on the skeleton of Cuf@Ni material in a contrast to the smooth surface of galvanostatically deposited Ni BL on Cuf. The elemental mapping of Cuf@Ni-$CoSe_2$ revealed the uniform distribution and presence of Cu, Ni, Co and Se in the as prepared catalyst as shown in Figure 6.2g-k. Corresponding Energy dispersive X-ray (EDX) spectrum study and atomic percentage of Cuf@Ni and Cuf@Ni-$CoSe_2$ were performed for quantification of the elements as shown in Figure 6.2 l and m, respectively.

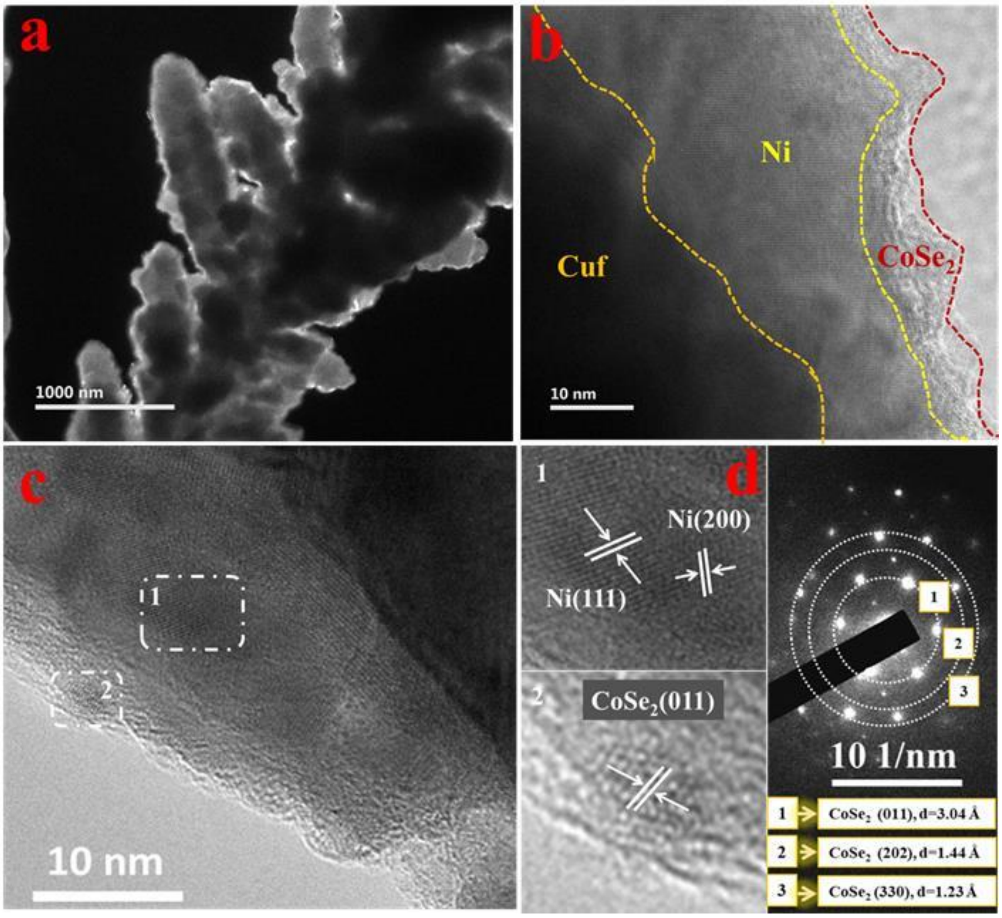

Figure 6.3. *(a) Transmission electron microscopy (TEM) of Cuf@Ni-$CoSe_2$ showing electrodeposited dendrites of Cuf. (b) TEM image showing the interfaces for the three layers of Cuf, Ni and CoSe (c) HRTEM fringe width (d) SAED pattern related with the planes*

The transmission electron microscopy (TEM) and high-resolution transmission electron microscopy (HRTEM) images were taken for more depth morphological study of the sample, which showed the evidences for the presence of $CoSe_2$ and Ni species in the catalyst. The image shown in Figure 6.3a shows the dendritic morphology of Cuf, on to which the as-deposited Ni (111), Ni (200) and $CoSe_2$ (011) layer is grown. Figure 6.3b clearly shows the three layers of Cuf, Ni and $CoSe_2$ with interfaces. The corresponding HRTEM and SAED study of the sample were also performed which was found to be well correlated with XRD pattern as shown in Figure 6.3c and d. X-ray photon spectroscopy (XPS) was employed to investigate the chemical states and coordination environment of the catalyst. The coordination environment and oxidation state of the catalyst are the responsible factors for the activity of the electrocatalyst in terms of water electrolysis.

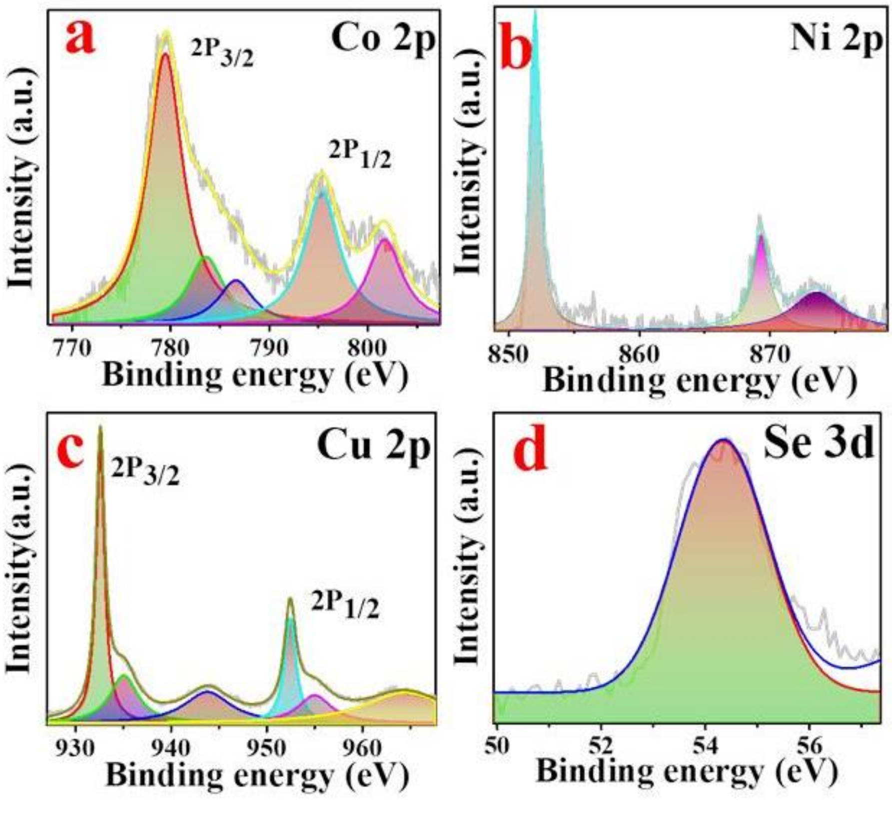

Figure 6.4. *High resolution XPS spectrum of (a) Co 2p (b) Ni 2p (c) Cu 2p (d) Se 3d*

The deconvolution of Co 2p spectra disclosed the binding states $Co2p_{3/2}$ and $Co2p_{1/2}$, where the peaks are located at 778.9 eV and 794.9 eV (Figure 6.4a), which is attributed to oxidize Co species present in the sample. The peaks appeared at 783.2 eV, 786.5 eV and 801.2 eV are the satellite peaks due to the antibonding orbital of CoSe present in the catalyst. Figure 6.4b denotes the XPS scan for Ni layer present in the sample and reflects the main peaks at 852.4 eV and 869.3 eV, which is due to the metal Ni present in the form of buffer layer. The peak around 873.5 eV, corresponds to the oxidized Ni species present in the sample which can be due to the air oxidation of the sample during atmospheric exposure. Furthermore, there were no evidence of nickel peak, Ni $^{\delta+}$ (around 854 eV) were investigated which confirms that Ni is not forming any bond with selenium. The binding energy of $Cu2p_{3/2}$ and $Cu2p_{1/2}$ is shown is Figure 6.4c, which depicts the presence of the peak at 932.2 eV and 952 eV, which is the metallic as well as oxidized species of Cu present as a substrate. The satellite peak was found to be located at 935.0 eV, 943.2 eV, 955 eV and 964 eV. The deconvoluted Se 3d spectra revealed the presence Se $3d_{5/2}$ and $3d_{3/2}$ peaks located at around 54-56 eV, which is due to the metallic Se present in $CoSe_2$ bond as shown in Figure 6.4d.

6.3.2 OER and HER Catalytic Performances

To evaluate the electrocatalytic activity of the as-synthesized catalysts, the working electrodes were tested in a 1.0 M KOH solution primarily in a three-electrode configuration.

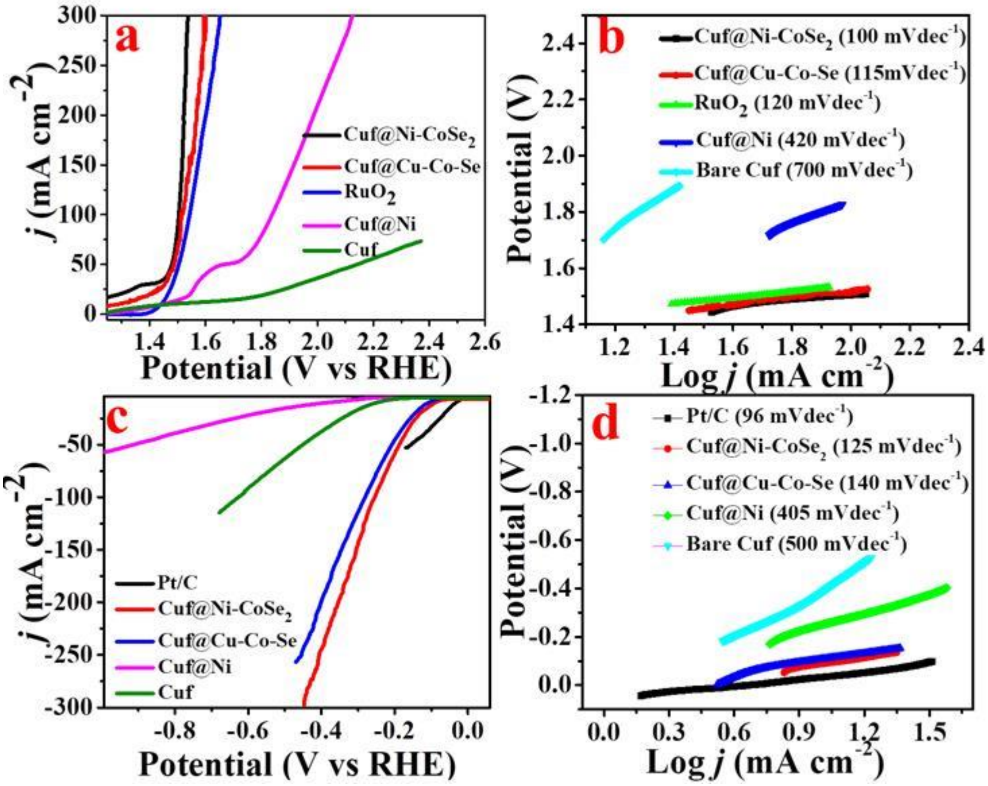

Figure 6.5. *(a) OER activity of Cuf@Ni-$CoSe_2$ compared with different control samples (b) Corresponding Tafel slope of OER activity of Cuf@Ni-$CoSe_2$ catalyst (c) HER activity of Cuf@Ni-$CoSe_2$ compared with different control samples (d) Corresponding Tafel slope of HER activity of Cuf@Ni-$CoSe_2$catalyst.*

For the comparison, bare Cuf, Cuf@Ni, our recently reported catalyst, Cuf@$Cu_2Se/CoSe_2$,[33] Pt/C and RuO_2 were also tested. All the LSV scans were i*R* compensated, unless mentioned otherwise. Firstly, the OER study of the catalysts were performed using the linear sweep voltammetry (LSV) technique. Figure 6.5a depicts the polarization curve of Cuf@Ni-$CoSe_2$ for OER along with all the control samples with i*R*-correction. The Cuf@Ni-$CoSe_2$ electrode as anode for OER showed the superior catalytic performance and a low overpotential of only 160 mV and 240 mV to drive a current density of 20 mA cm^{-2} and 50 mA cm^{-2}, respectively, which is less than that of Cuf@Cu-Co-Se (170 mV, j=20 mA cm^{-2}), RuO_2 (230 mV, j=20 mA cm^{-2}), Cuf@Ni (310 mV, j=20 mA cm^{-2}) and bare Cuf (630 mV, j=20 mA cm^{-2}). Figure 6.5b depicts the Tafel plot (overpotential(η) vs log(j)) for the analysis of electrode kinetics, which was plotted from LSV scan taken at a scan rate of 1 mVs^{-1}. The Tafel slope of Cuf@Ni-$CoSe_2$ was calculated to 100 mV dec^{-1}, which was found to be the lowest among all the control catalyst. The Tafel slope of Cuf@Cu-Co-Se was found to be 115 mV dec^{-1}, which was lower than that of RuO_2 (120 mV dec^{-1}), Cuf@Ni (420 mV dec^{-1}) and bare Cuf (700 mV dec^{-1}). The lower Tafel slope of Cuf@Ni-$CoSe_2$ indicates the faster kinetics of OER at applied overpotential which results in the high activity of the catalyst.

To further check the bifunctional activity of the catalyst, the HER activity of the catalyst was performed in a three-electrode system using the LSV technique (Figure 6.5c). The Pt/C dropcasted on Cuf showed the overpotential of 27 mV at 10 $mAcm^{-2}$ and the as-prepared Cuf@Ni-$CoSe_2$ showed the remarkable electrocatalytic activity with a high current density value. The overpotential of only 90 mV and 188 mV were required to attained the current density of 10 mA cm^{-2} and 50 mA cm^{-2}, respectively. These HER overpotential values were found to be better than Cuf@Cu-Co-Se (110 mV), Cuf@Ni (250 mV) and bare Cuf (395 mV), compared at a current density of 10 mA cm^{-2}. This improvement in the overpotential of Cuf@Ni-$CoSe_2$ with respect to Cuf@Cu-Co-Se due to synergy between Cuf@Ni and $CoSe_2$. The Tafel slope for the catalysts towards HER activity was also analysed in order to check the chemical kinetics of the catalyst towards electrocatalytic activity as shown in Figure 6.5d. The Tafel slope of Cuf@Ni-$CoSe_2$ was calculated to be 125 mV dec^{-1} which is greater than Pt/C (96 mV dec^{-1}) but smaller than Cuf@Cu-Co-Se (140 mV dec^{-1}), Cuf@Ni (405 mV dec^{-1}) and bare Cuf (500 mV dec^{-1}). This admirable performance of the catalyst may arise due to the efficient electron surge from the Cuf to the electrodeposited $CoSe_2$ through Ni BL as described below.

6.3.3 Full cell characterizations

Furthermore, the bifunctional activity of the catalyst, Cuf@Ni-CoSe$_2$, have been explored in order to check the full cell performance. The Cuf@Ni-CoSe$_2$ have been assembled as a cathode as well as anode in a two-electrode system containing 1.0 M KOH as shown in Figure 6.6a.

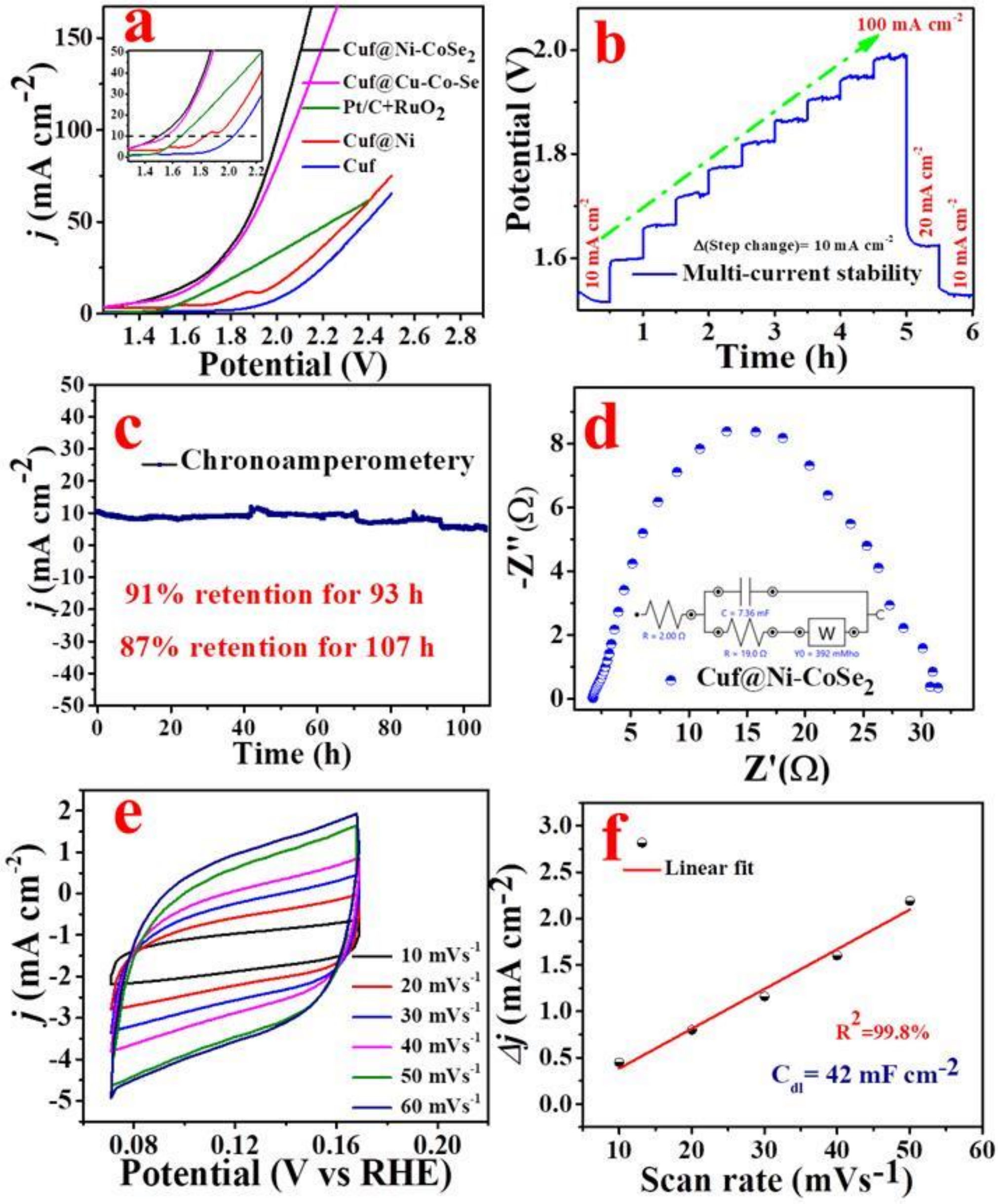

Figure 6.6. *(a) Polarisation curve of Cuf@Ni-CoSe$_2$ along with all other catalyst in a two electrode system (b) Chronopotentiometry (CP) current ramping of Cuf@Ni-CoSe$_2$ at different current density ranging from 10 mA cm^{-2} to 100 mA cm^{-2} (c) CP plot of Cuf@Ni-CoSe$_2$ in a two electrode system at a constant potential of 1.52 V (d) EIS analysis and Nyquist plot with fitted circuit in inset (e) Cyclic voltammetry of Cuf@Ni-CoSe$_2$ at different scan rates in non-faradic region for the calculation of electrochemically active surface area (ECSA).(f) Linear slope of Cuf@Ni-CoSe$_2$ with respect to current density and scan rate extracted from CV taken at different scan rate in a non-faradaic region.*

The LSV plot suggested that the full cell voltage of the Cuf@Ni-$CoSe_2$ at 10 mA cm^{-2} current density is very less (1.52 V) and a higher current density was achieved as compared to other electrocatalysts. A close look in to the zoomed version of the polarisation curve (inset of Figure 6.6a) gives the idea of full cell potential of Cuf@Cu-Co-Se (1.56 V), Pt/C+RuO_2 (1.66 V), Cuf@Ni (1.83 V) and bare Cuf (2.0 V). The activity of the as-synthesized catalyst Cuf@Ni-$CoSe_2$ was compared with the other recently reported electrocatalyst and found that the Cuf@Ni-$CoSe_2$ impart better performance than other water splitting catalyst as listed in Table 6.1.

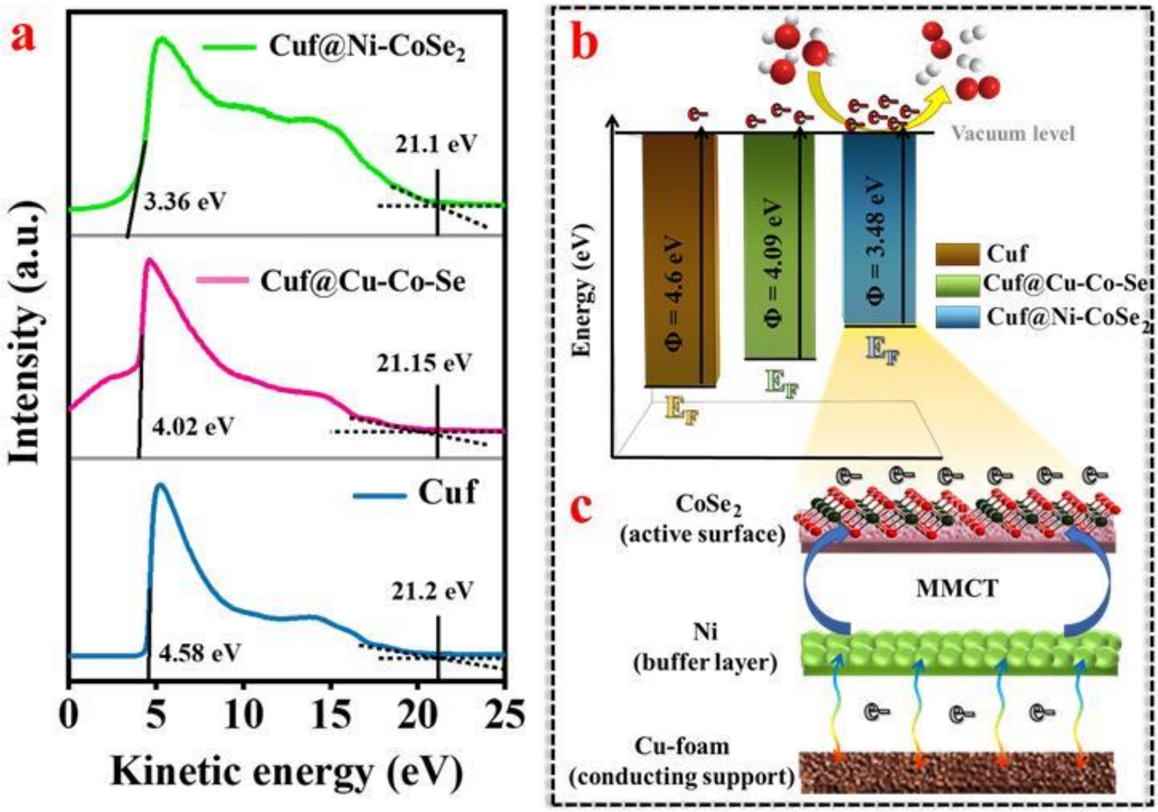

Figure 6.7 *(a) UPS spectra of Cuf, Cuf@Cu-Co-Se and Cuf@Ni-$CoSe_2$ catalysts showing Fermi energy (EF) at the low K.E region and the cut-off energy at the high K.E region; (b) corresponding work-functions of the materials and (c) charge transfer mechanism in Cuf@Ni-$CoSe_2$ facilitating HER and OER processes.*

The mechanical robustness and the stability of the electrocatalyst Cuf@Ni-$CoSe_2$, was investigated through multistep chronopotentiometry (CP) experiment. This parameter is very important and a stable electrocatalyst is critically required for industrial application purposes. Figure 6.6b shows multi-current analysis of Cuf@Ni-$CoSe_2$ electrocatalyst for 6 h using chronopotentiometry technique (the corresponding potential was recorded at different applied current densities in the range of 10 mA cm^{-2} to 100 mA cm^{-2} with a hold time of 1800 s). After 5 h CP run the current again set at the current density for 20 mA

cm^{-2} and 10 mA cm^{-2}, respectively, for next 1 h to return at their corresponding potential. It was observed that the potential remains same as of initial value at the particular current density, showing the excellent durability and mechanical robustness of the catalyst. This measurement approves that the as synthesized catalyst is a promising candidate for water splitting. The long-term durability of the catalyst was also tested for 107 h continuous CP run as can be seen from Figure 6.6 c. The performance of the catalyst after 93 h was found to be 91% retaintion of the potential of its initial value and maintained 87 % potential retention till 107 h run. This study proves the excellent stability of the catalyst. It is satisfying to note that the nickel BL actually protecting from the surface oxidation of Cuf and thus increases the stability. Electrochemical impedance spectroscopy (EIS) technique was adopted to further investigate resistance of the electrode-electrolyte interface. The corresponding Nyquist plot of the catalyst is shown in Figure 6.6 d. It has been revealed that Cuf@Ni-$CoSe_2$ has a very low solution resistance (R_s) of 2 Ω and a charge transfer resistance (R_{ct}) of 19 Ω. This smaller value of R_s and R_{ct} plays an important role for the faster kinetics in water electrolysis. The catalyst Cuf@Ni-$CoSe_2$ provided a large electrochemically active surface area (ECSA) of 1070 cm^{-2}, which was calculated from the double layer capacitance (C_{dl}) value of 42.8 mF cm^{-2} taken from CV scan in a non-faradaic region as shown in Figure 6.6 e and f. This large active surface area reflects to the better intrinsic activity and indicates the more availability of the catalytic active sites for hydrogen and oxygen formation.

Cu foam has sufficient d-electron density and is an ideal conductive support for a self-supportive electrode material, as already shown in our previous studies. As discussed above Ni is known to have a better metal-metal charge transfer (MMCT) activity with Co.[23,26] Hence, in order to have the advantages of both conductive support as well as better MMCT interactions, we have electrochemically grown a Ni BL as a connective link between Cu foam and $CoSe_2$ such that a greater surface area of Ni and Co layers could be in close proximity for an enhanced interaction. For any electrocatalytic process, it is highly desirable to have an electron sufficiency at the electrode surface capable of participating in the reaction steps. The addition of a sandwiched Ni layer behaves as a valve to enhance the electron thrust from the substrate to the material surface with no compromise in the overall material conductivity, ideally behaving as a “buffer layer”. The MMCT and the electron tunneling within the material upto the surface was supported with the help of UPS studies as shown in Figure 6.7 a, where a notable reduction in the work-function (calculated from Equation 1 and shown in Figure 6.7 b) of the final material Cuf@Ni-$CoSe_2$ (ϕ = 3.48 eV) supports our claim and advocates the role of Ni in reinforcing the internal electronic play resulting in an improved water splitting process than its control counterparts like bare Cuf and Cuf@$CoSe_2$ (mechanistically demonstrated in Figure 6.7 c).

$$\phi = h\upsilon - (E_{cut-off\ energy} - E_F) \tag{1}$$

where, ϕ is the work-function of the material, $h\upsilon$ denotes the energy of the incident photon of He (1) source (21.22 eV) and E_F is the energy at the Fermi edge level of the material.

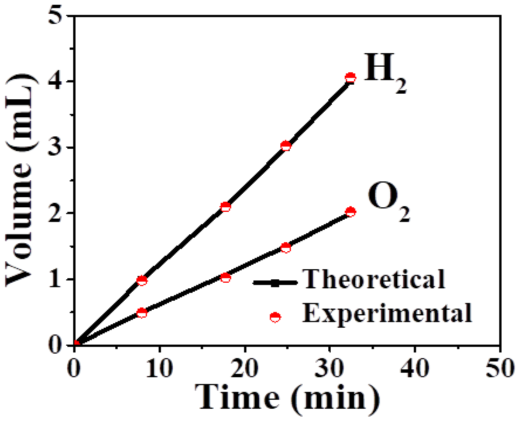

Figure 6.8. *Faradic efficiency calculation of H_2 and O_2 produced*

The Faradic efficiency of the as synthesized catalyst was evaluated in order to check the rate of evolution using water gas displacement method.[48] The Cuf@Ni-$CoSe_2$ electrodes were assmbled in a 2-electrode configuration (1.0 M KOH) using hoffmann voltameter and afterwards chronoamperometery technique was applied using electrochemical workstation. The corresponding readings of charge and displacement were recorded during the electrolysis process and the ratio of experimental and theoritical value of H_2/O_2 were calculated. The displacement of the H_2/O_2 (cathodic and anodic chamber) were maintained the ratio of 2:1 duing the whole period of electrolysis. The faradic efficiency was calculated to be

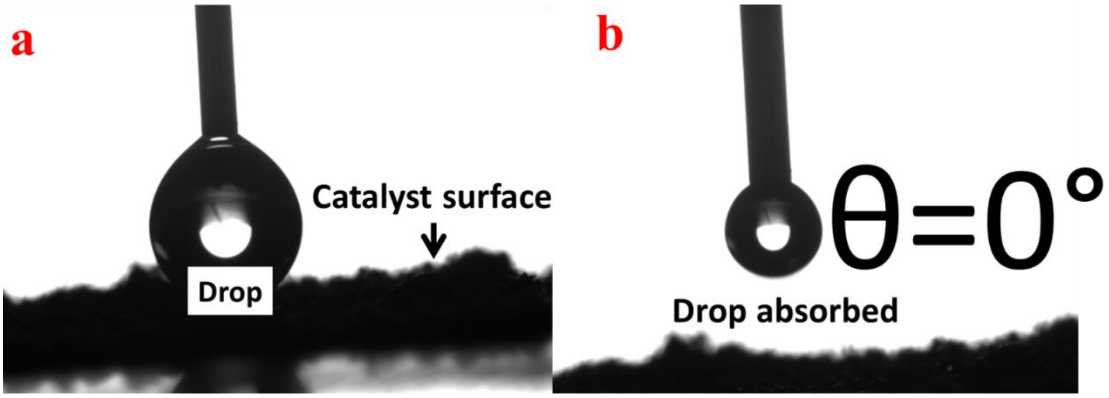

Figure 6.9. *Hydrophilicity analysis of Cuf@Ni-$CoSe_2$(a) before and (b) after the drop absorbed on the surface*

99.87 % as shown in Figure 6.8. The faradic efficiency was calculated using the formula given in equation 2:

$$FE = \frac{H_2\ /O_2(\text{Experimental})}{H_2\ /O_2\ (\text{Theoretical})} \qquad (2\ )$$

Table6.1. A comparison plot for HER, OER and full cell overpotential with recently reported catalyst.

Catalyst	***Overpotential for HER (mV)***	***Overpotential for OER (mV)***	***Full cell η@10 mA cm^{-2} (V)***	***References***
$CuCo_2Se_4$	η_{10} = 125	η_{50} = 320	η_{50} = 1.78	*ACS Appl. Energy Mater. 2020, 3, 3092−3103*
p-$CoSe_2$/CC	η_{10} = 138	η_{10} = 243	η_{10} = 1.62	*ACS Sustainable Chem. Eng*. 2018, 6, 11, 15374–15382
$NiCo_2S_4$@NiFe LDH/NF	η_{10} = 200	η_{60} =201	η_{10}=1.60	*ACS Appl. Mater. Interfaces* 2017, 9, 18, 15364–15372
Y–S Ni–Co-Se/CFP	η_{10} = 250	η_{10} = 300	η_{10}= -	*ACS Sustainable Chem. Eng*. 2018, 6, 8, 10952–10959
CoOx–CoSe/NF	η_{10} = 90	η_{500} = 380	η_{20} = 1.66	*J. Mater. Chem. A, 2016, 4, 10933–10939*
P,Cu-$Co_{0.85}$Se/NF	η_{10} = 96.8	η_{100} = 300	η_{10}=1.57	*j.jallcom.2021.161696*
CoNiSe/NC	η_{10} = 100	η_{10} = 270	η_{20} = 1.65	*j.jechem.2018.09.015*
Zn0.1Co0.9Se2	η_{10} =140	η_{10} = 340	η_{10}= -	*J. Mater. Chem. A*, 2017,5, 17982-17989
$Co_{0.75}Ni_{0.25}$Se/NF	η_{10} = 106	η_{50} = 269	η_{10} = 1.60	*Nanoscale*, 2019,11, 7959-7966
O-$Co_{0.5}Mo_{0.5}Se_2$	η_{10} = 102	η_{10} = 189	η_{10} = 1.53	*smll.202000797*
$CoNi_2Se_4$	η_{10} = 184	η_{10} = 244	η_{10} = 1.63	*j. ijhydene.2020.11.252*
(Fe-Co)Se2	η_{10} = 90	η_{10} = 251	η_{10} = 1.59	*j. jcis.2019.04.029*
Co-Fe(1/1)-Se	η_{10} = 129	η_{10} = 270	η_{10} = 1.68	*j.matchemphys.2021.125201*
$Co_{0.9}Fe_{0.1}$-Se/NF	η_{10} = 121	η_{10} = 292	η_{10} = 1.65	*j.jechem.2021.01.002*
0D−2D $CoSe_2/MoSe_2$	η_{10} = 90	η_{10} = 280	η_{10} = 1.63	*fchem.2020.00382*
EG/Ni3Se2/Co_9S_8	η_{20} = 170	-	η_{10} =1.62	*Nano Lett. 2017, 17, 7, 4202–4209*
Cuf@Ni-CoSe	η_{10} = 90	η_{20} = 160	η_{10} = 1.52	This work

Lesser contact angle between the electrode and the electrolyte interfaces leads to better facilitation of the mass transfer and reduction in the intrinsic resistance. Thus, the hydrophilic nature of the electrocatalyst is desired for better electrochemical activities. Interestingly, Cuf@Ni-$CoSe_2$ electrocatalyst showed superhydrophilic behaviour making a contact of 0° between water droplet and the electrode material (Figure 6.9 a and b).

6.4. Conclusion

The electrochemical deposition of cobalt selenide on the surface of galvanostatically deposited Cuf@Ni has been prepared. The binder-free electrocatalyst Cuf@Ni-$CoSe_2$ have been proved to be a promising bifunctional candidate for water electrolysis with an admirable activity. The Ni intermediate layer through MMCT interaction with Co facilitates better electron transfer from the substrate to catalyst, as evidenced from UPS technique, is actually responsible for high efficiency of the catalyst. Further, the as-deposited catalyst on the 3D porous dendritic copper foam was found to be superhydrophilic in nature that played a crucial role for the water adsorption and hence improved performance. The electrochemical characterizations justified that the catalytic activity was worthy in terms of overpotential, kinetics, stability and durability. Further, the full cell voltage of the catalyst Cuf@Ni-$CoSe_2$ was found to be only 1.52 V to drive a current density of 10 mA cm^{-2}. The CP and multistep current ramping stability demonstrated that the catalyst is mechanically robust and stable, which is favourable for commercialization.

6.5 References

(1) Dincer, I.; Acar, C. Review and Evaluation of Hydrogen Production Methods for Better Sustainability. *Int. J. Hydrogen Energy* **2015**, *40* (34), 11094–11111. https://doi.org/https://doi.org/10.1016/j.ijhydene.2014.12.035.

(2) Nicoletti, G.; Arcuri, N.; Nicoletti, G.; Bruno, R. A Technical and Environmental Comparison between Hydrogen and Some Fossil Fuels. *Energy Convers. Manag.* **2015**, *89*, 205–213. https://doi.org/https://doi.org/10.1016/j.enconman.2014.09.057.

(3) Dorian, J. P.; Franssen, H. T.; Simbeck, D. R. Global Challenges in Energy. *Energy Policy* **2006**, *34* (15), 1984–1991. https://doi.org/https://doi.org/10.1016/j.enpol.2005.03.010.

(4) Ibrahim, H.; Ilinca, A.; Perron, J. Energy Storage Systems-Characteristics and Comparisons. *Renewable and Sustainable Energy Reviews*. 2008, pp 1221–1250. https://doi.org/10.1016/j.rser.2007.01.023.

(5) Crabtree, G. W.; Dresselhaus, M. S.; Buchanan, M. V. The Hydrogen Economy. *Phys. Today* **2004**, *57* (12), 39–44. https://doi.org/10.1063/1.1878333.

(6) Li, X.; Hao, X.; Abudula, A.; Guan, G. Nanostructured Catalysts for Electrochemical Water Splitting: Current State and Prospects. *J. Mater. Chem. A* **2016**, *4* (31), 11973–12000. https://doi.org/10.1039/C6TA02334G.

(7) Shiva Kumar, S.; Himabindu, V. Hydrogen Production by PEM Water Electrolysis

– A Review. *Mater. Sci. Energy Technol.* **2019**, *2* (3), 442–454. https://doi.org/https://doi.org/10.1016/j.mset.2019.03.002.

(8) Wang, S.; Lu, A.; Zhong, C.-J. Hydrogen Production from Water Electrolysis: Role of Catalysts. *Nano Converg.* **2021**, *8* (1), 4. https://doi.org/10.1186/s40580-021-00254-x.

(9) Hu, C.; Zhang, L.; Gong, J. Recent Progress Made in the Mechanism Comprehension and Design of Electrocatalysts for Alkaline Water Splitting. *Energy Environ. Sci.* **2019**, *12* (9), 2620–2645. https://doi.org/10.1039/C9EE01202H.

(10) Song, J.; Wei, C.; Huang, Z.-F.; Liu, C.; Zeng, L.; Wang, X.; Xu, Z. J. A Review on Fundamentals for Designing Oxygen Evolution Electrocatalysts. *Chem. Soc. Rev.* **2020**, *49* (7), 2196–2214. https://doi.org/10.1039/C9CS00607A.

(11) Das, M.; Biswas, A.; Dey, R. S. Electronic Interplay: Synergism of Binary Transition Metals and Role of M–N–S Site towards Oxygen Electrocatalysis. *Chem. Commun.* **2022**, *58* (12), 1934–1937. https://doi.org/10.1039/D1CC06050C.

(12) Li, C.; Baek, J.-B. Recent Advances in Noble Metal (Pt, Ru, and Ir)-Based Electrocatalysts for Efficient Hydrogen Evolution Reaction. *ACS Omega* **2020**, *5* (1), 31–40. https://doi.org/10.1021/acsomega.9b03550.

(13) Shi, Q.; Zhu, C.; Du, D.; Lin, Y. Robust Noble Metal-Based Electrocatalysts for Oxygen Evolution Reaction. *Chem. Soc. Rev.* **2019**, *48* (12), 3181–3192. https://doi.org/10.1039/C8CS00671G.

(14) Khan, M. A.; Zhao, H.; Zou, W.; Chen, Z.; Cao, W.; Fang, J.; Xu, J.; Zhang, L.; Zhang, J. Recent Progresses in Electrocatalysts for Water Electrolysis. *Electrochem. Energy Rev.* **2018**, *1* (4), 483–530. https://doi.org/10.1007/s41918-018-0014-z.

(15) Cao, X.; Medvedeva, J. E.; Nath, M. Copper Cobalt Selenide as a High-Efficiency Bifunctional Electrocatalyst for Overall Water Splitting: Combined Experimental and Theoretical Study. *ACS Appl. Energy Mater.* **2020**, *3* (3), 3092–3103. https://doi.org/10.1021/acsaem.0c00262.

(16) Chen, W.-F.; Muckerman, J. T.; Fujita, E. Recent Developments in Transition Metal Carbides and Nitrides as Hydrogen Evolution Electrocatalysts. *Chem. Commun.* **2013**, *49* (79), 8896–8909. https://doi.org/10.1039/C3CC44076A.

(17) Anantharaj, S.; Ede, S. R.; Sakthikumar, K.; Karthick, K.; Mishra, S.; Kundu, S. Recent Trends and Perspectives in Electrochemical Water Splitting with an

Emphasis on Sulfide, Selenide, and Phosphide Catalysts of Fe, Co, and Ni: A Review. *ACS Catal.* **2016**, *6* (12), 8069–8097. https://doi.org/10.1021/acscatal.6b02479.

(18) Shi, Y.; Zhang, B. Recent Advances in Transition Metal Phosphide Nanomaterials: Synthesis and Applications in Hydrogen Evolution Reaction. *Chem. Soc. Rev.* **2016**, *45* (6), 1529–1541. https://doi.org/10.1039/C5CS00434A.

(19) Esposito, D. V; Hunt, S. T.; Kimmel, Y. C.; Chen, J. G. A New Class of Electrocatalysts for Hydrogen Production from Water Electrolysis: Metal Monolayers Supported on Low-Cost Transition Metal Carbides. *J. Am. Chem. Soc.* **2012**, *134* (6), 3025–3033. https://doi.org/10.1021/ja208656v.

(20) Chung, T.-F.; Zapien, J. A.; Lee, S.-T. Luminescent Properties of ZnO Nanorod Arrays Grown on Al:ZnO Buffer Layer. *J. Phys. Chem. C* **2008**, *112*, 820–824. https://doi.org/10.1021/jp076618d.

(21) Hu, Y.; Boudoire, F.; Mayer, M. T.; Yoon, S.; Graetzel, M.; Braun, A. Function and Electronic Structure of the SnO2 Buffer Layer between the α-Fe2O3 Water Oxidation Photoelectrode and the Transparent Conducting Oxide Current Collector. *J. Phys. Chem. C* **2021**, *125* (17), 9158–9168. https://doi.org/10.1021/acs.jpcc.1c01809.

(22) Cheng, H.; Deng, H.; Wang, Y.; Wei, M. Influence of ZnO Buffer Layer on the Electrical, Optical and Surface Properties of Ga-Doped ZnO Films. *J. Alloys Compd.* **2017**, *705*. https://doi.org/10.1016/j.jallcom.2017.01.172.

(23) Song, F.; Li, W.; Yang, J.; Han, G.; Liao, P.; Sun, Y. Interfacing Nickel Nitride and Nickel Boosts Both Electrocatalytic Hydrogen Evolution and Oxidation Reactions. *Nat. Commun.* **2018**, *9* (1), 4531. https://doi.org/10.1038/s41467-018-06728-7.

(24) Liang, H.; Meng, F.; Cabán-Acevedo, M.; Li, L.; Forticaux, A.; Xiu, L.; Wang, Z.; Jin, S. Hydrothermal Continuous Flow Synthesis and Exfoliation of NiCo Layered Double Hydroxide Nanosheets for Enhanced Oxygen Evolution Catalysis. *Nano Lett.* **2015**, *15* (2), 1421–1427. https://doi.org/10.1021/nl504872s.

(25) Liang, H.; Gandi, A. N.; Anjum, D. H.; Wang, X.; Schwingenschlögl, U.; Alshareef, H. N. Plasma-Assisted Synthesis of NiCoP for Efficient Overall Water Splitting. *Nano Lett.* **2016**, *16* (12), 7718–7725. https://doi.org/10.1021/acs.nanolett.6b03803.

(26) Morales-Guio, C. G.; Liardet, L.; Hu, X. Oxidatively Electrodeposited Thin-Film

Transition Metal (Oxy)Hydroxides as Oxygen Evolution Catalysts. *J. Am. Chem. Soc.* **2016**, *138* (28), 8946–8957. https://doi.org/10.1021/jacs.6b05196.

(27) Kong, D.; Wang, H.; Lu, Z.; Cui, Y. CoSe2 Nanoparticles Grown on Carbon Fiber Paper: An Efficient and Stable Electrocatalyst for Hydrogen Evolution Reaction. *J. Am. Chem. Soc.* **2014**, *136* (13), 4897–4900. https://doi.org/10.1021/ja501497n.

(28) Cao, X.; Johnson, E.; Nath, M. Identifying High-Efficiency Oxygen Evolution Electrocatalysts from Co–Ni–Cu Based Selenides through Combinatorial Electrodeposition. *J. Mater. Chem. A* **2019**, *7* (16), 9877–9889. https://doi.org/10.1039/C9TA00863B.

(29) Schwarzacher, W. Electrodeposition: A Technology for the Future. *Electrochem. Soc. Interface* **2006**, *15*, 32–33. https://doi.org/10.1149/2.F08061IF.

(30) Shin, H. C.; Liu, M. Copper Foam Structures with Highly Porous Nanostructured Walls. *Chem. Mater.* **2004**, *16* (25), 5460–5464. https://doi.org/10.1021/cm048887b.

(31) Ma, X.; Chang, Y.; Zhang, Z.; Tang, J. Forest-like NiCoP@Cu3P Supported on Copper Foam as a Bifunctional Catalyst for Efficient Water Splitting. *J. Mater. Chem. A* **2018**, *6* (5), 2100–2106. https://doi.org/10.1039/C7TA09619D.

(32) Gong, M.; Wang, D.-Y.; Chen, C.-C.; Hwang, B.-J.; Dai, H. A Mini Review on Nickel-Based Electrocatalysts for Alkaline Hydrogen Evolution Reaction. *Nano Res.* **2016**, *9* (1), 28–46. https://doi.org/10.1007/s12274-015-0965-x.

(33) Das, M.; Kumar, G.; Dey, R. S. Electrochemical Growth and Formation Mechanism of Cu2Se/CoSe2-Based Bifunctional Electrocatalyst: A Strategy for the Development of Efficient Material toward Water Electrolysis. *ACS Appl. Energy Mater.* **2022**. https://doi.org/10.1021/acsaem.1c03497.

(34) Das, M.; Kamboj, N.; Purkait, T.; Sarkar, S.; Dey, R. S. Revealing the Structural Aspect of Ultrastable Self-Supportive Bifunctional Electrocatalyst for Solar-Driven Water Splitting. *J. Phys. Chem. C* **2020**, *124* (25), 13525–13534. https://doi.org/10.1021/acs.jpcc.0c01409.

Chapter 7

Synergism of binary transition metals and role of M-N-S active sites towards efficient oxygen electrocatalysis

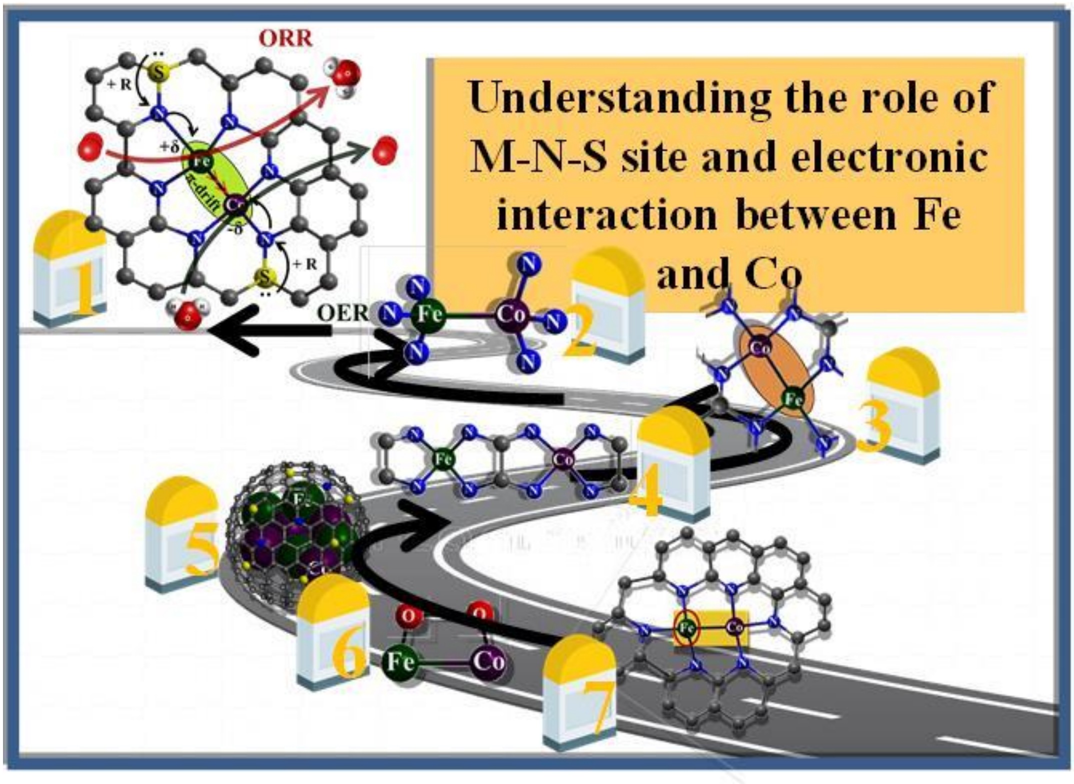

Understanding the role of M-N-S site and electronic interaction between Fe and Co

Abstract: Binary transition metals are being widely regarded as active sites for bifunctional electrocatalytic reactions, but it is hard to explain the origin of their efficiency. There is plenty of room for exploration of the "synergistic effect" of the binary metals reinforcing electrocatalysis. This work is focused on the systematic navigation of the π-electronic interaction between the e_g and a_{1g} orbitals of square-planar Fe and Co atoms, respectively, in the Fe-Co bimetallic catalyst (FeCoDACys). An extended electronic play prevails in the system, where –S-N moiety is present with both the metals, which trigger the oxygen electrocatalysis reactions at the cost of a low overpotential. This enhanced catalytic performance of the material is further exploited for liquid state Zinc-air battery, where it delivered an open circuit potential of 1.26 V and a peak power density of ∼125 mW cm^{-2}.

We acknowledge **RRCAT Indore, India** for EXAFS and XANES analysis.

7.1 Introduction

The growing energy concerns and rapid exhaustion of non-renewable energy sources tend the scientific findings to incline toward alternatives and sustainable energy.[1] As an attempt to address this issue, a major field of research is focused on commercializing fuel cells[2] and metal-air batteries. In particular, Zinc-air battery is considered to be quite promising owing to the abundance of metallic zinc anode, its environmental benignancy, low cost, and high theoretical specific capacity.[3–6] that are constituted of two important electrocatalytic processes such as oxygen reduction reaction (ORR) and oxygen evolution reaction (OER). This calls for the increasing demand for bifunctional electrocatalysts that would be cost-effective, easy to synthesize, can be rendered in a large-scale, should have abundant active sites with an appreciable electrocatalytic activity.[7–9]

Transition metals bonded with the hetero-atoms[10] and heteroatoms-doped carbonaceous matrix are much-surveyed electrocatalyst for ORR and OER. Among the transition metal cations, Fe and Co are found to be the most appreciated with respect to their oxygen electrocatalysis performance due to fair conductivity and availability of d-electrons.[8] Anionic heteroatoms like N, S, B, P, Si, embedded in metal doped carbon sheets not only act as a pillar to stabilize the transition metal atoms but they modify the electronic structure of the metal atoms by altering the Fermi energy levels and fine-tune the local electronegativity. [11,12] These factors directly improvise the adsorption of reactant molecules, the binding energy of oxygen in the intermediate compounds and finally desorption of the end products. Thus, it is clear that the coordination of the active sites has many roles to play in boosting the electrocatalytic performance of the electrocatalysts and should be ascertained with cutting edge characterization techniques. However, there is a huge scope to design an electrocatalyst with binary transition metal and heteroatoms doped carbon catalyst and understand the role of active sites during electrocatalysis.

To date, the suppositions regarding the active centre responsible for OER and ORR are a much-debated topic. Although not much has been established regarding the mechanistic elaboration of OER, but a synergistic concept validated between Fe and Co in enhancing the OER reaction kinetics by lowering the potential for Fe-O-O-Co bond (Figure 7.1a) formation, one of the key intermediates for OER.[13,14] With regards to ORR, Wang *et al.* presented a size-activity relationship of FeCo alloy embedded in the N-doped carbon matrix, where they opined that Fe-Co dual metal centre provided an active site for oxygen binding and its subsequent reduction at a low cleavage energy barrier (Figure

7.1b,c).[15,16] Although, with the help of DFT studies, they have explained that Fe is reasonably more responsible for ORR than Co, there is a mechanistic lagging that could not foretell how oxygen was binding together on Fe-Co site or what electronic interactions drew oxygen to bind on Fe-Co dual site and get reduced subsequently. Similarly, Chen *et al.* also showed that the combinatorial effect between Fe and Co is the key factor for enhancing the ORR catalytic performance of FeCo-IA/NC catalyst (Figure 7.1d).[17] But they also did not elaborate that what kind of mechanism was operating between the binary metals that boosted the oxygen reduction activity. For the combined oxygen electrocatalysis, the participation of Fe and Co has been quite mechanically reported by Chen *et al.* that although Fe is responsible for a remarkable ORR activity, the durability of the process is dictated by Co and a synergistic effect between the two metals has an impact on the improved OER performance of the NCAG/Fe-Co catalyst (Figure 7.1e).[8] So, there persists a genuine gap regarding the proper justification of the electronic

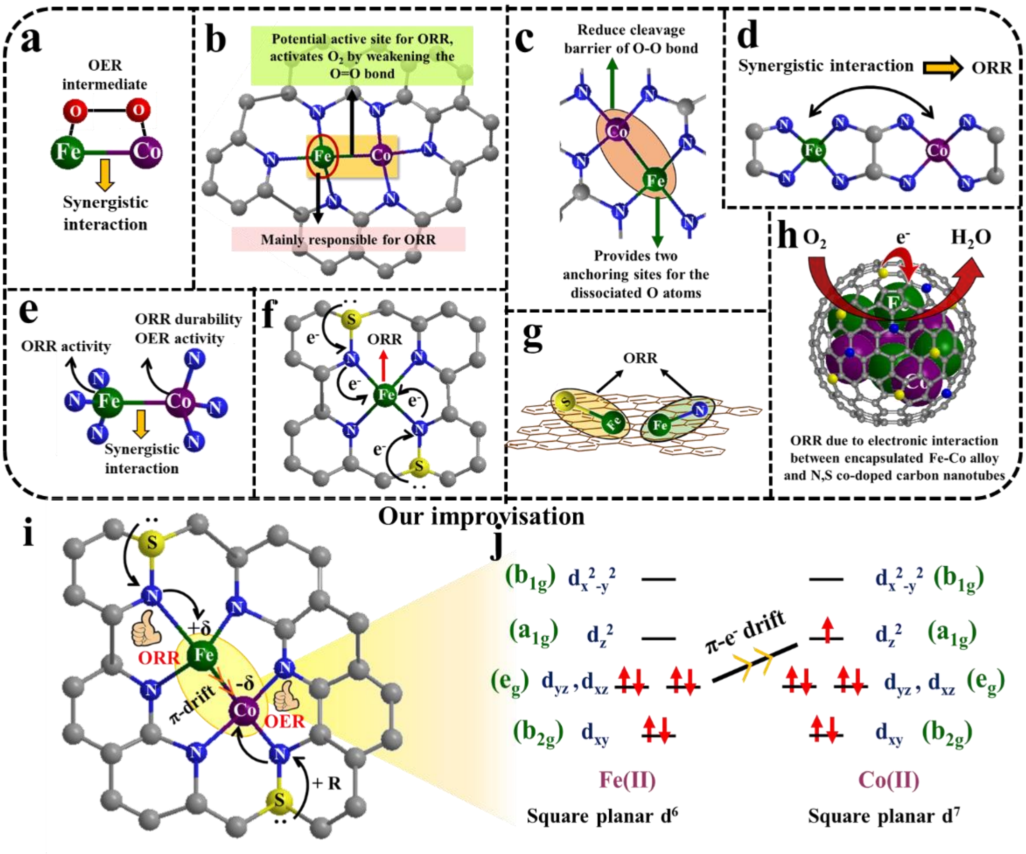

Figure 7.1. *(a-h) Different mechanistic approach proposed so far for ORR and OER on Fe and Co-based binary and dual active sites; (i) Schematic representation of the S-N-Fe-Co-N-S active site structure of the FeCoDACys catalyst; (j) Molecular orbital diagram showing the π-electronic interaction between the d_{xz} or d_{yz} orbital of square-planar d^6 Fe(II) and d_{z^2} orbital of square-planar d^7 Co(II).*

environment around the metal centres and how they complement each other in reinforcing the catalytic processes. When this matter still remains unresolved, another report from Huang *et al.* discussed the role of dual doping of metal as well as electronegative dopants like N and S in the carbon matrix (Figure 7.1f) for attainment of desirable ORR with minimum (~ 0.5 %) perturbation from side product formation H_2O_2.[18] Contrary to this, Zhang *et al.* showed that the electronegative dopants (nitrogen and sulphur), bonded together with the metal centre (Figure 7.1g) reinforced the ORR activity by suitably altering the electronic states of the associated atoms.[19] They further introduced the importance of N acting as a bridging atom between Fe and S towards the electronic movement and enhancement of electron density over the metal centre prior to initiation of ORR. Zhao *et al.* [20] made an attempt to collab the electronegative hetero-dopants like nitrogen[21] and sulphur with Fe-Co binary metals that contributed strongly to the ORR activity, including the improvement in the onset potential and limiting current density (Figure 7.1h). Therefore, it is crucial to explore the electronic movements within the active domain of the catalyst Herein, for our active system FeCoDACys, we aim to mechanistically justify the so-called “synergistic effect” between the metal atoms, the additional benefaction of N and S dopants and to bridge up their individual roles in the S-N-M_1-M_2-N-S active site, augmenting the electrochemical activity of the catalyst toward ORR and OER. We further extend our findings to demonstrate the performance of our material in liquid state Zinc-air battery.

7.2 Experimental

7.2.1 Methodical synthesis of the catalyst material to obtain S-N-Fe-Co-N-S active site

In this work, we designed a carbonaceous electrocatalyst based on Fe-Co dual site coordinated with N and S as co-dopant (Figure 7.1g), where dopamine and cysteine served as the source of N and S respectively. The synthesis of FeCoDACys electrocatalyst was done by grinding the mixture of dopamine, L-cystine, $FeSO_4.7H_2O$ and $CoCl_2.6H_2O$ using a mortar and pestle in a proportionate amount Fe:Co:DA:Cys (0.4:0.6:1:0.2) in molar ratios, followed by pyrolysis at 800°C for 2 h in an argon atmosphere (99.99%) at a constant heating rate of 3°C min^{-1}. The pyrolyzed sample was then ball milled at 300 rpm for 30 min to form a uniformly grinded fine powder. The obtained sample after ball milling was then washed with dilute HCl (6M) for 10 times to remove the inactive Fe and Co particles from the sample. The sample was then followed by the stepwise washing with Milli-Q water, until a neutral pH was attained and finally dried in a hot air oven at 60°C for 24 h. For the comparison of the activity and to understand the mechanism, FeDACys and CoDACys were also synthesized using the same protocol as stated above. A detailed synthesis route has been schematically represented in Figure 7.2. This method enabled us to have a precise control over the local coordination of the active site to achieve S-N-M$_1$-M$_2$-N-S architecture in the carbon framework, which favored the adsorption of H_2O and O_2 during the OER and ORR processes respectively. A delocalization of free electrons prevails between the positively charged metal centers (Fe-Co) and an energy transfer owing to this electronic movement provides thermal stability to this bimetallic system. In fact, the electron donating anionic dopants altered the electronic bands of the square planar metal centers [22] in such a way that a π-electron drift occurs from the e_g orbital (d_{xz} or d_{yz}) of Fe to more electronegative a_{1g} orbital (d_{z^2}) of Co (Figure 1h).[23]

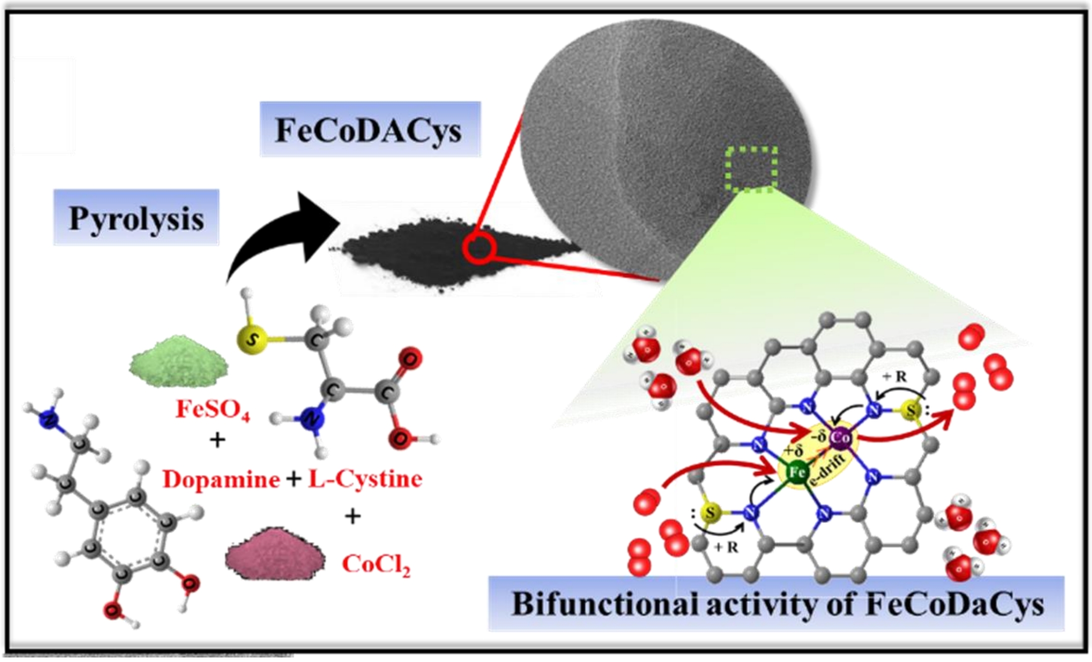

Figure 7.2. *Schematic representation of the synthesis of FeCoDACys catalyst and the S-N-Fe-Co-N-S active unit responsible for oxygen electrocatalysis*

7.3 Results and discussion

7.3.1 Physical characterizations of the FeCoDACys catalyst

The surface morphology of the FeCoDACys catalyst is inspected from scanning electron microscopy (SEM) and transmission electron microscopy (TEM) (Figure 7.3 a,b), which reveals a crumbled sheet like morphology of the carbon network. The elemental mapping in Figure 7.3c-h shows the presence of Fe, Co, S, N and C elements in the FeCoDACys sample. The high resolution (HR)-TEM image of the catalyst in Figure 7.3i displays lattice fringes corresponding to a width of 0.34 nm for the (002) plane of the carbon matrix. In the energy dispersive X-ray analysis (EDAX) (Figure 7.3j) distinct peaks for

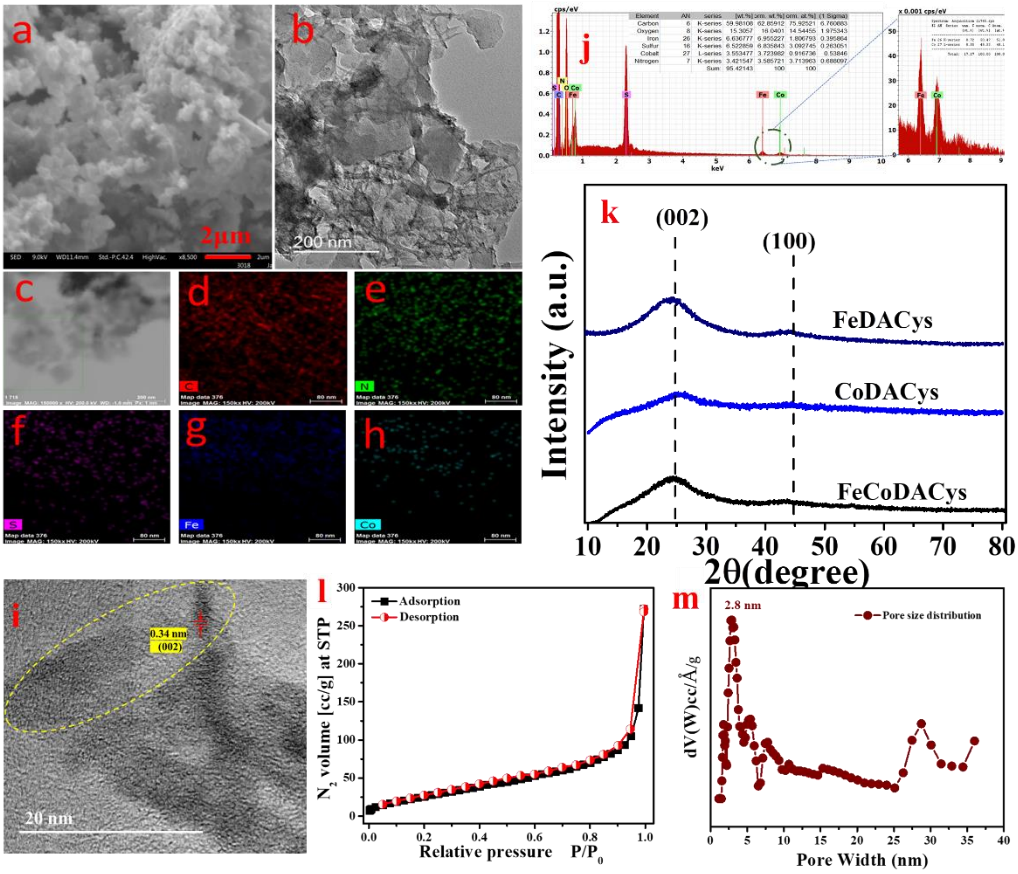

Figure 7.3. *(a-b) SEM/FESEM image of FeCoDACys at a magnification of 2 µm and 200 nm respectively; (c-h) Corresponding elemental mapping of the catalyst taken from SEM. . (i) : HRTEM image of FeCoDACys catalyst showing the fringe-width for carbon (002) plane (j) EDAX mapping for the elements present in the FeCoDACys electrocatalyst showing carbon, nitrogen, sulphur, iron, cobalt and oxygen (k X-ray diffractometry for FeCoDACys sample including all the control samples (l) BET adsorption-desorption isotherm (m) Pore size distribution of FeCoDACys catalyst.*

all the aforesaid elements could be visible. The X-ray diffraction (XRD) analysis as displayed in Figure 7.3k reveals two broad diffraction peaks at ~24° and ~44°, which is attributed to the (002) and (100) planes of the graphitic carbon in the sample**.** There was no trace of any metallic peak corresponding to Fe and Co that confirms the nullification of nanoparticle formation upon repeated washing and that Fe and Co are atomically dispersed in the carbon matrix as reported in the STEM image. FeCoDACys material possess mesoporosity which was confirmed from N_2 adsorption-desorption isotherm. The graph displays type IV isotherm with a hysteresis loop in the higher relative pressure region (P/P$_0$) along with a steep increment of adsorption capacity in 0.9-1 range of relative pressure (P/P$_0$) indicating the co-existence of mesoporosity and interparticle porosity in the sample (Figure 7.3l). The pore size distribution curve was obtained from the isotherm empolying nonlocal density functional theory (NLDFT) which ensures the presence of mesopores (2.8 nm) in FeCoDACys sample as shown in Figure 7.3m. The Brunauer–Emmett–Teller (BET) surface area of FeCoDACys catalyst was calculated to be 105 m^{2}g^{-1}.[1],[2] A more detailed insight regarding the elemental composition of the FeCoDACys catalyst is acquired from X-ray photoelectron spectroscopy (XPS) analysis (Figure 7.4). X-ray photoelectron spectroscopy (XPS) was performed to measure the

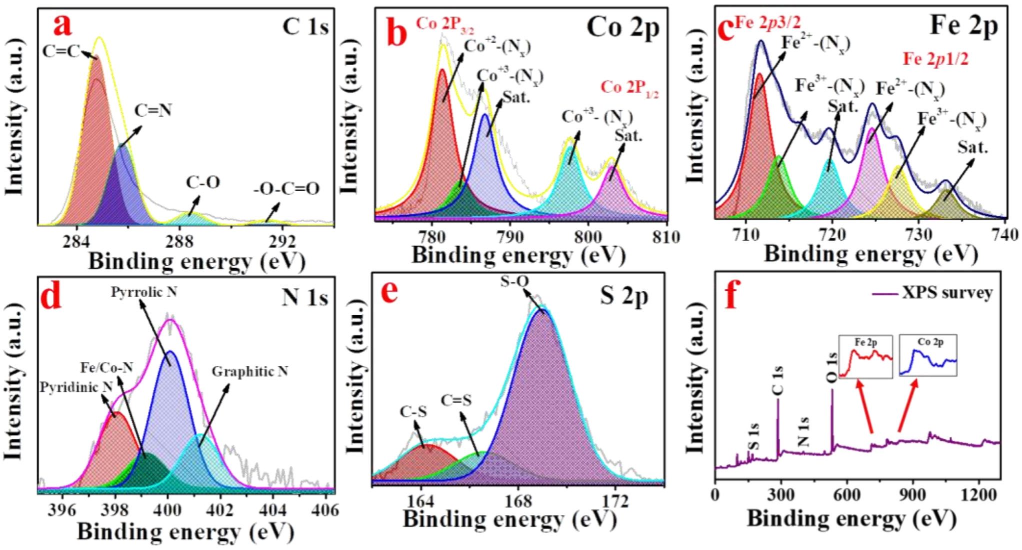

Figure 7.4. *XPS for different elements present in the as prepared bifunctional electrocatalyst FeCoDACys (a) Carbon (b) Cobalt (c) Iron (d) Nitrogen (e) Sulphur (f) XPS survey.*

chemical composition and oxidation state of FeCoDACys catalyst. The XPS survey scan depicted the presence of C, N, S, Fe and Co elements in the catalyst. High resolution spectra for C 1s is shown in Figure 7.4a, which shows the peaks present at 284.17, 285.77, 288.54 and 291.44 eV corresponds to C=C, C=N, C-O and -O-C=O bond. [3,4] The high-resolution Co 2p spectra of FeCoDACys (Figure 7.4b), shows that the spectrum being deconvoluted into different peaks, the peak at 781.27 and 783.62 eV in Co 2p$_{3/2}$ and at 797.62 eV in Co 2p$_{1/2}$ is due to Co^{+2}/ Co^{+3} because of the coordination of Co with O or N ions which is very likely due to Co-N$_x$ formation which was further confirmed through EXAFS data. Meanwhile, the peak present at 786.72 and 803.13 eV for Co 2p$_{1/2}$ is the shake-up satellite peak is the sign of Co-OH/Co-O formation, which indicates the formation of partial oxidation on the surface of FeCoDACys catalyst which might be occurred due to atmospheric exposure.[5,6] However, the presence of oxide peaks was not evidenced in the XRD characterization, which confirms the oxide formation is due to the surface oxidation. The spectrum corresponding Fe 2p was deconvoluted into six different peaks as shown in Figure S7.4c. The peaks at 711.49 and 713.84 eV for Fe $2p_{3/2}$ and the peaks at 724.59 and 727.56 eV for Fe $2p_{1/2}$ are attributed for Fe^{2+} and Fe^{3+}, respectively which is mainly due the presence of FeN bond. [7,8] The deconvolution of high-resolution N 1s spectra shows the four distinct peaks at 398.37 eV for Pyridinic N (CN=C), 399.1 eV for the coordination of Fe/Co-N_x bond, 400.43 eV for tertiary N [N-$(C)_3$] and 401.54 eV for the confirmation of amino (N-H) bond (Figure 7.4d). [9,10]The S 2p signal was further deconvoluted into three peaks as depicted in Figure 7.4e. The peaks at 164.12 and 166.52 eV are corresponding to the presence of bond between carbon and sulphur C-S and C=S, respectively. The analysis for the present of all the elements with their bonds and chemical environment was obtained from XPS, which reflects from XPS survey (Figure 7.4f). The deconvoluted N 1s XPS spectrum displayed the peak position corresponding to Fe/Co-N bond at 399.1 eV (~~Figure S6d),~~ which is near similar to the Fe-Co/N bond for NCAG/Fe-Co catalyst as reported by Chen *et al.* [11] but different from the Fe-N peak position (~398.3 eV)[12] and Co-N (~399.6 eV).[13] This not only emphasized the presence Fe-Co bond in our active system, but the difference of - 0.7 eV from Fe-N and + 0.5 eV from Co-N corroborated an obvious electronic interaction prevalent between the metal centers. The morphological properties were further analysed at a higher magnification in the transmission electron microscope (TEM) to obtain a fine carbonaceous sheet as shown in Figure 7.5a. Aberration-corrected high-angle annular dark-field scanning transmission electron microscopy (HAADF-STEM) characterizations were carried out and bright dots highlighted by yellow ellipses were identified, which are recognized as Fe-Co binary atoms dispersed within the carbon phase (Figure 7.5b). For further confirmation, a more cutting-edge characterization tool that is, XAS was adopted to investigate the oxidation states, bond lengths and local coordination around the metal centers was adopted, which has been discussed in the later section.

7.3.2 Estimation of the chemical bonds and local coordination environment of the active site

7.3.2.1 Fourier transform infrared (FTIR) survey of the FeCoDACys catalyst illustrating the non-metallic bonds

The FTIR spectrum of FeCoDACys catalyst in Figure 7.5c discloses all the non- metallic bonds that constitute the basic framework of the catalyst. More precisely, apart from C=C stretching vibration at 1640 cm^{-1}, the stretching frequencies at 1162 and 1304 cm^{-1} correspond to the –S-N and -C=S bonds that establish the proper S doping in the active catalyst forming the -C-S-N moiety[26] citation issue On the other hand, the characteristic peak at 1466 cm^{-1} denotes the C-N bond stretching. These data predict the presence of two different coordination environment of the N atoms to which the central bimetals are adhered as already shown in Figure 7.1g.

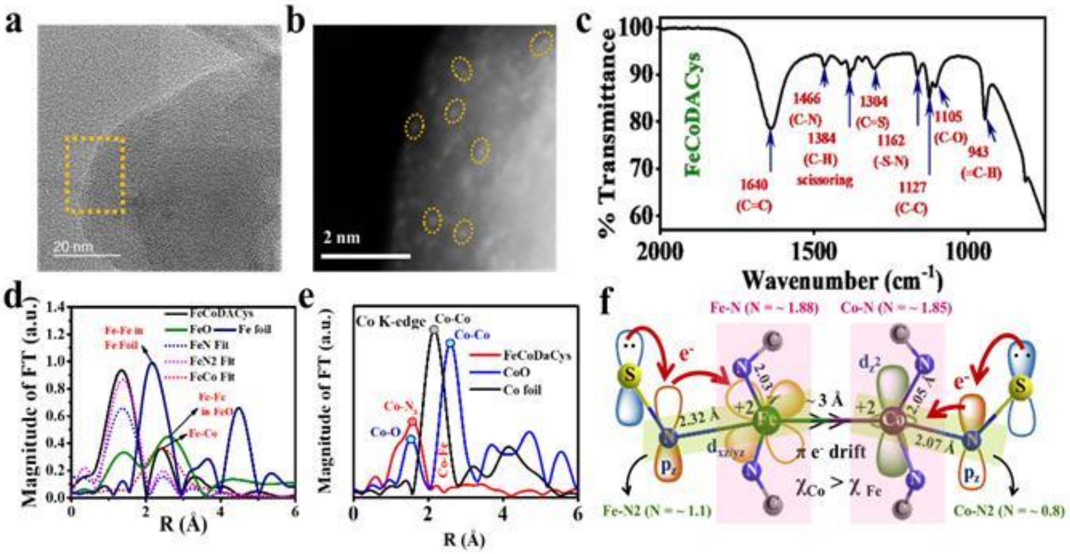

Figure 7.5. *(a) TEM image of FeCoDACys catalyst; (b) HAADF-STEM image of FeCoDACys catalyst (Fe-Co single atoms are marked with yellow ellipse); (c) (FTIR) spectrum of FeCoDACys; Fourier transforms of (d) k^3-weighted Fe and (e) k^3-weighted Co k-edge EXAFS experimental data for FeCoDACys and standard samples; (f) Proposed architecture of the active site part of FeCoDACys with bond lengths, coordination numbers and oxidation states of the concerned metals.*

7.3.2.2 XAS analysis of the material depicting the coordination bonds associated with the metal centers

Furthermore, the atomic coordination environment and the chemical state of the species (Fe, Co, N and S) at atomic level in the carbon matrix are confirmed by X-ray absorption spectroscopy (XAS) measurements. The (FTs) having k^3-weighted EXAFS spectrum of FeCoDACys at Fe K-edge shows an intense peak at 1.49 Å, which is due to the presence of Fe–N coordination in the carbon matrix.[14] The proclamation of Fe-Co metal-metal bond is advocated due to the peak at ~2.5 Å, which is different from what is obtained for

Fe-Fe (2.2 Å) from Fe foil and Fe-Fe (2.6 Å) from FeO (standard samples). The EXAFS data for FeCoDACys was further shell-fitted with Fe-Co bond (red dotted line in Figure 7.5d), which displayed an identical peak position as that of Fe-Co obtained for our material at 2.5 Å.

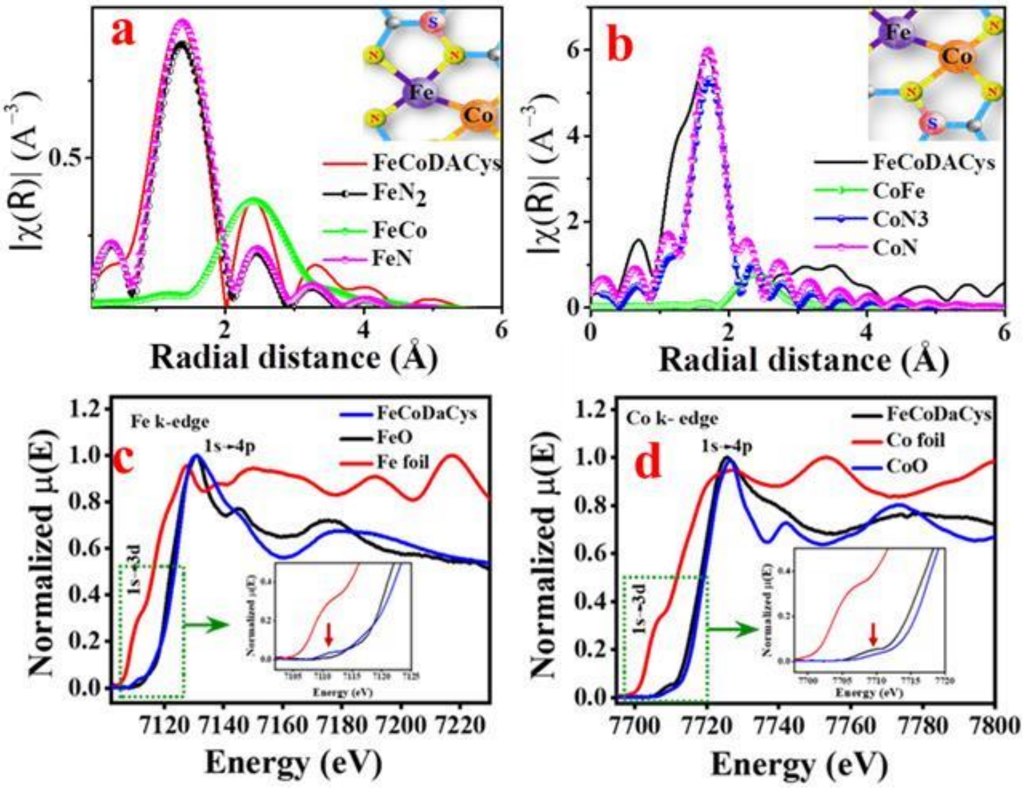

Figure 7.6. *(a) Fitting of FT-EXFAS signal for Fe K-edge (b)Fitting of FT-EXFAS signal for Co K-edge . The normalized XANES spectra of (c) Fe k-edge (inset shows enlarged pre-edge peaks) and (d) Co k-edge (inset shows enlarged pre-edge peaks) of FeCoDACys and all the standard samples*

Table 7.1. Different parameters obtained from the EXAFS fitting of FeCoDACys catalyst

Scattering Pair	Coordination (N)	R (Å)
Fe-N	1.88±0.30	2.03 ±0.030
Fe-N2	1.11±0.73	2.32±0.035
Fe-Co	1.23±0.42	3.01±0.085
Co-N	1.85±0.36	2.05±0.018
Co-N3	0.8±0.22	2.07±0.025
Co-Fe	1.15±0.53	3.34±0.089
N is the coordination number and R is the distance between absorber and back-scattered atoms.		

This is an indication that there was no self-aggregation of metals (Fe-Fe) in the FeCoDACys catalyst molecule.[15] There was also no trace of Fe-O (1.38 Å) or Fe-S (1.8 Å) bonds for FeCoDACys, which confirms that Fe was directly coordinated to N and Co atoms only in the first coordination sphere as revealed from Figure 7.5d. The FTs with k^3 weighted EXAFS spectrum at Co K-edge (Figure 7.5e) reveal the main peak at 1.5 Å, which is attributed to Co-N bond and the peak of Co-Fe (2.2 Å) further confirms the formation of metal-metal bond with no extra undesirable peaks for Co-O or Co-S (1.8 Å).[16],[17],[18] This deviation is certainly the indication of the N-S bond in the second coordination sphere of both the metals (Figure 7.5f), which is in accordance with the FTIR spectral data. The quantitative fitting of the EXAFS curves (Figure 7.6a-b) predicts that the coordination of both the metals is localized with one metal-metal bond and three N atoms, out of which two different M-N bond lengths are evidenced (Table 7.1).

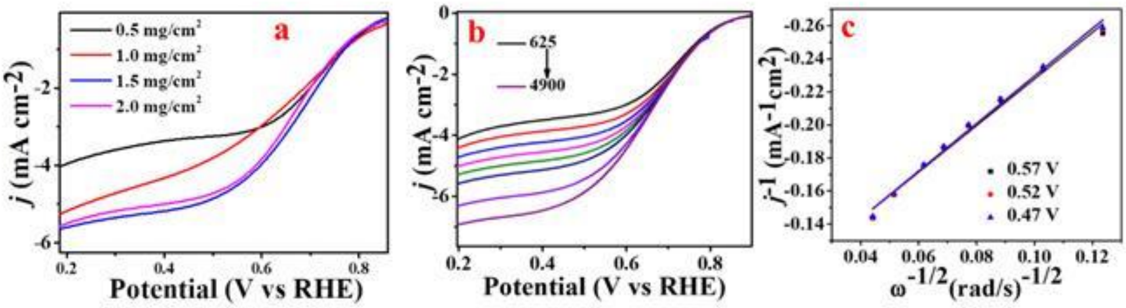

Figure 7.7. *(a) Mass loading optimization of FeCoDACys catalyst toward ORR (b) LSV polarisation curve for FeCoDACys electrocatalyst at rotating speed from 625 to 4900 rpm at a scan rate of 10mVs^{-1} (c) the K-L plot of the catalyst at different potentials.*

The X-ray absorption near edge structure (XANES) spectra of the FeCoDACys catalyst at Fe and Co K-edges reveal ~ +2 oxidation states of the Fe and Co species in the FeCoDACys catalyst both from the edge and pre-edge peak positions (Figure 7.6c-d). Interestingly, appearance of a well-defined pre-edge peak is possible for a non-centrosymmetric system where there is a p-d mixing of the metal orbitals. For our material in both the Fe and Co k-edge spectra, the prominent pre-edge peaks (denoted by red arrow, at 7112 eV for Fe k-edge and 7709 eV for Co k-edge of FeCoDACys) depicted that the surrounding of the metal centres were not symmetric with four N atoms. This gave an indication of the presence of metal-metal bond, which was subsequently established by the extended X-ray absorption fine structure (EXAFS) and Fourier transform (FT) k^3-weighted spectra.

7.3.2.3 Plausible electronic interactions prevalent in the active center leading to non-identical M-N bond lengths

Co, being more electronegative than Fe (χ_{Co} = 1.88, χ_{Fe} = 1.83) directs the electron drift towards itself, leaving Fe being partially positive in charge. This situation is although good for OER but uncooperative for ORR and here is why we incorporated S in the system. S has a predominant +R (R = resonating) effect owing to which it delivers its lone pair of electrons toward Fe via the vacant p-orbital of N directed perpendicular to the sp^2-conjugated system. But, the Fe-N-S interaction only compensates the electron loss over the Fe site to make it appropriate for ORR, whereas, a different story lies on the other side. The Co-N bond length (for Co-N-S) being shorter than Fe-N (for Fe-N-S), the +R effect of S is stronger here, leading to an excess of electron density over Co, beneficial for the initial metal-oxidative steps of OER at the cost of low Gibbs free energy change.

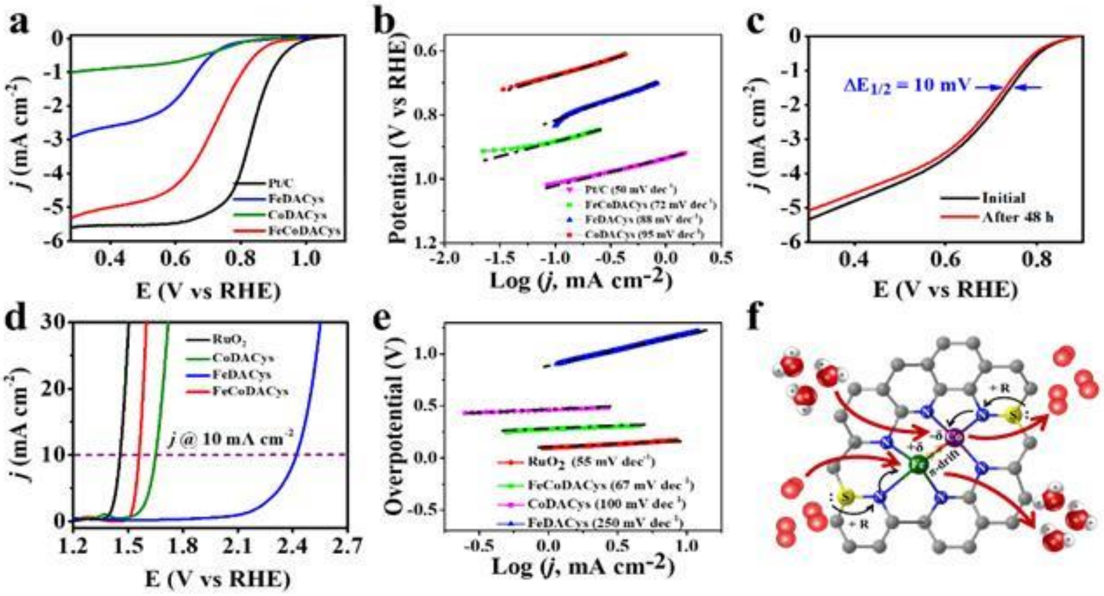

Figure 7.8. *(a) LSV polarization curves for ORR of the as-synthesized catalysts and 20% Pt/C in O_2 saturated 0.1 M KOH solution at a scan rate of 10 mV s^{-1} at a rotation speed of 1600 rpm; (b) Comparative tafel slope of FeCoDACys, Pt/C and all control catalysts for ORR extracted from LSV polarization curve taken in O_2 saturated 0.1 M KOH solution at 1 mV s^{-1}; (c) LSV for FeCoDACys catalyst before and after stability for 48 h; (d) OER polarization curves of all the catalysts; (e) Tafel slope for OER extracted from LSV polarization curves of all the concerned catalysts, taken at 1 mV s^{-1}; (f) Schematic representation of the ORR and OER processes occurring at the respective Fe and Co active sites.*

7.3.3 Electrochemical bifunctionality of the FeCoDACys catalyst (Catalytic reduction of oxygen and decomposition of water)

The performance of FeCoDACys catalyst toward the electrocatalytic reactions such as ORR and OER was assessed in a three-electrode set-up where all the potential values are designated with respect to reversible hydrogen electrode (RHE). The linear sweep voltammetry (LSV) measurements of our catalyst and the controlled samples with rotating ring disk electrode (RRDE) reveal that in O_2 saturated 0.1 M KOH electrolyte, FeCoDACys catalyst forecasted a half-wave oxygen reduction potential ($E_{1/2}$) of 0.74 V with the optimized mass loading of 1.5 mg cm^{-2} (Figure 7.7a).

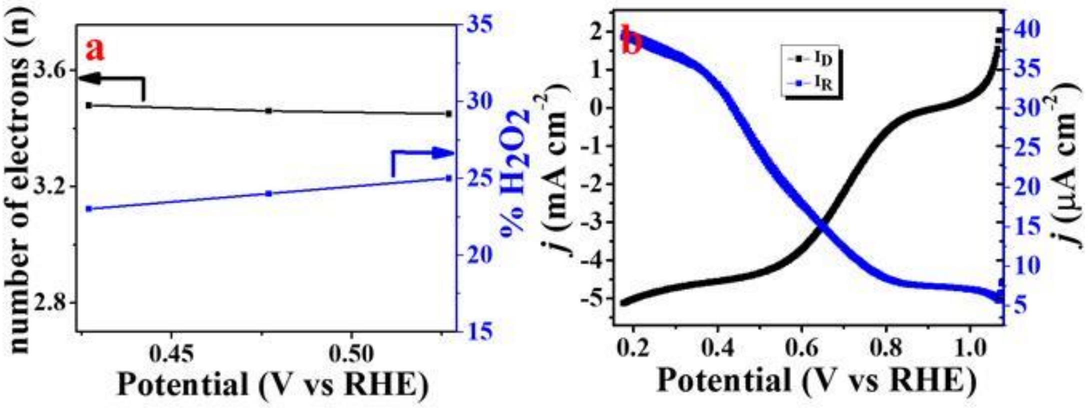

Figure 7.9. *(a) H_2O_2 tolerance and number of electrons taking part in the ORR for FeCoDACys catalyst (b) LSV polarization curves of FeCoDACys catalyst corresponding to ring (blue) and disc (black) currents in 0.1 M KOH at 1600 rpm*

A properly linear K-L plot was obtained from the LSV curves of the FeCoDACys catalyst at different rotation speeds (Figure 7.7b) suggesting a first-order kinetics of the concentration of dissolved oxygen[19] (Figure 7.7c). The kinetics of the ORR process was assessed from the intercept of the K-L plot that suggested a kinetic current density (J_k) of our active material FeCoDACys to be 11.64 mA cm^{-2}. The catalyst potential stood out to be the best as compared to FeDACys and CoDACys, where these catalysts are prepared following the same procedure as FeCoDACys but using only Fe and Co salts respectively (Figure 7.8a). This proves that there is certainly some role of the bimetallic bond, which is so far acknowledged as the "synergistic effect". A near similar diffusion limiting current density of -5.3 mA cm^{-2} for FeCoDACys and -5.6 mA cm^{-2} of Pt/C catalyst advocate a plentiful number of exposed active sites causing high oxygen diffusion rate onto the electrode surface.[20,21] The mass-transport corrected Tafel slope in Figure 7.8b (72 mV dec^{-1}) for FeCoDACys confirmed a much faster rate of transfer of the first electron from the catalytically active site to the oxygen molecule for initiating the ORR process, better than the control catalysts (FeDACys and CoDACys). The stability for ORR was run for 48 h and the corresponding LSV for before and after stability was recorded and a change of only 10 mV potential were observed which is shown In Figure 7.8c Similarly, as expected, FeCoDACys outperformed all the controlled samples with respect to OER potentials at 10 mA cm^{-2} as evident from Figure 7.8d. The kinetics of the electrochemical OER were investigated from Tafel slope analysis (Figure 7.8e). A schematic representation of the ORR and OER processes occurring at the respective Fe and Co active sites are shown In Figure 7.8f. A tabulated form for all the reported catalyst towards $E_{1/2}$ for ORR, Limiting Current density (J_L), $E_{j=10 \text{ mA cm-2}}$ for OER is shown in Table 7.2.

Table 7.2. Catalysts performances on the basis of electrocatalytic parameters for ORR and OER.

Catalysts	**Electrolyte**	**$E_{1/2}$ for ORR (V vs RHE)**	**Limiting Current density (J_L) (mA cm^{-2})**	**$E_{j=10 \text{ mA cm-2}}$ for OER (V vs RHE)**
FeCoDACys	0.1 M KOH for ORR and 1 M KOH for OER	0.74	-5.3	1.53
FeDACys		0.72	-4.29	2.41
CoDACys		0.70	-3.28	1.65
Pt/C		0.85	-5.6	-
RuO_2		-	-	1.43

An almost 4-electron reaction pathway of the ORR kinetics was verified on the basis of ~ 25% H_2O_2 formation on the disk and its detection on the ring at fixed ring potentials during RRDE measurements (Figure 7.9a). LSV polarization curves of FeCoDACys catalyst corresponding to ring currents in 0.1 M KOH at 1600 rpm Is shown In Figure 7.9b. This was also supported by the smaller charge transfer resistance in the electrochemical impedance spectra (EIS) of FeCoDACys as compared to FeDACys and CoDACys enabling a faster kinetics towards ORR (Figure 7.10a). Furthermore, the superior stability of FeCoDACys catalyst (~ 93 % retention of initial current density after 48 h of chronoamperometric run), which is assumed to be for the presence of Co[11] (Figure 7.10b) stands well in competition with the commercial Pt/C catalyst (Figure 7.10c). To establish the role of Co in enhancing the stability of our active catalyst, 12 h of continuous chronoamperometric run was performed with FeDACys and CoDACys. As shown in Figure 7.10d, while FeDACys catalyst exhibited 73 % of the initial current density, CoDACys displayed 86 % retention of the initial current density. This corroborates with our claim that the presence of Co with Fe in our final active material FeCoDACys improved the stability of our catalyst to 95 % after 12 h. This was corroborated with the LSV polarization curve before and after 48 h of stability test, which showed a deterioration of only 10 mV of the initial $E_{1/2}$ value (Figure 7.8c).

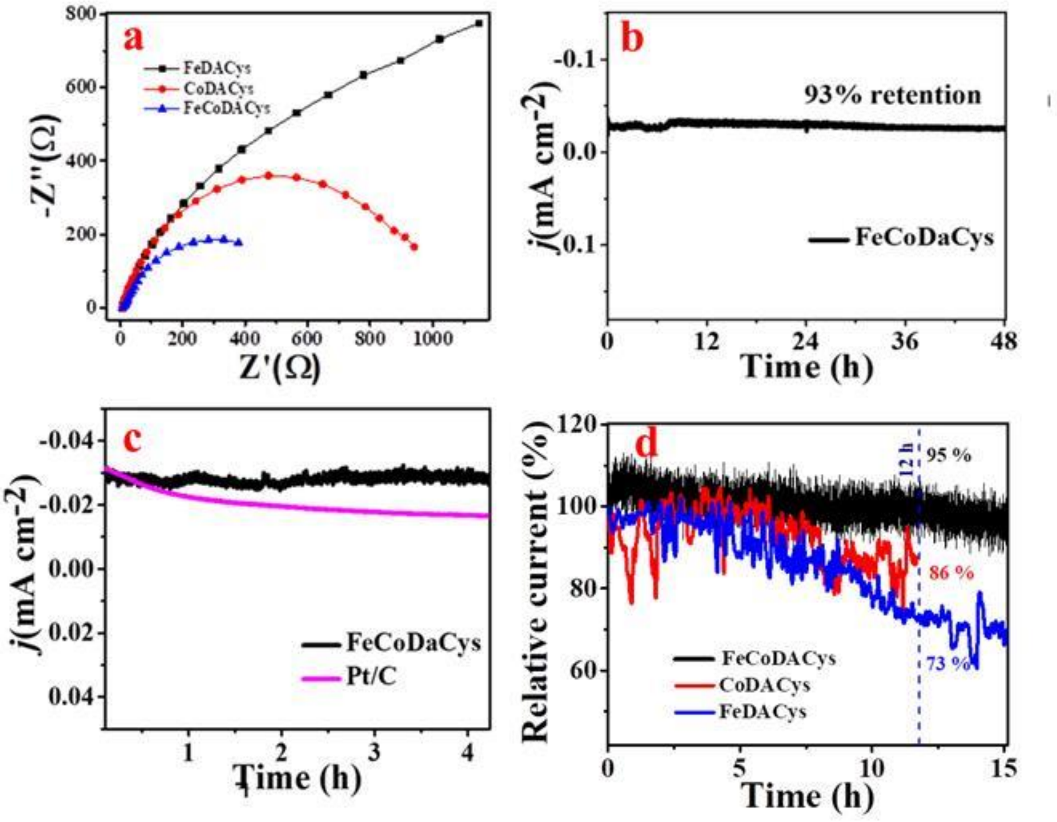

Figure 7.10. *Electrochemical impedance spectra recorded in 0.1 M KOH for all the control samples along with FeCoDACys catalyst (b) Chronoamperometry to check the stability of the sample for 48 h; (c) Comparitive plots showing better stability of FeCoDACys catalyst over the state-of-the-art Pt/C catalyst within ~ 4 h of chronoamperometric run (c) Stability (Chronoamperometry) in terms of relative current (%) of FeDACys, CoDACys and FeCoDACys catalysts towards ORR.*

Thus, although our catalyst lags a few units behind the commercial benchmark catalyst with respect to $E_{1/2}$, but it is far more competent in terms of catalyst stability and durability.

Table 7.3. Comparison table of FeCoDACys catalyst with previously reported binary (Fe,Co) metal based bifunctional electrocatalysts and OER.

Catalyst	**E_{10} (V vs RHE)**	**$E_{1/2}$ (V vs RHE)**	**ΔE**	**References**
$[Ni_{5.7}Ru_{0.3}(HHTP)_3(H2O)_x]n$	1.62	0.68	0.94	***Chem. Commun.***, 2020,**56**, 13615-13618
3D HNG	1.69	0.95	0.74	*Small Methods* 2018, 2,1800144
N, P /CoS_2@TiO_2NPFs	1.49	0.91	0.58	*Adv. Funct.Mater. 2018,28, 1804540*
Co-Ni-S@NSPC	1.7	0.82	0.88	*Carbon* 146(2019) 476-485

Co@Co_3O_4@NC-900	1.60	0.8	0.8	*J. Mater.Chem. A,2018, 6, 1443–1453*
Ni_3Fe/N-C sheets	1.60	0.90	0.7	*Adv. EnergyMater. 2017,7, 1601172*
NiFe-LDH/Co,NCNF	1.54	0.79	0.75	*Adv. Energy Mater. 2017,7, 1700467*
B and N dopants (B, N carbon)	1.56	0.88	0.76	*Adv. Sci.* ***2018,*** *5 (7), 1800036.*
N-HC@G-900	1.58	0.72	0.86	*Angew. Chem. Int. Ed.* ***2018,*** *57 (50), 16511-16515.*
Al_2O_3@Co/NG-800	1.58	0.9	0.68	*J. Power Sources* ***2017,*** *353, 28-39.*
$Sm_{0.5}Sr_{0.5}CoO_3$-δ – N Doped Graphene	1.63	0.81	0.82	*Small* ***2018,*** *14 (48), 1802767.*
N-doped ordered mesoporous carbon N-OMC_2	1.72	0.89	0.82	*J. Energy Chem.* ***2017,*** *26 (3), 422-427*
$ZnCo_2O_4$ / rGO	1.55	0.87	0.68	*Int. J. Hydrogen Energ.****2019,*** *44 (3), 1565-1578*
$YBaCo_4O_{7.3}$	1.68	0.68	1	*J. Mater. Chem. A* ***2019,*** *7 (1), 330-341.*
Co_3O_4/CNTs	1.54	0.88	0.66	*Sci. Rep.* ***2018,*** *8 (1), 2543*
RuO_2	1.79	0.79	1	*Nature Nanotechnol.* ***2015,*** *10, 444.*
NiFeCo-LDH	1.57	0.63	1.05	*Adv.Energy Mater.* ***2015,*** *5 (13), 1500245*
FeCo-ISAs/CN	No OER	0.92	-	*Chem. Commun., 2018,54, 4274-4277*
(Fe,Co)/CNT	No OER	0.881	-	*Energy Environ. Sci., 2018,11, 3375-3379*
N-GCNT/FeCo-3	1.73	0.92	0.81	*Adv. Energy Mater. 2017, 1602420*
FeCo/N-DNC	1.62	0.81	0.81	*Nanoscale 2018, 10, 19937*
FeCo/NPC	1.68	0.81	0.87	*ChemElectroChem 2019, 6, 1824*
FeCo@NCNS	1.597	0.827	0.772	*Electrochim. Acta 2020, 335, 135647*
CoFe/N-GCT	1.66	0.78	0.88	*Angew. Chem. Int. Ed. 2018, 57, 16166 – 16170*
FeCoDACys	**1.53**	**0.74**	**0.79**	**This work**

A mutual interaction (electron drift) between the Fe-Co bimetallic centers and the impact of local coordination consisting of electronegative dopants are likely to be responsible for the aforesaid observations facilitating facile adsorption and desorption of the reactants and products respectively.

7.3.4 Applicability of FeCoDACys catalyst in Zinc-air battery.

FeCoDACys catalyst possesses a reasonably low potential difference (ΔE) of 0.79 V between OER @10 mA cm^{-2} and ORR potential at $E_{1/2,}$ which suggests that the electrocatalyst holds good reversible activity for both OER and ORR (Figure 7.11a).

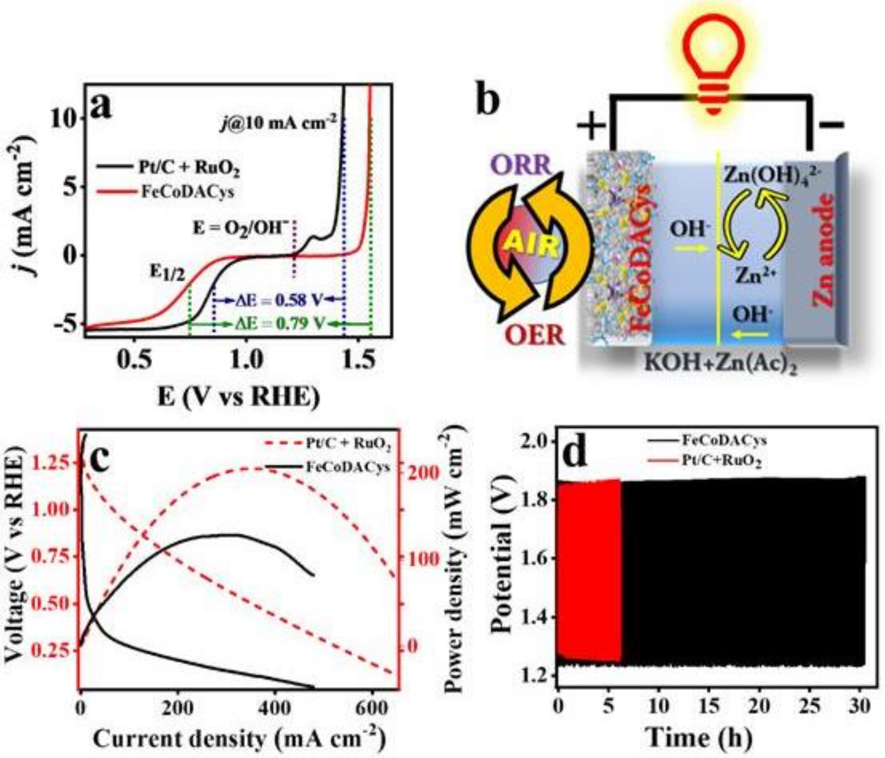

Figure 7.11. *(a) ΔE of FeCoDACys catalyst showing both ORR and OER activity. (b) Schematic representation for Zn-air battery assembled in a two-electrode system showing the bifunctional activity of the catalyst. (c) Polarization curve and power density plot of FeCoDACys and Pt/C+*RuO_2 *as cathode catalysts (1.5* $mgcm^{-2}$*) (d) Cycling stability of FeCoDACys catalyst and comparison with Pt/C+*RuO_2 *catalyst.*

The admirable OER and ORR activity of FeCoDACys catalyst as compared to the other controlled samples as well as the similar reported catalysts (Table 7.3) encouraged us to implement it as a cathode material in rechargeable Zn-air battery. A schematic diagram for Zn-air battery assembled in a 2-electrode system demonstrating bifunctional oxygen electrolysis of the catalyst FeCoDACys is shown in Figure 7.11b. The Zn-air battery performance of the bifunctional catalyst (FeCoDACys) was compared to the commercially used Pt/C+RuO_2 catalyst using Zn foil as the anode in a 6 M KOH + 0.2 M

$Zn(CH_3COO)_2$ solution. This electrolyte concentration was maintained for all the battery related studies done in this work. The open-circuit potential of FeCoDACys catalyst was found to be 1.26 V. The battery displayed a current density of ∼480 mA cm^{-2} and peak power density of ∼125 mW cm^{-2} with FeCoDACys catalyst as compared to Pt/C+RuO_2 (~643 mA cm^{-2} and 205 mW cm^{-2} respectively), shown in Figure 7.11c. The battery cycling stability of FeCoDACys and Pt/C+RuO_2 cathodes were further conducted at a current density of 2 mA cm^{-2} (Figure 7.11d) for 23 h. To our delight, the Zn-air battery stability for FeCoDACys catalyst showed a significant retention of the initial charge-discharge profile, depicting a better candidature of FeCoDACys catalyst than Pt/C+RuO_2 in terms of long duration of stable battery performance.

7.3.5 Electronic interplay between Fe and Co and distinct role of S dopant towards oxygen electrocatalysis

Herein, the catalyst FeCoDACys is consistent with distinct Fe and Co metal centers active toward ORR and OER, respectively, and the catalytic performance increases drastically upon metalation between Fe and Co (Fe-Co binary metal centers, equation 7.1 and 7.2).

$$Fe^{3+} + e^- \rightarrow Fe^{2+} \quad E = +0.77\,V \tag{7.1}$$

$$Co^{3+} + e^- \rightarrow Co^{2+} \quad E = +1.82\,V \tag{7.2}$$

From the electrochemical potentials of the two redox systems ($Fe^{2+/3+}$ and Co $^{2+/3+}$), it is convincing that Fe can cause an effective ORR than Co centre as Fe oxidises at a lower potential than cobalt.[22],[15] Moreover the +R effect of the S through N atom donates electron density towards Fe enabling facile oxygen adsorption onto Fe centre (as shown in Step-1 of Figure 7.12). The initiation of ORR occurs via synergistic σ-bonding and π-π non-interacting coupling interactions[23] between the chemisorbed O_2 and active Fe site (square planar d^6 system). This is followed by a series of superoxo and hydroperoxyl intermediates. The alkaline pH used in this study stabilizes the Fe-OOH^- intermediate and the reaction is kinetically primed towards the 4-electron product (OH^-) (Step-2). [24],[25] From the electrochemical potential values for Fe and Co redox couples, it is assumed that for the initiation of OER, adsorption of OH^- is favored over Fe (Step-4) with a subsequent partial bridging of the OH^- with the adjacent Co atom and a transient intermediate state is formed with a prevalent electron cloud over the Fe-OH-Co centers (Step-5). This step is crucial to switch over the OER process on the Co active site (square planar d^7 system). The intentional incorporation of electronegative N and S atoms induces electron density towards Co through +R effect (Step-6). The abundance of electrons enables Co to attain the higher oxidation state of +4 [26] during the initial stages of OER with a low positive onset potential (Step-7). This is the probable reasons why OER is not favorable on Fe surface, because, owing to a greater Fe-N-S bond distance, (as revealed from XAS data) the electronic interaction for Co is likely restricted in the case of Fe where the electronic movement from N and S atoms only negates the positive charge density formed over Fe. The release of dioxygen from Co surface, the rate determining step of OER,[26] is triggered due to the electron drift from Fe (d_{z^2}) to Co (d_{z^2}) enhancing the overall kinetics of the OER process (Step-8,9). Thus, the overpotential $\Delta E_{(ORR\text{-}OER)}$ for the cathode-anode processes is found to be lower in the case of Fe-Co bimetallic system than distinct Fe and Co single metal active centers as strongly evident from the electrochemical data. Therefore, it is clear that the presence of M-N-S moiety in Fe-Co binary metal active center actually triggered the performances of the FeCoDACys electrocatalyst.

From the electrochemical potentials of the two redox systems ($Fe^{2+/3+}$ and $Co^{2+/3+}$), it is convincing that Fe can cause an effective ORR than Co centre as Fe oxidises at a lower potential than cobalt.[22],[15] Moreover the +R effect of the S through N atom donates electron density towards Fe enabling facile oxygen adsorption onto Fe centre (as shown in Step-1 of Figure 7.12). The initiation of ORR occurs via synergistic σ-bonding and π-π non-interacting coupling interactions[23] between the chemisorbed O_2 and active Fe site (square planar d^6 system). This is followed by a series of superoxo and hydroperoxyl

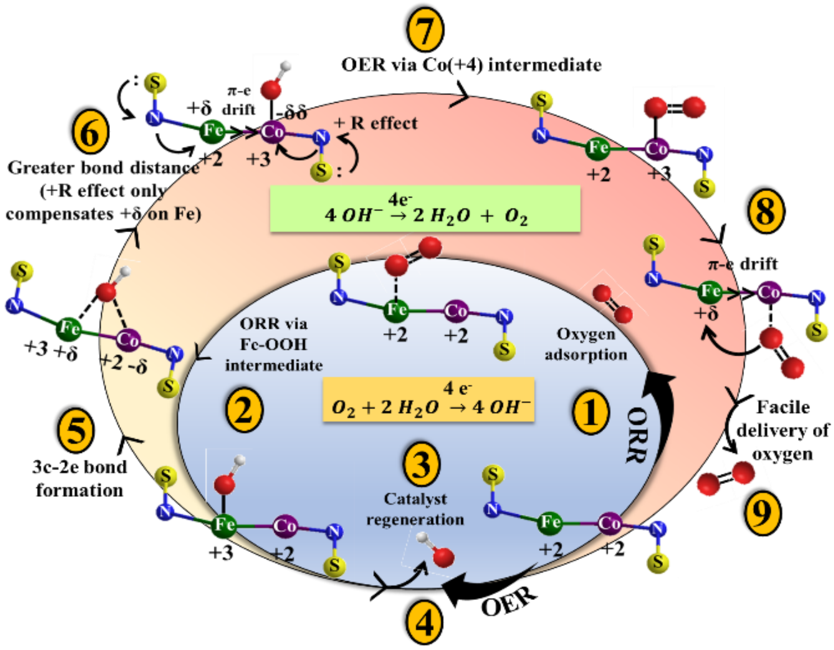

Figure 7.12. *Stepwise mechanistic illustration of ORR (blue circle) and OER (pink circle) over active sites of the catalyst.*

intermediates. The alkaline pH used in this study stabilizes the Fe-OOH$^-$ intermediate and the reaction is kinetically primed towards the 4-electron product (OH$^-$) (Step-2). [24],[25] From the electrochemical potential values for Fe and Co redox couples, it is assumed that for the initiation of OER, adsorption of OH$^-$ is favored over Fe (Step-4) with a subsequent partial bridging of the OH$^-$ with the adjacent Co atom and a transient intermediate state is formed with a prevalent electron cloud over the Fe-OH-Co centers (Step-5). This step is crucial to switch over the OER process on the Co active site (square planar d^7 system). The intentional incorporation of electronegative N and S atoms induces electron density towards Co through +R effect (Step-6). The abundance of electrons enables Co to attain the higher oxidation state of +4 [26] during the initial stages of OER with a low positive onset potential (Step-7). This is the probable reasons why OER is not favorable on Fe surface, because, owing to a greater Fe-N-S bond distance, (as revealed from XAS data) the electronic interaction for Co is likely restricted in the case of Fe where the electronic movement from N and S atoms only negates the positive charge density formed over Fe. The release of dioxygen from Co surface, the rate determining step of OER,[26] is triggered due to the electron drift from Fe (d_{z^2}) to Co (d_{z^2}) enhancing the overall kinetics of the OER process (Step-8,9). Thus, the overpotential $\Delta E_{(ORR\text{-}OER)}$ for the cathode-anode processes is found to be lower in the case of Fe-Co bimetallic system than distinct Fe and Co single metal active centers as strongly evident from the electrochemical data. Therefore, it is clear that the presence of M-N-S moiety in Fe-Co binary metal active center actually triggered the performances of the FeCoDACys electrocatalyst.

7.4 Conclusions

In conclusion, we successfully synthesized the FeCoDACys catalyst where the Fe-Co bond with adjacent N and S coordination formed the S-N-Fe-Co-N-S moiety, which actually served as the electroactive unit for ORR and OER. Henceforth, we identified the strengthened electronic interaction between the symmetry matched a_{1g} orbitals of square-planar Fe and Co atoms respectively in the Fe-Co bimetallic system resulting in Fe$^{+(2+\delta)}$ and Co$^{+(3-\delta)}$, which has been so far considered as the “synergistic effect” between the metals. The presence of M-N-S moiety in the bimetal doped carbon matrix increased the reactivity of the metal centers by directing the electron flow toward the metals via +R effect, which stabilized the ORR and OER intermediates at an optimum binding energy. This work thus provides elaborate chemistry of the entire structural finding as well as mechanistic approach occurring at the active site of the Fe-Co bimetallic centers benefitting the two important oxygen electrocatalysis reactions.

7.5 References

1. Das, S. K., Bhanja, P., Kundu, S. K., Mondal, S. & Bhaumik, A. Role of Surface Phenolic-OH Groups in N-Rich Porous Organic Polymers for Enhancing the CO2 Uptake and CO2/N2 Selectivity: Experimental and Computational Studies. *ACS Appl. Mater. Interfaces* **10**, 23813–23824 (2018).
2. Peña, A., Puerta, J., Guerrero, A., Cañizales, E. & Brito, J. L. Catalytic chemical vapor deposition synthesis of carbon aerogels of high-surface area and porosity. *J. Nanotechnol.* **2012**, 3010–3019 (2012).
3. Wang, J. *et al.* Space-confinement and chemisorption co-involved in encapsulation of sulfur for lithium-sulfur batteries with exceptional cycling stability. *J. Mater. Chem. A* **5**, 24602–24611 (2017).
4. Yang, Z. *et al.* Sulfur-doped graphene as an efficient metal-free cathode catalyst for oxygen reduction. *ACS Nano* **6**, 205–211 (2012).
5. Zhang, Y. *et al.* Rapid Synthesis of Cobalt Nitride Nanowires: Highly Efficient and Low-Cost Catalysts for Oxygen Evolution. *Angew. Chemie - Int. Ed.* **55**, 8670–8674 (2016).
6. Chen, P. *et al.* Metallic Co 4 N Porous Nanowire Arrays Activated by Surface Oxidation as Electrocatalysts for the Oxygen Evolution Reaction . *Angew. Chemie* **127**, 14923–14927 (2015).
7. Sarkar, S. *et al.* Universal Approach for Electronically Tuned Transition-Metal-Doped Graphitic Carbon Nitride as a Conductive Electrode Material for Highly Efficient Oxygen Reduction Reaction. *Inorg. Chem.* **59**, 1332–1339 (2020).
8. Wang, Y. *et al.* Porous cobalt-iron nitride nanowires as excellent bifunctional electrocatalysts for overall water splitting. *Chem. Commun.* **52**, 12614–12617 (2016).
9. Zhang, R., Cheng, S., Li, N. & Ke, W. N, S-codoped graphene loaded Ni-Co bimetal sulfides for enhanced oxygen evolution activity. *Appl. Surf. Sci.* **503**, (2020).
10. Sarkar, S. *et al.* Facile one step synthesis of Cu-g-C3N4 electrocatalyst realized

oxygen reduction reaction with excellent methanol crossover impact and durability. *J. Colloid Interface Sci.* **558**, 182–189 (2020).

11. Chen, Y. *et al.* Carbon aerogels with atomic dispersion of binary iron–cobalt sites as effective oxygen catalysts for flexible zinc–air batteries. *J. Mater. Chem. A* **8**, 11649–11655 (2020).
12. Zhang, J. *et al.* Tuning the Coordination Environment in Single-Atom Catalysts to Achieve Highly Efficient Oxygen Reduction Reactions. *J. Am. Chem. Soc.* **141**, 20118–20126 (2019).
13. Wang, Y. *et al.* Porous cobalt–iron nitride nanowires as excellent bifunctional electrocatalysts for overall water splitting. *Chem. Commun.* **52**, 12614–12617 (2016).
14. Shao, Q., Xu, L., Guo, D., Su, Y. & Chen, J. Atomic level design of single iron atom embedded mesoporous hollow carbon spheres as multi-effect nanoreactors for advanced lithium–sulfur batteries. *J. Mater. Chem. A* **8**, (2020).
15. Allen J. Bard and Larry R. Faulkner. Electrochemical Methods: Fundamentals and Applications, New York: Wiley, 2001, 2nd ed. *Russ. J. Electrochem.* **38**, 1364–1365 (2002).
16. Wang, J. *et al.* Design of N-Coordinated Dual-Metal Sites: A Stable and Active Pt-Free Catalyst for Acidic Oxygen Reduction Reaction. *J. Am. Chem. Soc.* **139**, 17281–17284 (2017).
17. Zitolo, A. *et al.* Identification of catalytic sites in cobalt-nitrogen-carbon materials for the oxygen reduction reaction. *Nat. Commun.* **8**, 957 (2017).
18. Song, S. *et al.* Operando X-ray spectroscopic tracking of self-reconstruction for anchored nanoparticles as high-performance electrocatalysts towards oxygen evolution. *Energy Environ. Sci.* **11**, 2945–2953 (2018).
19. Sarkar, S. *et al.* Unravelling the Role of Fe–Mn Binary Active Sites Electrocatalyst for Efficient Oxygen Reduction Reaction and Rechargeable Zn-Air Batteries. *Inorg. Chem.* **59**, 5194–5205 (2020).
20. Biswas, A., Sarkar, S., Das, M., Kamboj, N. & Dey, R. S. A No-Sweat Strategy for Graphene-Macrocycle Co-assembled Electrocatalyst toward Oxygen Reduction and Ambient Ammonia Synthesis. *Inorg. Chem.* **59**, 16385–16397 (2020).
21. Sarkar, S., Biswas, A., Kamboj, N. & Dey, R. S. Unveiling the Potential of an Fe Bis(terpyridine) Complex for Precise Development of an Fe-N-C Electrocatalyst to Promote the Oxygen Reduction Reaction. *Inorg. Chem.* **59**, 13453–13464 (2020).

22. Wang, J. *et al.* Synergistic effect of well-defined dual sites boosting the oxygen reduction reaction. *Energy Environ. Sci.* **11**, 3375–3379 (2018).
23. Gao, Q. *et al.* Monodisperse PdSn/SnOx core/shell nanoparticles with superior electrocatalytic ethanol oxidation performance. *J. Mater. Chem. A* **8**, 20931–20938 (2020).
24. Li, W., Yu, A., Higgins, D. C., Llanos, B. G. & Chen, Z. Biologically Inspired Highly Durable Iron Phthalocyanine Catalysts for Oxygen Reduction Reaction in Polymer Electrolyte Membrane Fuel Cells. *J. Am. Chem. Soc.* **132**, 17056–17058 (2010).
25. Li, J. *et al.* Structural and mechanistic basis for the high activity of Fe–N–C catalysts toward oxygen reduction. *Energy Environ. Sci.* **9**, 2418–2432 (2016).
26. Moysiadou, A., Lee, S., Hsu, C.-S., Chen, H. M. & Hu, X. Mechanism of Oxygen Evolution Catalyzed by Cobalt Oxyhydroxide: Cobalt Superoxide Species as a Key Intermediate and Dioxygen Release as a Rate-Determining Step. *J. Am. Chem. Soc.* **142**, 11901–11914 (2020).

Chapter 8

Conclusion and Future Prospective

Abstract: In this chapter, the whole work of the thesis and overall conclusion has been summarized. The degradation of the environmental condition due to the conventional energy technologies which are currently accomplished by fossil fuels is urgently needed to be addressed. This current energy scenario, non-renewable route for energy systems and global atmospheric conditions motivated us to work towards the generation of renewable fuel (hydrogen) and its applications. The current thesis highlights the facile synthesis of highly durable, low-cost and robust electrocatalyst for hydrogen generation from water. The generation of hydrogen via the electrolysis of water opens up an attractive route to store energy driven from solar power in a fully renewable fashion. So, the design of such an efficient catalysts that outperform the activity of established noble metals and can act as an electrode material for hydrogen evolution reaction (HER), oxygen evolution reaction (OER) and oxygen reduction reaction (ORR). We wish the readers find this work interesting and worth exploring towards the material designing in electrode fabrication for water oxidation processes in order to follow the path of sustainable energy.

8.1 Conclusion

The present thesis work consists of design and engineering of electrocatalysts for oxygen evolution, hydrogen evolution and oxygen reduction reactions aiming to achieve efficient and better activity of the electrocatalyst, which accelerates the energy generation, conversion and storage route in a fully renewable fashion.

The first part (**chapter 1**) of the thesis discusses the current energy demand and its global dependency. The environmental issues can only be addressed by replacing the conventional energy sources with some alternative energy sources, which are renewable as well as sustainable in nature. The production of hydrogen-based energy can be a way for the attainment of a sustainable energy system. In this context, the hydrogen-based economy and its different production techniques are discussed. Along with that, the benefits of electrochemical water splitting (hydrogen on cathode and oxygen on the anode) for hydrogen production over other production techniques are also highlighted. For the designing of the electrocatalyst in water splitting phenomena, various evaluation parameters such as overpotential, stability, Tafel slope and faradaic efficiency have also been briefly discussed in this chapter. The perks of the electrodeposition process for catalyst synthesis over the other methods for the synthesis are underlined in this chapter. An introduction to HER and OER and their mechanism along with reaction pathways are also covered in this section of the thesis. In order to achieve ~~the~~ energy generation (hydrogen production) in a renewable fashion, the importance of solar energy and the integration of solar power with the electrochemical water splitting unit is greatly emphasized. The introduction of metal-air battery (MAB) is highlighted which requires an electrocatalyst capable of oxygen reduction reaction (ORR) as well as oxygen evolution reaction (OER). The rational design and engineering of an electrocatalyst towards efficient HER, OER and ORR have been highlighted in this section. The rational importance of transition-metals (TMs) and heteroatom-doped nanocarbon-based electrocatalyst towards water splitting and ORR in order to supersede the benchmark Pt/C and RuO_2 catalyst, is focused in details. Various synthesis methods, instrumentation techniques for material characterization and electrochemical study performance have been explained in **chapter 2**. The physical characterization such as X-ray diffraction (PXRD), transmission electron microscopy (TEM), scanning electron microscopy (SEM), field emission scanning electron microscopy (FESEM), etc. for material characterization have been done before the electrochemical measurements. The electrochemical measurement techniques and the basics have been discussed in the following chapter.

Copper foam (Cuf) prepared by electrodeposition technique, is utilized as a working electrode in most of the work discussed in this thesis. Cuf as a substrate plays a crucial role in the activity of the catalyst as it provides plentiful active sites because of its 3D porous structure. Also, its dendritic structure is responsible for the superhydrophilic as well as aerophobic nature of the catalyst. First-row transition metals are earth-abundant materials and their derivatives such as sulphides, oxides, phosphides, selenides have emerged as highly efficient electrocatalysts for electrochemical water oxidation. Electrochemical deposition of single-phase nickel phosphide on galvanostatically deposited copper foam (Cuf@Ni_5P_4) core-shell nanostructure offers the innovation in structure designing and a new platform for novel electrocatalysts which is explained in **chapter 3**. The Cuf@Ni_5P_4 provided a superior three-dimensional conductive channel for ion transport during the catalysis process. The catalyst exhibited an excellent electrocatalytic activity towards hydrogen evolution reaction (HER) in acidic media. The superhydrophilic and aerophobic property of the porous electrode helps the in-time leaving of H_2 gas bubbles from the surface. The catalyst required a very less overpotential of 90 mV for HER at the current density of 10 mA cm^{-2}. The very small Tafel slope of 49 mV dec^{-1} and a very high exchange current density (~0.76 mA cm^{-2}) originated from large electrochemically active surface area and fast mass and electron transfer efficiency of the Cuf@Ni_5P_4 catalyst. Theoretical studies were carried out to investigate the mechanism underlying the HER activity in Cu-supported Ni_5P_4 at an atomic scale. DFT calculations suggest a very high negative Gibbs free energy change (ΔG_{H*}) in Ni_5P_4 (0001)/Cu(111) upon hydrogen adsorption, which is actually responsible for excellent HER activity of the catalyst. Furthermore, it showed remarkable durability of hydrogen generation under low (10 mA cm^{-2}) as well as high current density (160 mA cm^{-2}) for >84 hours with ~96% retention of overpotential in acidic media, establishing a low-cost and efficient catalyst for sustainable, future energy generation. But in order to utilize the catalyst in the industrial point of view, the particular catalyst must show the bifunctional activity towards HER and OER. Cuf@Ni_5P_4 electrocatalyst was further explored as a bifunctional material towards its activity in alkaline media in **chapter 4**. The full-cell attained a potential of 1.66 V to reach out a current density of 10 mA cm^{-2}. The Cuf@Ni_5P_4-based cell showed extraordinary stability in working electrolyte for 150 h at a current density of 10 mA cm^{-2} with 96% retention of its initial potential in alkaline media. The practice for the splitting of water in the presence of sunlight is highly recommended and admirable since this integrated system eliminates the use of grid power (which mostly comes from fossil fuels). The material was found to be super hydrophilic as well as aerophobic which resulted in stable electrodes for a solar-driven water-electrolysis system. Transition metal selenides have drawn growing attention in the field of water electrolysis due to their improved band structure. The electronegativity of selenium (2.55) is lesser than that of the sulphur (2.58) and oxygen (3.44), which helps to improve better covalency of the metal-chalcogen bond in selenide than sulphides and oxides. Higher covalency represents higher bond strength and as a result, metal selenides exhibit lower band gap and better electrical conductivity. In order to achieve lower full cell voltage, Cuf has been modified with electrodeposited cobalt selenide (Cuf@$Cu_2Se/CoSe_2$) is highlighted in **chapter 5**. The electrochemical cell composed of Cuf@$Cu_2Se/CoSe_2$ catalyst in a two-electrode system as an anode as well as a cathode showed high-performance overall water oxidation reaction with a very low applied potential of only 1.56 V at a current density of 10 mA cm^{-2}. The as-prepared electrode was proven to be superhydrophilic as well as aerophobic in nature. However, further improvement in the full cell voltage is still required for the practical implementation of electrocatalyst. The introduction of Ni layer in between Cuf and CoSe (Cuf@Ni-CoSe) further improved the HER and OER activity along with the improvement in 2-electrode full cell voltage have been discussed in **chapter 6**. The catalyst showed a full cell voltage of 1.52 V to attain a current density of 10 mA cm^{-2}. The catalyst active surface area was calculated to be 1070 cm^2 which is playing an important in the enhancement of the catalytic activity. The stability of the catalyst was found to be remarkable and suitable for the catalyst to be commercialized. Since, the solar power is dependent on climatic conditions that's why in order to get the hydrogen fuel in a non-sporadic fashion the water electrolyzer assembly must be integrated with some battery unit which can be accomplished using Zn-air battery. For, the realization of Zn-air battery, the design of an efficient electrocatalyst showing activity towards OER and ORR is essential which is highlighted in the next chapter.

Chapter 7 focuses on the approach for the search of nanocarbon-based electrocatalyst for bifunctional activities (ORR and OER) for metal-air batteries. Bi/tri-functional electrocatalyst have tremendous demand for renewable energy sources in order to provide the power to water electrolyzer units for the supply of hydrogen fuel in a non-sporadic fashion and thus avoid the dependency of water splitting on solar power and resume the hydrogen fuel generation during night time also. Binary transition metals are being widely regarded as active sites for bifunctional electrocatalytic reactions, but it is hard to explain the origin of their efficiency. There is plenty of room for exploration of the “synergistic effect” of the binary metals reinforcing electrocatalysis. This work is focused on the systematic navigation of the π-electronic interaction between the e_g and a_{1g} orbitals of square-planar Fe and Co atoms, respectively, in the Fe-Co bimetallic catalyst (FeCoDACys). An extended electronic play prevails in the system, where –S-N moiety is present with both the metals, which trigger the oxygen electrocatalysis reactions at the cost of a low overpotential. This enhanced catalytic performance of the material is further exploited for liquid state Zinc-air battery, where it delivered an open circuit potential of 1.26 V and a peak power density of ∼125 mW cm^{-2}. This versatile system opens up a new route for the generation of green fuel towards electrochemical hydrogen generation.

Thus, the water electrolyzer unit integrated with solar power and metal air batteries in order to receive hydrogen fuel in a fully renewable and non-sporadic fashion can be achieved by their proper assembly. Furthermore, the fuel cell fabrication to get the electricity using the produced hydrogen and oxygen gases is a sustainable and environment friendly route to gear up the green and clean energy system.

Table 8.1 Overall summary of the work included in the thesis.

Catalyst developed (work-wise)	**Highlights of the experiment**	**Result obtained**	**Room for the improvement**
WORK-1 Cuf@Ni_5P_4	HER in acidic medium	90 mV overpotential	Lack of bifunctionality for full water splitting
WORK-2 Cuf@Ni_5P_4	HER and OER in alkaline medium Hybridization of water electrolyzer with solar panel	1.66 V full cell potential Extraordinary stability in basic medium for 150 h	Applied potential for full water splitting can still be improved.
WORK-3 Cuf@$Cu_2Se/CoSe_2$	Phosphide to selenide transition for HER and OER	1.56 V potential for full water splitting Stability for 9 h	Full cell potential can be improved. Stability is also compromised.
WORK-4 Cuf@Ni-$CoSe_2$	Introduction of Ni layer to enhance charge transport	1.52 V full cell voltage 107 h stability	The H_2 production in a non-sporadic fashion. Battery development to generate fuel independent of climatic conditions
WORK-5 FeCoDACys	Development of bifunctional electrocatalyst (OER and ORR) and switch over to metal air battery	ΔE= 0.79 V	**Fully Renewable non-sporadic H2 fuel generation**

8.2 Future prospective

The main objective of the thesis is to generate fully renewable fuel in a very efficient and eco-friendly way. The proposed research basically focuses on designing and tailoring of an electrocatalyst that would generate uninterrupted H_2 fuel through self-powered water electrolysis system (using solar cell and a storage unit). There are still huge scope in the development of mutifunctional electrocatalyst and their electrocatalytic activity. The following points are a few scope in this directions as summarized below.

- Design of an electrocatalyst which imparts a full cell potential (2-electrode system) of <1.5 V and an excellent catalyst surface stability, which are key factors for commercial application.
- Design of the catalyst showing tri-functional activity towards HER, OER and ORR.
- The assembly of solar powered water electrolyzer and metal-air battery fabrication using tri-functional electrocatalyst.
- Storage of the produced hydrogen and their economy calculations (based on the photovoltaics power (efficiency, area of installation etc.) and hydrogen produced (Kg)) as compared to the existing fossil fuel-based economy.
- After the production of hydrogen and oxygen using water electrolysis, the device fabrication of fuel cell technologies using the stored hydrogen and oxygen is essential in achieving electric current in a renewable way since the fuel cell gives only water as a by-product upon combustion.
- Theoretical calculations of free energy changes to check the origin of the activity of the catalyst.

1. **M Das**, N Jena, T Purkait, N Kamboj, A De Sarkar, and R S Dey*, Single-phase Ni_5P_4-Copper foam superhydrophilic and aerophobic core-shell nanostructures for efficient hydrogen evolution reaction. (***J. Mater. Chem. A*, 2019,7, 23989-23999**)
2. **M Das**, N Kamboj, T Purkait, S Sarkar, and R S Dey*, Revealing the Structural Aspect of Ultrastable Self-Supportive Bifunctional Electrocatalyst for Solar-Driven Water Splitting. (***J. Phys. Chem. C* 2020, 124, 13525−13534**)
3. **M Das**, G Kumar, and R S Dey*, Electrochemical growth and formation mechanism of bimetallic transition metal selenide bifunctional electrocatalyst: A strategy for the development of efficient material for water electrolysis. **(ACS Applied Energy Materials doi.org/10.1021/acsaem.1c03497)**
4. **M Das**, Z Bashir, and R S Dey* Triggering the efficiency of water electrolysis by introducing Ni buffer layer between copper foam and electrodeposited cobalt selenide. **(Under revision in Inorganic chemistry)**
5. **M Das**,† Ashmita Biswas,† and R S Dey* Electrons on Play: Understanding the Synergism of Binary Transition Metals and Role of M-N-S Active Sites Towards Oxygen Electrocatalysis. 2021, **(Chem. Commun., 2022,58, 1934-1937)**
6. **M Das,** A Biswas, T Purkait, T Boruah, S Bhardwaj, S K Das, and R S Dey* The role of Dynamic Hydrogen Bubble Template Derived Honeycomb like Copper Foam in Energy Applications: Current Status, Trends, Technological Challenges and Future Prospects, **(Under revision in *J. Mater. Chem. A*)**
7. **M Das**†, Z B Khan†, N Kamboj, M Banerjee and R S Dey*, Facile single step Electrochemical growth of Ni_3P on carbon cloth for highly efficient hydrogen evolution reaction. **(Communicated in Journal of Electrochemical Society)**
8. **M Das**†, Z B Khan†, M Banerjee, A Biswas and R S Dey*, Three-dimensional nickel and copper-based foam-in-foam architecture as an electrode for efficient water electrolysis. **(Under review in Catalysis Today)**
9. N Kamboj, T Purkait, **M Das**, S Sarkar, K S Hazra, R S Dey*, Ultralong cycle life and outstanding capacitive performance of a 10.8 V metal free micro-supercapacitor with highly conducting and robust laser-irradiated graphene for an integrated storage device. (***Energy Environ. Sci.*, 2019,12, 2507-2517)**
10. T Purkait, G Singh, N Kamboj, **M Das**, R S Dey*, All-porous heterostructure of reduced graphene oxide–polypyrrole–nanoporous gold for a planar flexible

supercapacitor showing outstanding volumetric capacitance and energy density. **(*J. Mater. Chem. A*, 6, 22858–22869 (2018))**

11. S Sarkar, N Kamboj, **M Das**, T Purkait, A Biswas, R S Dey*, Universal Approach for Electronically Tuned Transition-Metal-Doped Graphitic Carbon Nitride as a Conductive Electrode Material for Highly Efficient Oxygen Reduction Reaction. (***Inorganic Chemistry*, 2020, 59, 1332-1339)**

12. S Sarkar, S S Sumukh, K Roy, N Kamboj, T Purkait, **M Das**, R S Dey*, Facile one step synthesis of Cu-g-C_3N_4 electrocatalyst realized oxygen reduction reaction with excellent methanol crossover impact and durability. **(*Journal of Colloid and Interface Science*, 2020, 558, 182–189)**

13. S Sarkar, A Biswas, T Purkait, **M Das**, N Kamboj, R S Dey*, Unravelling the Role of Fe–Mn Binary Active Sites Electrocatalyst for Efficient Oxygen Reduction Reaction and Rechargeable Zn-Air Batteries. **(*Inorganic Chemistry* 59 (7), 5194-5205)**

14. T Purkait, N Kamboj, **M Das**, S Sarkar, A De Sarkar, R S Dey* Electrochemically customized assembly of a hybrid xerogel material via combined covalent and non-covalent conjugation chemistry: an approach for boosting the cycling. (***Journal of Materials Chemistry A* 8 (14), 6740-6756)**

15. A Biswas, S Sarkar, **M Das**, N Kamboj, RS Dey*, A No-Sweat Strategy for Graphene-Macrocycle Co-assembled Electrocatalyst toward Oxygen Reduction and Ambient Ammonia Synthesis. (***Inorganic Chemistry* 59 (22), 16385-16397)**

16. S Bhardwaj, **M Das**, A Biswas, RS Dey *, Nanostructured Cu foam and its Derivatives: Emerging Materials for Heterogeneous Conversion of CO2 to Fuels. (***Sustainable Energy & Fuels*, 2021,5, 2393-2414)**

17. S K Das, S Shyamal, **M Das**, S Mondal, A Chowdhury, D Chakraborty, R S Dey, A Bhaumik* Metal-free Pyrene-based Conjugated Microporous Polymer Catalyst Bearing N and S-sites for Photo-Electrochemical Oxygen Evolution Reaction **(*Chemistry of frontiers*, doi.org/10.3389/fchem.2021.803860)**

18. S K Das, G Kumar, **M Das**, Ramendra Sundar Dey*A 2D Covalent Organic Framework as a Metal-free Cathode Material Towards Electrochemical Oxygen Reduction Reaction **(*Materials Today: proceeding, Volume 57, Part 1, 2022, Pages 228-233*)**

1. Book publication: *Carbonaceous Materials and Future Energy: Clean and Renewable Energy Sources, by Ramendra Sundar Dey, Taniya Purkait, Navpreet Kamboj,* ***Manisha Das*** CRC Press, Taylor & Francis Group, *2019,* ***(DOI: 10.1201/9781351120784, ISBN 978-0- 8153-4788-0).***

Workshops/Conference attended *Appendix* **B**

India International Science Festival (IISF 2020), Government of India	***2020***
CRICK Chemistry Symposium, IISER Mohali	***2019***
World Nano Congress on Advanced Science and Technology (WNCAST-2021)	***2021***
International Conference on Multidisciplinary Aspects of Materials in Engineering (ICMAME-2021) Oral presentation.	***2021***
RSC twitter conference 2020	***2020***

1. M Das, N Jena, T Purkait, N Kamboj, A De Sarkar, and R S Dey*, Single-phase Ni_5P_4-Copper foam superhydrophilic and aerophobic core-shell nanostructures for efficient hydrogen evolution reaction. (***J. Mater. Chem. A*, 2019,7, 23989-23999**)

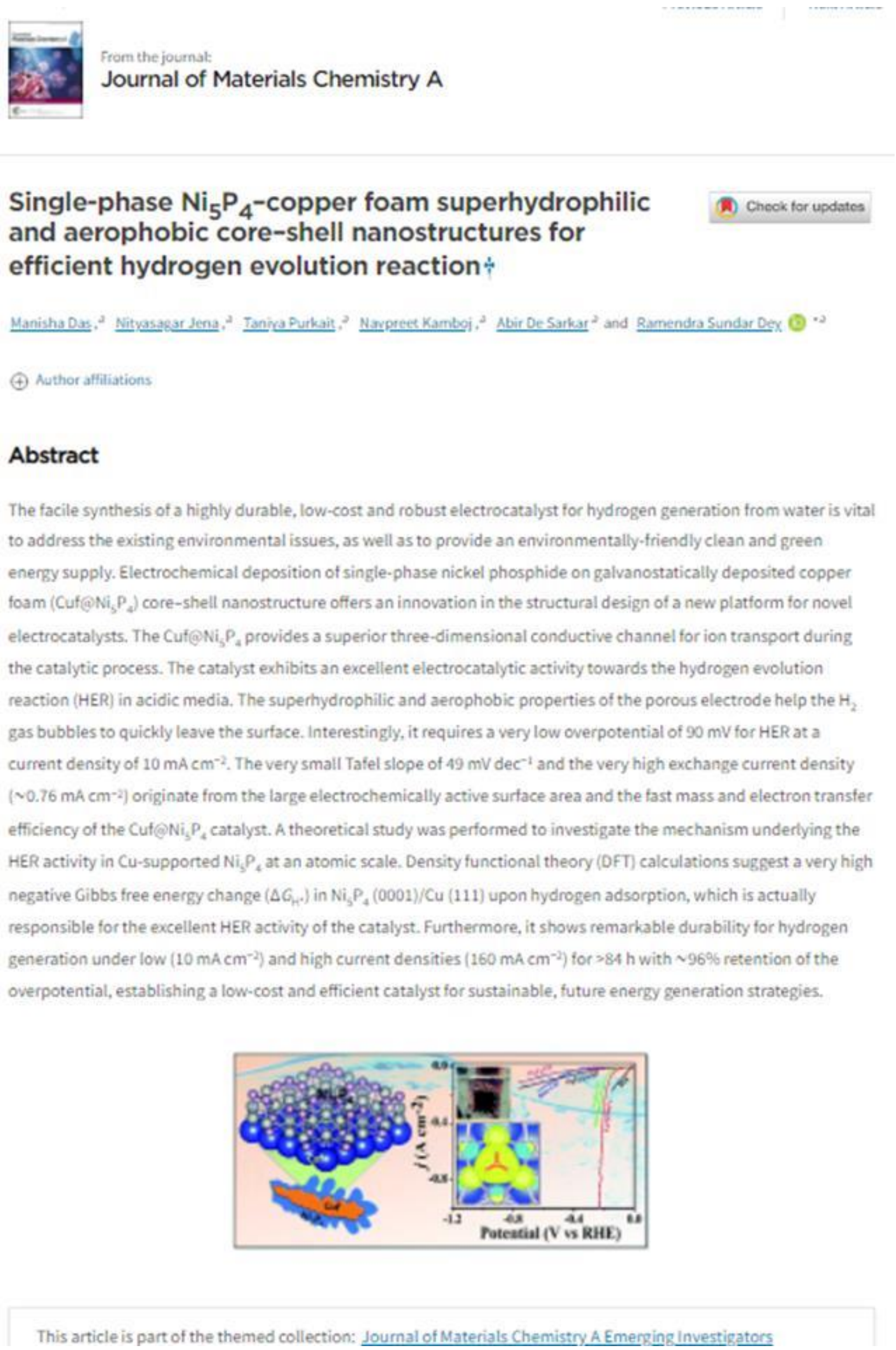

From the journal:
Journal of Materials Chemistry A

Single-phase Ni_5P_4-copper foam superhydrophilic and aerophobic core-shell nanostructures for efficient hydrogen evolution reaction†

Check for updates

Manisha Das,[a] Nityasagar Jena,[a] Taniya Purkait,[a] Navpreet Kamboj,[a] Abir De Sarkar[a] and Ramendra Sundar Dey *[a]

⊕ Author affiliations

Abstract

The facile synthesis of a highly durable, low-cost and robust electrocatalyst for hydrogen generation from water is vital to address the existing environmental issues, as well as to provide an environmentally-friendly clean and green energy supply. Electrochemical deposition of single-phase nickel phosphide on galvanostatically deposited copper foam (Cuf@Ni_5P_4) core–shell nanostructure offers an innovation in the structural design of a new platform for novel electrocatalysts. The Cuf@Ni_5P_4 provides a superior three-dimensional conductive channel for ion transport during the catalytic process. The catalyst exhibits an excellent electrocatalytic activity towards the hydrogen evolution reaction (HER) in acidic media. The superhydrophilic and aerophobic properties of the porous electrode help the H_2 gas bubbles to quickly leave the surface. Interestingly, it requires a very low overpotential of 90 mV for HER at a current density of 10 mA cm^{-2}. The very small Tafel slope of 49 mV dec^{-1} and the very high exchange current density (~0.76 mA cm^{-2}) originate from the large electrochemically active surface area and the fast mass and electron transfer efficiency of the Cuf@Ni_5P_4 catalyst. A theoretical study was performed to investigate the mechanism underlying the HER activity in Cu-supported Ni_5P_4 at an atomic scale. Density functional theory (DFT) calculations suggest a very high negative Gibbs free energy change (ΔG_{H^*}) in Ni_5P_4 (0001)/Cu (111) upon hydrogen adsorption, which is actually responsible for the excellent HER activity of the catalyst. Furthermore, it shows remarkable durability for hydrogen generation under low (10 mA cm^{-2}) and high current densities (160 mA cm^{-2}) for >84 h with ~96% retention of the overpotential, establishing a low-cost and efficient catalyst for sustainable, future energy generation strategies.

This article is part of the themed collection: Journal of Materials Chemistry A Emerging Investigators

2. M Das, N Kamboj, T Purkait, S Sarkar, and R S Dey*, Revealing the Structural Aspect of Ultrastable Self-Supportive Bifunctional Electrocatalyst for Solar-Driven Water Splitting. (***J. Phys. Chem. C* 2020, 124, 13525−13534**)

THE JOURNAL OF PHYSICAL CHEMISTRY C

pubs.acs.org/JPCC Article

Revealing the Structural Aspect of Ultrastable Self-Supportive Bifunctional Electrocatalyst for Solar-Driven Water Splitting

Manisha Das, Navpreet Kamboj, Taniya Purkait, Subhajit Sarkar, and Ramendra Sundar Dey*

Cite This: *J. Phys. Chem. C* 2020, 124, 13525−13534 Read Online

ACCESS | Metrics & More | Article Recommendations | Supporting Information

ABSTRACT: Ultrastable electrode materials for spontaneous fuel production by electrochemical water splitting have received tremendous amounts of attention, because the conventional water electrolysis system is not fully renewable as it needs power from nonrenewable sources. The design of a self-supportive and ultradurable electrocatalyst that is budget-friendly and obtained via a less time-consuming method is therefore extremely necessary to split water into hydrogen and oxygen. It is therefore important to divulge the structural information of a catalyst in order to have extraordinarily stable electrodes for a solar-driven water-electrolysis system. This paper reports a facile electrochemical method for the synthesis of single-phase Cuf@Ni_5P_4 core−shell nanostructures for overall water splitting in alkaline media. The Cuf@Ni_5P_4-based cell shows extraordinary stability in working electrolyte for 150 h at a current density of 10 mA cm^{-2} with 96% retention of its initial potential. The Cuf@Ni_5P_4||Cuf@Ni_5P_4 cell hybridized with a solar cell demonstrates the suitability of the concept toward a hybrid energy device and impulsive generation of H_2 and O_2. This versatile system opens up a new route for the generation of green fuel toward renewable energy applications.

■ INTRODUCTION

Presently, the world is facing an energy crisis, as well as global warming and climate change due to excessive use of fossil fuels.[1,2] Thus, to avoid serious issues, a route for the development of completely self-sustainable green energy technology is highly desired. An integrated self-powered ultrastable water electrolysis system with a sustainable power harvester system has immense appeal to society to meet the demand for the production of green fuel.[3,4] Fuel generation from electrolysis of water ($H_2O \rightarrow H_2 + 1/2O_2$, $E_0 = 1.23$ V) is no doubt renewable in nature,[5−8] but the electricity required to split water is still obtained from nonrenewable energy sources. An alternative way to overcome this problem is to use a self-powered system that harvests ambient energy to generate power, which can be integrated with the water electrolyzer.[9−14] There are several forms of energy available in the environment for producing electricity, like mechanical, solar, thermal, and wind energy, which are of recent research interest for a long-term need of clean and sustainable fuel generation.[15,16] An efficient and influential source of energy is solar energy for the production of electricity.[17] The photovoltaic units when coupled with electrolyzers for direct conversion of solar energy into hydrogen fuel is the best choice for energy conversion systems.[10,12,13] The proposed electrocatalyst efficiently splits water utilizing the power coming from solar panel when illuminated in a very stable way. Sivanantham et al. demonstrated a full water-splitting electrolyzer using as catalyst hierarchical $NiCo_2S_4$ nanowire arrays on Ni foam and a commercially available GaAs-based thin film solar cell for the first time, but the current density achieved in that case was very small.[18] Another example for electrochemical full water splitting using solar energy was represented by Ali Han et al. where they have shown a Janus-like Cu_3P@NF electrode, and the catalytic current density of 10 mA/cm^2 was achieved at 1.7 V when potential was supplied using a solar cell.[19] Overall, water splitting is a thermodynamically arduous reaction and demands enormously efficient and active electrode materials that considerably accelerate the sluggish kinetics of the two half-reactions ocurring simultaneously at both cathode (HER) and anode (OER).[20−22] Electrocatalysts, the heart of an electrochemical water-splitting system, is preferred to be bifunctional in nature and has attracted immense amounts of research interest since a decade. There are two critical points that should be considered for the development of a water-splitting catalyst with respect to commercialization and industrial applications. First, the electrocatalyst needs to

Received: February 18, 2020
Revised: May 20, 2020
Published: May 20, 2020

https://dx.doi.org/10.1021/acs.jpcc.0c01409
J. Phys. Chem. C 2020, 124, 13525−13534

3. M Das, G Kumar, and R S Dey*, Electrochemical growth and formation mechanism of bimetallic transition metal selenide bifunctional electrocatalyst: A strategy for the development of efficient material for water electrolysis. **(ACS Applied Energy Materials doi.org/10.1021/acsaem.1c03497)**

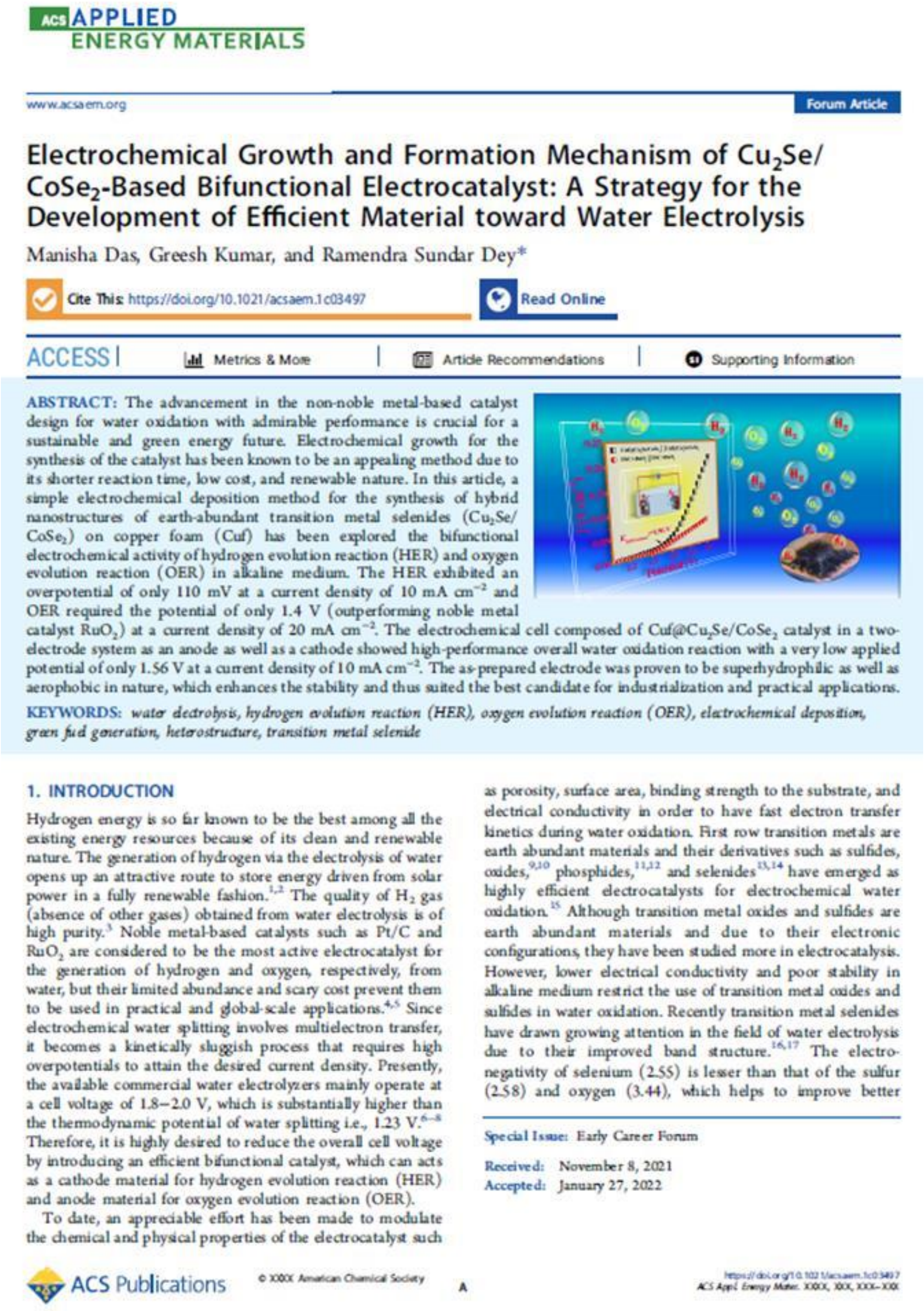

ACS APPLIED ENERGY MATERIALS

www.acsaem.org

Forum Article

Electrochemical Growth and Formation Mechanism of Cu_2Se/$CoSe_2$-Based Bifunctional Electrocatalyst: A Strategy for the Development of Efficient Material toward Water Electrolysis

Manisha Das, Greesh Kumar, and Ramendra Sundar Dey*

Cite This: https://doi.org/10.1021/acsaem.1c03497

Read Online

ACCESS | Metrics & More | Article Recommendations | Supporting Information

ABSTRACT: The advancement in the non-noble metal-based catalyst design for water oxidation with admirable performance is crucial for a sustainable and green energy future. Electrochemical growth for the synthesis of the catalyst has been known to be an appealing method due to its shorter reaction time, low cost, and renewable nature. In this article, a simple electrochemical deposition method for the synthesis of hybrid nanostructures of earth-abundant transition metal selenides (Cu_2Se/$CoSe_2$) on copper foam (Cuf) has been explored the bifunctional electrochemical activity of hydrogen evolution reaction (HER) and oxygen evolution reaction (OER) in alkaline medium. The HER exhibited an overpotential of only 110 mV at a current density of 10 mA cm^{-2} and OER required the potential of only 1.4 V (outperforming noble metal catalyst RuO_2) at a current density of 20 mA cm^{-2}. The electrochemical cell composed of Cuf@Cu_2Se/$CoSe_2$ catalyst in a two-electrode system as an anode as well as a cathode showed high-performance overall water oxidation reaction with a very low applied potential of only 1.56 V at a current density of 10 mA cm^{-2}. The as-prepared electrode was proven to be superhydrophilic as well as aerophobic in nature, which enhances the stability and thus suited the best candidate for industrialization and practical applications.

KEYWORDS: *water electrolysis, hydrogen evolution reaction (HER), oxygen evolution reaction (OER), electrochemical deposition, green fuel generation, heterostructure, transition metal selenide*

1. INTRODUCTION

Hydrogen energy is so far known to be the best among all the existing energy resources because of its clean and renewable nature. The generation of hydrogen via the electrolysis of water opens up an attractive route to store energy driven from solar power in a fully renewable fashion.[1,2] The quality of H_2 gas (absence of other gases) obtained from water electrolysis is of high purity.[3] Noble metal-based catalysts such as Pt/C and RuO_2 are considered to be the most active electrocatalyst for the generation of hydrogen and oxygen, respectively, from water, but their limited abundance and scary cost prevent them to be used in practical and global-scale applications.[4,5] Since electrochemical water splitting involves multielectron transfer, it becomes a kinetically sluggish process that requires high overpotentials to attain the desired current density. Presently, the available commercial water electrolyzers mainly operate at a cell voltage of 1.8–2.0 V, which is substantially higher than the thermodynamic potential of water splitting i.e., 1.23 V.[6−8] Therefore, it is highly desired to reduce the overall cell voltage by introducing an efficient bifunctional catalyst, which can acts as a cathode material for hydrogen evolution reaction (HER) and anode material for oxygen evolution reaction (OER).

To date, an appreciable effort has been made to modulate the chemical and physical properties of the electrocatalyst such as porosity, surface area, binding strength to the substrate, and electrical conductivity in order to have fast electron transfer kinetics during water oxidation. First row transition metals are earth abundant materials and their derivatives such as sulfides, oxides,[9,10] phosphides,[11,12] and selenides[13,14] have emerged as highly efficient electrocatalysts for electrochemical water oxidation.[15] Although transition metal oxides and sulfides are earth abundant materials and due to their electronic configurations, they have been studied more in electrocatalysis. However, lower electrical conductivity and poor stability in alkaline medium restrict the use of transition metal oxides and sulfides in water oxidation. Recently transition metal selenides have drawn growing attention in the field of water electrolysis due to their improved band structure.[16,17] The electronegativity of selenium (2.55) is lesser than that of the sulfur (2.58) and oxygen (3.44), which helps to improve better

Special Issue: Early Career Forum

Received: November 8, 2021
Accepted: January 27, 2022

4. M Das,[†] Ashmita Biswas,[†] and R S Dey* Electrons on Play: Understanding the Synergism of Binary Transition Metals and Role of M-N-S Active Sites Towards Oxygen Electrocatalysis. 2021, **(Chem. Commun., 2022,58, 1934-1937)**

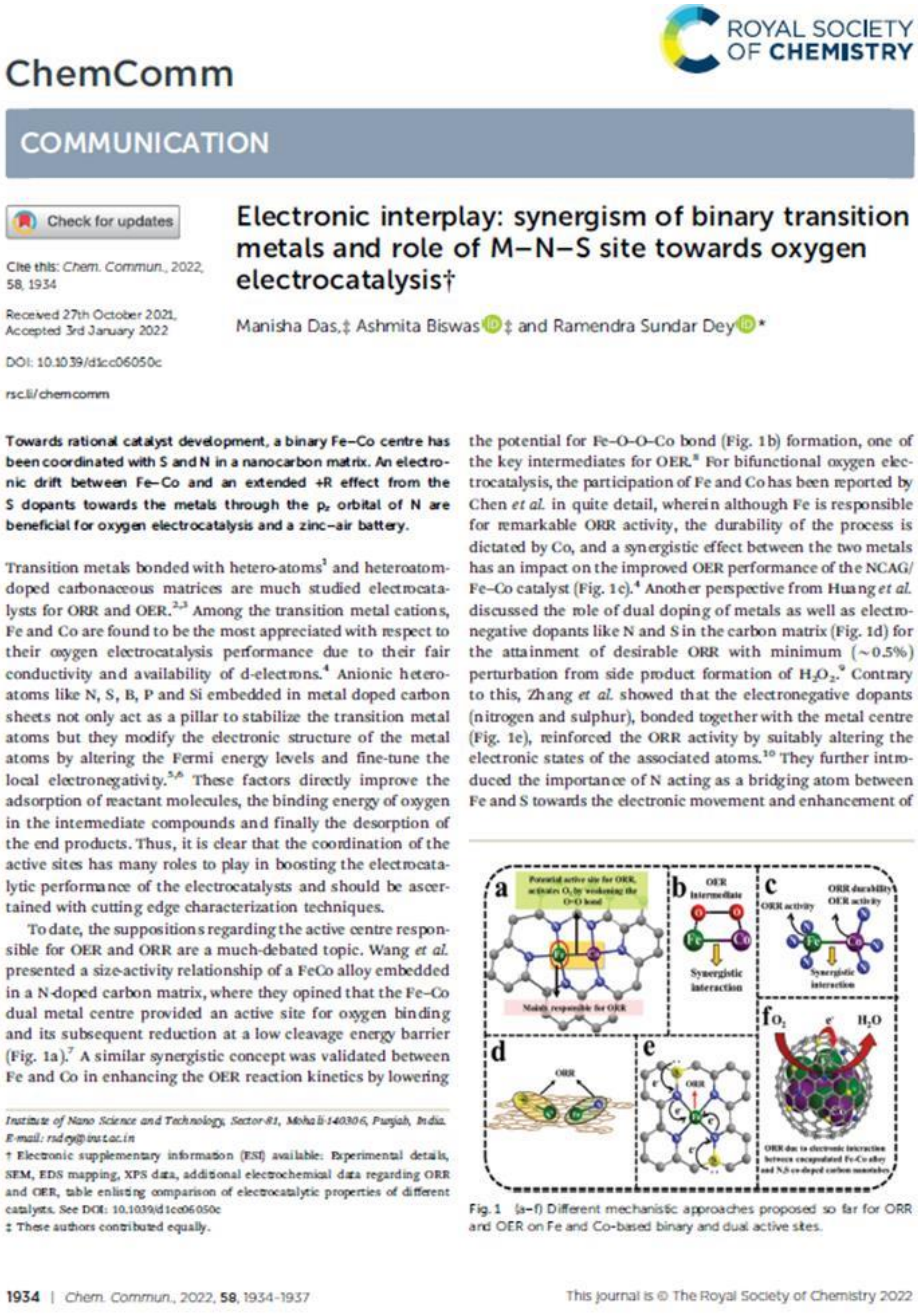

ChemComm

COMMUNICATION

Cite this: *Chem. Commun.*, 2022, 58, 1934

Received 27th October 2021, Accepted 3rd January 2022

DOI: 10.1039/d1cc06050c

rsc.li/chemcomm

Electronic interplay: synergism of binary transition metals and role of M–N–S site towards oxygen electrocatalysis†

Manisha Das,‡ Ashmita Biswas ‡ and Ramendra Sundar Dey *

Towards rational catalyst development, a binary Fe–Co centre has been coordinated with S and N in a nanocarbon matrix. An electronic drift between Fe–Co and an extended +R effect from the S dopants towards the metals through the p_z orbital of N are beneficial for oxygen electrocatalysis and a zinc–air battery.

Transition metals bonded with hetero-atoms[1] and heteroatom-doped carbonaceous matrices are much studied electrocatalysts for ORR and OER.[2,3] Among the transition metal cations, Fe and Co are found to be the most appreciated with respect to their oxygen electrocatalysis performance due to their fair conductivity and availability of d-electrons.[4] Anionic hetero-atoms like N, S, B, P and Si embedded in metal doped carbon sheets not only act as a pillar to stabilize the transition metal atoms but they modify the electronic structure of the metal atoms by altering the Fermi energy levels and fine-tune the local electronegativity.[5,6] These factors directly improve the adsorption of reactant molecules, the binding energy of oxygen in the intermediate compounds and finally the desorption of the end products. Thus, it is clear that the coordination of the active sites has many roles to play in boosting the electrocatalytic performance of the electrocatalysts and should be ascertained with cutting edge characterization techniques.

To date, the suppositions regarding the active centre responsible for OER and ORR are a much-debated topic. Wang *et al.* presented a size-activity relationship of a FeCo alloy embedded in a N-doped carbon matrix, where they opined that the Fe–Co dual metal centre provided an active site for oxygen binding and its subsequent reduction at a low cleavage energy barrier (Fig. 1a).[7] A similar synergistic concept was validated between Fe and Co in enhancing the OER reaction kinetics by lowering the potential for Fe–O–O–Co bond (Fig. 1b) formation, one of the key intermediates for OER.[8] For bifunctional oxygen electrocatalysis, the participation of Fe and Co has been reported by Chen *et al.* in quite detail, wherein although Fe is responsible for remarkable ORR activity, the durability of the process is dictated by Co, and a synergistic effect between the two metals has an impact on the improved OER performance of the NCAG/Fe–Co catalyst (Fig. 1c).[4] Another perspective from Huang *et al.* discussed the role of dual doping of metals as well as electronegative dopants like N and S in the carbon matrix (Fig. 1d) for the attainment of desirable ORR with minimum (~0.5%) perturbation from side product formation of H_2O_2.[9] Contrary to this, Zhang *et al.* showed that the electronegative dopants (nitrogen and sulphur), bonded together with the metal centre (Fig. 1e), reinforced the ORR activity by suitably altering the electronic states of the associated atoms.[10] They further introduced the importance of N acting as a bridging atom between Fe and S towards the electronic movement and enhancement of

Fig. 1 (a–f) Different mechanistic approaches proposed so far for ORR and OER on Fe and Co-based binary and dual active sites.

Institute of Nano Science and Technology, Sector-81, Mohali-140306, Punjab, India. E-mail: rsdey@inst.ac.in

† Electronic supplementary information (ESI) available: Experimental details, SEM, EDS mapping, XPS data, additional electrochemical data regarding ORR and OER, table enlisting comparison of electrocatalytic properties of different catalysts. See DOI: 10.1039/d1cc06050c

‡ These authors contributed equally.